Chambres MICROMEGAS pour la calorimétrie hadronique, recherche d'une nouvelle physique dans le domaine du quark top

Ambroise Espargilière

UNIVERSITÉ DE GRENOBLE

THÈSE

Pour obtenir le diplôme de

DOCTEUR DE L'UNIVERSITÉ DE GRENOBLE

Spécialité : **Physique/Physique Subatomique & Astroparticules**

Arrêté ministérial : 7 août 2006

Présentée par

AMBROISE ESPARGILIÈRE

Thèse dirigée par **Catherine ADLOFF**
et codirigée par **Yannis KARYOTAKIS**

préparée au ***Laboratoire d'Annecy-le-vieux de Physique des Particules***
et de **l'École Doctorale de Physique de Grenoble**

Chambres MICROMEGAS pour la Calorimétrie Hadronique, Recherche d'une Nouvelle Physique dans le Domaine du Quark Top

R&D pour un futur collisionneur linéaire

Thèse soutenue publiquement le **21 septembre 2011**,
devant le jury composé de :

Dr. Jean-Jacques BLAISING
Directeur de Recherche au LAPP, Annecy-le-Vieux, Président
Dr. Felix SEFKOW
Directeur de Recherche à DESY, Hambourg, Rapporteur
Dr. Paul COLAS
Directeur de Recherche au CEA, Saclay, Rapporteur
Dr. Yorgos TSIPOLITIS
Professeur associé au N.T.U.A., Athènes, Examinateur
Dr. Lucie LINSSEN
Directeur de Recherche au CERN, Genève, Examinateur
Dr. Yannis KARYOTAKIS
Directeur du LAPP, Annecy-le-Vieux, Examinateur
Dr. Catherine ADLOFF
Maitre de Conférence à l'Université de Savoie, Chambéry, Directeur de thèse

Thesis of Ambroise Espargilière
Under the direction of Dr. Catherine Adloff and Dr. Yannis Karyotakis.

MICROMEGAS Chambers for Hadronic Calorimetry, Search for New Physics in the Field of the Top Quark

R&D towards a future linear collider

À ma famille, mes amis et mes professeurs
qui m'ont construit
et me permettent aujourd'hui d'écrire ces quelques lignes.
Et à Dorothée et Célestin,
pour qui j'écris toutes les autres ...

Contents

Introduction

This document reports on the work performed during my thesis at LAPP under the direction of Dr. Catherine Adloff and Dr. Yannis Karyotakis for the period starting from October 2008 to the end of September 2011. My thesis lies in the framework of the preparation of future linear e^+e^- collider experiments. This manuscript is divided into three parts.

The first part introduces various topics useful for the understanding of the two other parts. It offers in chapter 1 an overview of what is particle physics and why large experiments like LHC or ILC are designed. Chapter 2 is an introduction to particle acceleration and collision and then to detectors, with emphasis on calorimetry.

The second part reports on the R&D for prototypes of gaseous detectors called MICROMEGAS. Chapter 3 introduces the concept of gaseous detectors through a brief history of their development and then presents in details the MICROMEGAS technology and the R&D project. X-ray laboratory tests of our prototypes are described in chapter 4 and beam tests at CERN in chapter 5. Chapter 6 presents the global activities and main results of our group at LAPP in the global effort towards future linear colliders. Chapter 7 concludes this part.

The third part reports on physics simulation studies in the framework of the CLIC experiment. Chapter 8 describes the production and detection of top quark pairs at CLIC and chapter 9 shows how the top quark becomes a window to new physics through the study of a non SUSY model predicting an additional Z' boson together with a Dark Matter candidate. Chapter 10 concludes the last part.

Ce document rapporte le travail réalisé au cours de ma thèse au LAPP sous la direction des Dr. Catherine Adloff et Yannis Karyotakis pour la période allant d'octobre 2008 à septembre 2011. Ma thèse réside dans le cadre de la préparation des expériences auprès des futurs collisionneurs linéaires e^+e^-. Ce manuscrit est divisé en trois parties. A la fin de chaque chapitre, un résumé en langue française rassemble les principaux points abordés dans celui-ci.

La première partie introduit divers sujets utiles à la compréhension des deux autres parties. Elle offre dans le chapitre 1 un aperçu de ce qu'est la physique des particules et de pourquoi de grandes expériences comme LHC et ILC sont conçues. Le chapitre 2 est

une introduction à l'accélération et à la collision des particules puis aux détecteurs avec un accent particulier sur la calorimétrie.

La seconde partie relate l'activité de R&D sur des prototypes de détecteurs gazeux nommés MICROMEGAS. Le chapitre 3 introduit le concept de détecteur gazeux à travers un bref historique de leur développement et présente ensuite la technologie MICROMEGAS ainsi que notre projet de R&D. Des tests en rayons X de nos prototypes sont décrits dans le chapitre 4 et des tests en faisceaux au CERN dans le chapitre 5. Le chapitre 6 présente plus globalement les activités du groupe ainsi que les principaux résultats. Le chapitre 7 conclut cette partie.

La troisième partie relate des études de simulation de physique dans le cadre de l'expérience CLIC. Le chapitre 8 décrit la production et la détection de paires de quarks top à CLIC et le chapitre 9 montre comment le quark top devient une fenêtre sur la nouvelle physique à travers l'étude d'un modèle non super-symétrique prédisant un boson additionnel ainsi qu'un candidat de matière noire. Le chapitre 10 conclut cette dernière partie. Des résumés en français de chaque chapitre sont fournis à la fin de ces derniers. Dans le cas des chapitres de conclusion une simple traduction est donnée.

Part I

Introductory Topics

CHAPTER 1

Fundamental particles

In this chapter, a brief description of particle physics is given together with a landscape of today experiments in particle and astro-particle physics and their main goals.

1.1 Glimpse of Particle Physics

Particle physics is the field of physics dealing with the smallest and most fundamental constituents of our universe and the laws governing their behaviour and properties. Matter divisibility has been studied for centuries and Democritus (460 BC – 370 BC) was already speaking of *atoms* and building a theory of their interactions[1]. The fundamental question concerning the origin of the Universe has been also present in the human mind since thought began. Such questions are the basis of fundamental science and especially particle physics. More and more complex theories and experiments have been conceived in the hope one day to unveil some of the deepest mysteries of nature.

In the following a succinct overview of the present day knowledge about the fundamental particles and the way they interact with each other is presented.

1.1.1 Particles and their interactions

Fundamental particles The particles that are dealt with in this field are the most basic constituents of matter. Imagine scratching a piece of wood, say. You would get small fragments that you can break into smaller and smaller fragments, if you spent enough time on it. With improving technology you would obtain molecules composing the wood (*e.g.* cellulose, water, ...) and you would manage to break it further into fragments as well until you break them into single atoms. These atoms were originally considered to be the most basic bricks of matter (atoms ($\alpha\tau o\mu o\zeta$) = "what can't be split"). Since then, they were also found to be composed of tinier particles, electrons and

[1] Democritus' atomism presents the universe as a discontinuous assembly of undividable elementary particles baptised "atoms". These atoms differ from each other only by their shape. Their shape deffines the way they can assemble into larger compounds *i.e.* the way they interact with each other.

nucleons. Today the electrons are still considered as fundamental but the nucleons are known to be composed of quarks bound together by gluons (Murray Gell-Mann, Nobel price in 1969). The 20^{th} century has seen the birth of the modern theory of fundamental particles and their interactions, namely the Standard Model (SM). The fundamental particles are divided into two groups, namely the fermions, which constitute the matter, and the bosons, which transmit the interactions. The group of the fermions is divided into two families: the leptons and the quarks. For each of the stable fermions some "big brothers" have also been discovered (*e.g.* the muon for the electron or the strange quark for the down quark). These have similar properties but a higher mass and a shorter lifetime.However, the case of neutrinos is somehow different since their mass is unknown and they are all stable. Three generations of particles have thus been established. The lepton and the quark families are thus further divided into those three generations, each comprising a pair of particle. The electron and his heavier siblings, the muon and the tau, are paired with their corresponding neutrino to constitute the lepton family. The electron, the muon and the tau have the same electric charge $Q_{\text{e}} = 1.6 \cdot 10^{-19}\,C$ while the neutrinos are electrically neutral. The quarks constitute the second family, each generation is also organised in pair of one quark of positive charge ($Q_{\text{up}} = 2/3\,Q_{\text{e}}$) and one quark of negative charge ($Q_{\text{down}} = -1/3\,Q_{\text{e}}$). The structure of the particle families is represented in table 1.1 where the list of the bosons is also given.

Table 1.1: Summary of the known fundamental particles

Fermions				Bosons
leptons	Electron	Muon	Tau	Photon
	Neutrino e	Neutrino μ	Neutrino τ	Z^0
quarks	Up	Charm	Top	$W^{\pm}$
	Down	Strange	Bottom	Gluon
				Higgs
				Graviton

Fundamental interactions Interactions between fundamental particles are due to an exchange of another class of particles, called vector bosons. There are four ways for those particles to interact: the four fundamental interactions, characterised by the nature of the vector boson responsible for it. In the following, the four interactions are qualitatively described and their relative intensity is given for low energy scales[2].

- The electromagnetic interaction: every charged particle is sensitive to the electromagnetic interaction. This means that they are able to emit and capture a photon, which is the vector boson of this interaction. The electric charge is a scalar number.

- The strong interaction: only the quarks and the particles composed of them (the hadrons) are sensitive to this interaction. The vector boson is the gluon. Their is an analogous of the electric charge called the *colour charge* with the difference that

[2]The relative intensity of the interactions evolves with the energy at which the experiment is performed, for instance the weak and electromagnetic end up with the same intensity above energies around 200 GeV (electroweak scale) and merge into the so-called electroweak force.

it is not a scalar number. There are three "colours" that can be handled like the set of complex numbers $\{1, \frac{1+i\sqrt{3}}{2}, \frac{1-i\sqrt{3}}{2}\}$. There are 8 different gluons carrying the colour charge from one quark to another. The intensity of this interaction is 100 times higher than the electromagnetic force.

- The weak interaction: all fermions are sensitive to this interaction. It allows unstable particles to decay into lighter and more stable ones, it plays then a major role in radioactivity and in flavour physics. There are three vector bosons, namely the Z^0, the W^+ and the W^-. The intensity of this interaction is 1000 times weaker than the electromagnetic interaction (justifying the name).

- The gravitational interaction: Well described by classic and relativistic mechanics, all particles feel gravity. Particle physics expects also that a vector boson for this interaction should exist, the graviton. It has not been discovered yet. The intensity of the gravitation is extraordinary feeble, 10^{-37} times the electromagnetic interaction intensity.

Composite particles Fundamental particles are often (or always for some of them) bound into systems of particles which can appear as particles on their own. In nature, electrons are usually found bound into the electronic cloud of an atom, the other leptons are usually free[3]. However, the case of quarks is different because the strong interaction is so intense, and even increasing with distance, that quarks are always confined into some kind of composite systems. In terms of the colour charge carried by quarks, schematically, a system must be white, *i.e.* hold an equal amount of the three colours or one colour for one quark together with the corresponding anti-colour carried by an anti-quark. If sufficient energy was given to tear apart a system of quarks, the binding energy between them would be enough to create a pair of quark/anti-quark so that each out-going quark finds a new partner and recreates a new "white" particle. This explains why neither quarks, nor any coloured object, have been observed freely so far, with the exception of the top quark, as described in [1].

The most classical example of such a composite system is the proton, which consist of three light quarks (up, up, down) bound together by the strong interaction. The same stands for the neutron, differing only by the nature of one of the three quarks (up, down, down). The proton and the neutron are the most stable members of a family of composite particles known as the baryon family. The baryon family gathers together all the composite particles made of three quarks. The particles composed of one quark bound to an anti-quark are classified into the meson family. The most stable of these are charged pions and kaons. Baryons and mesons are two subdivisions of a broader family called hadrons, that gathers together all the particles subject to the strong interaction (*i.e.* made of quarks).

1.1.2 The quarks

During the 50's and the early 60's a large number of new particles were discovered in cosmic rays as well as in particle accelerators. To explain this large number of observed

[3]The muon, due to it's rather long life time ($\approx 2\,\mu$s), might form transient electromagnetic bound states before decaying — *e.g.* muonic hydrogen

particles, in 1964 Murray Gell-Mann [2] and George Zweig [3] proposed a model involving only a few fundamental particles. These particles were capable of forming many combinations, representing all the so-called hadrons already detected as well as more of them waiting to be discovered. These fundamental particles were fancily called "quark"[4] by Gell-Mann whereas Zweig named them "*Aces*". Gell-Mann's name prevailed and the model proved very successful. The large range of new particles gave birth to the particle family called hadron (from the Greek *hadros* meaning strength). The hadrons are not fundamental particles, they are made out of quarks and anti-quarks bound together by the strong nuclear interaction.

The observations called for three different quarks: the up quark u, the down quark d and the strange quark s, with the properties shown in table 1.2.

name	symbol	spin	charge
up	u	1/2	2/3 e
down	d	1/2	-1/3 e
strange	s	1/2	-1/3 e

Table 1.2: The three quarks in 1964. Symbol e denotes the electronic elementary charge.

Nevertheless, this model was not fully satisfactory. Although the three flavours were able to explain and predict the diversity of the hadrons, they posed a theoretical issue regarding for instance the weak interaction. The weak current should be written in the form

$$J_\mu = \bar{q}_1 \gamma_\mu (1 + \gamma_5) q_2 \,,$$

but the weak interaction should not discriminate the down quark from the strange one, so $\bar{q}_1$ can be replaced by $\bar{u}$, but q_2 should stand for a mixing of d and s. If one defines a mixing angle θ, two mixed states then appear:

- $d_{\text{mix}} = \cos\theta\, d + \sin\theta\, s$
- $s_{\text{mix}} = -\sin\theta\, d + \cos\theta\, s$

One of them must be chosen to write the expression of the weak current, say d_{mix}. Then:

$$J_\mu = \bar{u} \gamma_\mu (1 + \gamma_5) d_{\text{mix}}$$

and s_{mix} is left free by the weak interaction. This idea was a bit disturbing and Sheldon Glashow, Jean Iliopoulos and Luciano Maiani, in 1970 [4], proposed to *magically*[5] introduce a fourth quark, called *charm*, denoted c, to restore the symmetry between the up-like quarks and the down-like ones. This assumption was not warmly welcomed. However, this model predicted a new scope of hadrons not yet discovered and was therefore experimentally verifiable. In 1974, the J/ψ[6] was discovered to prove them right.

[4] Gell-Mann introduced this name by simply evoking the book from James Joyce, *Finnegan's Wake* (reference number 6 in [2]), the word "quark" appears once in chapter 4 of the second volume in the sentence: "*three quarks for Muster Marks*", which exact meaning is not obvious.

[5] Like casting a spell, or a *charm*. This is the actual origin of the name *charm* for the fourth quark.

[6] The charm/anti-charm meson ($c\bar{c}$).

With the discovery of the charm quark, the model was fully symmetric and satisfactory. But in 1976 at Stanford Linear Accelerator Center, California (SLAC) and 1976 at Fermi National Accelerator Laboratory, Illinois (FNAL) respectively, the tau lepton and the b quark were also discovered. Together with the tau lepton, a tau-flavoured neutrino was expected and, to restore the symmetry, an up-like companion of the bottom quark was already baptised "*top*". According to the mass hierarchy between the known quarks, the mass of the top quark was expected of the order of $10\,\mathrm{GeV}/c^2$. But only in 1993, Large Electron Positron collider (LEP) electroweak data predicted the top mass around $166\,\mathrm{GeV}/c^2$ [5] and the latter was finally discovered in 1995, in the 2 TeV $p\bar{p}$ collisions of the Tevatron at Fermilab with a mass of $175\,\mathrm{GeV}/c^2$.

1.1.3 Standard Model

The so-called Standard Model (SM) is the theoretical framework encompassing all the laws describing the behaviour and interactions of the particles described above except gravitation. Particles are represented by quantised fields (generalisation of the quantum wave functions) and their interactions correspond to transformations of those fields. Each interaction corresponds to a different set of symmetries of the SM Lagrangian[7]. These sets of symmetries have the properties of algebraic groups.

- Electromagnetic interaction corresponds to the unitary group $U(1)$
- Weak interaction, to the special unitary group of dimension 2, $SU(2)$,
- Strong interaction to the special orthogonal group of dimension 3, $SU(3)$.

The SM is therefore based on the cross product of these three groups as:

$$G_{\mathrm{SM}} = SU(3) \otimes SU(2) \otimes U(1)$$

So far this model have described with outstanding precision most of the observed phenomena in particle physics. However, many reasons (described later in sections 1.2) lead to the conclusion that a deeper theory should exist.

1.2 Today's questions and experiments

Today's questions are somehow the same as ever. *Where do we come from?* , *what are we made of?* ... But the way to ask them has evolved. Today, particle physicists wonder about the final block of the SM, namely the Higgs boson, and about the physics beyond it. Many theories have been imagined with the ultimate aim to gather within a single framework all fundamental laws of nature from which every phenomenon would derive. Such theories are often referred to as the Grand Unified Theory (GUT) or Theory Of Everything (TOE). In this section, some hints about why the present SM is not sufficient are summarised, and therefore why a new theory is needed.

With the start of the Large Hadron Collider (LHC) at the *Organisation Européenne pour la Recherche Nucléaire* (CERN), the discovery of the last missing SM particle, the

[7] A Lagrangian is a mathematical quantity, having the dimension of an energy, to which the Euler-Lagrange equation is applied to produce the equation of evolution of the system.

Higgs boson, is perhaps just around the corner. Its existence or non-existence will be definitively proven. But particle physics will not come to an end when this question is answered. The SM, as suggested by the name, is a model and not a complete theory. Although its predictive power is stunningly precise, the SM still relies on several free parameters that are only given by experimental measurements. A satisfactory theory would link them altogether to very few fundamental constants. However, this is perhaps mainly an aesthetic argument. Another argument is yet only false assumption of the SM. Neutrinos are taken massless but the observed oscillation phenomenon is only possible if they have mass.

There are two other arguments towards the non-completeness of the SM. Each one is sufficient on its own to prove that the SM is not complete. The first one is the existence of black holes, predicted and described by general relativity but completely absent from the SM which does not include gravitational interaction. What may happen in the vicinity of the centre of a black hole is completely beyond our current knwoledge. Such a concern addresses gravity and microscopic physics at once and would be studied in the framework of some quantum gravity theory. Quantum gravity has been addressed since the thirties and was already a step beyond the present SM (see an historical review of quantum gravity in [6]). The second argument is the mystery of Dark Matter (DM): one of the main components of our universe and which seems only sensitive to gravitation. The first clues of invisible matter influencing the behaviour of galaxies was given in 1933 thanks to the observation of the coma galaxy cluster and was first considered as due to imprecisions in the computation methods [7]. The mass of the galaxies computed from light emission did not match the mass computed from the star velocity profiles for at least one order of magnitude. It is now broadly admitted that the Universe energy budget holds about 5% of stable baryonic "ordinary" matter and ≈25% of this DM the remaining beeing the so-called dark energy. About 90% of the mass of the galaxies is due to DM and no particle within the SM gathers the properties of a DM particle.

Therefore, there is physics expected beyond the SM. There exist many models describing as many possible extensions or even replacements of the SM. They predict a wide range of effects that might be detected in current of future experiments. Among these, the Super Symmetry (SUSY), one of the most popular, predicts that to every presently known particle corresponds a "super-partner" with spin shifted of 1/2. This theory, based on a symmetry of the SM Lagrangian, naturally predicts a particle that gather the expected properties of DM. Aside of those fundamental questions, there is also a need to measure ever more precisely the SM parameters, for the knowledge itself but as well because new physics models expect deviations from the SM predictions that can only be detected if the SM parameters are very well known.

The only way to get answers to those questions is to conceive and build dedicated experimental instruments. Today's most famous one is the LHC with its four large experiments "A Toroidal Large System" (ATLAS), "Compact Muon Solenoid" (CMS), "A Large Ion Collider Experiment" (ALICE) and "LHC experiment for B physics" (LHCb). The older American $p\bar{p}$ accelerator Tevatron is running as well, at a lower energy and lower luminosity with two experiments D0 and CDF. Its stop is scheduled for the end of the year 2011. The LHCb detector is optimised for the study of the b quark through the observation of B mesons, it takes over the Babar and Belle experiments that ended recently and is now the only running B-factory. ALICE is dedicated to the

observation of heavy ion collisions to study the physics of the very first moments of the universe, immediately after the big-bang. More precisely ALICE has the objective to study the plasma of quarks and gluons that should elusively appear in multi-TeV collisions of gold or lead nuclei. ATLAS, CMS, CDF, and D0 are generalist experiments designed for a wide range of studies with a high discovery potential. CDF and D0 have discovered the top quark in the mid 90's [8] and they still have a chance to get hints on the Higgs boson. But, with the LHC high luminosity, ATLAS and CMS are now at the front line for the next discoveries. Those two experiments will allow cross checked measurements towards the discovery of the Higgs boson, but as well many aspects of new physics. If SUSY happens to be a true symmetry of nature, then it will be discovered in the years to come. The experimental measurements may soon discriminate among the many new physics scenarios.

Particle physics does not only take place in collider facilities. Fixed targets experiments are developed for neutrino physics for instance (OPERA, T2K), large neutrino telescopes are being built as well (ANTARES, AMANDA). Ground gamma observatories are set for the study of the cosmic rays and the search for DM (HESS, MAGIC). The detector AMS looks for DM and anti-matter anomalies in the cosmic rays directly from space. Giant interferometers (VIRGO, LIGO) are "listening" to gravitational wave bursts predicted by general relativity at the coalescence of two compact object (neutron stars or black holes).

Since the SM has been established, for the first time in history, new theories and models have grown without experimental facts neither to guide them nor to validate or invalidate them. With all the present day starting experiments in particle and astro-particle physics, new experimental data will soon be made available and will give a strong input to theories and might deeply affects our understanding of the universe.

1.3 New Physics

The needs for physics beyond the Standard Model have been mentioned in section 1.2. The main reasons are summarised here:

- Gravitation is not described in the standard model, but compact cosmic objects like black holes need a quantum description of gravitation. The description of the very early universe also calls for quantum gravity [6].

- Luminous matter only accounts for $\approx 1\%$ of the universe mass ($\approx 5\%$ if considering all ordinary baryonic matter), 25% of universe energy content is made of the so-called Dark Matter (DM) and wich is mainly due to unknown particles, absent from the SM. The remaining 70% is accounted for by the so called Dark Energy about which very little is known.

- Neutrino flavour oscillations prove these particles to have a non zero mass, but in the minimal SM they must be massless [9].

- The coupling constants of the fundamental interactions tend to shift towards each other at higher energies giving a hint of unification of all interactions at very high energies ($O(10^{16}\,\text{GeV})$). But within the SM they do not converge, whereas in extensions like Super Symmetry (SUSY) they do.

- The hierarchy problem concerns the apparent huge gap between scales in laws of nature like the difference between gravity intensity and the other forces, or the Plank energy scale ($O(10^{19}\,\mathrm{GeV})$), the grand unification scale ($O(10^{16}\,\mathrm{GeV})$) and the electroweak symmetry breaking scale($O(200\,\mathrm{GeV})$). The SM does not provide any answer to this problem, whereas many extensions do.

Many solutions have been envisioned to solve these problems and unify all fundamental interactions into a single framework called Grand Unified Theory (GUT) or Theory Of Everything (TOE). Among the most promising ones are the Super Symmetric (SUSY) theories like String Theory and the M-Theory and the Universal Extra Dimension (UED) theories like Kaluza-Klein (KK) and Randall-Sundrum (RS) theories.

1.3.1 Super Symmetry

SUSY is probably the most studied solution towards physics beyond the SM. SUSY is an external transformation extending the the Poincaré transformation group[8]. It was demonstrated in 1967 by Coleman and Mandula [10] that no symmetries of nature could be added to the Poincaré group. However this theorem is bound to assumptions that might be loosened. The Poincaré algebra relies solely on commutation relations, but, by allowing anti-commutation relations as well, a new transformation becomes possible. This new transformation casts fermonic states onto completely identical bosonic ones and *vice versa*. This transformation was soon envisioned as a new (broken) symmetry of nature in the framework of the String theory.

By considering the minimal SUSY extension of the SM (Minimal Super-symmetric Standard Model (MSSM)), no new interaction is proposed, the only modification is due to the fermion/boson matching. As the SM particles can't be super-partners of each others, new particles must be included, the number of particles must therefore be doubled and the SM Higgs boson is replaced by a system of 5 Higgs bosons (a pseudo scalar A, two neutral scalar, H_1^0 and H_2^0, and two charged ones, H^+ and H^-). Another quantity is necessary to maintain the proton stability, an additional quantum number of the particles, called R-parity, that must be conserved in any interaction, defined as:

$$\mathrm{R_p} = (-1)^{3(B-L)+2S}\,,$$

where B is the baryonic number, L the leptonic number and S the spin of the particle. Immediately, one can verify that the R-parity takes the value 1 for all SM particles and the value -1 for all their super-partners.

Naming convention and notation The bosonic super-partners have the same name as their SM fermionic partner but with the 's' letter prefixed. For instance, the super-partner of the electron is named "selectron". The fermionic super partners have the same name as their SM bosonic partner but with the 'ino' suffix. The super partner of the photon is then the "photino" and the one of the Higgs boson is the Higgsino. The symbols denoting the super-partners are the same as the corresponding SM particles but with a tilde accentuation, *e.g.* $\tilde{e}$ for the selectron.

[8] Usual group of classical rotations, translations in space and time and relativistic Lorentz boost

In addition to the proton stability, the conservation of R-parity prevents the Lightest SUSY Particle (LSP) to decay into SM particles and therefore ensures its stability as well. The LSP arises from the mixing of the bino ($\tilde{B}$ super-partner of the B boson), the wino ($\tilde{W}$) and the two neutral Higgsinos ($\tilde{H^{\pm}}$) and is called neutralino 1 ($\tilde{\chi}_1^0$). This neutralino has the right properties to play the role of dark matter particle. Much more about SUSY can be found for instance in [11, 12, 13] and references therein.

1.3.2 Kaluza-Klein models

Through a completely different, however compatible approach, the SM incompleteness may be solved by considering that space is not three dimensional but that extra dimensions, invisible to us, are influencing the microscopic realm. The first use of extra space dimensions was aimed to unify Einstein equations of gravity with those of electromagnetism. The idea was first evoked in 1914 by Gunnar Nordström [14], then, independently, by Theodor Kaluza in 1921 [15] and Oscar Klein in 1926 [16] who explained the non-observability of a fifth dimension by requiring it to be periodic around a tiny radius. They found that considering a fifth dimension (*i.e.* a fourth space dimension) allows an action to be built that could, on the one hand, lead to Einstein's equation of General Relativity

$$R_{\mu\nu} - \frac{1}{2} g_{\mu\nu} R = 0\,,$$

where $R_{\mu\nu}$ is the Ricci tensor[9], $g_{\mu\nu}$ is the space time metric and $R = R^{\mu}_{\ \mu}$ the scalar curvature, and on the other hand, this 5-dimensional action also led to Maxwell's relativistic equations of electromagnetism

$$\begin{aligned} \partial_\mu F^{\mu\nu} &= 0 \\ \partial_\mu {}^*F^{\mu\nu} &= 0\,, \end{aligned}$$

with $F^{\mu\nu} = \partial^\mu A^\nu - \partial^\nu A^\mu$ is the Electromagnetic tensor, ${}^*F^{\mu\nu} = \frac{1}{2}\epsilon_{\mu\nu\rho\sigma}F^{\rho\sigma}$ it's Hodge dual, $A^\mu = (V/c, \vec{A})^T$ being the electromagnetic potential four-vector and $\epsilon_{\mu\nu\rho\sigma}$ the krœnecker tensor[10].

However, these early theories did not take into account of the weak and strong nuclear forces which were not known before the 70's. The present day SM unifies into a single theoretical frame the electromagnetic, the weak and the strong interactions, but so far has failed to include gravitation.

More recently, an original approach to extra dimensions was proposed by Lisa Randal and Raman Sundrum [17] where a single compact curled dimension is added as a phase. Namely, an elementary path length ds^2, which in the conventional four-dimensional space time reads

$$ds^2 = g_{\mu\nu} dx^\mu dx^\nu\,,$$

would now read

$$ds^2 = e^{-2kr_c\phi} g_{\mu\nu} dx^\mu dx^\nu + r_c^2 d\phi^2\,,$$

[9] The Ricci tensor only depends on the space-time metric: $R_{\alpha\beta} = \Gamma^{\epsilon}_{\alpha\beta,\epsilon} - \Gamma^{\epsilon}_{\alpha\epsilon,\beta} + \Gamma^{\epsilon}_{\epsilon\sigma}\Gamma^{\sigma}_{\alpha\beta} - \Gamma^{\epsilon}_{\beta\sigma}\Gamma^{\sigma}_{\epsilon\alpha}$, with $\Gamma^{\alpha}_{\beta\gamma} = \frac{1}{2}g^{\alpha\epsilon}(g_{\beta\epsilon,\gamma} + g_{\gamma\epsilon,\beta} + g_{\beta\gamma,\epsilon})$, $X_{YZ,\alpha} = \frac{\partial X_{YZ}}{\partial q^\alpha}$ being the derivative of X_{YZ} along the α^{th} dimension.

[10] $\epsilon_{\mu\nu\rho\sigma} = 1$ for $\mu\nu\rho\sigma$ in circular permutation of 1234, -1 for anti-circular permutation and 0 otherwise.

where $\phi \in [0, \pi]$ is the extra-dimension coordinate[11], r_c is the radius of this circular extra-dimension and k is a scaling constant that should be of the order of the Planck scale. The first success of this theory was to explain the large hierarchy between TeV and Planck scales ($O(10^{19}\,\text{GeV})$) as a consequence of this small extra dimension and and a very small hierarchy between fundamental parameters, namely $kr_c \sim 10$.

The framework of RS theory has led further theoretical investigation to raise it as a GUT. Some details are expressed in [18, 19] where a non SUSY dark matter candidate is identified in RS context in the form of a right handed neutrino.

1.3.3 The expected role of the top quark

After its discovery in 1995, its intrinsic properties were carefully measured (mass, width, couplings, decay channel branching ratios). Because of its surprisingly large mass ($\approx$ the mass of a gold nucleus), the top quark is expected to play a key role in the physics beyond the standard model. This high mass of the top quark goes together with an incredibly short life time of $5 \cdot 10^{-25}$ s [20] which falls below the characteristic Quantum Chromo-Dynamics (QCD) hadronisation time of $2.8 \cdot 10^{-24}$ s. This aspect implies that the top quark does not have time to form any bound state before decaying and therefore the top quarks is so far the only observable free coloured object. A glimpse of some aspects of the top physics is presented in this section. An overview of top physics can be found in [21] and references therein and in [1].

- Many non SUSY models predict anomalous coupling of the top quark to the weak gauge bosons Z^0 and W. The International Linear Collider (ILC), for instance, is expected to measure those couplings at a 1% accuracy.

- The largely dominant decay mode of the top is into W and b, taken to be 100% presently. The large mass of the top quark may allow it to decay into a light Higgs boson, therefore rare decays may be observed in this sense and give precious information on the type of Higgs boson faced (SM, charged Higgs, multi-Higgs).

- A non SUSY model inspired from Randall and Sundrum [22] described in section 9.1 predicts a right handed Dirac neutrino as DM candidate together with an additional Z' boson. This Z' links the new physics sector to the SM sector thanks to a strong coupling to the top quark and a very small mixing with the standard Z^0 with all other standard couplings suppressed. This Z' could then be seen in an excess of four top events if it is heavy enough[12] to be able to decay in two tops, or as a subtle signal of $t\bar{t}$ + missing energy when the Z' decays into Weakly Interactive Massive Particles (WIMPs).

All those aspects show that the top quark physics should play a key role in the understanding of the physics beyond the SM.

[11] The extra-dimension is supposed symmetric around 0: $-\phi = \phi$

[12] Scenario well disfavoured by the LHC data.

Résumé du chapitre

Ce chapitre fournit une description succincte des particules fondamentales et de leurs interactions. Le paysage actuel des expériences de physique des particules et des astroparticules ainsi que leurs principaux enjeux y sont résumés.

La Physique des Particules

La physique des particules est une branche de la physique dont l'objet est l'étude des constituants les plus infimes de notre univers ainsi que des lois qui régissent leurs interactions. La divisibilité de la matière fut étudiée par les grecs anciens et déjà Démocrite parla d'atomes (*"ceux qu'on ne peut scinder"*). La question de l'origine de l'univers taraude l'esprit humain depuis la nuit des temps. Ces questions, entre autres, sont aux fondements de la physique des particules qui construit des modèles, des théories, et des expériences de plus en plus complexes dans l'espoir d'élucider un jour les mystères de la nature.

Les particules dont nous parlons ici sont les constituants les plus infimes de la matière. Pour comprendre de quoi il s'agit, imaginons que l'on essaye d'émietter un morceau de matière, du bois par exemple, on pourra en obtenir des morceaux de plus en plus petits au prix d'efforts de plus en plus importants. Il viendra un moment ou les miettes de matière deviennent à peine visibles à l'œil nu, voire invisibles, mais on peut continuer d'émietter notre morceau de bois en utilisant d'abord une loupe et des pincettes puis un microscope ... Il arrivera un moment où ce que nous subdivisons ne sera plus du bois à proprement parler mais un groupe de molécules, de cellulose par exemple, celles-ci pourront être séparées (au prix d'effort encore plus importants) et on pourra les isoler une à une et les fragmenter elles aussi jusqu'à obtenir des atomes individuels, les briques élémentaires de tous les matériaux qui nous entourent, qu'ils soient solides, liquides ou gazeux. Ces atomes si chers à Démocrite, s'avèrent être eux aussi des assemblages de constituants plus petits encore. Ces constituants sont de deux espèces, les électrons, de la famille des leptons et les nucléons, de la famille des hadrons. Ces nucléons, comme leur nom l'indique forment le noyau des atomes, ils sont de deux sortes : les protons et les neutrons. Ce noyau est environ dix mille fois plus petit que l'atome dont le volume est finalement assuré par les électrons uniquement. Cette structure de l'atome fut au cœur des préoccupations à la fin du 19^{e} et au début du 20^{e} siècle. Plus tard, une structure interne a été découverte pour les nucléons qui sont finalement constitués de quarks liés ensemble par des gluons (Murray Gell-Mann — prix Nobel en 1969). Aujourd'hui, on connaît 12 fermions: 6 leptons et 6 quarks, ainsi qu'un système de bosons, particules transmettant l'interaction entre les fermions (*cf.* tableau 1.1). On y trouve le photon, transmettant l'interaction électromagnétique entre les particules chargées, les bosons Z^0, W^+ et W^- assurant l'interaction nucléaire faible et les gluons, responsables de l'interaction forte. On voit aussi dans le tableau 1.1 le graviton, boson hypothétique sensé être responsable de la gravitation au niveau quantique ainsi que le boson de Higgs dont le rôle serait d'expliquer les masses des particules.

Questions d'actualité

Les questions qui animent la recherche fondamentale sont finalement les mêmes depuis que l'homme est capable de penser : *D'où venons nous ?*, *De quoi sommes nous faits ?* ... Mais la manière d'y répondre a beaucoup évolué au fil du temps. Les lois qui régissent le comportement des particules quantiques sont rassemblées dans le "Modèle Standard" de la Physique des Particules. Ce modèle décrit quasiment tous les phénomènes connus à ce jour à l'exception de la gravitation. Une autre lacune, de taille, est l'absence d'explication quant à la matière noire, qui compose près d'un quart du bilan énergétique de l'univers. C'est notamment pour pallier à ces manquements que de nombreuses extensions au Modèle Standard ont été échafaudées. Avec le démarrage récent du Grand Collisionneur de Hadron (LHC) au CERN, de nombreuses réponses sont attendues. Le boson de Higgs, la clé de voute du Modèle Standard, assurant sa cohérence, devrait y être découvert s'il existe bel et bien. La super-symétrie, une extension du modèle standard prédisant un large spectre de nouvelles particules, pourra aussi y être découverte et donner de précieux indices notamment sur la nature de la matière noire.

De nombreuses autres expériences investiguent les secrets de l'univers. AMS depuis la station spatiale internationale scrute le rayonnement cosmique en quête d'antimatière. Des réseaux de télescopes comme HESS(2), VERITAS, CANGAROO observent le ciel dans le domaine des rayons gamma. VIRGO et LIGO guettent les ondes gravitationnelles produites par des cataclysmes cosmiques et prédites par la relativité générale. ANTARES et AMANDA observent les sources de neutrinos cosmiques. OPERA et T2K étudient les oscillations de saveurs des neutrinos.

Depuis l'établissement du Modèle Standard, pour la première fois dans l'histoire, des constructions théoriques ont foisonné sans aucun support expérimental. Avec le démarrage de toutes ces expériences, de nouvelles observations vont très bientôt discriminer entre les différentes théories et probablement modifier profondément notre compréhension de l'Univers.

Nouvelle Physique

Le terme "Nouvelle Physique" désigne tout phénomène et toute théorie s'écartant du Modèle Standard de la Physique des Particules. Les principaux scénarios de Nouvelle Physique sont la super symétrie (SUSY) et les théories de dimensions supplémentaires. La quête de la Nouvelle Physique peut s'accomplir de multiple façon, comme la recherche directe de nouvelle particules (particules super-symétriques, résonances de Kaluza-Klein, ...) ou la mesure très précise de certains couplages dans le but de trouver des incohérences avec le Modèle Standard, signes de mécanismes exotiques à l'œuvre. On introduit ici le quark top, qui de part sa masse très élevée est soupçonné de jouer un rôle clé dans les mécanismes au delà du Modèle Standard.

CHAPTER 2

Particle colliders and detectors

In science, direct observation of nature provide precious informations and are usually preliminary to any laboratory investigation. In particle physics, this observation is done thanks to astroparticle experiments. Laboratory experiments, whatever the field of science, give complementary informations through observations in a controlled environment. In particle physics those laboratory experiments are mainly done thanks to particle colliders.

2.1 Accelerating particles

Even if beams of neutral particles can be produced, mainly charged particles are used in collider experiments. They can be directly accelerated and steered and their trajectory can be easily monitored. Such operations are done thanks to electric and magnetic fields. Namely, magnets are used to generate a magnetic field to bend the beam particle trajectories. In the early 30's the first techniques to accelerate particles used some very high voltage power supplies intended to transfer the highest possible energy to a bunch of particle in a constant homogeneous electric field (Cockroft-Walton in 1930, Van de Graaff in 1931). Nowadays resonant cavities are used to provide an electric field that accelerates them. The oscillating field provided by Radio Frequency (RF) resonance allows much higher accelerating power.

2.2 Colliding particles

A particle collider basic working principle is rather simple. It accelerates two beams of particles until a given energy. Then, it crosses the beams at one or more given locations where detectors are placed. The detectors are set to record what happen when beam particles eventually collide.

To increase the collision rate, the beam particles are arranged into compact bunches

where a very large number[1] of particles are gathered. Therefore a collider does not launch one single particle towards another but rather drives two bunches of particles towards one another. The compactness and the geometry of the bunch together with the bunch crossing rate define a crucial parameter of particle colliders called *luminosity*. It denotes the number of collision trial per time unit and per area unit, a simple computation is:

$$\mathcal{L} = \frac{f\, N_1\, N_2}{4\pi\, \sigma_x\, \sigma_y}\,,$$

where $\mathcal{L}$ stands for the luminosity, f the bunch crossing frequency, $N_{1,2}$ for the number of particles composing the bunches and $\sigma_{x,y}$ the transverse dispersions of the bunches. The luminosity has the dimension of an inverse area per unit of time (e.g. $\mathrm{cm}^{-2}\ \mathrm{s}^{-1}$). This formula is however rather idealistic because it suppose identical bunches and neglect the effect of a possible crossing angle but gives a rather good approximation and an intuitive idea of what is luminosity.

The rate r of a physics process is related to luminosity *via* the so-called cross section of the process σ:

$$r = \sigma\, \mathcal{L}\,.$$

The cross section is the analogy of what would be the projected area of an incoming particle if it's probability of interacting were proportional to its size. The cross section is therefore measured in area unit. The usual unit is the barn ($1\,\mathrm{barn} = 10^{-24}\,\mathrm{cm}^2$). This quantity depends on the process to observe.

2.3 Future colliders

The next generation of particle colliders is already being designed to succeed the LHC. The LHC, as a hadron collider, has a very large discovery potential, but as a drawback, it suffers from limited precision in certain areas of measurement because the exact energy of the collision is unknown. This is due to the composite aspect of the proton. The energy of a proton is shared between its constituents and, at high energy, the collision occurs between constituents rather than entire protons. Therefore, only a small random fraction of the proton energy is involved in the hard collision. This leads to large uncertainty in the initial state of the collisions resulting in a limited precision of the measurements. On the other hand, the possibility of continuously browsing a wide scope of collision energies without modifying the machine settings gives a high discovery potential. Moreover, given the large mass of the proton (compared to electron), the synchrotron radiation is much lower and therefore much higher energies are possible. These are major advantage of hadron colliders, sometimes dubbed "discovery machines".

As electrons are elementary particles, the initial energy of an e^+e^- collision is well known. Limited discrepancies from nominal energy come from energy spread within particle bunches and electromagnetic radiation of the incoming particles before the collision. Nevertheless, the initial centre of mass energy precisely peaks at the nominal value. Such a knowledge of the initial state opens to measurements impossible or very difficult at hadron colliders.Therefore, e^+e^- colliders are envisioned to succeed the LHC to obtain precise measurements on its discoveries and perhaps even more.

[1] *e.g.* LHC: $5 \cdot 10^{11}$ protons per bunch, CLIC: 4–7$\cdot 10^9$ $e^\pm$ per bunch

Two projects are currently under development: the ILC[23] and the Compact Linear Collider (CLIC)[24]. These are based on different acceleration technologies, each of which will reach different energies with a very different collision environment. ILC is designed to run at centre of mass energies from the Z^0 resonance (91 GeV) to 500 GeV with a possible upgrade to 1 TeV. CLIC is meant to operate at a centre of mass energy of 3 TeV. However, whilst both projects have their own discovery potential, their fate is bound to the LHC discoveries. The scale of the new physics will choose whether ILC or CLIC will be built.

Why linear? To be prepared for a collision, the particles must be accelerated and driven towards an interaction point; this is why only charged particles are used in colliders. A property of charged particles is that they radiate when they are accelerated (including when they are forced into a circular trajectory), *i.e.* they loose a part of the energy transferred to them in the form of photon emission. This energy loss, called synchrotron radiation on a circular trajectory, or bremsstrahlung in case of straight accelerations, increases with the energy of the particle, the bending of the trajectory and is highly dependent on the particle mass: the lighter the particle, the stronger the radiation. For electrons, the highest energy that has been reached was in the LEP tunnel (presently LHC, ≈ 27 km circumference) at about 200 GeV. Above this value, the energy loss due to synchrotron radiation in a tunnel such as the LEP or LHC one becomes too high. The only solutions are either to build a much larger ring, but it's unlikely to be done on earth, either to build a linear collider where the electrons will be accelerated at collision energy in only one passage.

What physics? The discovery potential of the LHC is incredibly broad. If the masses of the particles are indeed generated by the Higgs mechanism, if super symmetry is a true broken symmetry of nature, if our universe is fundamentally higher dimensional than four and if there are additional fundamental interactions, the LHC will be able to figure it out. But all those answers give rise to new questions: what kind of Higgs? what parameters for SUSY? what structure for the extra-dimensions? what properties for the new interaction? To answer all those new questions an e^+e^- collider could be the ideal tool.

2.3.1 The International Linear Collider

The ILC [23] is intended to collide e^- on e^+ at a nominal centre of mass energy of 500 GeV, tunable by little energy steps from the Z^0 mass resonance to perform threshold scans. Low energy collisions allow the rediscovery of all the particles already known, which is very useful for calibration purpose, as has already been done by CMS and ATLAS experiments with early LHC data (See figure 2.1). Low energy collisions also allow to perform new measurements on already known process to improve the current precision and perhaps find out some anomalies indicating new physics signature? For this purpose ILC has considered the so-called "GigaZ option" which schedules a high luminosity run at the Z^0 mass resonance (see [21] and references therein).

The ILC will accelerate $e^{\pm}$ with a nominal gradient of $\approx 35\,\mathrm{MV\,m^{-1}}$ necessitating therefore more than 14 km of acceleration to reach 500 GeV. The baseline design,

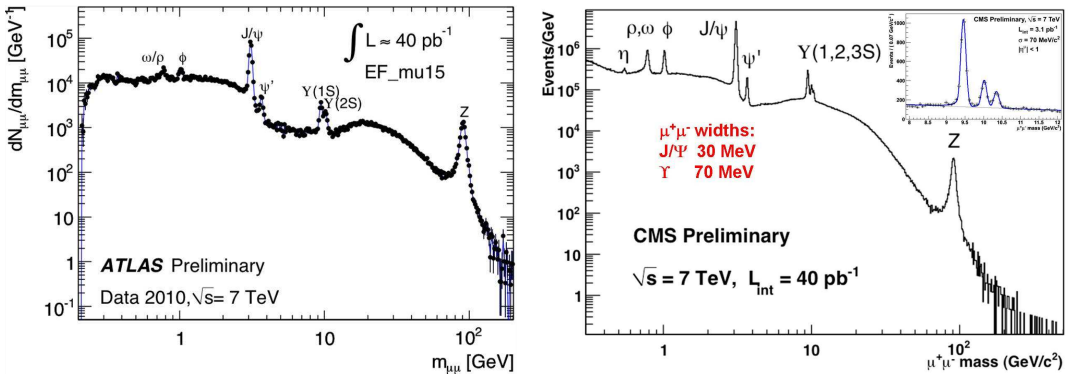

(a) (b)

Figure 2.1: Di-muon invariant mass spectrum from ATLAS (a) and CMS (b) experiment early data. Taken from LHC public plots.

sketched in figure 2.2, includes two branches, more than 15 km long each. The baseline beam parameters are summarised in table 2.1. An upgrade is envisioned to reach a centre of mass energy of 1 TeV by doubling the machine size.

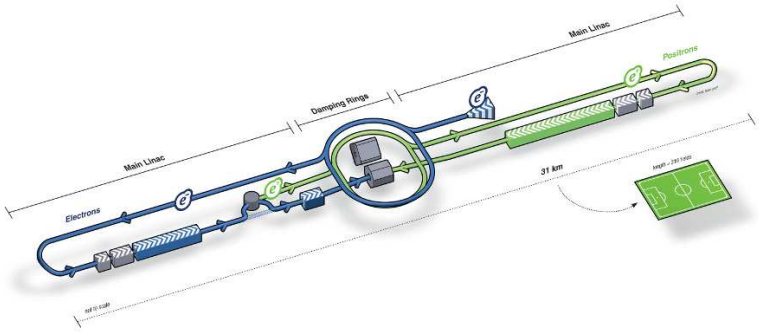

Figure 2.2: layout of the ILC machine.

2.3.2 The Compact Linear Collider

CLIC is a e^+e^- linear collider designed to operate at energies between 0.5 TeV to 3 TeV and very high luminosity ($5.9 \cdot 10^{34}\,\mathrm{cm}^{-2}\,\mathrm{s}^{-1}$). The CLIC project relies on an innovative acceleration technology functioning at room temperature, under development at CERN by the CLIC Test Facility 3 (CTF3) collaboration [26]. The so-called *main beam*, intended for the high energy physics experimental collisions, is accelerated thanks to a secondary beam called *drive beam*. The drive beam is an intense low energy beam running parallel to the main beam (a 28 MeV, 3.5 A beam is used by CTF3 [27], nominal CLIC drive beam would be 2.37 GeV and 4.2 A). Its purpose is to interact with the so-called Power Extraction and Transfer Structure (PETS) to convert its kinetic energy into a 12 GHz electromagnetic wave. This wave is driven by wave-guides to the main

Table 2.1: ILC baseline beam parameters [25]

Centre of mass energy range	200–500 GeV
Peak Luminosity	$2{\cdot}10^{34}$ cm^{-2} s^{-1}
Pulse rate	5 Hz
Pulse duration	≈1 ms
Number of bunch / pulse	1000–5400
Number of $e^{\pm}$/ bunch	$\approx 2{\cdot}10^{10}$

beam RF accelerating structures that provide an accelerating gradient for the main beam of about 100 MV$\cdot$ m^{-1}. For comparison, the accelerating gradient foreseen in the ILC project [23], using supra-conductive cold technologies, would be of around 35 MV$\cdot$ m^{-1}. The very high beam accelerating gradient of CLIC allows much shorter accelerating distance to reach a given energy and hence justifies the name of the machine. For comparison again, the 500 GeV ILC length would be ≈ 31 km whereas the 500 GeV CLIC length would be only ≈ 13 km. The overall Layout of the CLIC machine for operation at a nominal centre of mass energy 3 TeV is displayed in figure 2.3.

The complete list of CLIC parameters can be found in [28]. The main parameters concerning the 3 TeV physics beam are summarised in table 2.2. All informations about CLIC are available in dedicated documentations (*e.g.*: [24, 28, 29]).

Table 2.2: CLIC main beam parameters (extracted from [28]).

Luminosity	$5.9{\cdot}10^{34}$ cm^{-2} s^{-1}
Number of particles per bunch	$3.72{\cdot}10^{9}$
Bunch separation	0.5 ns
Number of bunches per train	312
Train repetition rate	50 Hz

2.4 Recording collisions

Accelerating and colliding particles is one step. To learn from collisions, sophisticated sensors are placed around the collision point (also called primary vertex or interaction point (IP)) and record a maximum of relevant information. The first problem is that the interesting phenomena implies in general very short lived particles that travel no more than a few microns or even much less before decaying. There is no possibility to place a sensor so close to the interaction point. The strategy is therefore to look at the stable[2] particles emanating from the IP. These can be directly produced in the collision but are more generally decay products of IP emanating particles. For instance, if a $\tau^+\tau^-$ lepton pair is produced in a collision, the two τ leptons will travel a few μm and therefore will not be detectable, but they decay for instance in a muon and a pair of

[2]Stable means here that they live long enough to travel across the detectors, e.g. the muon which lives about 2 μs is actually considered very stable, kaons and charged pions can as well travel several meters before decaying.

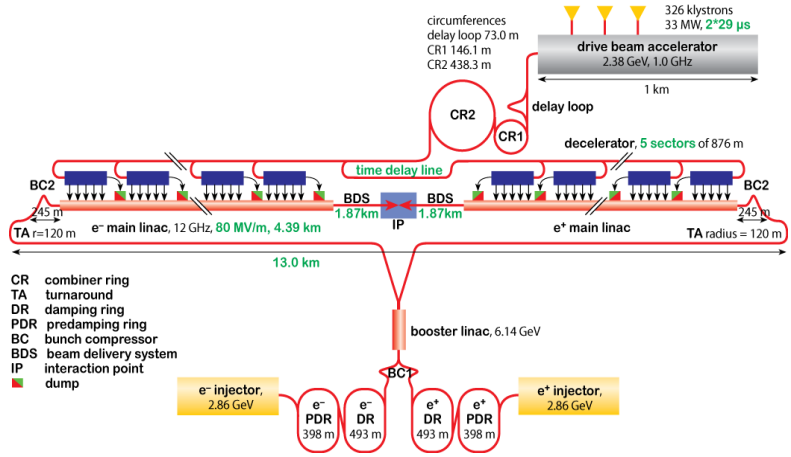

(a)

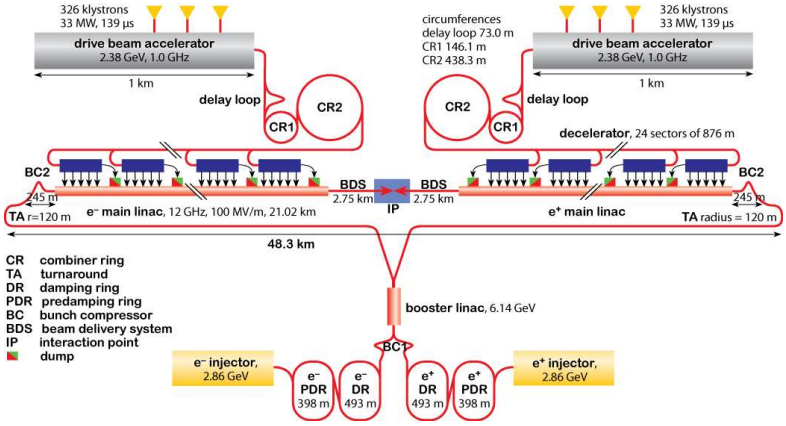

(b)

Figure 2.3: Layout of the low energy (a) and the nominal (b) version of the CLIC machine.

neutrinos ($Br(\tau^- \to \mu^- \nu_\mu \nu_\tau) \approx 18\%$). The neutrinos are stable but completely invisible to detectors[3] whereas the muons are charged and may travel hundreds of meters before decaying, leaving a clear signal in the detectors. In addition, the tracks of the two muons will not point exactly at the IP but at the place where the mother particles decayed, called a secondary vertex. A detailed and carefull analysis of such final states allows the understanding of the events which occured at the IP. The detectable particles and their basic properties are summarised in table 2.3.

Physics detectors at particle colliders comprise several sub-detectors aimed at very specific tasks. A magnetic field bends the charged particle trajectories allowing charge distinction and momentum measurement. The sub-detectors are organised in concentric layers from innermost to outermost as follows:

- Tracking system: it records the trajectory of the charged particles and which is further divided into two sub-systems:

[3]They are nevertheless detectable at a very low rate in dedicated experiments.

Table 2.3: Detectable particle characteristics, see [30] for further details.

Particle name	Symbol	mass [MeV/c^2]	|Charge| [e]	Mean life	$c\tau$
photon	γ	0	0	∞	∞
electron	$e^{\pm}$	0.511	1	∞	∞
muon	$\mu^{\pm}$	105.7	1	2.197 μs	658.7 m
pion	$\pi^{\pm}$	139.6	1	26.0 ns	7.8 m
charged kaon	$K^{\pm}$	493.7	1	12.3 ns	3.7 m
neutral kaon	K^0_L	497.6	0	51.2 ns	15.3 m
proton	p,$\bar{p}$	938.3	1	∞	∞
neutron	n,$\bar{n}$	939.6	0	885.7 s	$2.65 \cdot 10^8$ km

  - Inner tracker or vertex detector: usually made of very fine segmented silicon detectors which determines the starting point of the tracks to identify secondary vertexes.
  - Outer tracker: it measures the momentum of the charged particles thanks to the bending of the trajectory in the magnetic field. The outer tracker must represent the lowest possible material budget in order to minimise the rate of interactions within its scope and limit the scattering that would degrade the momentum measurement. This apparatus can be made of a few silicon layers giving point collections to reconstruct the particle tracks. It can as well be a Time Projection Chamber (TPC), a gaseous chamber providing a detailed 3-dimensional image of the particle trajectories.

- Electromagnetic Calorimeter (ECAL): it is made of dense material to stop the so-called electromagnetic particles (photons, electrons and positrons). Their energy is completely absorbed and hence measured. An ECAL can be either "homogeneous" when the dense material is also sensitive or "sampling" when instrumented sensors are interleaved with dense material layers. The ECAL is generally rather thin to reduce the probability that hadrons might start showering in it. Details about calorimetry are developed in section 2.5.

- Hadronic Calorimeter (HCAL): it is also made of dense material and is the heaviest part of a collider detector. It is usually of the "sampling" kind and hence consists of passive dense layers (lead, iron ...) interleaved with instrumented detection layers (active layers). Its role is to stop the hadrons and measure their original energy by sampling their energy loss across the detector.

A summary of the detectable particles and their signal in the various sub-detectors is presented in table 2.4 and illustrated in figure 2.4.

2.5 Calorimetry

In particle physics, calorimetry is the general concept of particle energy measurement and a calorimeter is the apparatus responsible for this task. The interaction of particles and radiations in matter is a complete field on its own. Many dedicated books and

Table 2.4: Detectable particles and their signal in the sub-detectors. "—": Nothing is seen ; "Track": the particle passage can be detected and the trajectory can be monitored ; "E.M.Sh" : the particle is stopped and its energy absorbed *via* electromagnic showering ; "H.Sh" : the particle is stopped and its energy absorbed *via* hadronic showering.

		Sub-detector			
Particle name	Symbol	Tracker	ECAL	HCAL	Muon chamber
photon	γ	—	E.M.Sh.	—	—
electron	$e^{\pm}$	Track	E.M.Sh.	—	—
muon	$\mu^{\pm}$	Track	Track	Track	Track
pion	$\pi^{\pm}$	Track	Track	H.Sh.	—
charged kaon	$K^{\pm}$	Track	Track	H.Sh.	—
neutral kaon	K^0_L	—	—	H.Sh.	—
proton	p,$\bar{p}$	Track	Track	H.Sh.	—
neutron	n,$\bar{n}$	—	—	H.Sh.	—

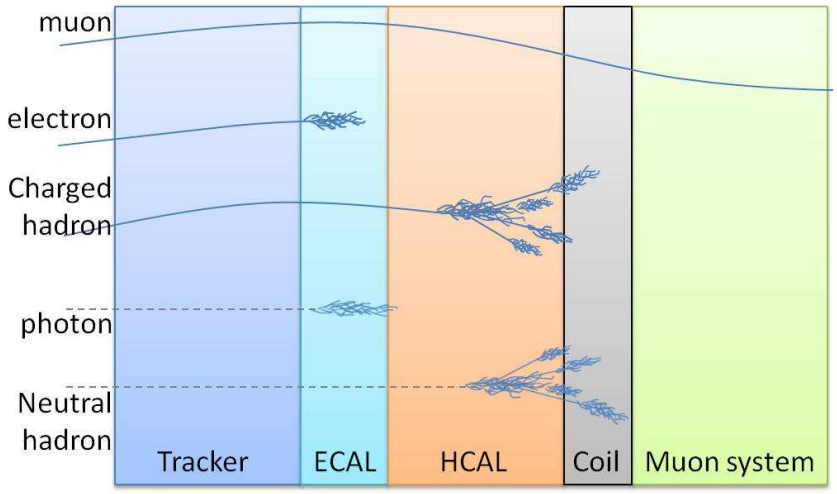

Figure 2.4: Schematic view of the detectable particles and their signal in the sub-detectors.

courses are available and the reader is referred for instance to [30] or [31] and references therein for more details about calorimetry and the related physics. Some basic principles of classical calorimetry are presented as follows.

2.5.1 Particle showers

Calorimeters are instrumented blocks of dense matter in which particles interact and deposit all their energy by producing a cascade of secondary particles of decreasing energy. This cascade is called a "shower". There are two types of such showers: elecromagnetic and hadronic depending on the type of particle initiating it.

2.5.1.1 Calorimeters

Calorimeters can be classified in different ways:

- According to their function:
  - Electromagnetic Calorimeter (ECAL): intended for the energy measurement of electrons, positron and photons.
  - Hadronic Calorimeter (HCAL): intended for the energy measurement of all kind of hadrons.
- According to their structure:
  - Sampling calorimeter: thin sensitive layers (Si, Gas, Scintillator), so-called active layers, are interleaved with thick dense plates (W, Fe, Pb, ...), so-called passive layers or absorber, where the particle interactions occur. The main part of the incoming energy is deposited into the passive layers but the energy sampled in the active layers is related to the total energy and therefore allows its measurement.
  - Homogeneous calorimeter: the dense material responsible for the particle energy dissipation is also sensitive and instrumented (*e.g.* dense scintillating crystals: PbO, $PbWO_4$, or Čherenkov materials like PbF_2) and a direct measurement of the deposited energy is therefore possible.
- According to their readout technique:
  - Analogue readout: the energy deposited in the active medium is precisely measured and used to reconstruct the incoming particle or incoming jet energy.
  - Digital readout: The number of calorimeter cells activated by the passage of particles, or *hits*, are counted. For high transverse and longitudinal granularity the number of hits recorded is proportional to the incoming particle energy.

The calorimeter functioning principle relies on the proportionality of the calorimeter response to the initial particle energy. This condition is well realised for ECALs but is more difficult for hadrons in which case an energy dependent fraction of the energy goes to pure electromagnetic contribution *via* emission of π^0 mesons[4]. Electromagnetic contribution gives a higher calorimeter response than the purely hadronic one and therefore the conversion factor between the visible energy and the initial hadron energy is energy dependent: the calorimeter response is no longer linear.

2.5.1.2 Electromagnetic showers

Electromagnetic showers are generated by electromagnetic particles, namely electrons, positrons and photons. Quantum Electrodynamics (QED) describes very well their

[4]The π^0 decays extremely quickly into two photons (mean life: $8.4 \cdot 10^{-17} s$).

dynamics and an analytical description is even possible in principle. However, the complexity of the shower process is such that simplified models are generally used. Here follows a brief description of the phenomena implied in electromagnetic showers to give an intuitive picture of the process.

When an electromagnetic particle enters the dense medium of the calorimeter, it interacts electromagnetically to produce either bremsstrahlung photons, e^+e^- pairs or ionization of the medium. In the case of an incoming electron (or positron) the primary energy is lost through a successive emission of bremsstrahlung[5] photons until the primary particle energy becomes too low and the remaining energy is lost only *via* ionisation and excitation of the medium. The emitted bremsstrahlung photons can convert into e^+e^- pairs if their energy is sufficient or ionise the medium through Compton or photoelectric effect at lower energies.

In the case of an incoming photon, the first interaction is likely to be an e^+e^- pair creation (dominant at hight energy, the other effects are Compton scattering and photoelectric effect). The so-created particles initiate the same process as described just before. Photon and electron or positron showers have very similar properties. Event displays of electromagnetic showers are given in figure 2.5(a) and (b) for a 20 GeV electron and a 20 GeV photon respectively. The typical size of an electromagnetic shower depends on the calorimeter absorbing material. The radiation length X_0 is the mean distance over which the incoming particle energy is reduced by a factor $1/e$ and the Molière radius R_M is the distance from the shower axis conaining 80% of the shower. Both quatities relates *via* an empirical relation:

$$R_\mathrm{M} = 0.0265\,\mathrm{X}_0(Z + 1.2)\,,$$

where Z stands for the atomic number of the absorbing material. This and other formulas can be found in [31].

2.5.1.3 Hadronic showers

Hadronic showers are initiated by hadronic particles. The hadron family gathers together all the particles that are sensitive the strong interaction which is described by QCD. For this reason, their interaction in matter is not very well understood because of the lack of precision achievable in QCD[6]. A qualitative description of hadronic showers follows.

When a hadron enters the dense medium of a calorimeter, it has a probability to interact with the atomic nuclei of the medium. This probability is characterised by the so-called interaction length λ_I relating the path length x to the interaction probability P through:

$$P(x) = e^{-x/\,\lambda_\mathrm{I}}\,.$$

Such an interaction generally leads to the destruction of the incoming hadron and the targeted nucleus projecting a number of energetic hadronic fragments. Those fragments

[5] Bremsstrahlung is the light emission by a charged particle that occurs when it is accelerated or slew down (from German: braking radiation). The same phenomenon happen when the particle is bent (centripetal acceleration) but is called in this case synchrotron radiation.

[6] A precise description of the Strong Interaction is possible at very high energy (idealy about the Plank energy) thanks to the asymptotic freedom because the strong coupling constant becomes low and allows perturbative calculations. At lower energies, the pertubative calculations are less reliable and a non-perturbative description is needed, like lattice QCD (however yet limited to small systems).

propagate through the medium until they interact with another atomic nucleus and produce subsequent less energetic fragments repeatedly until the initial energy is totally diluted. At each point where a strong interaction occurs, a part of the energy is emitted electromagnetically mainly by the production and decay of π^0 mesons. Thus a hadronic shower has a complex shape showing a network of smaller electromagnetic showers and tracks with large fluctuations from one event to another. A hadronic shower of a 20 GeV pion is displayed in figure 2.5(c). Nuclear interactions involved in the hadronic shower processes induce large fluctuations in the final shower since a variable amount of energy can be dissipated in nuclear excitations. For this reason, the hadronic shower energy measurement is fundamentally less precise than the electromagnetic one.

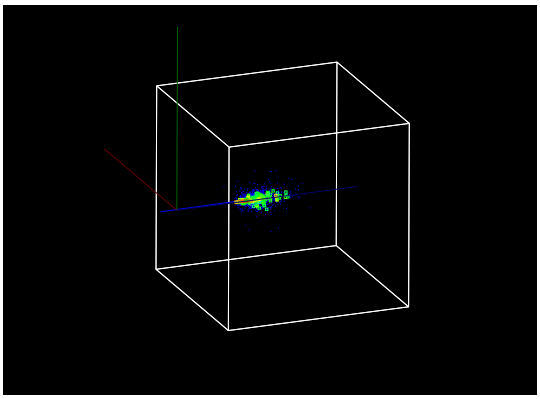

(a) Shower of a 20 GeV electron

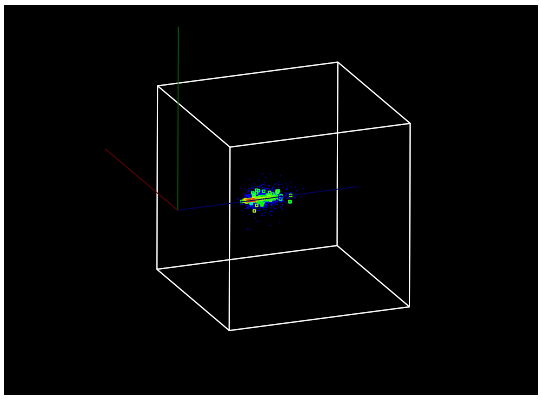

(b) Shower of a 20 GeV photon

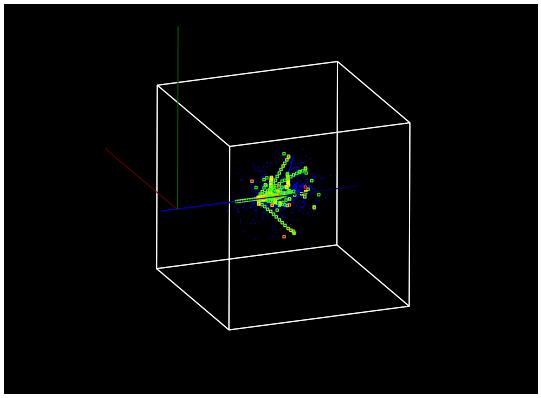

(c) Shower of a 20 GeV pion

Figure 2.5: Display of particle showers in a $1\,m^3$ Fe Calorimeter (40 layers of 2 cm thick Fe absorber, gaseous active medium with $1\,cm^2$ lateral segmentation).

2.5.2 Energy measurement and resolution

The measurement of particle energy can be performed in various ways. Fundamentally, the energy of the initial particle is proportional to the number of particles produced in the shower. However counting directly the number of particles is not possible with the currently available technologies. There are two solutions to this problem. The first one,

and the most used so far in high energy physics experiments, consists simply in measuring the energy deposited by the shower in the sensitive medium of the calorimeter. The measured deposited energy is therefore close to the initial particle energy in the case of homogeneous calorimeters or proportional to it in the case of sampling ones. The second solution, possible only with a highly granular calorimeter, consists in counting the number of calorimeter cells activated by the shower particles (or hits, for short). In this case, the number of hits is proportional to the initial particle energy. This solution is called digital calorimetry and is one of the options foreseen for future linear colliders. The report focuses on sampling calorimeter properties. At first, electromagnetic calorimetry aspects are discussed and then applied to the more complicated case of hadronic calorimetry.

2.5.2.1 Energy measurement in electromagnetic calorimetry

As already mentioned, in the case of electromagnetic particles, the calorimeter response, or *visible energy* $E_{\rm vis}$ is proportional to the initial energy E. The proportionality factor depends on the calorimeter structure and material. Two energy independent factors relate $E_{\rm vis}$ to E, the "sampling fraction" and the e/mip ratio.

- The sampling fraction $F_{\rm S}$ is the fraction of a Minimum Ionizing Particle (MIP) energy loss specific to the calorimeter active medium. It reads:

$$F_{\rm S} \;=\; \frac{\left(\frac{dE}{dx}\right)_{\rm activ.} L_{\rm S}}{\left(\frac{dE}{dx}\right)_{\rm passiv.} L_{\rm abs}}\,, \tag{2.1}$$

  with $L_{\rm abs}$ the absorber thickness, $L_{\rm S}$ the active layer thickness and in the limit $\left(\frac{dE}{dx}\right)_{\rm activ.} \ll \left(\frac{dE}{dx}\right)_{\rm passiv.}$, which is generally true for sampling calorimeters. Note that the quantity $E \cdot F_{\rm S}$ represents the visible energy from a MIP loosing the energy E in the complete calorimeter. $F_{\rm S}$ can not be directly measured and has to be computed from the calorimeter layout.

- The e/mip ratio denotes the relative intensity of the calorimeter response to electromagnetic particles in unit of its response to MIPs. It is defined as the ratio between the calorimeter response to an electron $E_{\rm vis}$ and its response to an ideal MIP[7] loosing in the calorimeter the same energy E. It is given by:

$$e/mip \;=\; \frac{E_{\rm vis}}{E\,F_{\rm S}}\,,$$

  and can be directly measured from calibration data from the considered calorimeter.

Now, the relation between the visible and the initial energy reads:

$$E_{vis} \;=\; (e/mip)\,F_{\rm S}\,E\,. \tag{2.2}$$

[7] An ideal Minimum Ionizing Particle (MIP) is a particle traversing matter with a constant and minimal energy loss without emission of secondary radiation. Real muons constitute a good approximation of ideal MIPs. They are really at the minimum of ionisation when their energy is $\approx 0.35\,\text{GeV}$ and are only slightly above for higher energies up to $\approx 1\,\text{TeV}$. They also traverse matter without any showering process.

Energy resolution The question of how precise is the relation 2.2 to determine the initial energy from the calorimeter response arises. The shower process is a stochastic phenomenon and therefore the precise shape and the number of particles fluctuate on an event by event basis and the relation 2.2 is only an average. The error depends obviously on the one hand on the precision of the estimate of F_{S} and e/mip, but on the other hand, the intrinsic energy resolution comes from statistical effects. The visible energy is closely related to the number of particles traversing the active medium and therefore its fluctuations as well. Let N_{p} be the number of particles crossing the active layers and $\sqrt{N_{\mathrm{p}}}$ be its error. To have an estimate of N_{p}, divide the visible energy E_{vis} by the average energy loss of an electron in an active layer E_{el}:

$$N_{\mathrm{p}} \approx \frac{E_{\mathrm{vis}}}{E_{\mathrm{el}}}\,.$$

E_{el} is given by:

$$E_{\mathrm{el}} \;=\; k\left(\frac{dE}{dx}\right)_{\mathrm{passiv.}} L_{\mathrm{S}}\,\frac{1}{\langle\cos\theta\rangle}\,, \tag{2.3}$$

with the $k = 1.1$ factor accounting for the fact that $\left(\frac{dE}{dx}\right)_{\mathrm{passiv.}}$ is evaluated for MIPs and real electrons give roughly a 10% higher signal, L_{S} is the active layer thickness and $\langle\cos\theta\rangle$ is the average cosine of the particle incidence angle in the active medium. From this follows:

$$\begin{aligned}\frac{\sigma_E}{E} &= \frac{\sigma_{E_{\mathrm{vis}}}}{E_{\mathrm{vis}}}\\ &= K\sqrt{\frac{\tau}{E}}\,,\end{aligned} \tag{2.4}$$

with

$$K = \sqrt{\frac{10^{-3}\epsilon_{\mathrm{ca}}}{e/mip\,\langle\cos\theta\rangle}}\,,$$

ϵ_{ca} being the critical energy of the absorbing medium corresponding the the threshold energy of an electron at which radiative energy losses are equivalent to collision energy losses. This threshold is of the order of 10 to 100 MeV depending on the material. The value of $\langle\cos\theta\rangle$ is given by $\langle\cos\theta\rangle \approx \cos\left(\frac{E\,F_{\mathrm{S}}}{\pi\epsilon_{\mathrm{ca}}}\right)$.

2.5.2.2 Energy measurement in hadronic calorimetry

The basic principle of hadronic calorimetry is the same as in the electromagnetic case but the main difference is that the visible energy is usually not linearly proportional to the initial particle energy. This is due to the fact that hadronic showers are composed of a pure hadronic component but also of an electromagnetic one. Both components give different response, the electromagnetic one being usually higher, and the relative contribution of both components is energy dependent leading to the non linearity of hadron energy measurement.

Pure hadronic contribution Hadronic interactions in the passive (or absorbing) medium produce a number of hadronic particles that travel in the calorimeter leaving a signal in the traversed active planes until they are stopped in a new hadronic interaction. The probability of a hadronic interaction in the calorimeter depends on the interaction length $\lambda_{\rm I}$ of the material used, corresponding to the mean free path of a hadron in the considered material. The probability of a hadronic interaction is therefore given by:

$$P(x) = e^{-x/\,\lambda_{\rm I}}\,,$$

where x is the particle path length. Part of the energy, during hadronic interactions, is lost in breaking atomic nuclei, in atomic excitations, or in production of low energy neutrons or neutrinos. This lost energy is the so-called "invisible hadronic energy" responsible for the large event to event fluctuation of hadronic showers. In the end, the pure hadronic contribution to hadron showers is more diluted and less populated than an electromagnetic shower and therefore, at a given energy, the pure hadronic signal is lower than the electromagnetic one.

Electromagnetic contribution During hadronic interactions, π^0 mesons are often produced. The π^0 does not propagate but decays almost immediately into two photons. Consequently, the energy of a π^0 is absorbed electromagnetically in the calorimeter, in the form of a small electromagnetic shower.

Real hadrons The visible energy $E_{\rm vis}(\pi)$ from an incoming real hadron of energy E is a combination of the visible energy that would be produced by an electromagnetic particle of the same energy ($E_{\rm vis}(e)$) and an ideal hadron[8] of the same energy ($E_{\rm vis}(h)$):

$$E_{\rm vis}(\pi) = f_{\rm em}E_{\rm vis}(e) + (1 - f_{\rm em})E_{\rm vis}(h)\,. \tag{2.5}$$

The electromagnetic fraction $f_{\rm em}$ is energy dependent and can be parametrised by:

$$f_{\rm em}(E) \approx 0.1\,ln(E)$$

for E below $\approx 200\,\text{GeV}$ and by

$$f_{\rm em}(E) \approx 1 - E^{-0.15}$$

for E above $\approx 5\,\text{GeV}$.

To measure the energy of a real hadron, a relation similar to eq. 2.2 can be drawn as:

$$E_{\rm vis}(\pi) = \pi/mip\,F_{\rm S}\,E\,,$$

where π/mip is not energy independent. A clearer view is obtained by introducing $h/mip = \frac{E_{\rm vis}(h)}{E\,F_{\rm S}}$ and $e/h = \frac{E_{\rm vis}(e)}{E_{\rm vis}(h)}$. Therefore, from eq 2.5 one gets:

$$E_{\rm vis}(\pi) = E\,F_{\rm S}\,h/mip\;(1 + (e/h - 1)f_{\rm em}(E))\;, \tag{2.6}$$

where h/mip and e/h are energy independent characteristics of the calorimeter. The relation 2.6 shows that the non-linearity can be minimised and even suppressed if e/h is close to or equal to 1.

[8] A hadron that never produce a π^0 in its shower, *i.e.* no electromagnetic component.

e/h ratio, compensation and energy resolution constant term As shown above the e/h ratio, defined by $e/h = \frac{E_{\text{vis}}(e)}{E_{\text{vis}}(h)}$, if equal to one, restores the linearity of the calorimeter. This condition is called "compensation", in the sense that the difference between electromagnetic and hadronic response is compensated. However, reaching the compensating condition is not trivial. A careful choice of the calorimeter material can lead to the compensation. For instance, Uranium absorbers produce additional neutrons and thus enhance the hadronic response of the calorimeter to reach compensation. The e/mip ratio can be tuned as well by a careful choice of the calorimeter materials and layout, a lower e/mip ratio correspond to a lower response to electromagnetic signal and therefore a smaller hierarchy between $E_{\text{vis}}(e)$ and $E_{\text{vis}}(h)$ is achieved.

The e/h ratio, contribute to a constant term in the energy resolution of a hadronic calorimeter through the e/π ratio which relates to e/h *via*:

$$e/\pi = \frac{E_{\text{vis}}(e)}{E_{\text{vis}}(\pi)} = \frac{e/h}{1 + f_{\text{em}}(e/h - 1)}$$

which gives the calorimeter energy resolution constant term $\phi(e/\pi)$, that vanishes for $e/h = e/\pi = 1$:

$$\begin{aligned} \phi(e/\pi) &\approx -0.207 ln(e/\pi) - 4.5 \cdot 10^{-3} \quad \text{for } e/\pi < 0.955\,, \\ \phi(e/\pi) &\approx -0.281 ln(e/\pi) - 2.1 \cdot 10^{-2} \quad \text{for } e/\pi > 1.115\,. \end{aligned}$$

This constant term is the main contribution to energy resolution at high energy. The other term, the stochastic term, decreases as $1/\sqrt{E}$ and takes into account the sampling fluctuations and the intrinsic hadronic invisible energy fluctuations. They are summed quadratically as:

$$\text{Stochastic term} = \sqrt{\frac{\sigma^2_{\text{intr.}} + \sigma^2_{\text{sampl.}}}{E}} = \frac{C}{\sqrt{E}}$$

Finally the hadron calorimeter energy resolution reads:

$$\frac{\sigma_E}{E} = \frac{C}{\sqrt{E}} \oplus \phi(e/\pi)$$

2.6 Particle Flow Algorithm

An event reconstruction and analysis method called Particle Flow Algorithm (PFA) is envisioned for future linear collider experiments to achieve the excellent jet energy resolution (stochastic term below $30\%/\sqrt{E}$) required for the foreseen precision measurements [32, 33].

The concept of particle flow techniques is to consider the physics events in terms of reconstructed particles rather than signal in detectors and use the most suitable sub-detector to measure a particle four-vector. As mentioned in table 2.4 (p. 24), different kinds of particles give specific signals in the different sub-detectors allowing them to be individually identified. In a PFA, the electron energy is deduced from its momentum measurement in the tracker rather than from the direct energy measurement in the ECAL. The same stands for charged hadrons. Only neutral particle energies are measured in calorimeters.

A detector optimised for the application of particle flow techniques must be able to distinguish single particle signals in every sub-detector. This task is already well undertaken by trackers, which can easily distinguish separate particle tracks provided they don't completely overlap. On the contrary, calorimeters are usually made out of large tiles representing a certain segmentation of the solid angle (*e.g.* segmentation of $\Delta\Phi\Delta\eta = 0.1 \times 0.1$ in ATLAS HCAL[34]) making single particle shower separation impossible. To allow single particle recognition, a particle flow optimised calorimeter must have an unprecedented lateral and longitudinal segmentation ($3 \times 3\,\mathrm{cm}^2$ for the Analog Hadronic Calorimeter (AHCAL) project and $1 \times 1\,\mathrm{cm}^2$ for the Digital Hadronic Calorimeter (DHCAL) ones), giving rise to the concept of "imaging calorimetry". This way, hit clusters in calorimeters can be isolated and matched with tracks from the tracker to reconstruct the entire signal from individual particles. Placing the magnet coil outside of the HCAL would be necessary to allow an efficient matching of reconstructed tracks with clusters and is therefore mandatory for a particle flow optimised detector.

The main successive steps of the PFA are summarised as follows:

1. Reconstruct tracks
2. Regroup calorimeter hits in clusters
3. Match together clusters and tracks pointing to them to build the charged particles
4. Isolated clusters remaining must be taken as neutral particles
5. Charged particle energy is deduced from its precise momentum measurement and the deduction of its mass after the particle identification:
   - Cluster mainly in ECAL: electron
   - Cluster mainly in HCAL: pion
   - Track across the whole detector: muon
6. Charged clusters are removed and the energy of neutral particles only is measured thanks to classical calorimetry

Figure 2.7 illustrate the interest of imaging calorimetry. The capability to clearly identify and separate contribution from different particles is a fundamental aspect of PFA.

Jet energy resolution using PFA In traditional calorimetry, the jet energy resolution is governed at low energy by a stochastic term of the order of $50\% - 100\%/\sqrt{E}$ and by leakage at high energy ($\propto \log(E)$). Many interesting processes at future linear colliders require a good discrimination between W and Z^0 bosons in their hadronic decay, wich in turn require a jet energy resolution better that $30\%/\sqrt{E}$ [32]. The PFA, by optimising the energy measurement, allows a reduction of the impact of leakage and stockastic terms and fulfils the requirement. Nevertheless, a new source of uncertainty is introduced because of the probability of errors and mismatch in the hit clustering and the cluster/track association. This effect is called "confusion". Its various consequences are:

- hadronic showers may be split into one charged cluster (matched with a track) and one or more neutral clusters
- true neutral clusters can be associated with a charged one and therefore missed,
- in case of partial overlap between charged and neutral clusters the association of hits to one cluster or another is subject to uncertainties,
- photon clusters close to a charged hadron cluster could be merged with the latter and missed.

Confusion mainly affects the resolution on the energy of the neutrals and is therefore balanced by the low proportion of neutral particles within a jet, as given in table 2.5. A semi-empirical formula is given in [33] to describe the overall jet energy resolution. It reads:

$$\frac{\mathrm{rms}_{90}}{E} = \underbrace{\frac{21\%}{\sqrt{E}} \oplus 0.7\%}_{\substack{\text{classical stochastic} \\ \text{and constant terms}}} \oplus \underbrace{0.004\,E}_{\substack{\text{leakage and} \\ \text{threshold effect}}} \oplus \underbrace{2.1\% \left(\frac{E}{100\,\mathrm{GeV}}\right)^{0.3}}_{\text{confusion term}}, \qquad (2.7)$$

where rms_{90} represent the standard deviation of the energy distribution containing 90% of the entries around the mean value. The various contributions to jet energy resolution are represented in figure 2.6, left, and the right side show a comparison of the PFA jet energy resolution with classical calorimetry. Above 400 – 500 GeV, the confusion dominates and reduces the advantage of PFA against classical calorimetry. To balance this, one solution is to stop the topological separation of the particles when the overlap is too large and simply measure the energy of the global cluster. The contribution of the charged particles is subtracted and the remaining energy is attributed to neutrals. This method is called "energy flow".

Table 2.5: Average composition of jets (figures from [33])

Type of particle	Proportion	Energy resolution	Contrib. to jet energy resolution
Charged	62%	$10^{-4}E^2$	$< 3.6 \cdot 10^{-5} E_j^2$
Photon	27%	$0.15\sqrt{E}$	$0.08\sqrt{E_j}$
Neutral hadron	10%	$0.55\sqrt{E}$	$0.17\sqrt{E_j}$
invisible	∼1%	—	—

PFA is in the backdrop of all the work reported in this thesis. The optimisation of a DHCAL for the application of PFA calls for compact and highly segmented active layers to achieve the required imaging capability. This is precisely the context of the first part of this thesis, reporting on Research and Development (R&D) on gaseous detectors, called MICROMEGAS, as condidate for PFA optimised DHCAL active layer. The PFA has been implemented (among others) in a software called PandoraPFA [33] which is used for the benchmark studies of the CLIC Conceptual Design Report (CDR) preparation physics studies. The data for the top quark study described in the second part of this thesis are taken from the CLIC CDR production data. Therefore the PFA is used and its performance in a realistic physics case are illustrated.

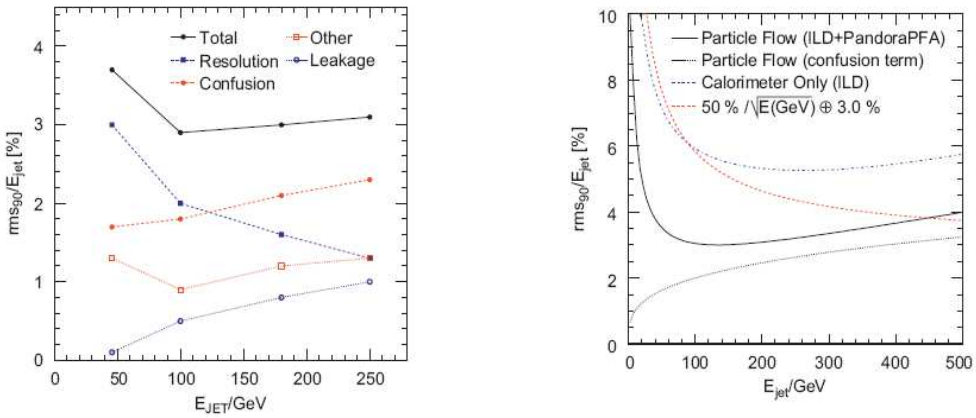

Figure 2.6: Contributions to jet energy resolution with the PFA (left); Comparison of PFA against classical calorimetry (right). Taken from [33]

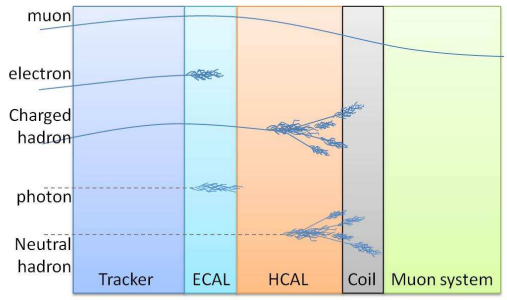

(a)

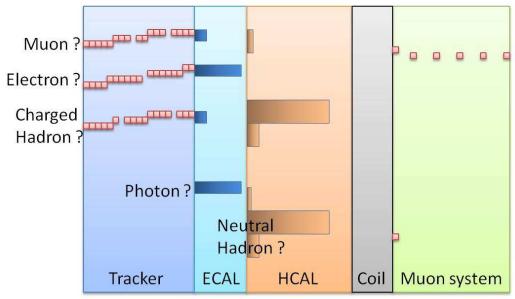

(b)

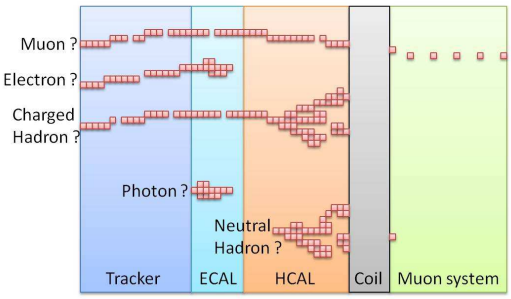

(c)

Figure 2.7: Illustration of particles interaction in the various subdetectors (a), of the corresponding signal in classical detectors (b) and in a PFA optimised detector (c).

Résumé du chapitre

De manière générale, en sciences, l'observation directe des phénomènes naturels précède les études en laboratoire qui, quant à elles, fournissent de précieux renseignements grâce

à des mesures en environnement contrôlé. En Physique des Particules, cette observation de la nature est faite par exemple grâce à l'étude des rayons cosmiques, et les expériences en laboratoire sont faites à l'aide d'accélérateurs de particules.

On s'intéressera plus particulièrement aux collisionneurs de particules, appareils constitués de deux systèmes d'accélération, conduisant les particules accélérées vers un ou plusieurs points de collision, où des systèmes de détection sophistiqués enregistrent l'issue des collisions.

A l'heure actuelle le LHC (*Large Hadron Collider*) tient le devant de la scène en physique des particules et devrait permettre des avancées décisives dans cette quête de Nouvelle Physique. Cependant, les découvertes éventuelles du LHC appelleront à des mesures de précisions complémentaires impossibles auprès d'un collisionneur de hadrons qu'est le LHC. Pour ce faire, des collisionneurs linéaires électron/positron sont envisagés. Deux projets sont en développement : ILC (*Internationnal Linear Collider*) et CLIC (*Compact Linear Collider*) différenciés en pratique par la gamme d'énergie accessible pour les collisions e^+e^- (énergie nominale : 500 GeV pour ILC et 3 TeV pour CLIC).

Détecteurs et calorimétrie Un collisionneur utilise des champs électriques et magnétiques pour accélérer et contrôler les particules, pour les amener à une énergie donnée, à un point de collision. Le point de collision d'un collisionneur est équipé d'un système de détection sophistiqué constitué de plusieurs sous-détecteurs organisés en pelures d'oignon. Dans l'ordre, du cœur vers l'extérieur, on trouve : les trajectographes, très précis mais sensibles seulement aux particules chargées ; les calorimètres, composés de matériaux denses, ils ont pour rôle de stopper les particules afin de mesurer leur énergie, leur résolution est bien moins bonne que celle d'un trajectographe ; les chambres à muons, seuls les muons parviennent à traverser les calorimètres et peuvent alors être observés dans ses détecteurs. Un champ magnétique est utilisé pour courber la trajectoire des particules chargées et ainsi mesurer leur impulsion dans les trajectographes. Ce champ magnétique est généré par un aimant solénoïdal.

Flux de particules et calorimétrie Pour réaliser les mesures de précision prévues auprès de ces futurs collisionneurs linéaires, une technique de reconstruction des événements appelée algorithme de flux de particules est envisagée et implique de fortes contraintes sur la conception des détecteurs aux points de collision de ces collisionneurs.

Un algorithme de flux de particules signifie penser l'étude de l'issue d'une collision en terme de particules sortantes plutôt qu'en terme de dépôts d'énergie. Ceci implique de reconstruire intégralement et fidèlement les particules de l'événement. L'intérêt est qu'une fois que tous les signaux de chaque sous détecteur sont attribués à un ensemble de particules reconstruite, l'énergie des chargées pourra être déduite de la mesure très précise de leur impulsion et de la connaissance de leur masse suite à leur identification lors de le reconstruction. Sachant que dans un jet, environ 60% de l'énergie est portée par des hadrons chargés, la mesure de l'energie d'un jet a beaucoup à gagner à mesurer cette contribution à l'aide du trajectographe plutôt que des calorimètres. La résolution atteignable serait meilleure que 3–4% sur toute la gamme d'énergie envisagée, soit environ deux fois meilleure que l'état de l'art actuel. L'utilisation optimale d'un algorithme de flux de particules implique de fortes contraintes sur la conception des détecteurs. Entre autre, le calorimètre hadronique doit être placé à l'intérieur de l'aimant et donc

doit être le plus compact possible. Le calorimètre doit aussi disposer d'une segmentation transverse et longitudinale sans précédent en calorimétrie hadronique (ex : 40 couches longitudinalement et $1 \times 1\,\mathrm{cm}^2$ latéralement) et les zones mortes doivent être minimisées.

Part II

Characterisation and Development of MICROMEGAS Chambers for Hadronic Calorimetry at a Future Linear Collider

CHAPTER 3

MICROMEGAS chambers for hadronic calorimetry

After a brief introduction on gaseous detectors, the MICRO MEsh GAseous Structure (MICROMEGAS) technology is presented. The Research and Development (R&D) project on large area MICROMEGAS chambers using bulk technology for application to digital hadronic calorimetry is introduced. The different prototypes are described and the road map of the project is presented.

3.1 A brief overview of gaseous detectors

The principle of particle detection with gas is based on electromagnetic interactions. As a charged particle moves close to an atom, an energy transfer occurs and, if sufficient, can result in its ionisation. Depending on the detection technique, this ionization leads to a phase transition (cloud or bubble chambers) or, by applying an electric field, ionised electrons can be manoeuvred and multiplied to produce an electric signal that can be processed by an electronic circuit.

The first gaseous detector was the well known Geiger-Müller tube, or Geiger counter. Its principle was described by Hans Geiger in 1908 [35] and the first counter was built in 1928 [36]. A Geiger counter consists of a grounded conductive tube enclosing a low pressure gas volume in the middle of which a high voltage wire is stretched. Any ionising radiation penetrating the gas volume provokes a discharge in the gas and therefore allows the detection of the radiation. Such devices are very rate limited, a dead time of about 200 μs occurs after a discharge. Because of the saturated functioning, no signal amplitude is measured. These simple detectors are still largely in use nowadays for measurements of weak activity sources.

Among the first gaseous detectors were also the cloud chambers developed by the Scottish physicist Charles Thomas Rees Wilson in the early 20$^{\text{th}}$ century [37]. They allowed several great discoveries, like anti-matter (1933 [38]) or new particles in the cosmic rays (*e.g.* the muon in 1937 [39]). Originally, physics events were recorded thanks to emulsions or cloud chambers coupled to cameras furnishing photographs of events that

had to be carefully analysed one by one. In 1968, Georges Charpak invented the Multi-Wire Proportional Counter (MWPC) [40] allowing particle positions or trajectories to be electronically recorded and hence processed thanks to the development of early computers. This innovation revolutionised experimentation in particle physics. High rate experiments were then possible allowing massive data acquisition.

The main limitation of electron multiplying gaseous detectors is their rate capability determined by ion occupancy in the amplification region. As long as the ions are not collected, they are screening the electric field responsible for electron multiplication which is hence nearly suppressed, resulting in a dead time causing a drop of detection efficiency. The performance of the first of these detectors however complied with the need of the early collider experiments.

Some gaseous detectors are presented now, namely the Multi-Wire Proportional Counter (MWPC) being the first electron amplifying gaseous detector, the Micro-Strip Gas Chamber (MSGC) and the Micro-Gap Chambers (MGC) as major evolutions that preceded the development of the MICRO MEsh GAseous Structure (MICROMEGAS). This presentation is non-exhaustive and aims at illustrating the evolution of gaseous detector technologies.

3.1.1 Multi-Wire Proportional Counter

The Multi-Wire Proportional Counter (MWPC) [41] is a chamber filled with a noble gas based mixture. Two cathode planes define a drift gap in the middle of which thin ($\approx$20–50 μm) anode wires at high voltage generate an accelerating electric field at their vicinity. The MWPC working principle resides in the drifting of ionised electrons towards the anode wires where the intense electric field at the wire surface multiplies them *via* an avalanche process. The so-produced moving charges induce a signal on the wires that can be electronically read out.

Figure 3.1 illustrates the electric field configuration in a MWPC. Figure 3.1(a) emphasises the drift region far from the wires where the field is uniform. Figure 3.1(b) focuses on the amplification region close to the wires where the electric field equipotential lines are concentric. The field strength close to the wires depends on the applied voltage and on the wire diameter and can reach several $10^5\,\mathrm{V}\cdot\mathrm{cm}^{-1}$.

However, the MWPCs have certain limitations. The spatial resolution is limited by the wire spacing, limited itself by mechanical constraints due to electrostatic repulsion between the thin wires. The best spatial resolution is of the order of 1 mm. The rate of the MWPCs is limited by a drop of the gain due to the avalanche ions drifting back from the anode wires towards the cathode planes and thus compensating the electric field. Rates about $10^5\,\mathrm{Hz}/$ wire can be achieved [40].

Efforts have been made to improve the MWPC spatial resolution and rate capability. The use of a segmented ion collecting cathode (with pads or strips) can improve the spatial resolution together with providing two dimensional information. The fine segmentation allows the computation of the barycentre of the charge deposition on the cathode and thus provide very precise two dimensional spatial information. Resolution of a few tens of microns have been achieved this way.

The use of a grid as intermediate electrode between the drift region, where the field lines are parallel, and the amplification region, where they start to bend towards the

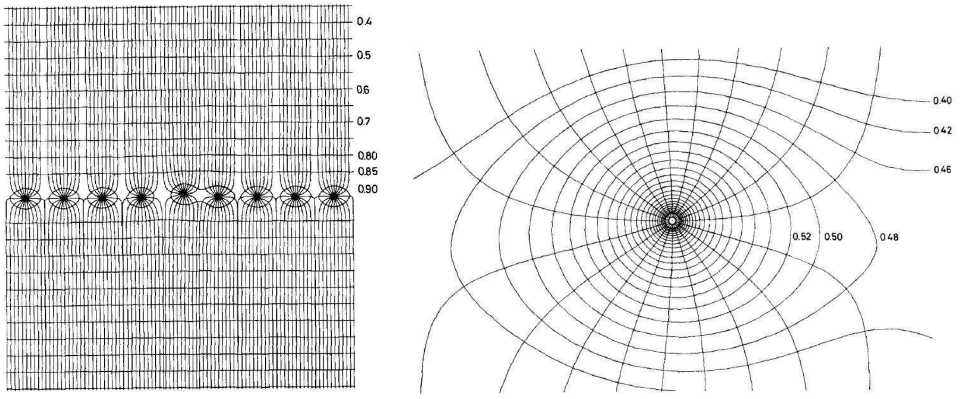

(a) (b)

Figure 3.1: Field line configuration in a MWPC[41].

wires, allows the drift field to be raised thus increasing the drift velocity of the primary electrons. The intermediate grid can also reduce the ion back-flow towards the drift region. With a higher electron drift velocity, a slightly higher rate capability can be achieved. Details about developments of this solution are found in [41].

Along with the development of electronics, particle physics could take great advantage of the possibilities of particle accelerators, and called for detectors with higher rate capabilities than those of the MWPC.

Among various different types of gaseous detectors (see [42] for a broader overview of the different types of gaseous detectors), some were especially designed to outperform the MWPCs in terms of rate capability.

3.1.2 Some electron amplifying gaseous detectors

3.1.2.1 Micro-Strip Gas Chamber

In 1988, almost twenty years after the invention of MWPC, the Micro-Strip Gas Chamber (MSGC) [43], a new design of detector, was introduced based on the same principle: electron amplification resulting from the high electric field in the vicinity of thin electrodes.

To obtain a better spatial resolution than the basic MWPC, wires are replaced by strips of the same thickness printed by photolithography on a insulating substrate or a Printed Circuit Board (PCB). Thus the mechanical constraints concerning the wire spacing does not hold anymore and the MSGC strips can be much closer to each other than the MWPC wires. As displayed in figure 3.2(a), the strips can be set as close to each other as $\approx 200\,\mu$m, leading to a spatial resolution of $\approx 60\,\mu$m orthogonal to the strips. Using a segmented ion collecting cathode still brings the same advantages as for the MWPC.

To improve the rate capability, a solution has been found to more rapidly evacuate the ions: cathode strips are interleaved with anode ones (see schematics in figure 3.2(a). In this case, ionised electrons are driven to the amplification strips from anywhere in the gas volume along the field lines and the ions, produced in the vicinity of the amplifying strips are attracted and quickly collected by the nearby cathode strips. The electric field

configuration is displayed in figure 3.2(b).

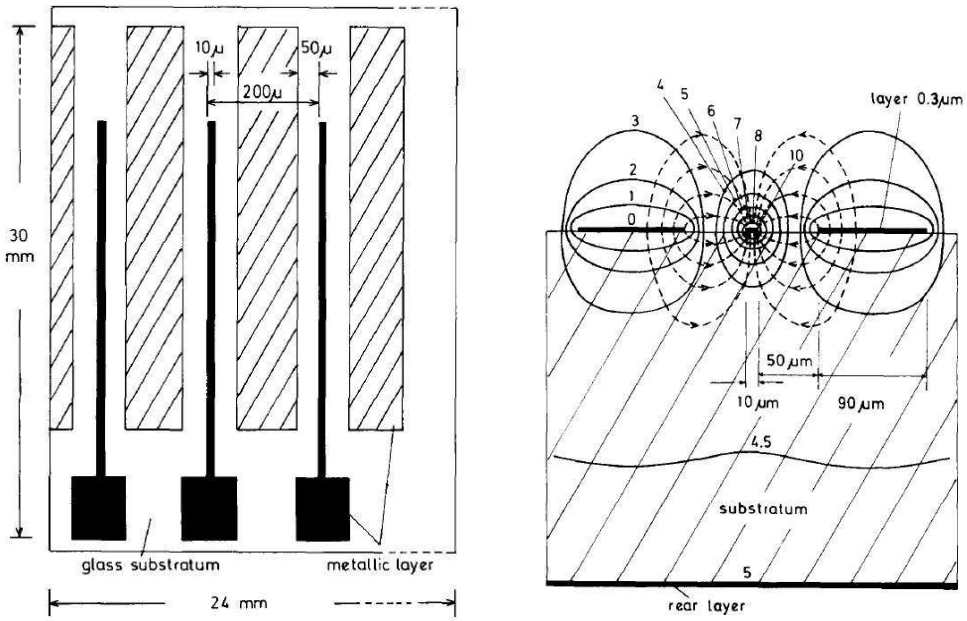

(a) (b)

Figure 3.2: MSGC principle (taken from [43]).

Unfortunately, this development produced a new issue: the ions moving between the strips are very close to the substrate surface and tend to get stuck on it by diffusion and thus to tend to charge the substrate up. This charging up causes a distortion of the electric field configuration, lowering progressively the detector gain and increasing the breakdown probability. Several solutions where tested (electrode at the back of the PCB to repulse the ions from the substrate surface, resistive coating of the substrate ...) leading to some improvement, but the ageing of the MSGCs remained a problem.

3.1.2.2 Micro-Gap Chambers

In 1993, Micro-Gap Chambers (MGC) [44] were introduced as a successor of the MSGCs, with comparable or even better performance and no charging up problem. The basic principle is still the same as MWPC and MSGC, but here the anode strips are not directly deposited on the substrate, they stand on wider insulating strips (only a few microns wider) which lie on a conductive plane fixed on the substrate. This metallic plane plays the role of the ion collecting cathode. The very small surface of the insulator does not lead to any charging up and the proximity of the cathode to the anode (a few microns) leads to faster evacuation of the ions, a lower ion back-flow towards the drift electrode and a higher field near the anode strips. A scheme of the MGC is sketched in figure 3.3.

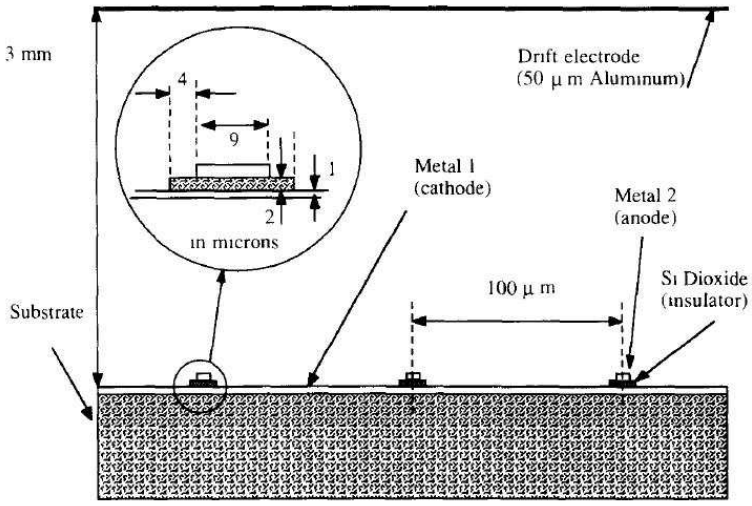

Figure 3.3: Scheme of the MGC principle [44].

3.2 MICROMEGAS technology

Another generation of gaseous electron amplifying detectors is now presented. For these detectors, drift and amplification of ionised electrons occur in different gas regions separated by a conductive mesh nearly transparent to electrons. Ionization takes place in the large (few mm to 1 meter or more) drift volume and electrons are driven to the $\approx$ 50–150 μm thick amplification volume where the high electric field lying between the mesh and the segmented anode plane allows electron avalanche amplification.

3.2.1 Description and basic principle

The MICRO MEsh GAseous Structure (MICROMEGAS) chamber was introduced in 1996 [45] as a fast signal, position-sensitive, radiation hard gaseous detector. It consists of a gas chamber where two asymmetric gaps are defined by three electrodes. The drift gap lies between the drift electrode and a conductive mesh, and is usually a few millimetres thick[1]. The amplification gap is located between the mesh and the segmented anode and is only about a few tens of microns thick. The drift gap is also called conversion gap because the ionization of the gas by incoming radiation occurs mainly in it.

In both gaps, a specific electric field is defined by the voltage applied to each electrode. The field in the drift space is rather low (around $100\,\mathrm{V}\cdot\mathrm{cm}^{-1}$) and is meant to drift ionised electrons to the mesh. The field in the amplification gap is very high (several tens of $\mathrm{kV}\cdot\mathrm{cm}^{-1}$) and catches the free electrons from the drift gap to forcefully accelerate them through the small amplification gap. They then acquire enough energy to ionise surrounding gas. The newly ionised electrons gain as well sufficient energy to ionise the gas again and again, thus forming an avalanche and leading to a measurable electric signal on the anode and on the mesh. The MICROMEGAS principle is illustrated in figure 3.4.

[1]MICROMEGAS TPCs present a much larger drift gap, up to several meters.

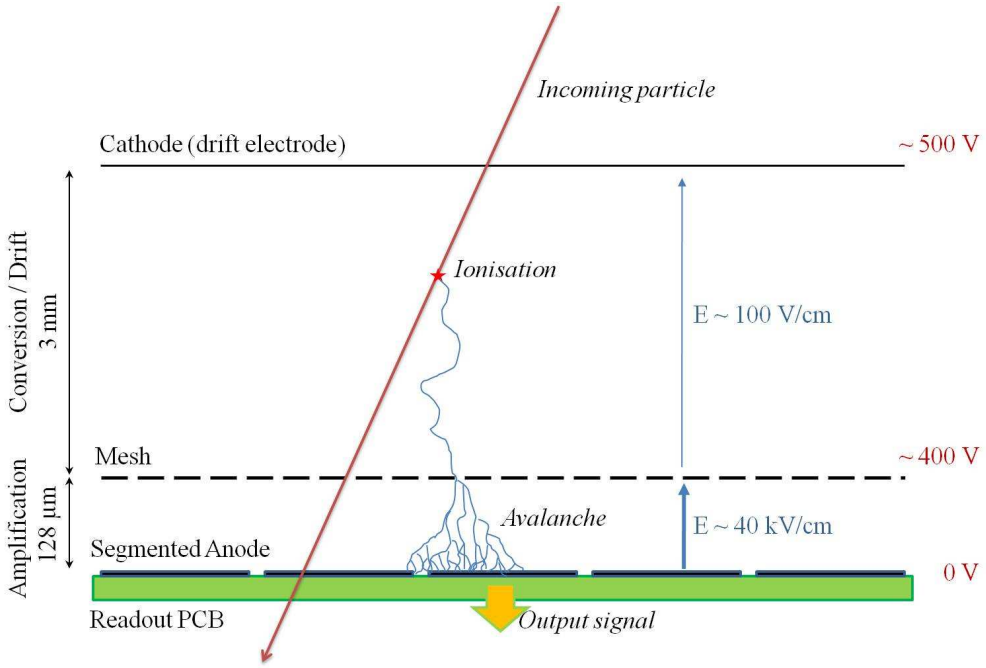

Figure 3.4: Scheme of MICROMEGAS principle.

3.2.2 The MICROMEGAS signal

Electron amplification The electron avalanche occurring in the amplification gap (see working principle in section 3.2.1) produces a high number of ionisations (up to more than 25 000 per primary electron). The average of this number is called the *multiplication factor* or *(gas) gain* of the chamber. The size of the avalanche shows large variations around its average value. A model of gas amplification, established in [46], gave the number of electrons n in an avalanche through a simple exponential probability distribution (valid for $\bar{n} \gg 1$):

$$p(n) = \frac{1}{\bar{n}}\, exp\left(-\frac{n}{\bar{n}}\right) . \tag{3.1}$$

where $\bar{n}$ is the average number of electron in the avalanche. $\bar{n}$ is given by :

$$\bar{n} = exp\left(\int_0^x \alpha(x')\, dx'\right) , \tag{3.2}$$

where x denotes the distance covered by the avalanche and $\alpha(x)$ is the first Townsend coefficient which depend on the gas mixture and the electric field configuration. Typical values of this coefficient, in the present application are expected around $\approx 0.075\,\mu\mathrm{m}^{-1}$.

Induced signal The current generated by the moving charges in the amplification gap has two contributions:

- A brief and fast signal due to the electrons, generated mostly close to the anode plane and quickly collected (1–2 ns). The drift velocity of electron in gas is of several $\mathrm{cm}\cdot\mu\mathrm{s}^{-1}$.

- A long signal due to the ions moving slowly towards the mesh (100–200 ns), their drift velocity is at least two order of magnitude lower than the electrons' one.

Figure 3.5 illustrates the calculation in annex A (page 151) of the time development of the MICROMEGAS signal and the integration of the anode deposited charge. It is interesting to note that the total charge is simply the gain multiplied by the primary charge (see equation A.13), and that in fact the amplified electrons do not contribute much to the final detected charge. The main contribution is clearly due to ions.

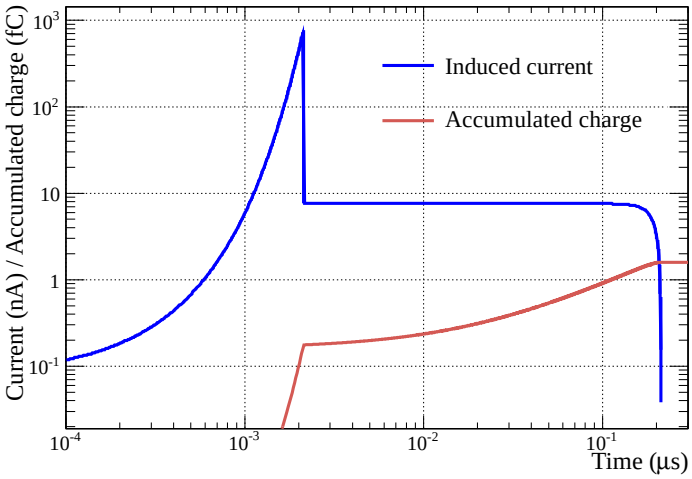

Figure 3.5: Plots of the MICROMEGAS induced current and accumulated charge versus time.

The proportion between the two contributions relates directly to the gain of the chamber. The fraction η_e of the signal due to electrons is given by (see equation A.15 recalled here):

$$\eta_e = \frac{Q_e}{Q_{TOT}} = \frac{1}{\alpha\, g} = \frac{1}{ln(G)}\,,$$

with Q_e, the charged induced by electrons, Q_{TOT}, the total induced charge, α, the first Townsend coefficient, g the gap width and G the gas gain.

3.2.3 Bulk MICROMEGAS

The fabrication process of the first MICROMEGAS chambers did not allow the mass production of sensitive areas larger than a few square centimetres The largest MICROMEGAS chambers built with electroformed nickel meshes are used in the COMPASS experiment [47, 48]. Eleven $40 \times 40\,cm^2$ MICROMEGAS chambers are part of the experiment tracking system. [45, 49, 50]. In 2006, a new way to manufacture MICROMEGAS chambers was established based on the PCB technology [51]. This so-called "bulk" technology consists of laminating one or more thin layers of photo-resistive film on the anode PCB, then laminating the micro mesh and another layer of the same film (see

figure 3.6). The photo-resistive film is then irradiated with UV light to print insulating pillars by photo-lithography. The top photo-resistive layer, after the photolithography process, ensures a strong encapsulation of the mesh giving a robust final device. The former thin electroformed nickel micro-mesh is then replaced by an industrial stainless steel micro-woven mesh made of 30 μm thick wires.

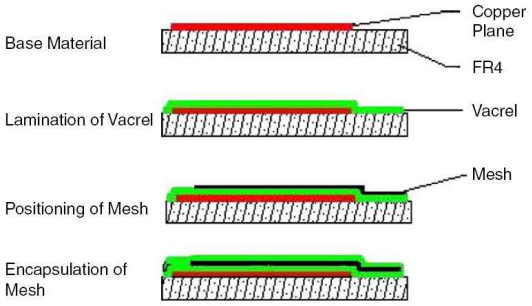

Figure 3.6: The MICROMEGAS bulk fabrication process [51].

This industrial process allows massive production of cheap and robust MICROMEGAS chambers and thus to evolve towards very large area detectors needed for instance in hadronic calorimetry at future linear colliders ($\approx$3000 m^2 for the SiD detector [52]).

3.3 Context of the R&D project

The use of the Particle Flow Algorithm (PFA) technique [32, 33] for event reconstruction and analysis at future linear colliders calls for detectors to be optimised for this purpose. One of the main requirements is that the signal induced by single particles must be individually identifiable. This calls for highly segmented calorimeters together with a high efficiency and low hit multiplicity in order to topologically separate the contribution of each particle in the calorimeters and to efficiently spot shower starts and hadronic interactions. To efficiently match a charged track with a calorimeter cluster, a prime requirement is that the Hadronic Calorimeter (HCAL) must be inside the solenoid and thus minimisation of the HCAL thickness is highly desired. For the sake of compactness, another requirement is that the power consumption of the readout electronics must be below 10 μW per channel in order to limit the size of the cooling system.

The final calorimeter will hold several thousands of square meters of active medium indicating a need for developments directed at very large area detectors.

Several technological solutions are envisaged to fulfil those requirements [52, 53], scintillators with analog readout or gaseous detectors with digital readout (Gas Electron Multipliers (GEMs), Resistive Plate Chambers (RPCs) and MICROMEGAS). The digital readout is needed to reduce the impact of the data handling and storage and thus the power consumption together with allowing a thinner lateral segmentation. Additionally, the digital readout tends to reduce the effect of energy deposition fluctuations in gas and therefore increase precision of gaseous detectors for this application. All these developments are carried out within the Calorimetry for Linear Colliders Experiments (CAL-

ICE) collaboration [54]. The GEM and MICROMEGAS activities are as well part of the RD51 collaboration [55]. These solutions need to be carefully analysed in order to select the one best suited for the final application. A detailed evaluation of the advantages and drawbacks of each is mandatory. In the following, a study of bulk MICROMEGAS chambers as a candidate for the active medium of a Digital Hadronic Calorimeter (DHCAL) is presented.

3.4 R&D project outline

The bulk technique makes MICROMEGAS an appealing solution for equipping a HCAL and calls for further study in this direction. A R&D project was therefore started at the *Laboratoire d'Annecy-le-vieux de Physique des Particules* (LAPP) in 2007 to investigate the application of bulk MICROMEGAS to hadronic calorimetry.

The study of bulk MICROMEGAS chambers as candidate for the active medium of a DHCAL can be imagined in several distinct phases, as follows:

1. Successfully assemble a MICROMEGAS chamber satisfying the thickness requirements
2. Perform a series of tests on small prototypes to evaluate their basic performance
3. Test the chip embedding process for MICROMEGAS chambers
4. Develop dedicated digital readout chips and a Data Acquisition System (DAQ)
5. Evolve towards larger area detectors: produce a functional square meter prototype with embedded readout electronics and verify the conservation of performance
6. Build a cubic meter calorimeter to evaluate its performance and perform physics measurements

Phase 1 has already been done during my Master internship where the detection of cosmic signals was achieved with the first prototypes [56]. The second phase is the main topic of this part of the thesis and is detailed in chapter 4, where laboratory X-ray tests are described, and in chapter 5, where beam test studies are presented. The remaining phases will be addressed in the last chapter of this part (chapter 6). Phase number 5 shares problems common to other experiments using similar MICROMEGAS chambers (mainly T2K experiment [57]). Phases 3 and 5 are key stages in the development of the project to prove the feasibility of large area MICROMEGAS chambers with embedded readout electronics, showing the very good performance promised by the small prototypes used in phase 2. Phase 4 is undergo in tight collaboration with our electronics engineers who designed a key element of the common CALICE DAQ, namely the Detector Interface (DIF) board. They also developed a high gain, low noise Application Specific Integrated Circuit (ASIC) in collaboration with the *Laboratoire de l'Accélérateur Linéaire, Paris* (LAL). The last phase of the list is of particular interest since the hadronic showering process has only very recently been observed with a granularity as fine as $1 \times 1\,\mathrm{cm}^2$[58] and only with RPCs as active medium.

3.5 Description of the prototypes

3.5.1 Common features

Each prototype consists of a bulk MICROMEGAS chamber with a 3 mm drift gap and a 128 μm amplification gap. The drift cathode is a 5 μm thick copper foil fixed on a 75 μm thick Kapton[2] film. The whole is glued on a 2 mm thick steel plate, forming the device's lid. The steel cover plate is part of the absorber and therefore would not contribute to the HCAL active layer's thickness. The 3 mm drift gap is ensured by a 3 mm thick resin frame enclosing the chamber and providing the gas inlet and outlet (see photography in figure 3.7(a)).

The mesh used is an industrial micro woven stainless steel mesh made of 30 μm diameter wires interwoven at a pitch of 80 μm. The mesh is held at 128 μm above the anode plane by 300 μm diameter pillars placed on a square lattice with a 2 mm pitch. The anode plane consists of $0.98\times0.98\,\mathrm{cm}^2$ pads separated by 200 μm lying on the detector's PCB. The $1\,\mathrm{cm}^2$ pattern made of a pad and the free space around will be denoted hereafter as a 1 pad area where 'pad' will be the area unit symbol.

3.5.2 Analogue prototypes

Before building large digital prototypes, a detailed characterisation of the technology is needed. For this purpose, four small prototypes with an analogue readout have been built and extensively tested.

Three of them have a $6\times16\,\mathrm{cm}^2$ active area (96 pads) and the fourth one is four times larger with a $12\times32\,\mathrm{cm}^2$ active area (384 pads). The mesh voltage of the small chambers is supplied through a dedicated pad while a $4\,\mathrm{mm}^2$ sidelong mesh voltage pad is used for the large chamber (see figure 3.7). The analogue readout is provided by GASSIPLEX boards [59]. (see detailed description in section 5.1.2, page 63) In the following, the three small chambers will be denoted CH0, CH1 and CH2 and the large one, CH3.

3.5.3 Digital prototypes

Several readout chips have been designed and tested on various PCB designs. The innovative aspect is that the chips must be embedded on the detector PCB to minimise the detector thickness and the dead zones due to readout boards outside the detectors. The readout chips are designed to ensure signal collection and preamplification very close to the detector, its digitisation and storage in a multi-event memory. The base-line design is that a single chip can handle 64 detector readout channels. The chip must be able to be power pulsed, namely, it will be switched on and off repeatedly in order to be on only during the bunch trains[3] and off the rest of the time. The aim of the power pulsing is to reduce the average power consumption, minimise the cooling needs and thus the amount of dead material inside the detector.

The readout chips involved in this project are summarised in table 3.1.

[2] polyimide: $C_{22}H_{10}N_2O_5$

[3] The beam is not continuously delivered but the particle bunches are organised in trains of given durations. Bunch trains are sometimes separated by long dead times.

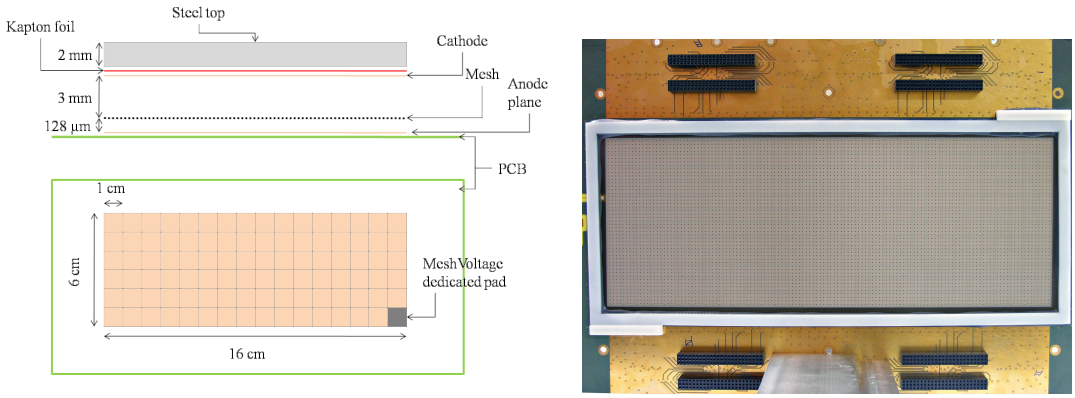

(a) (b)

Figure 3.7: Analogue readout prototypes. The left sketch gives CH0 to CH2 dimensions and can be straightforwardly extended to CH3. The right picture shows the bulk, the resin frame and the electronic board connectors of CH3 before its lid was glued.

Table 3.1: Summary of the digital chips

Chip	Info.	Developer	Detector
DIRAC(2)	[60]([61])	LAPP and IPNL	8×8 pad
HARDROC	[62]	LAL/Omega	8×32 pad and 32×48 pad
HARDROC2(b)	[62]	LAL/Omega	32×48 pad
MICROROC	[63]	LAPP and LAL/Omega	8×8 pad

One of the challenges of this project is that the chips have to be cabled in a soldering oven, but the bulk pillars do not tolerate this treatment. So the lamination process for the bulk installation must take place after the chip soldering. But these latter are way not robust enough to resist such a process. The solution is to solder the electronics on the naked PCB and then place a rigid mask on the electronic side to protect it during the lamination phase. Using this technique the first MICROMEGAS with embedded digital readout has been successfully assembled and tested [64]. All following prototypes have been mounted using this technique.

Résumé du chapitre

Dans ce chapitre, on introduit le principe des détecteurs gazeux, dans lequel un rayonnement ionisant crée des paires électron-ion qui sont ensuite amplifiées afin d'induire un signal électrique mesurable dans un système de lecture *ad hoc*. On s'intéressera en particulier à la technologie MICROMEGAS.

MICROMEGAS Un détecteur MICROMEGAS est une chambre remplie d'un mélange gazeux à base d'un gaz noble tel que l'Argon. Le volume gazeux est séparé en deux régions asymétriques définies par trois électrodes planes : la cathode ou électrode de

dérive, la micro-grille et l'anode. La première région, épaisse de quelques millimètres à quelques mètres (chambres à dérive), située entre l'électrode de dérive et la micro-grille, est appelée "espace de dérive", elle est le siège de l'ionisation du gaz et de la dérive des électrons primaires vers la micro-grille séparant les deux régions. La deuxième région, appelée "espace d'amplification", située entre la micro-grille et le plan d'anode, ne mesure que quelques dizaines de microns ($50 - 100\,\mu$m), il y règne un champ électrique suffisamment intense ($40 - 50\,\mathrm{kV}\cdot\mathrm{cm}^{-1}$) pour que les électrons primaires traversant la grille soient amplifiés ($\times \approx 10\,000$) par ionisations en cascade, induisant ainsi un signal sur la grille et sur le plan d'anode. Les ions générés lors du processus d'avalanche sont captés par la micro-grille et donc, grâce à la faible épaisseur de l'espace d'amplification, sont rapidement ($\approx 100\,$ns) évacués, permettant ainsi des utilisations à haut flux.

Prototypes MICROMEGAS pour la calorimétrie hadronique auprès d'un futur collisionneur linéaire Pour satisfaire aux pré-requis d'un calorimètre hadronique optimisé pour l'application d'un PFA, des prototypes de détecteurs gazeux MICROMEGAS sont développés au LAPP. Nos prototypes sont construits suivant la récente technologie *bulk*. Deux couches de film photorésistif ($64\,\mu$m chacun) sont laminées sur le circuit imprimé supportant le plan d'anode, puis la micro-grille, tendue sur un cadre le temps de l'installation, subit le même processus, et enfin une troisième couche de ce même film est encore laminée par dessus. Par photolithographie, des piliers destinés à soutenir la grille sont imprimés dans le film et maintienne la grille fermement en place à une distance constante de l'anode. Le produit final s'avère robuste et industrialisable, idéal pour une production à grande échelle.

Le plan d'anode est segmenté en carreaux de $1 \times 1\,\mathrm{cm}^2$, l'espace d'amplification mesure $128\,\mu$m d'épaisseur et l'espace de dérive est assuré par un cadre en résine de 3 mm d'épaisseur fournissant également les entrée et sortie du gaz. L'électrode de dérive est collée sur une plaque d'acier de 2 mm fermant la chambre. Ces deux millimètres d'acier comptent dans le budget du milieu passif du calorimètre.

Ce design doit subir différentes étapes de développement et de test avant une production à grande échelle :

1. Construction d'un premier prototype fonctionnel.
2. Évaluation des performances.
3. Test de l'embarquement de l'électronique de lecture.
4. Développement d'une électronique de lecture dédiée optimisée.
5. Évolution vers de plus grandes surfaces : production de prototypes d'un mètre carré avec électronique de lecture embarquée et conservation des performances.
6. Construction d'un calorimètre d'un mètre cube.

Les étapes de caractérisation des performances sont effectuées à l'aide de prototypes à lecture analogique. Ces prototypes sont au nombre de quatre, trois d'entre eux présentent une surface active de $6 \times 16\,\mathrm{cm}^2$ et le dernier, une surface active de $12 \times 32\,\mathrm{cm}^2$. La lecture est assurée par des cartes GASSIPLEX montées en mezzanine sur le coté du plan

d'anode (*cf.* fig. 3.7). Cette caractérisation est l'objet des deux prochains chapitres de ce manuscrit.

Les différentes puces de lecture digitale, impliquées dans le projet à ce jour, sont présentées dans la table 3.1. Lors de la fabrication des prototypes digitaux, l'installation de puces de lecture sur le circuit imprimé d'anode se fait préalablement à la pose du *bulk* car ce dernier ne supporte pas un passage en four à soudure. Ensuite un masque de protection en résine est installé sur le coté composant du circuit imprimé afin de protéger l'électronique lors du passage en laminoir pour la pose du *bulk*.

CHAPTER 4

X-ray tests

X-ray tests using an ^{55}Fe source have been performed to measure the basic performance of our MICROMEGAS prototypes. For each of the prototypes, holes are drilled into the steel lid in a few locations to allow X-ray injection through the thin cathode and Kapton foil.

Electron collection efficiency[1] and gas gain in Ar/iC_4H_{10} (95/5) and Ar/CO_2 (80/20) were deduced from the ^{55}Fe K_α photopeak value given by a fit of three gaussian functions to the ^{55}Fe spectrum (figure 4.1). Gain measurements were used to predict gain dependency versus pressure, temperature and amplification gap thickness variations. Those predictions are compared to direct measurements in section 4.5.

4.1 Experimental setup

For the X-ray study, only one chamber with a readout system based on the mesh signal was used. The mesh signal was read out by an ORTEC 142C charge preamplifier linked to its corresponding amplifier/shaper. The amplifier output was recorded with a CAEN V550 10-bit ADCs (VME modules) sequenced by a CAEN V551B C-RAMS sequencer VME module. Data was then collected by the computer through an optical VME/PCI bridge. A Labview based software, called CENTAURE [65], was used to timestamp the recorded events for condition database matching. This software was optimised for the data acquisition and on-line monitoring of the pad readout of the prototypes but was perfectly usable for the mesh readout as well. The calibration constant of the mesh readout chain was precisely measured to be 2.199±0.026 ADU/fC (Analog to Digital Unit).

[1] Or equivalently: mesh transparency to electrons

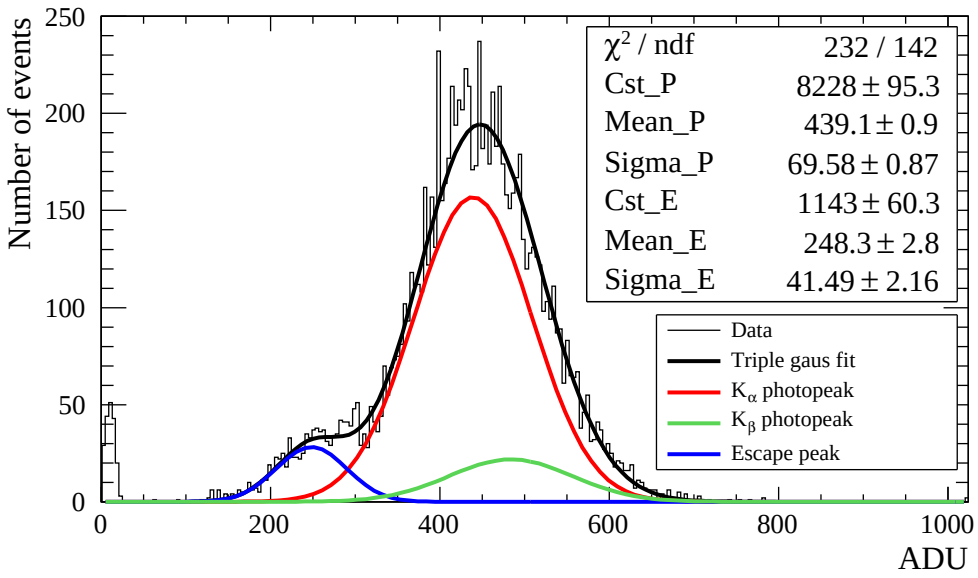

Figure 4.1: ^{55}Fe spectrum with gaussian fits of the two photopeaks and of the escape peak.

4.2 Electron collection efficiency

The ratio between amplification and drift electric fields affects the mesh transparency to the electrons (or collection efficiency) by contracting the field lines so that the electrons are mostly driven through the center of the mesh's holes and reach the amplification gap. Figure 4.2 shows the variation of the ^{55}Fe peak value *versus* the field ratio in Ar/iC$_4$H$_{10}$ (95/5) and Ar/CO$_2$ (80/20). The amplification field was kept constant while the drift field varied to set the field ratio. The mesh voltage was 420 V in Ar/iC$_4$H$_{10}$ (95/5) and 570 V in Ar/CO$_2$ (80/20).

The curves displayed in figure 4.2 (right) show a maximum at a field ratio of about 150 – 200 for both gas mixtures. The measurements reported in the following were performed at ratios within this range.

A explanation for the decline at high field ratio observed in figure 4.2 is the attachment of some primary electrons in the drift region by electronegative impurities (*e.g.* oxygen, water vapour). For a constant amplification field, a higher ratio means a lower drift field and consequently the primary electrons tend to have less energy. Since the attachment cross section of some impurities peaks at low energy (*e.g.* ≈ 0.1 eV for oxygen [66]), a lower drift field can therefore lead to a higher attachment probability, resulting in a reduction of the number of electrons reaching the amplification region.

4.3 Gas gain

The amplification gap gain, so-called gas gain, is determined through a fit of three gaussian functions to the ^{55}Fe spectrum (figure 4.1) assuming 230 and 209 primary electrons in the Ar/iC$_4$H$_{10}$ (95/5) and Ar/CO$_2$ (80/20) mixtures respectively and using the mesh

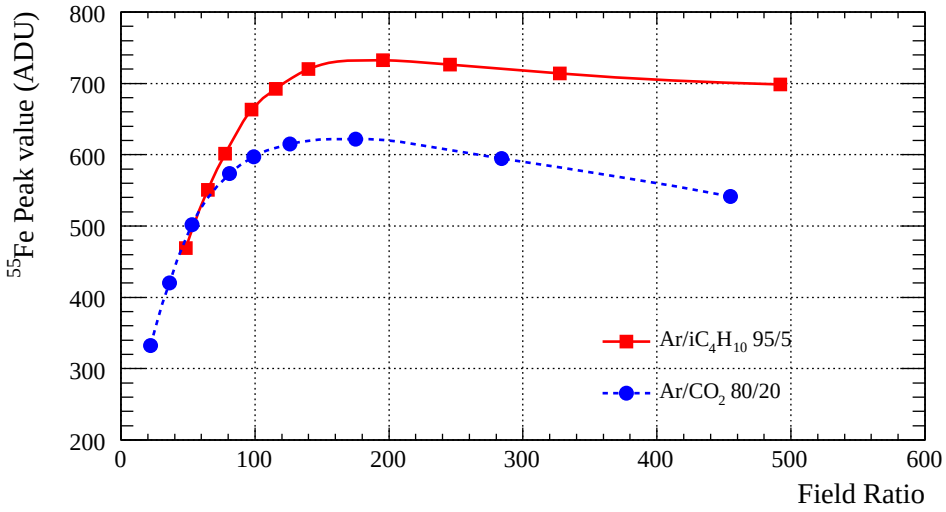

Figure 4.2: ^{55}Fe peak value variation *versus* field ratio.

readout calibration constant (2.19 ADU/fC). Keeping the drift field at 150 V·cm^{-1}, a set of measurements at 954 mbar in the Ar/iC$_4$H$_{10}$ mixture, 961 mbar in Ar/CO$_2$ and at a temperature of 293 K with various voltage settings gave the curves displayed in figure 4.3. The maximum gas gain for each gas mixture is given by the last point of the gain curves and corresponds to a spark rate of about one per minute. A much higher maximum gain ($4{\cdot}10^4$) can be achieved in Ar/iC$_4$H$_{10}$ than in Ar/CO$_2$. Also the mesh voltage, for a given gain, is 180 V lower in Ar/iC$_4$H$_{10}$.

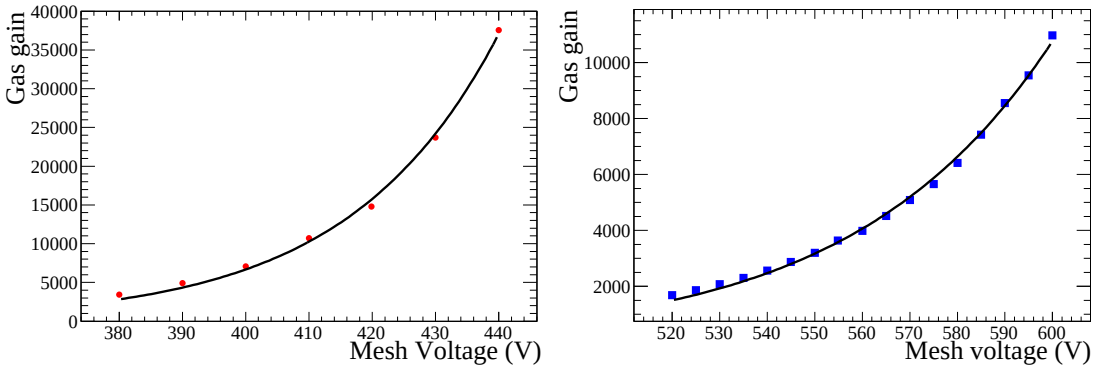

(a) (b)

Figure 4.3: Gas gain versus mesh voltage fitted with the gas gain formula in Ar/iC$_4$H$_{10}$ (95/5) [4.3(a)] and in Ar/CO$_2$ (80/20) [4.3(b)].

4.4 Method for pressure and temperature correction

4.4.1 Gas Gain Model

The gas gain of the chambers is given by the exponential of the average number of primary ionizations from a single avalanche initiating electron. In a uniform field, this number is given by the first Townsend coefficient, denoted α, multiplied by the amplification gap thickness, denoted g:

$$G = e^{\alpha \cdot g} \,. \tag{4.1}$$

The Townsend coefficient can be parameterised by the Rose and Korff formula [67]:

$$\alpha = n \cdot A_0 e^{-B_0 n/E} \,, \tag{4.2}$$

where A_0 and B_0 are constants that depends on the gas mixture, E is the electric field and n the gas density. Using the ideal gas law to express n and combining equations 4.1 and 4.2, one obtain:

$$G = exp\left[\frac{APg}{T} \cdot exp\left(-\frac{BPg}{TV}\right)\right] \,, \tag{4.3}$$

with $A = A_0/k_{\mathrm{B}}$, $B = B_0/k_{\mathrm{B}}$ and $V = E \cdot g$, where k_{B} is the Boltzmann constant. Equation 4.3 leads to the variation of the gas gain versus pressure (P), temperature (T) and amplification gap thickness (g) through

$$\Delta G/G = C_P \Delta P + C_T \Delta T + C_g \Delta g \,,$$

where C_x, $x \in \{C, P, T\}$, are the environmental dependency coefficients, expressed as follows:

$$C_P = \frac{1}{G}\frac{\partial G}{\partial P} = \left(\frac{Ag}{T} - \frac{ABPg^2}{T^2V}\right) exp\left(-\frac{BPg}{TV}\right) \tag{4.4}$$

$$C_T = \frac{1}{G}\frac{\partial G}{\partial T} = \left(\frac{ABP^2g^2}{T^3V} - \frac{APg}{T^2}\right) exp\left(-\frac{BPg}{TV}\right) \tag{4.5}$$

$$C_g = \frac{1}{G}\frac{\partial G}{\partial g} = \left(\frac{AP}{T} - \frac{ABP^2g}{T^2V}\right) exp\left(-\frac{BPg}{TV}\right) \,. \tag{4.6}$$

In practice, it is convenient to apply one single correction for pressure and temperature variations using the coefficient:

$$C_{P/T} = \frac{1}{G}\frac{\partial G}{\partial (P/T)} = \left(Ag - \frac{ABPg^2}{TV}\right) exp\left(-\frac{BPg}{TV}\right) \,. \tag{4.7}$$

A correction is applied by multiplying the gain by the correction factor f_x given by:

$$f_x = 1 - C_x \cdot \Delta\left(x\right) \,, \tag{4.8}$$

where x stands for g, P, T or P/T.

Table 4.1: Gas gain model fit results.

Gas	A ($\mathrm{K\,mbar^{-1}\,\mu m^{-1}}$)	B ($\mathrm{K\,V\,mbar^{-1}\,\mu m^{-1}}$)
Ar/iC_4H_{10}	0.14 ± 0.01	1.8 ± 0.1
Ar/CO_2	0.10 ± 0.01	2.1 ± 0.2

Table 4.2: Environmental dependency coefficients predicted from the gain curves in Ar/iC_4H_{10} (95/5) and Ar/CO_2 (80/20).

Gas	C_P ($\%\,\mathrm{mbar^{-1}}$)	C_T ($\%\,\mathrm{K^{-1}}$)	C_g ($\%\,\mu\mathrm{m^{-1}}$)	$C_{P/T}$ ($\%\,\mathrm{K\ mbar^{-1}}$)
Ar/iC_4H_{10}	-0.8 ± 0.1	2.6 ± 0.3	-6.6 ± 0.6	-236 ± 24
Ar/CO_2	-0.5 ± 0.1	1.6 ± 0.4	-3.8 ± 0.9	-145 ± 35

4.4.2 Application to Ar/iC_4H_{10} and Ar/CO_2

The gain dependencies on P, T, P/T and g can be predicted from a gain curve by adjusting the constants A and B on the measured trend *via* formula 4.3. The fit results are gathered in table 4.1 and the dependencies calculated using the formulae 4.4 – 4.7 are gathered in table 4.2.
The predicted values of C_P, C_T and $C_{P/T}$ in Ar/CO_2 are compared to direct measurements in the next section. Over a period of about two weeks, natural temperature variations are about 5 K and pressure variations are around 20 mbar, daily variations of the P/T ratio are of the order of $3\,\mathrm{mbar \cdot K^{-1}}$ climbing to $8\,\mathrm{mbar \cdot K^{-1}}$ over a 2 week period. Those natural variations hence induce typical natural gain fluctuations of the order of 10% over a two week period.

4.5 Environmental study in Ar/CO_2 (80/20)

4.5.1 Experimental conditions

During two weeks, the amplitude of some 10^8 pulses from ^{55}Fe quanta conversions in Ar/CO_2 (80/20) were recorded, enabling a precise monitoring of the detector gain as a function of time. In parallel, gas pressure and temperature were also recorded. The mesh voltage was set to 570 V at which a gain of about $5{\cdot}10^3$ was measured (see figure 4.3(b)). The drift field was kept at $100\,\mathrm{V \cdot cm^{-1}}$. The Ar and CO_2 gas flows were equal to 0.97 and 0.24 l/h, yielding a total flow of 1.21 l/h. The mean pressure was 959.7 mbar and the mean temperature was 298.2 K. The temperature was controlled with the help of an air conditioner and the gas pressure fluctuated according to the atmospheric pressure variations.

4.5.2 Pressure corrections

During part of the run, the gas temperature was maintained around 298 K to examine the gas gain dependency on pressure only. Figure 4.4 shows the ^{55}Fe peak value versus pressure recorded at a temperature $T = (298.0 \pm 0.5)$ K. A linear behaviour is observed

and fitted with a slope α_P which relates to the C_P coefficient according to:

$$\alpha_P = \bar{v} \cdot C_P \,,$$

where $\bar{v}$ is the average ^{55}Fe peak value over the fitted range. With $\alpha_P = (-2.686 \pm 0.004)\,\mathrm{mbar}^{-1}\,\mathrm{ADU}^{-1}$ and $\bar{v} \approx 440\,\mathrm{ADU}$, computation gives:

$$C_P = (-0.61 \pm 0.01)\%\,\mathrm{mbar}^{-1} \,,$$

which is consistent with the predicted value (section 4.5.1).

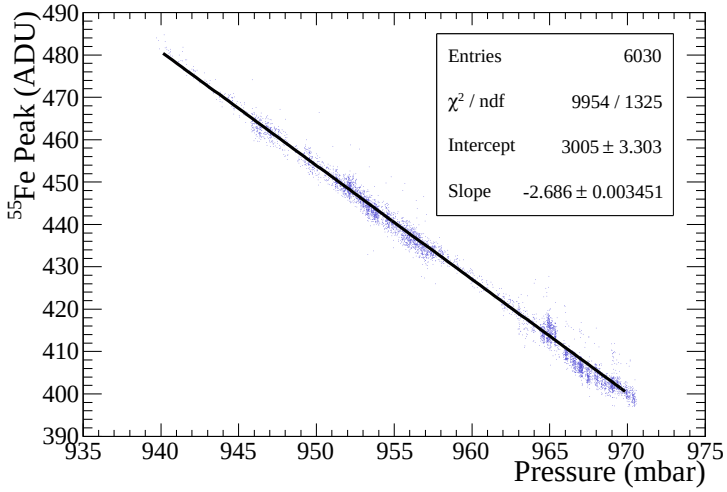

Figure 4.4: ^{55}Fe peak value versus atmospheric pressure at constant temperature (T=298 K).

4.5.3 Temperature corrections

Data recorded during a period with temperature variations of a few kelvins have been corrected for pressure variations using C_P from section 4.5.2 and formula 4.8. The corrected ^{55}Fe peak value, v_{corr_P}, is given by:

$$v_{\mathrm{corr}_P} = v \cdot (1 - C_P \cdot \Delta P) \,, \tag{4.9}$$

where v is the raw peak value, and is plotted in figure 4.5. A linear fit was performed and its slope α_T gave the C_T coefficient through $\alpha_T = \bar{v} \cdot C_T$. With $\alpha_T = 5.75\,\mathrm{K}^{-1}\,\mathrm{ADU}^{-1}$ and $\bar{v} \approx 420\,\mathrm{ADU}$, computation leads to:

$$C_T = (-1.37 \pm 0.01)\%\,\mathrm{K}^{-1} \,,$$

which is consistent with the value predicted in section 4.5.1.

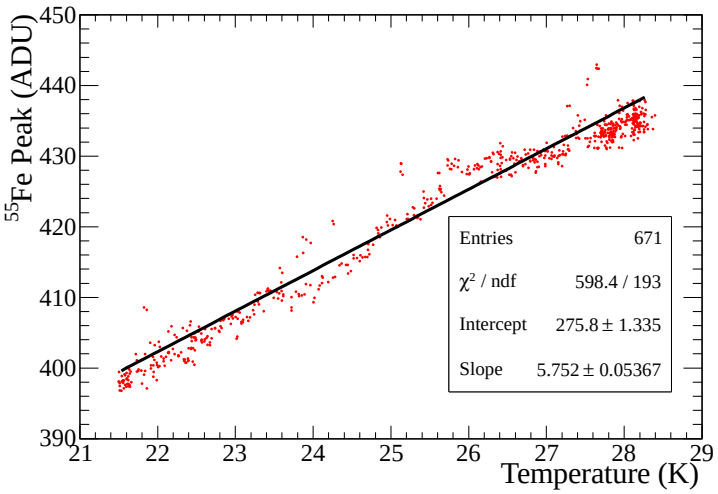

Figure 4.5: Pressure corrected ^{55}Fe peak value versus temperature.

4.5.4 Corrections using the ratio of pressure over temperature

The evolution of the ^{55}Fe peak value along the whole data set versus the ratio of pressure over temperature is plotted in figure 4.6. A straight line was adjusted on the points and its slope $\alpha_{P/T}$ gave the $C_{P/T}$ coefficient through $\alpha_{P/T} = \bar{v} \cdot C_{P/T}$. With $\alpha_{P/T} = -722\,\mathrm{K}^{-1}\,\mathrm{ADU}^{-1}$ and $\bar{v} \approx 440\,\mathrm{ADU}$, its value is:

$$C_{P/T} = (-164 \pm 1)\%\,\mathrm{K\,mbar}^{-1}\ ,$$

which is within the error range of the value predicted in section 4.5.1.

4.5.5 Conclusion of the study

Direct measurement of the coefficients C_P, C_T and $C_{P/T}$ have shown good agreement with the gas gain model prediction (table 4.3). Using those coefficients, the ^{55}Fe peak value has been corrected for pressure and temperature variations according to:

$$v_{\mathrm{corr}_P} = v \cdot (1 - C_P \cdot \Delta P) \quad (4.10)$$

$$v_{\mathrm{corr}_T} = v \cdot (1 - C_P \cdot \Delta P) \cdot (1 - C_T \cdot \Delta T) \quad (4.11)$$

$$v_{\mathrm{corr}_{P/T}} = v \cdot \Big(1 - C_{P/T} \cdot \Delta\,(P/T)\Big)\ . \quad (4.12)$$

The effect of those corrections are illustrated in figure 4.7. The ^{55}Fe peak value is very scattered before applying any correction. The successive corrections for pressure and temperature leads to a major improvement of the ^{55}Fe peak value regularity. The direct correction using the ratio of pressure over temperature is also valuable. The correction yielding the strongest reduction of the distribution r.m.s. is the one based on C_P because the temperature was controlled during the data acquisition and showed limited variations.

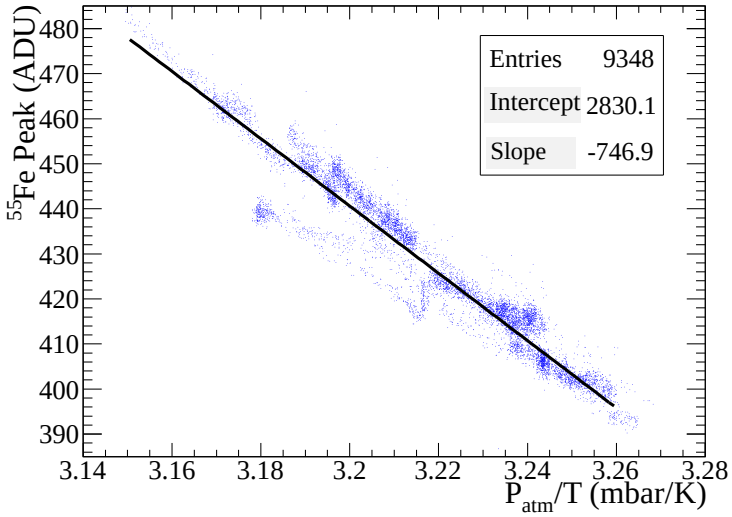

Figure 4.6: ^{55}Fe peak value versus the ratio of pressure over temperature, using all data without any correction.

Table 4.3: Summary of predicted and measured values for environmental coefficients in $Ar/CO_2(80/20)$

Coefficient	C_P	C_T	$C_{P/T}$
Predicted Value	$(-0.5 \pm 0.1)\%\,\mathrm{mbar}^{-1}$	$(1.6 \pm 0.4)\%\,\mathrm{K}^{-1}$	$(-145 \pm 35)\%\,\mathrm{K\,mbar}^{-1}$
Measured Value	$(-0.61 \pm 0.01)\%\,\mathrm{mbar}^{-1}$	$(1.37 \pm 0.01)\%\,\mathrm{K}^{-1}$	$(-164 \pm 1)\%\,\mathrm{K\,mbar}^{-1}$

Those results validate the gas gain model and the method for environmental corrections of the data. It also opens the possibility of an on-line correction of the gas gain *via* the control of the mesh voltage to compensate for the environmental induced variations.

Résumé du chapitre

Les tests en rayons X décrits dans ce chapitre ont permis d'établir le point de fonctionnement de nos prototypes, d'une part par des mesures d'efficacité de collection des électrons primaires et d'autre part par des mesures de gain. Les études en rayons X ont également permis d'établir la sensibilité du gain de nos prototypes vis à vis de paramètres environnementaux tels que la pression atmosphérique et la température. Les tests ont été réalisés à l'aide d'une source de ^{55}Fe émettant des photons de 5.9 keV injectés dans l'espace de dérive des prototypes à travers l'électrode de dérive *via* des trous aménagés dans le capot d'acier refermant le détecteur. Lors de ce type de test, la valeur centrale du pic K_α du spectre de la réponse du détecteur (voir fig. 4.1) est prise comme indicateur du facteur de conversion du détecteur entre l'énergie déposée dans le gaz et le signal de sortie de l'électronique de lecture. Ce facteur correspond au gain de détecteur multiplié par les constantes de calibration de la chaine de lecture et par l'efficacité de collection

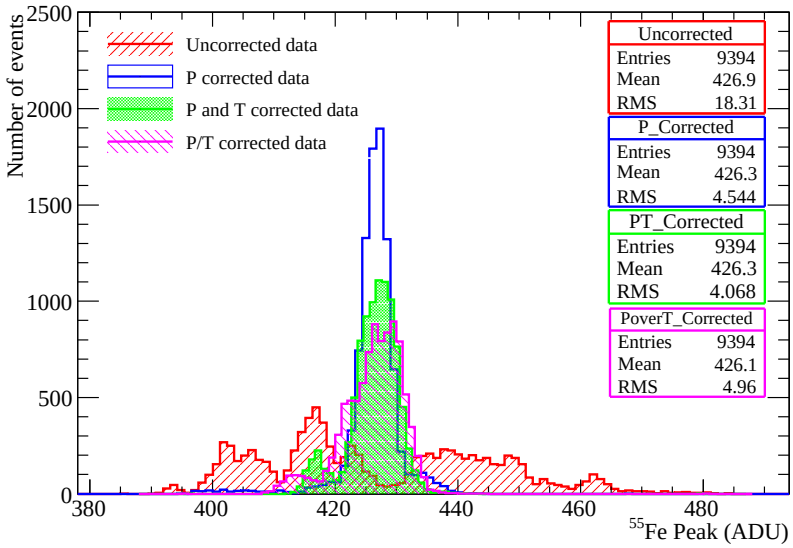

Figure 4.7: Summary of the corrections applied to the data.

des électrons primaires.

Efficacité de collection L'efficacité de collection, ou transparence électronique de la grille, a été mesurée en utilisant une tension de grille constante de -400 V et une tension de dérive variable de sorte à faire varier le rapport des champs électriques d'amplification et de dérive à gain constant. Le résultat de la mesure est illustré sur la figure 4.2 (p. 55) et montre qu'un rapport des champs compris entre 150 et 200 fournit la réponse maximale et correspond donc au réglage optimal du détecteur avec, pour une tension de grille aux environs de -400 V, une tension de dérive -50 V plus haute.

Mesures de gain En conservant un rapport des champs optimal, le gain a été mesuré en fonction de la tension de grille pour deux gaz différents (Ar/iC_4H_{10} (95/5) et Ar/CO_2 (80/20)). Les courbes obtenues apparaissent sur la figure 4.3 (p. 55) et permettent de définir le gain maximal atteignable pour chaque gaz. L'ajustement sur chacune des courbes de la fonction 4.3 permet de déterminer les propriétés du gaz quant à la dépendance du gain vis à vis de la pression (eq. 4.4) et de la température (eq. 4.5) du gaz ou encore de l'épaisseur de l'espace d'amplification (eq. 4.6).

Étude environnementale Une étude de l'évolution de la réponse du détecteur au fil des changements météorologiques permet de mesurer directement la dépendance du gain en fonction de la pression et de la température du gaz, qui suivent directement les variations atmosphériques. Les mesures furent effectuées sur une période de deux semaines. La température était régulée au moyen d'un climatiseur. Un mélange Ar/CO_2 (80/20) a été utilisé dans le détecteur. Les variations du gain en fonction de la pression, de la température et du rapport des deux sont illustrées dans les figures 4.4 (p. 58), 4.5

(p. 59) et 4.6 (p. 60) respectivement. La mesure directe est comparée au calcul dans la table 4.3 (p. 60) et montre un bon accord au regard des incertitudes sur les valeurs calculées. Ces coefficients de dépendance permettent d'envisager une correction des données analogiques ou, dans le cas d'une lecture digitale, une correction en ligne de la tension de grille afin de compenser les fluctuations atmosphériques et ainsi réguler le gain du détecteur.

CHAPTER 5

Tests in particle beams

Tests in particle beams are a crucial step in the characterization of a detector. The first MIP spectra obtained with cosmic particles have proven the detector functionality (work performed in my master internship). Then, tests in particle beams at the *Organisation Européenne pour la Recherche Nucléaire* (CERN) facilities allows detailed and systematic studies of the detector characteristics.

5.1 Experimental layout

5.1.1 Detector stack

The detector stack has been set up with the small chambers at the front and the large one at the rear (figure 5.1). The distance between each chamber has been set to 10 cm. Three scintillator paddles have been placed in front of the stack, producing the trigger signal by the triple time coincidence of their output. Two of them are $8\times32\,\mathrm{cm}^2$ and the last one has the exact dimensions of the small chambers ($6\times16\,\mathrm{cm}^2$).

A pre-mixed $\mathrm{Ar}/i\mathrm{C}_4\mathrm{H}_{10}$ (95/5) gas has been used and the voltage applied on the prototype meshes has been set to -420 V, -420 V, -430 V and -410 V, for CH0 to CH3, respectively. These voltage values have been considered as a trade off between a high gain and a spark rate below about one per hour[1]. The drift voltages have been set to 50 V below the mesh ones so that the field ratios were always corresponding to the maximum collection efficiency (see section 4.2).

5.1.2 Readout system

The anode analogue readout was provided by 16-channel ASICs called GASSIPLEX [59]. Boards[2], each equipped with 6 GASSIPLEX chips, were mounted on the side of

[1] Here we are speaking about sparks causing a high voltage power supply trip.
[2] CEA DAPNIA Board N°613V, 96 channels, 6 GASSIPLEX chips 0.7 v3.

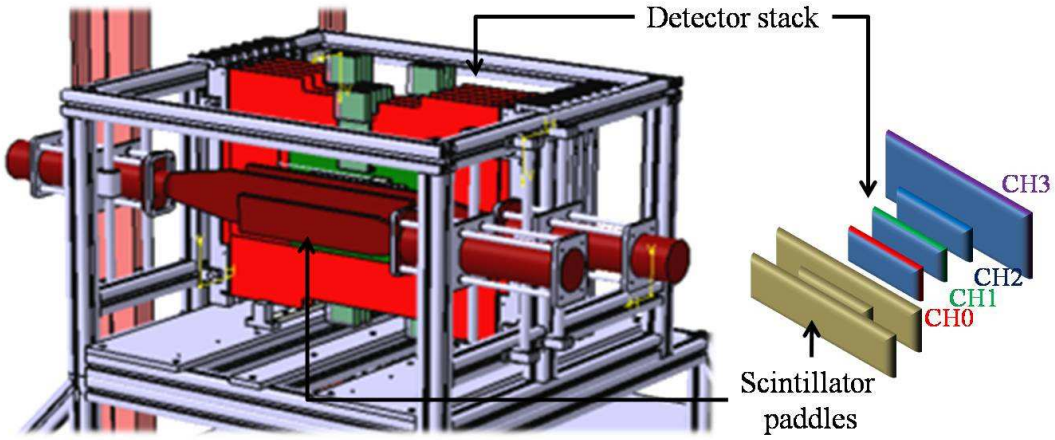

Figure 5.1: The test beam layout, including detectors, scintillator paddles and mechanical structure (left). A corresponding schematic view (right).

the chambers. (see black components on the photography in figure 3.7(b)). One board was used for each of the small chambers and four for the large one.

GASSIPLEX chips, when triggered, gather signal from each channel and build one single multiplexed differential output with a nominal conversion factor of 3.6 mV/fC and a peaking time of 1.2 μs.

The multiplexed signal from GASSIPLEX boards was digitised by CAEN V550 10-bit ADCs (VME modules) sequenced by a CAEN V551B C-RAMS sequencer VME module. Data was then collected by the computer through an optical VME/PCI bridge. A Labview based software, called CENTAURE [65], was used for on-line monitoring and data recording. Some developments were made to customise this software to a dedicated use for our setup. A very similar readout system was used for the CAST experiment and is described in [68]. The global conversion ratio of the GASSIPLEX-based readout chain was measured to be (4.69±0.25) ADU/fC. Its r.m.s. over all 672 channels is 2.5%.

5.1.3 Calibration

A calibrated pulse was injected through the GASSIPLEX internal test capacitance. The output was stored for further analysis. This process was repeated for three values of the input charge (voltage of 250, 80 and 25 mV). For any particular charge injection, the spectrum showed a peak clearly above pedestal (see figure 5.2(a)). A straight line was obtained by plotting this peak mean value versus the injected charge (see figure 5.2(b)). Its slope corresponds to the electronic gain in Analog to Digital Unit (ADU) per fC.

The gains for all channels of each board are gathered on the histogram in figure 5.3(a).

The overall gain disparity showed a 2.5% disparity (see figure 5.3(a)), thus no inter-calibration have been applied and a global conversion factor for all readout channels has been set. The gain for boards number 55, 30 and 59 is 4% higher than the average of the other boards and thus induces a 2% increase of the average gain. Three chambers

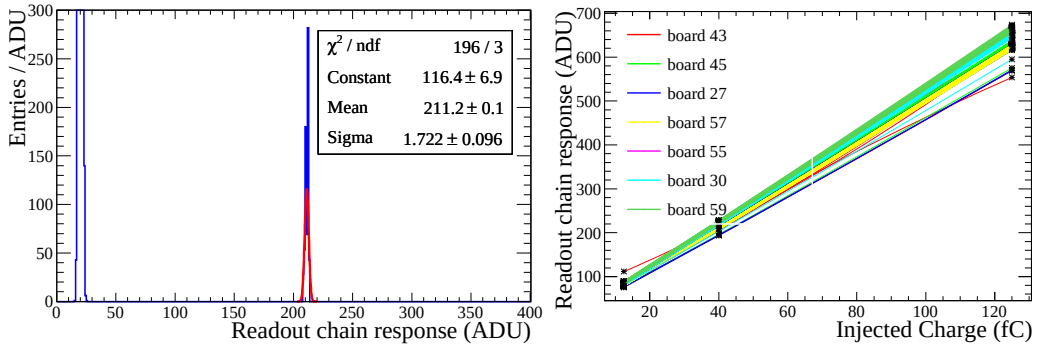

(a) Response of the readout chain to an injected charge of 40 fC.

(b) Calibration peak versus injected charge.

Figure 5.2: Electronic gain measurement.

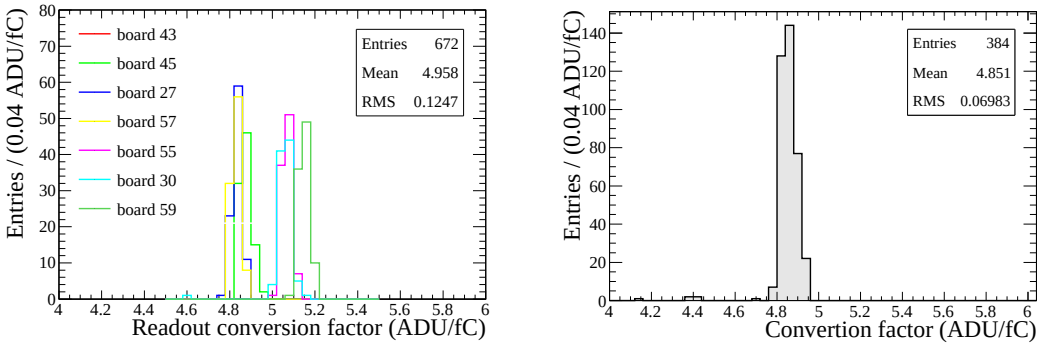

(a) Electronic gain for all 613V boards.

(b) Electronic gain of GASSIPLEX 613V boards for CH0, CH1, CH2 and first sector of CH3.

Figure 5.3: Electronic gain disparity measurement.

out of four were not concerned by these boards, therefore to avoid an overestimation of the conversion factor, those boards were excluded from its computation. The remaining channel gains are shown in figure 5.3(b). The resulting value of the global conversion factor of the GASSIPLEX readout chain measured using the internal test capacitor is then (4.85±0.07) ADU/fC.

Because of a 3.29% difference between internal and external test capacitor (see [69] for details) a correction has been applied and the final value has been set to (4.69±0.25) ADU/fC.

5.1.4 Particle sources

5.1.4.1 CERN/SPS, H2 beam line

The Super Proton Synchrotron (SPS) delivers a 400 GeV/c proton beam for fixed target experiments. Data was taken with a secondary 200 GeV/c negative muon beam. The beam was available during a 9 s spill period every machine cycle. Each machine cycle

lasted for 33 s during night time and 48 s during day time. The beam was intense enough to saturate the acquisition rate at about 130 events/s. Data was recorded during August 2008 beam test session.

5.1.4.2 CERN/PS, T9 beam line

The Proton Synchrotron (PS) delivers a 28 GeV/c proton beam for injection in SPS and CERN's East Area's Fixed target experiments. Data was recorded with a secondary 7 GeV/c positive pion beam. The beam was available during one to three 0.4 s spill periods every machine cycle. A machine cycle lasted for a variable time around 40 s. The beam was intense enough to saturate the acquisition rate at about 130 events/s. Data was recorded during November 2008 beam test session.

5.2 Data quality

5.2.1 Environmental and noise conditions

During the data acquisition, the atmospheric pressure and the gas temperature were monitored. Using $C_{P/T} = -2.36\,\mathrm{K\,mbar^{-1}}$, a gain correction factor was computed *via* formula 4.8 and found always below 10% with an r.m.s. below 4% (see figure 5.4). In accordance with section 4.5.5 environmental corrections are sufficiently small and have been considered negligible. Moreover, in a digital detector those corrections could not be applied at all[3]. Therefore, for the purpose of a DHCAL, the results given here remain uncorrected.

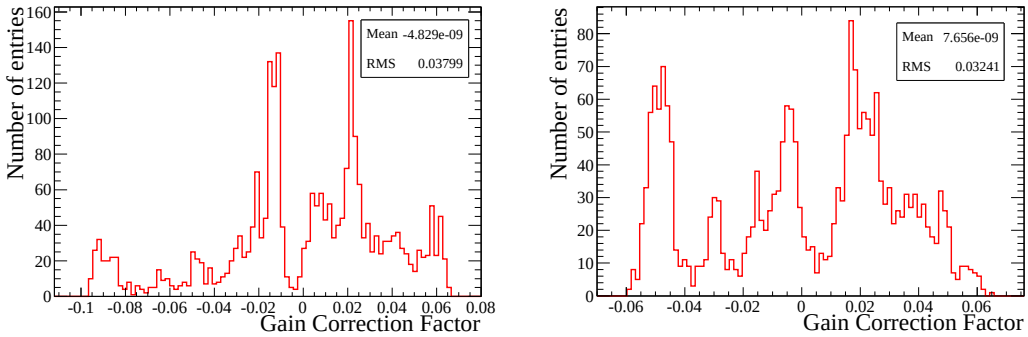

Figure 5.4: Histograms of the correction factors for data from August (left) and November (right).

The GASSIPLEX pedestals were periodically aligned at 20 ADU on the V550 ADC modules. They were measured at this value with 2% r.m.s. variations over all channels through the whole data set (see figure 5.5, left). The pedestal widths were obtained as the sigmas from a gaussian fit and showed an average value of 1.5 ADU corresponding to 0.3 fC or 2000 e^- (figure 5.5, right). These figures demonstrate very good noise conditions.

[3] nevertheless those correction may be used through an on-line tuning of the gas gain.

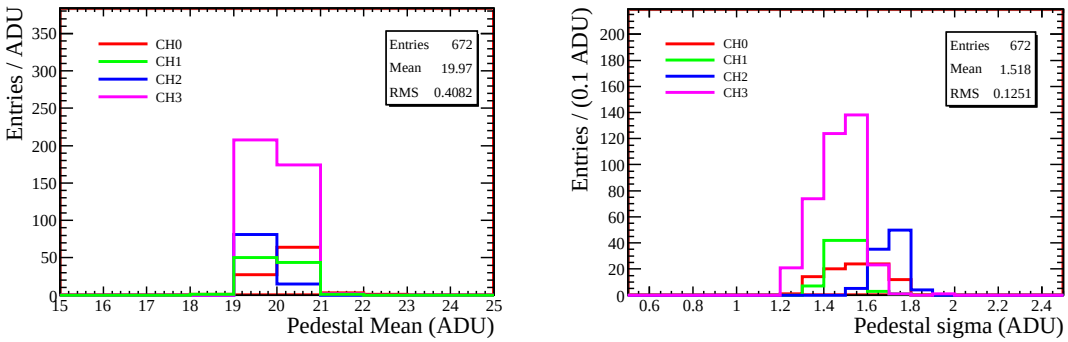

Figure 5.5: Pedestal Mean (left) and sigma (right) distributions.

5.2.2 Event tags

All channels have been recorded without any threshold. A hit is defined by applying an off-line threshold equal to 1.5 fC (7 ADU above pedestal). Events were categorised regarding some basic criteria on the hit distribution. The categories are enumerated and described below. Dedicated data files were produced for each category in order to simplify the analysis.

- **Platinum events**: an event is tagged as "platinum" by requiring one single hit in each of the four chambers. These events were used for gain and pedestal studies since they ensure a very low noise hit contamination. An example of platinum event is shown in figure 5.6(a).

- **Golden events**: a "golden" event is selected by requiring one single hit in three out of the four chambers. These events were used for efficiency and multiplicity studies. An example of golden event is shown in figure 5.6(b).

- **Silver Events:** in these events, several hits are allowed per chamber but only in a 3×3 pad area around the hottest one, we have the option to apply this condition on all chambers ("platinum" like) or on three of them ("gold" like). Multiple hits allow computing a weighted position for the hit, thus increasing tracking accuracy. Such events have been used to check chamber alignment. An example of silver event is shown in figure 5.6(c).

5.2.3 Chambers alignment

The precise position of each chamber relatively to each other can be computed using particle tracks. Silver Events (Platinum-like) have been used to compute the hit position by considering the mean between the actual hits weighted by their corresponding deposited energy. This method is supposed to be more accurate than attributing hit position at pad centres. After hit positions have been computed within a particular event, a straight line was fitted through them. Afterwards, the distance, separately along x and y axis, between effective hits and the fitted straight line was computed and plotted

in figure 5.7. If the chambers were perfectly aligned the resulting distribution would be centred on zero.

This study revealed a 2 mm misalignment along x axis of CH3, 1.6 mm along y axis for CH1 and 5.7 mm for CH2. Because the tracking capability of such a stack of detector is too limited, an off-line correction of the chambers position in the analysis programs is unable to prevent from inefficiencies biases due to misalignment. The particle position can only be considered being at the centre of the pad. Hence, a small misalignment lead the particles passing on pad borders to induce signal on a pad alongside the expected one. Such an information can't be retrieved in the data and there is therefore no way to identify this kind of events (see scheme in figure 5.8). This information implied to perform efficiency measurements with a 3×3 pad target area and omit the border pads of the chambers.

5.2.4 Noise contamination

While performing efficiency or multiplicity measurements, hits are searched in the 3 × 3 pad area around the predicted position. As there is a probability that a counted hit results from noise contamination instead of physical signal, the contribution must be evaluated in order to correct the raw measurement.

Direct measurement For each processed event, the target area has been taken as the area unit. The number of hits outside the target area was normalised to the area unit and stored. The mean of this number over all the events is then the average number of fortuitous[4] hits per area unit and per event. If the detectors were completely noisy (*e.g.* by setting the threshold below pedestal) this number would then be about 9, but for a reasonable threshold the average number of fortuitous hits per area unit and per event is expected to be relatively low and would then coincide with the probability of counting at least one fortuitous hit in a 3×3 pad target area, denoted p hereafter. This assumption has been made for the estimation of the noise contribution to efficiency and multiplicity measurements.

Computation from single pad noise Another possibility was to compute the single pad fortuitous hit probability p_1 and then deduce the corresponding 3×3 pad probability of spotting at least one hit. This probability is given at the second order in p_1 by:

$$p = 9p_1(1-p_1)^8 + 36p_1^2(1-p_1)^7 + o(p_1^3)\,, \tag{5.1}$$

with error:

$$\begin{aligned}\Delta p &= \Delta(9\cdot p_1(1-p_1)^8) + \Delta(36\cdot p_1^2(1-p_1)^7)\\ &= 9\cdot p_1(1-p_1)^8\left(\frac{\Delta p_1}{p_1} + 8\frac{\Delta p_1}{(1-p_1)}\right)\\ &+ 36\cdot p_1^2(1-p_1)^7\left(2\frac{\Delta p_1}{p_1} + 7\frac{\Delta p_1}{(1-p_1)}\right)\,.\end{aligned} \tag{5.2}$$

[4] 'Fortuitous' hits denotes hits that appeared randomly, likely from electronic noise contamination but any other potential source is included (radioactivity, cosmic rays, sparks ...)

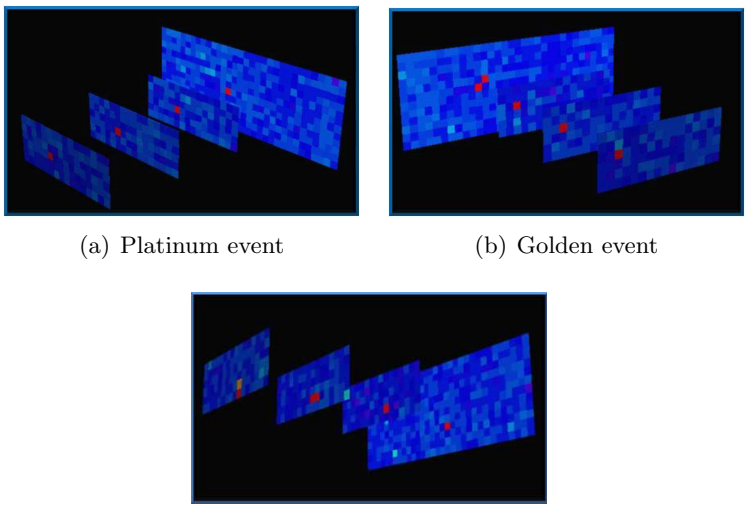

(a) Platinum event (b) Golden event

(c) Silver event

Figure 5.6: Display of events of each type.

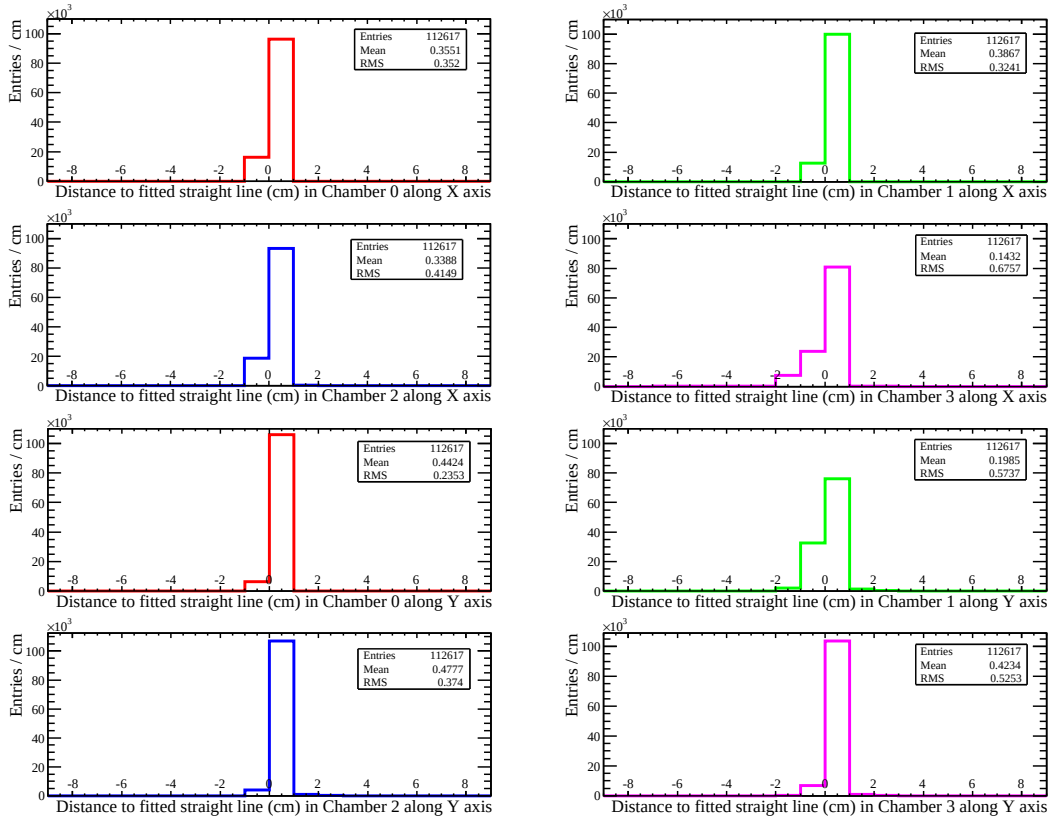

Figure 5.7: Measurement of all chambers relative misalignment.

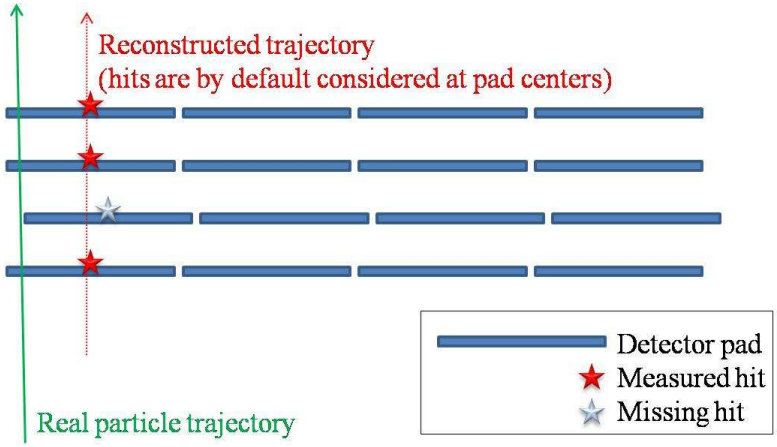

Figure 5.8: Geometrical inefficiency

Table 5.1: Comparison between 3×3 pad fortuitous hit probability direct measurement and 3×3 pad fortuitous hit probability computation from single pad noise.

Chamber	direct	computed
CH0	(1.30±0.08)%	(1.71±0.28)%
CH1	(1.33±0.08)%	(1.87±0.29)%
CH2	(2.00±0.10)%	(2.60±0.33)%
CH3	(1.65±0.09)%	(1.39±0.26)%

The results are compatible, but the error margin on the computed values are higher than for the directly measured ones, and the values are mainly higher as well. This difference can be explained by the fact that by looking at only one pad to search for noise contribution, any secondary hit due to signal multiplicity is automatically considered as noise. Computed values are therefore biased by the hit multiplicity. The direct method has been kept to perform the correction to efficiency and multiplicity. A quantity Q, standing either for efficiency or multiplicity, is corrected for noise contribution using the simple formula:

$$Q_{corr} \quad = \quad Q \cdot (1 - p)\,, \tag{5.3}$$

where p is the noise hit probability of the chamber.

5.3 Gain distribution measurement

For every channel, a Landau function has been fitted to the data from platinum events (see figure 5.9 (left)) and its Most Probable Value (MPV) has been defined as the detector global gain for charged particles (conversion, mesh amplification and electronics amplification). The resulting values are mapped in figure 5.10.

The most probable deposited charge, averaged over all channels of each chamber has been measured at 22.6, 22.9, 24.5 and 17.5 fC for CH0 to CH3 respectively. The relative

gain distribution of all the channels is shown in figure 5.9 (right) having an r.m.s. of 11.25%. Since the electronics gain distribution has a very low r.m.s. (see section 5.1.2 and 5.1.3), this value is expected to be mainly due to drift and/or amplification gap non-uniformity.

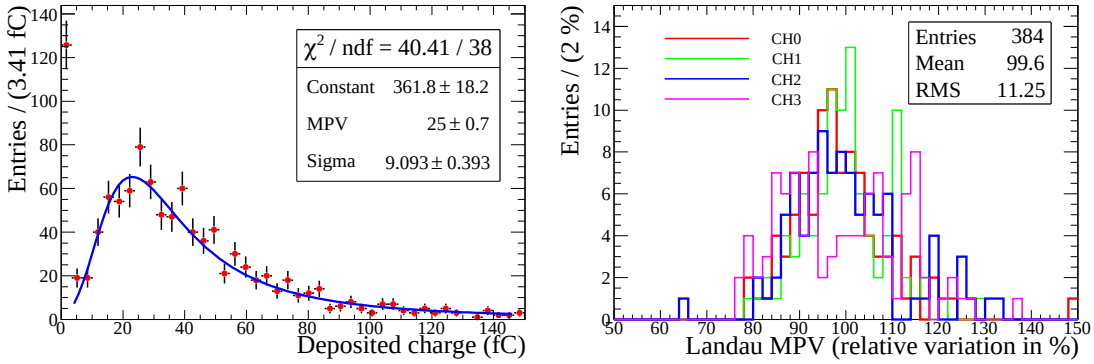

(a) (b)

Figure 5.9: Fit of a Landau function to the data for a single channel, the pedestal has been scaled to fit in the vertical range. The spectrum was built using Platinum events (left). Landau MPV distribution normalised to 100, for all chambers (right).

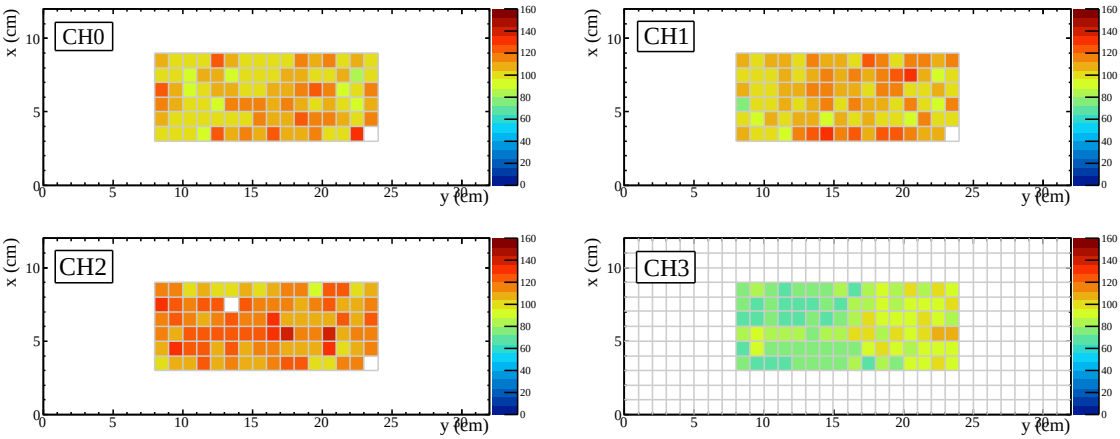

Figure 5.10: Landau MPV maps of all prototypes (colour axis in ADU).

5.4 Efficiency measurement

In order to measure the efficiency of a given chamber, the three others have been taken as a tracker. A sample of golden events was selected by requesting three aligned hits in the three "tracking" chambers to define a particle track. A safety threshold of 12.5 fC was applied for the three reference chamber hits to completely avoid taking noise hits into account. In each processed event, a hit has been searched in a 3×3 pad area centred at the intersection between the extrapolated reconstructed particle track and the chamber

plane. The predicted position was stored in a 2D histogram (see example in upper left map of figure 5.11), if a hit was actually found, the same bin in a second 2D histogram was filled (example in upper right map of fig 5.11). The ratio of those two histograms gave the chamber efficiency map. The resulting efficiencies are mapped in figure 5.12 and their distribution is shown in figure 5.13. The error on efficiency is computed through the usual formula:

$$\Delta\epsilon \quad = \quad \sqrt{\frac{\epsilon \cdot (1-\epsilon)}{N_{tot}}}\,, \tag{5.4}$$

where ϵ is the efficiency and $\Delta\epsilon$ its error, N_{tot} is the total number of events in the selected sub-sample when computing global efficiency and the number of times a pad has been tested when computing local efficiency.

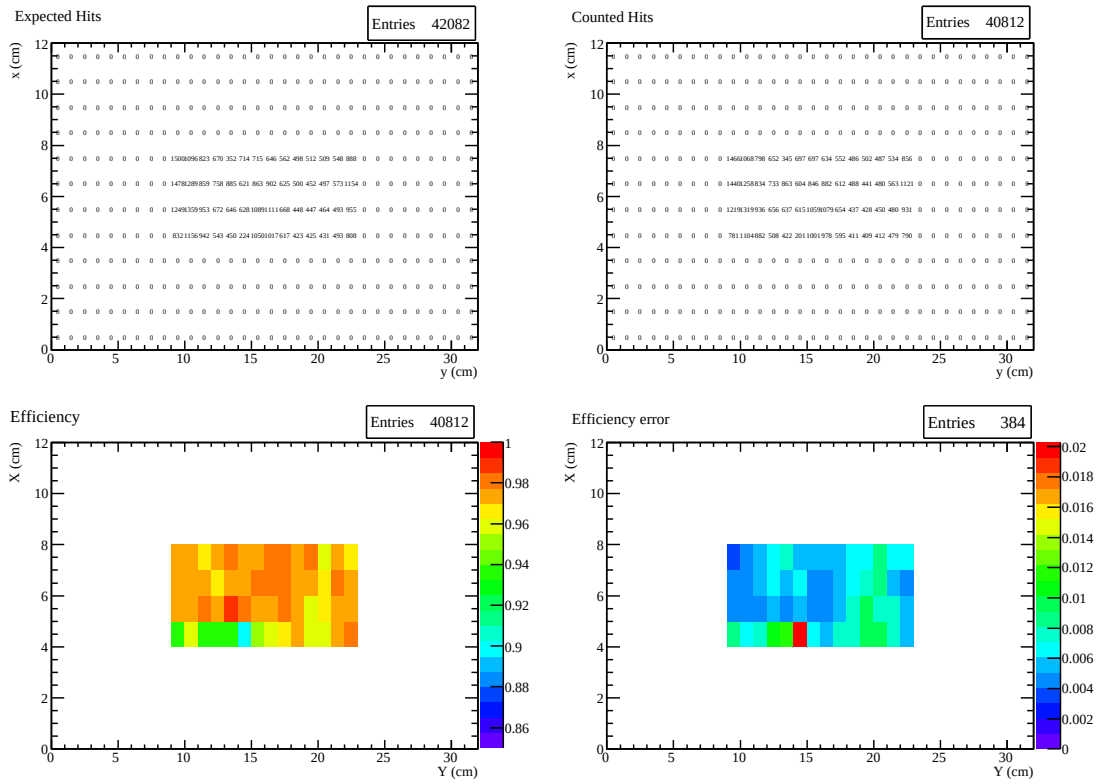

Figure 5.11: Efficiency map, principle of calculation.

The hit background was estimated by counting the number of hits outside the 3×3 pad area. This number, normalised to the 3×3 pad area, was subtracted to measure the final efficiency (Table 5.2). Because of the very low threshold, three chambers show an excellent efficiency, larger than 97%. CH2 shows a lower efficiency (91%). The dead channel in the readout GASSIPLEX board, as shown on the MPV map in figure 5.10 (CH2, lower left) should be responsible for a $\approx 2\%$ loss of the global efficiency. The remaining loss of efficiency might be due to the lower tension of its mesh or to the broader pedestals of its electronics.

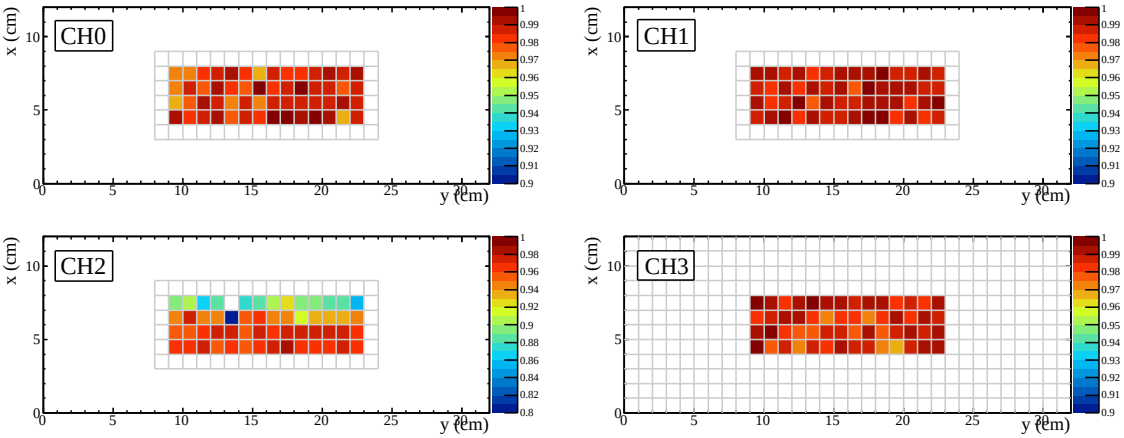

Figure 5.12: Maps of prototype efficiencies. The measurement was performed for a fiducial area omitting all border pads and using a 3×3 pad area around the expected hit to avoid misalignment issues.

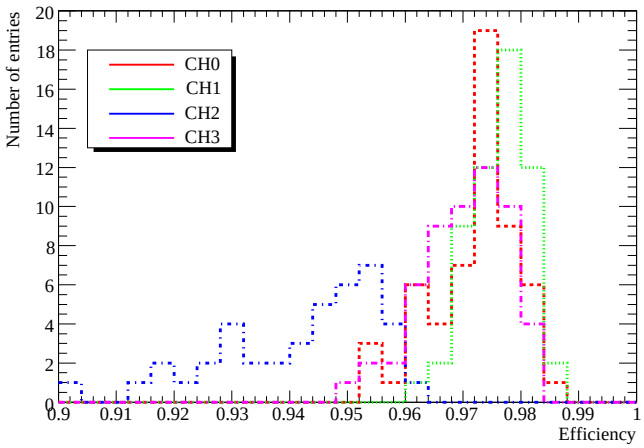

Figure 5.13: Pad efficiency distribution for each chamber.

Table 5.2: Efficiency measurements for a 1.5 fC threshold.

Chamber	Raw efficiency	Noise hit fraction	Noise corrected efficiency
CH0	(99.0±0.1)%	(1.3±0.1)%	(97.7±0.1)%
CH1	(99.0±0.1)%	(1.3±0.1)%	(97.7±0.1)%
CH2	(93.0±0.1)%	(2.0±0.1)%	(91.2±0.1)%
CH3	(98.8±0.1)%	(1.6±0.1)%	(97.2±0.1)%

In a DHCAL, the threshold is a fundamental parameter, the same study was therefore carried out for each chamber varying the threshold from 1.5 fC to 200 fC. The dependency between efficiency and threshold is represented in figure 5.14. A steep drop of efficiency with threshold is observed. A maximum efficiency above 97% is reached at

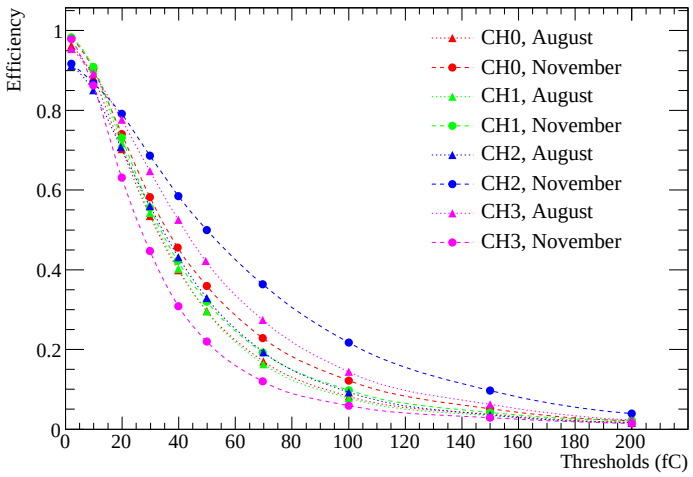

Figure 5.14: Efficiency versus threshold (CH1).

a threshold as low as 1.5 fC. The efficiency is about 70% at a threshold of 20 fC and drops below 10% for thresholds higher than 100 fC. Ongoing simulations [70] tend to suggest that the energy resolution of the DHCAL would be independent of the efficiency from 100% down to ≈70%. Such efficienciencies would be easily reached by the foreseen low power digital readout chips.

Figure 5.15 shows the efficiency disparity versus the threshold. This parameter is of interest for digital readout and for the PFA since it leads to systematic uncertainties about the number of hits measured in the MICROMEGAS DHCAL. The trend is completely linear for thresholds below 90 fC (0.15%/ fC). For higher thresholds, the statistics available are rather low , nevertheless the trend seems to be maintained.

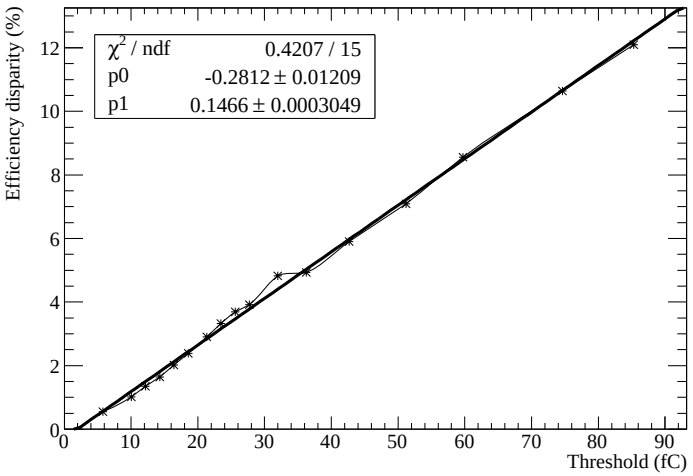

Figure 5.15: Efficiency disparity over 56 pads versus threshold for CH0.

5.5 Multiplicity measurement

The same sub-sample of golden events as for efficiency measurement(section 5.4) has been used. For each event, the number of hits in a 3×3 pad area around the pad expected to be hit has been counted. The average of this number over all the processed events is the multiplicity of the chamber. It can be formulated through:

$$mult. \quad = \quad \frac{1}{N_{\rm tot}} \cdot \sum_{i=1}^{N_{\rm max}} i \times N_i \,, \tag{5.5}$$

where N_{tot} is the number of processed events, $N_{max} = 9$ is the maximum multiplicity in a 3×3 pad area, N_i is the number of events which showed a multiplicity of i. The error is given by:

$$\frac{\Delta mult.}{mult.} = \frac{\sum_i N_i}{\sum_i i \cdot N_i} + \frac{\Delta N_{\rm tot}}{N_{\rm tot}} \,. \tag{5.6}$$

Table 5.3: Multiplicity for a 1.5 fC threshold.

Chamber	Raw multiplicity	Noise corrected multiplicity
CH0	1.070±0.008	1.057±0.008
CH1	1.080±0.008	1.065±0.008
CH2	1.090±0.008	1.070±0.008
CH3	1.114±0.008	1.096±0.008

The four chambers showed a noise corrected multiplicity between 1.06 and 1.10, which is a benefit for a PFA algorithm. The behaviour of multiplicity versus threshold was also studied and is illustrated in figure 5.16. After a quick fall, the multiplicity rises slowly and then decreases at high threshold. At very low threshold, almost all pads receiving charge are seen and the maximum multiplicity is measured. With increasing threshold, secondary hits due to small charge overflows are quickly vanishing, leading the multiplicity to decrease dramatically down to 1.03 – 1.04 at 30 – 40 fC. Above this value, low energy single hit events are ignored, therefore, only events with a large energy deposit are normally considered.These events likely contain δ-rays[5] leading to some ionization far from the track and hence to a higher multiplicity. Above 150 fC, as a consequence of the decreasing detection efficiency with threshold, the multiplicity declines again as expected.

5.6 MICROMEGAS in high energy hadronic showers

A 200 GeV/c pion beam from CERN/SPS/H2 line was used to test the chambers in dense high energy hadronic showers. Iron block were available to set a 30 cm thick wall upstream of the chambers to trigger the showers. Considering a single channel allows

[5]Ionised electrons emitted with high energy and capable of crossing large distance and ionizing the medium along the way.

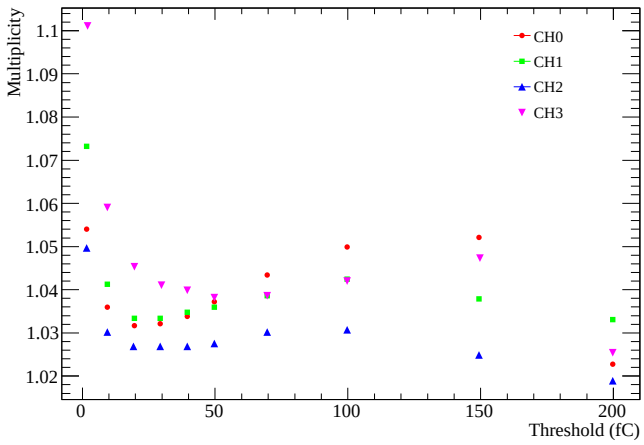

Figure 5.16: Multiplicity versus threshold for the four chambers.

to get rid of every chamber or readout disparity. Channel 38 has been chosen because it was the one gathering the most statistics under 200 GeV/c pion beam before placing the absorber blocks upstream the detectors. In this way, this channel response could be compared with the case when the absorber blocks were in place.

While collecting data without any absorber, the pions had very little probability to interact in the thin steel top of the chambers and thus behaved mostly like muons. A Platinum Event folder with pion data was built and a landau function has been fitted on single pad responses. The fit results showed no difference between pions and muons until the iron absorber blocks were placed upstream the detector stack (see table 5.4).

In the latter, the 30 cm thick iron block, representing about 2 interaction lengths, provoked a shower in roughly more than 80% of the events. The interaction probability p is given by:

$$\begin{aligned} p &= 1 - e^{-x/\lambda} \\ &= 1 - e^{-2} \\ &= 0.86\,, \end{aligned}$$

where x is the absorber thickness and λ the interaction length.

200 GeV/c pion showers produce a high number of secondary particles in very dense jets. It is obvious that, in shower events, more than one particle can cross the same pad at the same time and therefore modify the measured signal. On the one hand the combination of the deposited energy from several particles at the same time must enlarge the distribution. On the other hand, as the showers have been produced with 200 GeV/c pions, thus not at minimum ionization but on the relativistic rise, they have an average energy loss ≈50% higher than the minimum. Then, as the secondaries have to share the primary energy, they have much lower energy and thus are much closer to the minimum ionization (as illustrated in figure 5.17), that is why the distributions MPV are lower in the case of showers.

The two first rows of table 5.4 show that the signal from pions is similar to the one from the muons. The last one gives the corresponding result in the case when pions

Table 5.4: Summary of the results given by the fit of a landau function on single pad signal for the three small chambers for three different situations.

Muons	MPV (ADU)	σ (ADU)
CH0	132.7±3.2	42.3±2.1
CH1	124.4±3.2	42.0±2.0
CH2	137.3±4.4	54.4±3.0
Pions	MPV(ADU)	σ(ADU)
CH0	130.0±2.7	40.8±1.7
CH1	122.4±2.6	42.5±1.7
CH2	137.7±3.4	51.1±2.2
Showers	MPV(ADU)	σ(ADU)
CH0	126.8±3.2	78.6±1.4
CH1	108.2±3.4	70.2±1.4
CH2	124.3±3.0	68.9±1.4

interacted with iron blocks placed in front of the chambers. In the two first cases, the σ of the distributions are identical for CH0 and CH1 and a little higher for CH2. In the shower case the σ are decreasing from CH0 to CH2, accordingly to their distance from the interaction point. This is in agreement with a decreasing particle density. Figure 5.18 has been made using some toy Monte Carlo (MC) and shows the energy loss distribution of a single Minimum Ionizing Particle (MIP) crossing the detector (red curve). The one in green shows the energy loss distribution of two MIPs crossing the detector simultaneously and the black one is the same for three MIPs at once

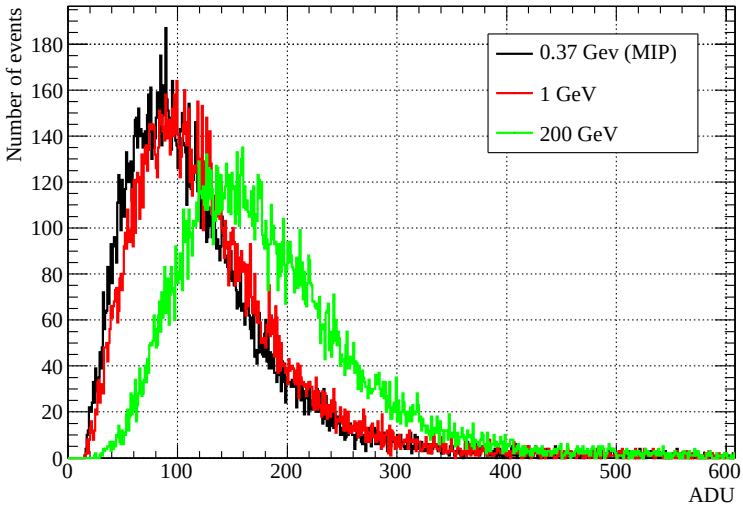

Figure 5.17: GEANT4 simulation of distribution of energy loss for muons crossing 3 mm of Ar/iC$_4$H$_{10}$ (95/5)

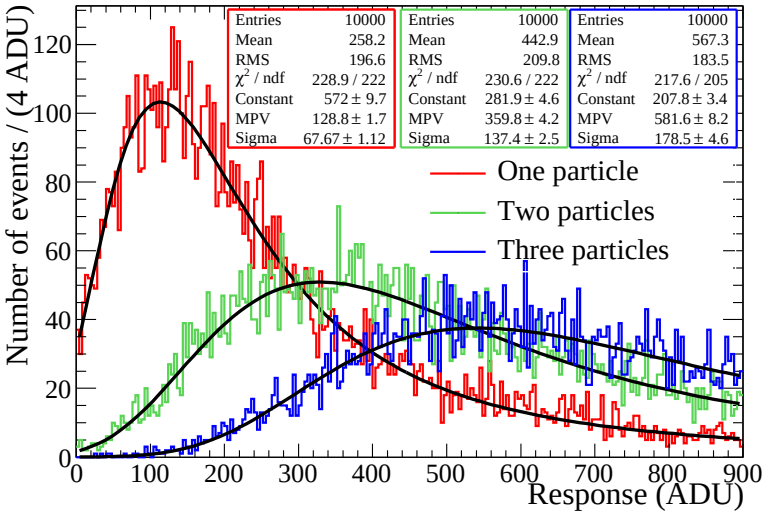

Figure 5.18: Distribution of energy loss for one, two and three particles at once in the same readout pad.

5.7 Calorimetry measurements

As part of the study, a "mini" calorimeter was set up and sprayed with electrons and pions at various energies in June 2009 at CERN/PS/T10 test facility. Shower profiles and further interpretation are presented for 2 GeV/c electrons and pions as a preliminary study. A few analysis benchmarks are presented (like e/mip and e/h ratios) and call for further analysis.

5.7.1 Experimental setup

The four prototypes described in section 3.5 (p. 48) were used to set up a "mini" calorimeter. They have a $1 \times 1\,\mathrm{cm}^2$ segmentation, a 3 mm drift gap and a 128 μm amplification gap. They are closed by a 2 mm steel top which counts as part of the absorber. The three small chambers (6×16 pad) played the role of a beam telescope for event selection whilst the large one (12×32 pad) was used as the calorimeter active medium. The data acquisition was triggered by the coincidence of three scintillator paddles. The layout of the set-up is sketched in figure 5.19. To perform measurements of particle showers, a varying number (ranging from 0 to 12) of 2 cm steel plates where placed between the set of the three small chambers and the large one. The absorber plates where equipped with 8 mm spacers to ensure a regular and rather realistic imitation of the complete calorimeter. MC simulations have driven those choices, they are summarised in [71].

The readout used V613 boards equipped with GASSIPLEX chips [59], read by VME ADC and sequencer. Data was recorded by the CENTAURE software from SUBATECH [65]. The readout system and its calibration are described in details in sections 5.1.2 and 5.1.3.

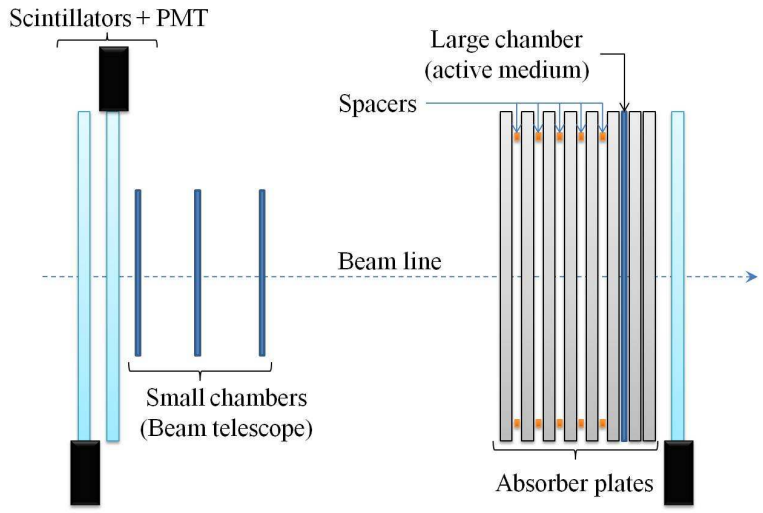

Figure 5.19: Scheme of beam test set-up.

5.7.2 Event selection

Data from the small chambers was used to perform the event selection. A pre-selection was done first by requesting one single cluster of hits in each of the three small chambers, regardless of the response of the large one ($\approx$ 50–60% yield). As a second step, for each chamber, a weighted hit position was computed from each hit and its value and the position of those hits is requested in the $2 \times 4\,\mathrm{cm}^2$ central area of the chambers to select central events in order to maximise the shower containment in the selected sample. Afterwards, a straight line has been fitted through the weighted hits and the following cuts have been applied: the χ^2/NDF of this fit below 5 and the slopes below 0.1. Figure 5.20 shows the values of those variables and indicates that the major cut was actually done by the pre-selection.

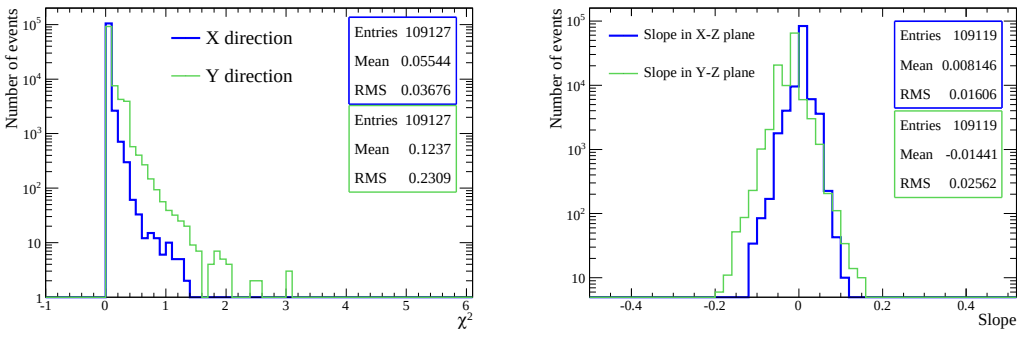

Figure 5.20: Straight line fit χ^2 before applying cuts and slopes after the χ^2 cut for all preselected events in the three small chambers (electron sample).

5.7.3 Electron shower profile

Data was recorded from 2 GeV/c electrons with 0, 2, 3, 4, 5, 6, 8, 10 and 12 layers of absorber plates upstream the large chamber. For cross checking the results, the same measurement were simulated with GEANT4 using LHEP physics list. The resulting curves are displayed in figure 5.21. The agreement was rather good and suffered only from small deficit in the simulated values. Nevertheless, this did not detract from considering the event selection and shower profile reconstruction as trustworthy.

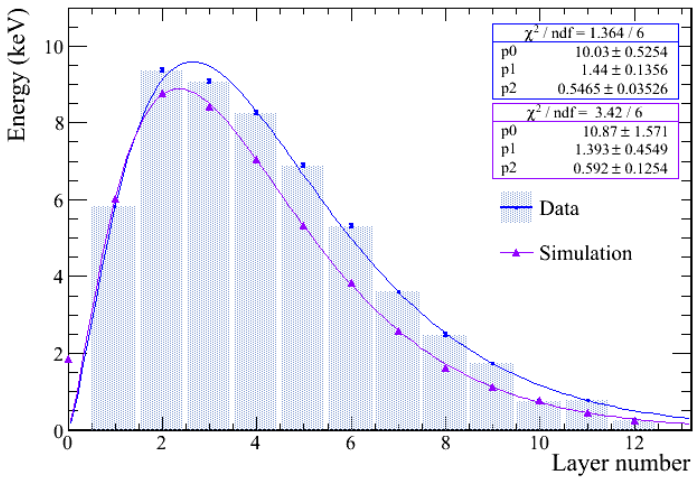

Figure 5.21: Electron shower profile from data and GEANT4 simulation.

In order to estimate the deposited energy in a 12 layer calorimeter made of MICROMEGAS chambers interleaved with 2 cm thick steel plates, the deposited energy in the missing active layers, namely the layers 1, 7, 9 and 11, were interpolated thanks to the data fitted curve:

$$f(z) \quad = \quad p_0 \cdot z^{p_1} \cdot e^{-p_2 \cdot z} \,, \tag{5.7}$$

where z denotes the depth in unit of absorber plate thickness (namely 2.2 cm, 1.25 X_0 or 0.13 λ_I) denoted *abs* hereafter. The values of p_0, p_1 and p_2 have been fitted to the data and summarise in table 5.5.

Table 5.5: Summary of electron shower profile fit parameters.

Parameter	Value from fit
p_0	10.03 ± 0.53 keV
p_1	1.44 ± 0.14
p_2	0.55 ± 0.04 abs^{-1}

The interpolated points appear in figure 5.21 as the error-less points of the data based plot. The average energy deposited by 2 GeV/c electrons in such a 12 layer MI-

CROMEGAS calorimeter is:

$$E_{\text{mes}}(e) \quad = \quad 54.27 \pm 0.30\,\text{keV}\,, \tag{5.8}$$

with a containment of $(98 \pm 5)\%$.

Afterwards, one can also extrapolate what energy would be measured in a 40 layer such calorimeter by multiplying $E_{\text{mes}}(e)$ by the ratio of the integrals of $f(z)$ for $z \in [0, 12]$ and $z \in [0, 40]$, ie:

$$E_{\text{vis}}(e) \quad = \quad E_{\text{mes}}(e) \times \frac{\int_0^{12} f(z)dz}{\int_0^{40} f(z)dz} \tag{5.9}$$

$$= \quad 55.41 \pm 2.88\,\text{keV}\,, \tag{5.10}$$

where the error takes the fit uncertainties into account. As a 40 layer calorimeter is sufficient to contain 2 GeV showers, the energy given in eq. 5.9 corresponds to the one appearing in eq. 2.2 (p. 28). The two other parameters of eq. 2.2, namely F_{S} and e/mip, are calculated in the next section to characterise the electromagnetic response of our "mini" MICROMEGAS calorimeter.

5.7.4 Interpretation in terms of electromagnetic calorimetry

5.7.4.1 The MIP shared energy

The so-called MIP shared Energy, denoted E_{S}, is defined as the energy fraction that is lost in the active medium by an ideal Minimum Ionizing Particle (MIP) of energy E.

$$E_{\text{S}} \quad = \quad \frac{E \times (dE/dx)_{readout} \times L_{readout}}{\sum_i (dE/dx)_i \times L_i}$$

$$\approx \quad \frac{E \times (dE/dx)_{readout} \times L_{readout}}{(dE/dx)_{absorber} \times L_{absorber}}\,, \tag{5.11}$$

with all energy losses given for minimum ionizing particles, E is the incoming particle energy and L_{X} is the thickness of component X. One also introduce the MIP shared fraction F_{S} given by:

$$F_{\text{S}} \quad = \quad \frac{E_{\text{S}}}{E}$$

$$= \quad \frac{(dE/dx)_{readout} \times L_{readout}}{(dE/dx)_{absorber} \times L_{absorber}}\,, \tag{5.12}$$

with all energy losses given for minimum ionizing particles. F_{S} is independent of the energy and is thus a intrinsic constant of the calorimeter. In the present case, with $(dE/dx)_{readout} = 2.68\,\text{keV}\,\text{cm}^{-1}$, $L_{readout} = 0.3\,\text{cm}$, $(dE/dx)_{absorber} = 11.46 \cdot 10^3\,\text{keV}\,\text{cm}^{-1}$ and $L_{absorber} = 2.0\,\text{cm}$, one obtains:

$$F_{\text{S}} \quad = \quad 3.19 \cdot 10^{-5}\,. \tag{5.13}$$

Therefore, at $E = 2\,\text{GeV}$:

$$E_{\text{S}} \quad = \quad 63.8\,\text{keV} \tag{5.14}$$

5.7.4.2 The e/mip ratio

The e/mip ratio is defined as:

$$e/mip \;=\; \frac{E_{\rm vis}(e)}{E_{\rm S}}\,, \tag{5.15}$$

which gives, by taking the measured values of $E_{\rm vis}(e)$ and $E_{\rm S}$ from eq. 5.10 and 5.14 respectively:

$$e/mip \;=\; 0.87 \pm 0.05\,. \tag{5.16}$$

The e/mip ratio is energy independent and is, as such, an intrinsic characteristic of a calorimeter, many details about this feature lies in [31]. For instance this ratio relates to the electromagnetic energy measurement and its resolution, as introduced in section 2.5 and illustrated in the following section.

5.7.4.3 Energy measurement and resolution

Energy measurement The proportionality between the visible energy in our "mini" calorimeter (extrapolated to 40 layers) and the incoming energy lies in the definition of the e/mip ratio (eq. 5.15) which leads to:

$$\begin{aligned} E_{\rm vis}(e) &= e/mip\; E_{\rm S} \\ &= e/mip\; F_{\rm S}\; E \qquad (5.17)\\ E_{\rm vis}(e) &= (2.77 \pm 0.16)\cdot 10^{-5}\; E\,. \qquad (5.18) \end{aligned}$$

Energy resolution The prediction of energy resolution involves a number of constants. Let $\tau = 1.25\,{\rm X_0}$ be the sampling fraction of the calorimeter in unit of radiation length. Let $\epsilon_{\rm c}$ be the critical energy of a given medium, this is the energy of a particle for which the radiation and the collision energy losses in this medium are equivalent. For iron: $\epsilon_{\rm c} = 21.04\,{\rm MeV}$ ([31], page 44, table 2.3). $\langle cos\theta \rangle$ is the cosine of the average angle of the particles crossing the active medium and is defined by:

$$\begin{aligned} \langle cos\theta \rangle &= cos\left(\frac{21.2\,{\rm MeV}}{\pi\epsilon_{\rm c}}\right) \\ \langle cos\theta \rangle &= 0.949\,. \qquad (5.19) \end{aligned}$$

The above constants combine to predict the electromagnetic energy resolution of the calorimeter *via*:

$$\frac{\sigma(E)}{E} \;=\; 3.16\%\sqrt{\frac{\epsilon_{\rm c}\;\tau}{e/mip\,\langle cos\theta\rangle}} \times \frac{1}{\sqrt{E}}\,, \tag{5.20}$$

which gives the electromagnetic resolution of our "mini" calorimeter:

$$\frac{\sigma(E)}{E} \;=\; \frac{(18 \pm 1)\%}{\sqrt{E}}\,. \tag{5.21}$$

The predictions performed in this section can be used for further study of 2009 beam test data to compare the coherence of the results.

5.7.5 Hadron shower profile

The data acquired with the June 2009 set-up does not give access to the event-by-event shower start. In the case of the electrons this was not a problem, since electrons interacted mostly at the very beginning of the calorimeter and the spread of the shower start can be neglected. However, in the hadron case, showers can start anywhere in the calorimeter following the law:

$$P(z) \quad = \quad e^{-z/\lambda_{\mathrm{I}}}\,, \tag{5.22}$$

where $P(z)$ is the probability that a pion had not interacted at depth z and $\lambda_{\mathrm{I}} = 16.78\,\mathrm{cm}$ is the iron interaction length. Figure 5.22 illustrates this probability law using unit of absorber plate thickness.

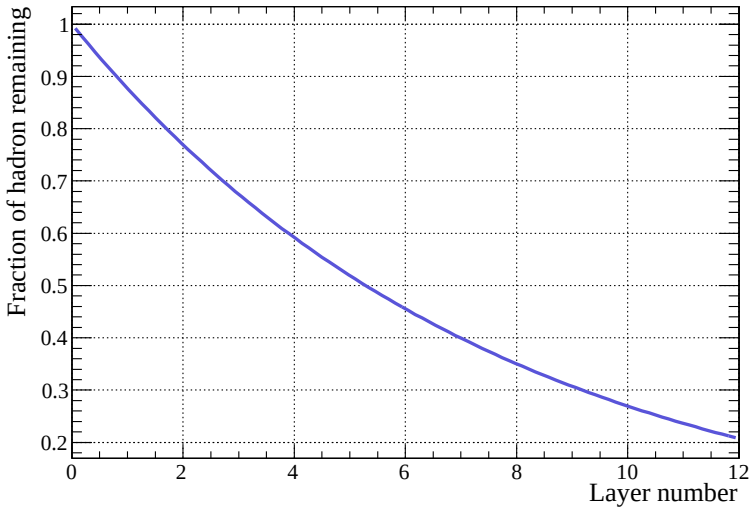

Figure 5.22: Hadron fraction which haven't interacted versus depth in unit of absorber plate thickness.

For a preliminary study, the raw data was not corrected for shower start position. The obtained profile is displayed in figure 5.23 and its interpretation is derived in the next section. The experimental points were fitted with expression 5.7 to interpolate the deposited energy in the missing layers, namely layers 1, 5, 7, 9 and 11, and to estimate the shower containment as in eq. 5.10. The simulated profile was obtained with a GEometry ANd Tracking, version 4 (GEANT4) simulation based on the LHEP physics list as for the electron case. However, this physics list happen to be imprecise for hadronic physics. This explains the disagreement between data and simulation in figure 5.23.

The measurement thus gives:

$$E_{\mathrm{mes}}(\pi) \quad = \quad (16.51 \pm 0.12)\,\mathrm{keV}\,.$$

With the same method as in the electron case, the shower containment in the 12 layer "mini" calorimeter is $(43 \pm 12)\%$ and therefore:

$$E_{\mathrm{vis}}(\pi) \quad = \quad (38.3 \pm 10.8)\,\mathrm{keV}\,. \tag{5.23}$$

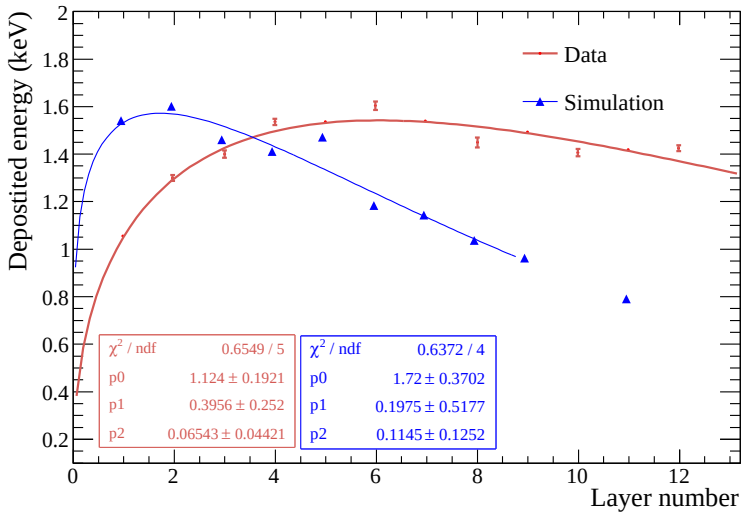

Figure 5.23: Hadron shower profile at 2 GeV.

5.7.6 Interpretation in terms of hadronic calorimetry

A crucial criterion for a hadronic calorimeter is the e/h ratio, defined in section 2.5. This quantity relates to the response linearity and to the energy resolution constant term of the calorimeter and also to its compensating condition. The e/h ratio can not be directly measured and must be computed from the measurement of the e/π ratio (as well defined in section 2.5 as the average calorimeter response ratio of an electron and a real hadron).

The calorimeter response to real hadron is not absolutely proportional (except for compensating calorimeter). As a charged hadron can radiate photons or produce π^0 quickly decaying into two photons, there is always a fraction of the incoming hadron energy, the so-called electromagnetic fraction f_{em}, which is converted into electromagnetic processes (see section 2.5 for details). The electromagnetic fraction f_{em} of the real hadron cascade is logarithmically energy dependent and is responsible for the non-proportionality of the calorimeter response.

5.7.6.1 The e/π ratio

Consider now the π/mip ratio. It is the hadronic analogy of the e/mip ratio, but is not energy independent and is derived for our "mini" calorimeter as:

$$\pi/mip = \frac{E_{\mathrm{vis}}(\pi)}{E_{\mathrm{S}}} = 0.60 \pm 0.17\,, \tag{5.24}$$

where the values of $E_{\mathrm{vis}}(\pi)$ at 2 GeV/c and E_{S} are taken fron eq. 5.23 and 5.14 respectively. The e/π ratio at 2 GeV/c is then derived as:

$$e/\pi = \frac{e/mip}{\pi/mip} = 1.45 \pm 0.49\,.$$

Energy resolution constant term The constant term of the hadron calorimeter energy resolution at 2 GeV/c, for $e/\pi > 1.115$, is given by ([31], p. 510):

$$\begin{aligned} \Phi(e/\pi) &\approx 0.281\ ln(e/\pi) - 2.1 \cdot 10^{-2} \\ &= (8.3 \pm 9.5)\% \,. \end{aligned} \tag{5.25}$$

The large error bar finally only permits a prediction of the constant term below about 18%.

5.7.6.2 The e/h ratio

The electromagnetic fraction of the real hadron cascade ($f_{\rm em}$) is involved in the calculation of the e/h ratio. The $f_{\rm em}$ is given by empirical formulas. According to various sources [31, 30], the value of $f_{\rm em}$ ranges from 7.6% to 12.9%. The value 7.6% comes from the formula:

$$f_{\rm em} = 0.11\, ln(E)\,, \tag{5.26}$$

which is considered to be more accurate at "low" energy [31], and is used hereafter. The e/h ratio is then given by:

$$\begin{aligned} e/h &= \frac{e/\pi(1 - f_{\rm em})}{1 - f_{\rm em} e/\pi} \\ &= 1.51 \pm 0.52\,. \end{aligned} \tag{5.27}$$

The uncertainty on e/h is too large to make any assumption on the compensating condition of the calorimeter.

Calorimeter response The calorimeter response to real hadron, $E_{\rm vis}(\pi)$, relates, one the one hand, to the incoming energy *via*:

$$\begin{aligned} E_{\rm vis}(\pi) &= \pi/mip\, F_{\rm S}\, E \\ &= \pi/e\ e/mip\, F_{\rm S}\, E\,, \end{aligned} \tag{5.28}$$

and on the other hand, by:

$$\begin{aligned} E_{\rm vis}(\pi) &= f_{\rm em} E_{\rm vis}(e) + (1 - f_{\rm em}) E_{\rm vis}(h) \\ \Leftrightarrow\ \pi/mip &= f_{\rm em} e/mip + (1 - f_{\rm em}) h/mip \\ \Leftrightarrow\ \pi/e &= f_{\rm em} + (1 - f_{\rm em}) h/e \\ &= f_{\rm em}(1 - h/e) + h/e\,. \end{aligned} \tag{5.29}$$

From eq. 5.28 and 5.29, the real hadron visible energy can be written as:

$$E_{\rm vis}(\pi) = NL(E) \cdot E + h/mip\, F_{\rm S} \cdot E\,, \tag{5.30}$$

with $NL(E)$, the energy dependent non linear term, expressed as:

$$NL(E) = \left(\frac{e/h - 1}{e/h}\right) e/mip\, F_{\rm S}\, f_{\rm em}(E)\,. \tag{5.31}$$

The deduced numerical values for our "mini" calorimeter are then, for the constant term:

$$h/mip\, F_{\rm S} \quad = \quad 1.8 \pm 0.5 \cdot 10^{-5}\,, \tag{5.32}$$

and for the non linearity term at 2 GeV/c:

$$NL(E) \quad = \quad 0.7 \pm 0.3 \cdot 10^{-6}\,. \tag{5.33}$$

Figure 5.24 displays the evolution of this non linear term versus incoming energy. $NL(E)$ varies of about a factor 5 between 2 and 200 GeV. Figure 5.24 also displays $NL(E)$ for the high energy definition of $f_{\rm em}$ (taken from [30], with $m = 0.87^{(6)}$). The two curves are very close at a few GeV and around 80 GeV where they cross each other. A Difference up to about 20% between the prediction of the two models appear around 20 GeV and diverge for increasing energies above 80 GeV. For energies below 200 GeV, the difference for $E_{\rm vis}(\pi)$ between the two models is less than 2%.

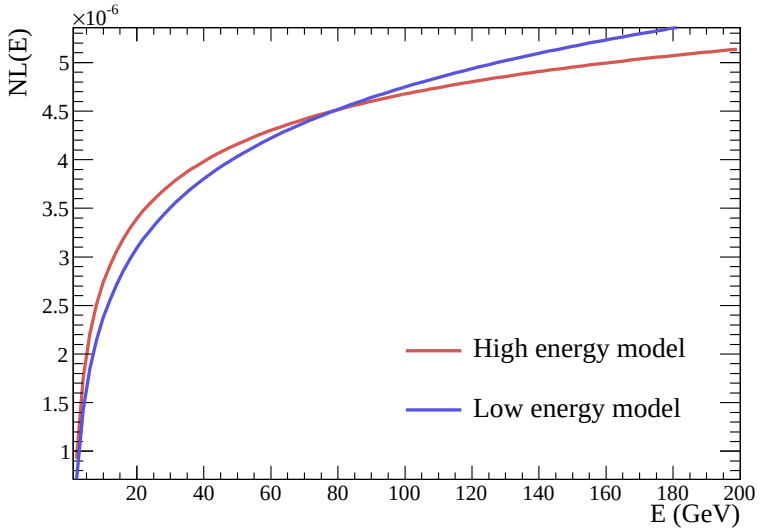

Figure 5.24: Predicted evolution of the non-linear term of the hadronic visible energy ($NL(E)$) of our "mini" calorimeter versus the incoming energy E.

5.7.7 Predictions for 4 GeV/c data

Data has also been acquired at a momentum of 4 GeV/c with electrons and hadrons. The deposited energy can be predicted from the above results and should be checked with direct measurements.

[6] The "high energy" model is also described in [31], where the machine dependent parameter m is fixed at $m = 0.85$.

Showers from 4 GeV/c electrons By simply applying eq. 5.18, one predicts for 4 GeV/c electron:

$$\begin{aligned} E_{\text{vis}}(e) &= 2.77 \pm 0.16 \cdot 10^{-5} \times 4\,\text{GeV} \\ &= 11.1 \pm 0.7 \cdot 10^{-5}\,\text{GeV} \\ &= 111 \pm 7\,\text{keV}\,. \end{aligned} \tag{5.34}$$

Showers from 4 GeV/c hadrons The same way, by using formula 5.30, the 4 GeV/c hadron shower visible energy can be predicted:

$$\begin{aligned} E_{\text{vis}}(\pi) &= (NL(4\,\text{GeV}/c) \\ &\quad +(1.8 \pm 0.5) \cdot 10^{-5}) \times 4\,\text{GeV} \\ &= ((1.4 \pm 0.6) \cdot 10^{-6} \\ &\quad +(1.8 \pm 0.5) \cdot 10^{-5}) \times 4\,\text{GeV} \\ &= 1.9 \pm 0.6 \cdot 10^{-5} \times 4\,\text{GeV} \\ &= 76 \pm 24\,\text{keV}\,. \end{aligned} \tag{5.35}$$

The analysis described in section 5.7.5 should be redone for the 4 GeV data in order to compare with these predictions.

5.7.8 Conclusion of the study

The average shower profile of 2 GeV/c electrons and hadrons has been measured in beam test at CERN. The simulation of hadron shower profile need to be improved to get better agreement with data and understand the reason of this large difference. A better choice of the GEANT4 physics list for the simulation might greatly improve the result in the hadronic case, possible promising list could be "QGSP_BERT" or "BIC_FTP".

The "mini" calorimeter characteristics give preliminary predictions of the characteristics of a real MICROMEGAS calorimeter. The limitations of the set-up used forbid to reach very precise results but the calculations performed here may serve as guidelines for a future MICROMEGAS calorimeter prototype characterisation.

Résumé du chapitre

Un ensemble de quatre chambres MICROMEGAS à lecture analogique (carte de lecture GASSIPLEX, trois chambres $6 \times 16\,\text{cm}^2$ et une $12 \times 32\,\text{cm}^2$) maintenues dans une structure métallique a été exposé à un faisceau de muons afin de mesurer l'efficacité des détecteurs sur les signaux faibles laissés par les muons (particules au minimum ionisant — MIP) ainsi que la multiplicité de ce signal et encore l'homogénéité de la réponse. Pour l'application de la technologie MICROMEGAS dans un calorimètre optimisé pour l'usage du PFA une efficacité proche de 100% et une multiplicité proche de 1 sont préférables.

Les événements ont été classés en différentes catégories (voir fig. 5.6). Les événements de type *gloden* et *platinum* sont utilisés pour cette étude. Ils correspondent respectivement à des événements où chacune des chambres ne présente qu'un et un seul *hit* et à des

événements où trois des chambres ne présentent qu'un et un seul *hit* indépendamment de la dernière.

Les événements *platinum* ont été utilisés pour scanner l'homogénéité des chambres en mesurant la réponse aux muons dans chacun des canaux de lecture. Une amplitude typique pour le signal des MIPs a été mesurée de l'ordre de 20 fC (voir exemple sur fig. 5.9 à gauche) avec une disparité relative de 11.25% sur les 384 canaux en jeu (voir fig. 5.9 à droite).

Dans le reste, des événements *golden* ont été utilisés. Pour mesurer l'efficacité, une droite est ajustée à travers les trois *hits* des chambres de référence et est extrapolée vers la quatrième chambre pour définir une zone cible de 3×3 pad dans laquelle on vérifie la présence ou l'absence du *hit* attendu. Le rapport du nombre d'événement où le *hit* a été trouvé sur le nombre total d'événements utilisés pour l'analyse donne l'efficacité du détecteur. Des valeurs supérieures à 97% après correction pour le bruit ont été établies pour trois des quatre chambres. De la même manière on peut compter le nombre moyen de *hits* présent dans la zone cible de la chambre à tester (en ignorant les 0) et obtenir la multiplicité moyenne du détecteur au signal des MIPs. Une mutiplicité inférieure à 1.1 a été établie.

Ces deux grandeurs dépendent du seuil de détection appliqué, les valeurs ci-dessus correspondent à un seuil de 1.5 fC. Les valeurs en fonction du seuil sont illustrées sur la figure 5.14 pour l'efficacité et sur la figure 5.16 pour la multiplicité. Ces résultats montrent qu'une bonne efficacité peut être atteinte avec une lecture autorisant des seuils de l'ordre du femto-coulomb et que la multiplicité reste toujours proche de 1 quelque soit le seuil au dessus de 1.5 fC.

La non-uniformité de l'efficacité a aussi été mesurée et, malgré une disparité du gain de l'ordre de 10%, celle de l'efficacité est inférieure à 1% pour un seuil de 1.5 fC et croit linéairement avec le seuil. Hors, dans un calorimètre digital, l'uniformité de l'efficacité donne celle du calorimètre, ainsi pour de bas seuils, une excellente uniformité pourra être atteinte.

Tous ces résultats montrent l'excellent accord entre la technologie MICROMEGAS et les besoins d'un calorimètre optimisé pour l'application du PFA.

CHAPTER 6

Development of the project

Results on the development of the MICROMEGAS DHCAL project are presented here. They address the points 5–6 of the list in section 3.4 (p. 47).

6.1 Embedded readout chip

6.1.1 Readout chips catalog

At the beginning of the project, two types of readout chips were envisioned, the HARDROC and the DIRAC chips. A third type of chips called MICROROC were developed later and benefited from the experience earned from the former ones.

- HARDROC [62]: Developed by LAL, they exist in three successive versions: 1, 2, 2b. These chips were available in their first version from the beginning. They were especially designed towards application to ILC experiments (ILC synchronous clock, power pulsing) but were optimised for the use of RPC detectors and offered a tunable shaping time of about 10–20 ns whereas 150–250 ns would have been suitable for MICROMEGAS application. This shaping time issue results in a partial collection of the MICROMEGAS signal estimated around 10%. As R&D chips, they suffered from a number of malfunctions which were resolved in subsequent versions. The first version chips were very fragile and tended to die during tests. No significant measurements were achieved (only beam profiles and rough efficiency estimations). The HARDROC2 version was much more robust and was used to build the first $32 \times 48\,\mathrm{cm}^2$ Active Sensor Units (ASUs) holding one mesh and 24 chips. However, they suffered from a tendency to fail to transmit the configuration signals. This was solved in the 2b version.

- DIRAC [60, 61]: Developed by LAPP and *Institut de Physique Nucléaire de Lyon* (IPNL), this chip is meant to be much simpler and cheaper than the HARDROC and offers two functioning modes: low gain for RPC readout and high gain for GEM or MICROMEGAS readout. The first version showed promising results and

has represented a key step in the LAPP project by demonstrating the feasibility of a bulk MICROMEGAS with embedded readout electronics [72] (see photography in figure 6.1). The second version of this chip solved a few minor defaults but suffered unfortunately from a harsh weakness against sparks.

- MICROROC: This chip, developed in collaboration between LAL/Omega and LAPP, corresponds to the integration of the optimised and debugged DIRAC input stage into the HARDROC frame. Extensive tests have shown excellent results [63] and therefore, in summer 2011, the 2nd MICROMEGAS square meter was equipped with 144 MICROROC. This new prototype is under test in particle beam at CERN at the time of writing.

6.1.2 Performance of the DIRAC1 prototype

The first MICROMEGAS chamber with embedded readout electronics was built and successfully tested in a particle beam during august 2008 beam tests. A unique 8×8 pad chamber equipped with DIRAC chips [60] was exposed to 200 GeV/c muons. Data was acquired with a 19 fC threshold, in Ar/iC$_4$H$_{10}$ (95/5), at a mesh voltage of 410 V and a drift voltage of 460 V. The data acquisition was self-triggered by the ASIC using an external clock with a 200 ns period. The chip has proved to survive the lamination process by showing the beam profile displayed in figure 6.2. A raw hit multiplicity of 1.1 has been measured. The related study is described in details in [72].

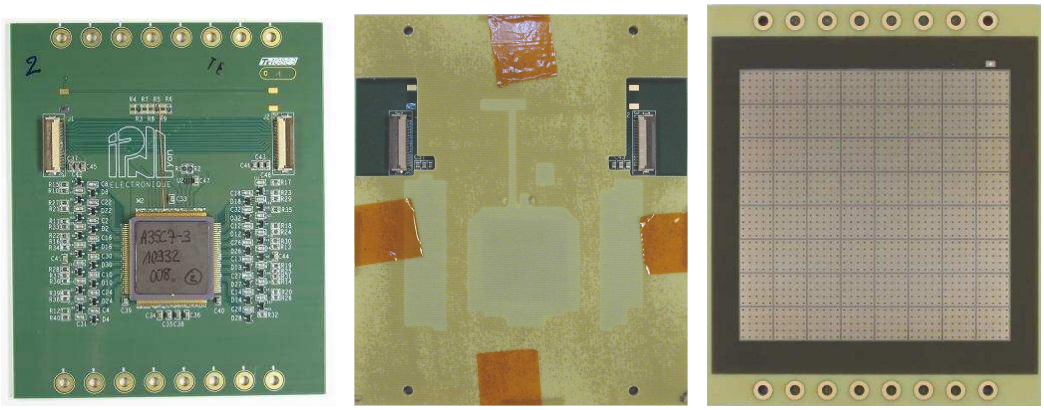

(a) (b) (c)

Figure 6.1: DIRAC MICROMEGAS prototype. View from chip side without (a) and with (b) protection mask. View from mesh side (c).

6.1.3 DIRAC2 performance

A second version of the DIRAC chip has been developed at LAPP. A stack of four 8×8 pad MICROMEGAS chambers equipped with DIRAC2 chips was mounted and exposed to 6 GeV/c hadron beam at CERN/PS/T9 facility in 2009. Unfortunately, a weakness against sparks in the chambers resulted in the loss of readout channels. The chips became completely blind after a few hours functioning. Very little data was acquired

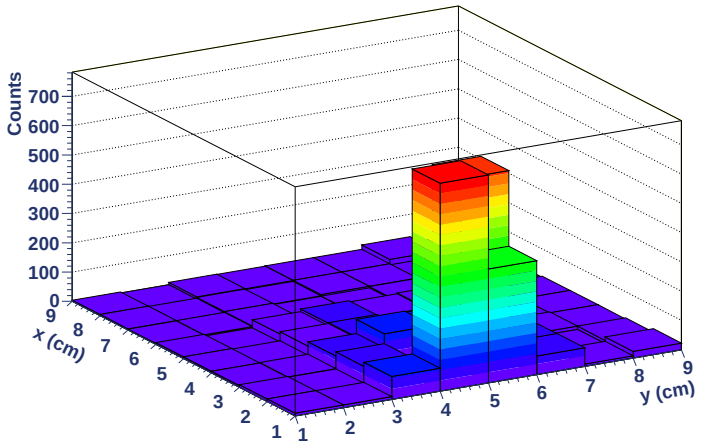

Figure 6.2: Beam profile obtained with digital readout using the DIRAC ASIC.

and no optimization of the chip configuration could be done. Nevertheless, some raw measurements were performed and are summed up in table 6.1. The method based on the golden events described in section 5.4 could not be applied because of the very low statistics available. Hence, the efficiency was computed as the ratio of the number of triggers to the number of counted hits. The multiplicities are consistent with the expected values but the result for efficiency is not well understood. A veto was put for triggers occurring during the blind time of the chips, therefore the expected efficiency was around $\approx$ 70–80 % (see plots in figure 5.14 p. 74). Following this experience, a new branch of the project was set to develop optimised and reliable spark protections for MICROMEGAS readout chips.

Table 6.1: Summary of the DIRAC2 MICROMEGAS prototypes measurements

Quantity	Threshold (fC)	Multiplicity	Efficiency
Chamber 1	6	1.13	0.4 ± 0.1
Chamber 2	6	1.11	0.5 ± 0.1
Chamber 3	14	1.07	0.5 ± 0.1
Chamber 4	14	1.06	0.5 ± 0.1

6.2 Large area MICROMEGAS for a DHCAL

Large area MICROMEGAS chambers can have a wide range of applications. In particle physics application, large MICROMEGAS chambers are envisioned to equip, for instance, the $\approx$3000 m^2 of active medium of Silicon Detector (SiD) HCAL [52], two times $\sim$ 10 m^2 for the International Large Detector (ILD) Time Projection Chamber (TPC) [73] or the muon system of "A Toroidal Large System" (ATLAS) upgrade developed by the Muon ATLAS MICROMEGAS Activity (MAMMA) [74] collaboration. Application in fix target experiments are also possible, like T2K [57]. Beyond particle physics applications, large area MICROMEGAS chambers could be used for geophysical muon

imaging [75]or as neutron detectors [76] for territorial safety to scan large containers for radioactive freight. Medical imaging is also demanding for efficient, cheap and reliable detectors (see a first test of application of MICROMEGAS to medical imaging [77]).

The capability for large area bulk production is limited to $150 \times 50\,\mathrm{cm}^2$ by CERN's infrastructure dedicated to Micro-Pattern Gaseous Detector (MPGD). T2K and MAMMA collaborations are demanding for even larger area and an upgrade of the facility is foreseen for producing $200 \times 100\,\mathrm{cm}^2$ individual bulks. This new infrastructure will allow the production of larger MPGD of all types [78].

In the context of the DHCAL active medium, embedded readout electronics is required to optimize the detector compactness and minimize dead zones. Therefore, despite the possibility to provide bulks as large as $200 \times 100\,\mathrm{cm}^2$, such large area bulk MICROMEGAS with embedded readout electronics can not be presently produced. The reason comes from the complexity of the involved PCBs. Embedding chips on a PCB implies the routing of a large number of tracks for physics and electronics control signals, ground layers, shielding between signals and power supply for electronic components. Moreover, the PCB must be gas tight, as part of the envelope of the gas volume of a gaseous detector. This results in multi-layer PCBs (6–8 layers) with very thin printings and blind and buried vias. Today's available equipment in the industry does not allow the production of such PCBs larger than $\sim 50 \times 50\,\mathrm{cm}^2$ at a sensible price.

6.2.1 Square meter prototype design and assembly process

6.2.1.1 Design

The extension to larger area bulk MICROMEGAS with embedded readout electronics has however been performed by sharing a larger gas volume between several moderate sized ASUs. The square meter prototype consists of six $32 \times 48\,\mathrm{cm}^2$ ASUs sharing the same gas volume. Each ASU bears its own mesh and 24 ASICs. Segmenting the mesh as such reduces by a factor 6 the energy released in case of spark ($< 1\,\mathrm{mJ}$ instead of $6\,\mathrm{mJ}$) thus providing safer condition for the readout electronics (compared to a $1\,\mathrm{m}^2$ mesh). DIF boards are employed to pilot the configuration of the chips and the data transfer. A single DIF can handle a range of chained ASUs. It is connected to the first ASU by an intermediate board playing the role of a plug adaptor and also providing voltage distribution. The ASUs are chained together by relaying data and control signals *via* flexible connectors. The last ASU of the chain is terminated to send back the signal through the chain to the DIF. To achieve a square meter chamber, three independent chains consisting of one DIF, one intermediate board and two chained ASUs, are fixed onto a 2 mm thick square meter iron base. A 5 mm gap is maintained between all ASUs thanks to 3 mm high resin walls proving support to the 2 mm thick iron top lid. In addition, the 3 mm MICROMEGAS drift gap is ensured by a 3 mm high resin frame enclosing the chamber, providing gas inlet and outlet, and by the spacer walls between the ASUs. The total thickness of the prototype is 11.5 mm. The final device is robust and a square meter prototype, even encapsulated between 2 mm thick steel plates can be manipulated by hands. The design is illustrated in figure 6.3.

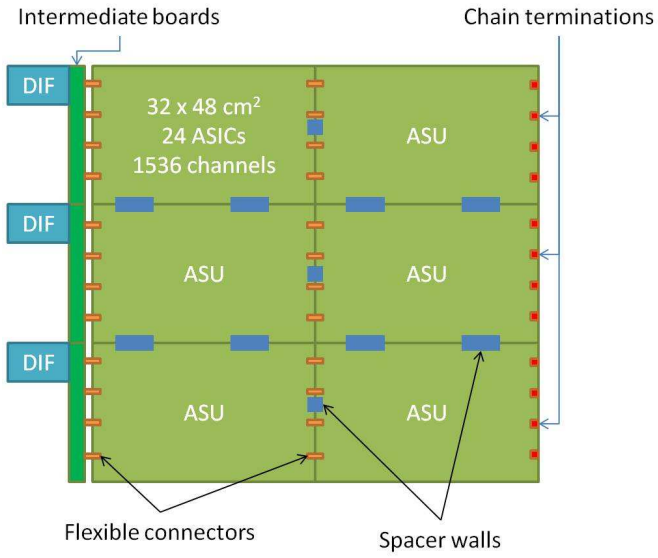

(a)

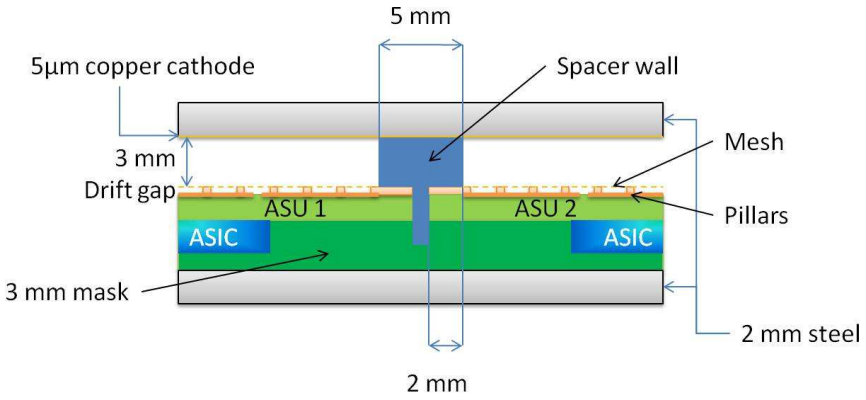

(b)

Figure 6.3: (a): Design of the m^2 prototype ; (b): Spacer wall scheme.

6.2.1.2 Assembly process

The ASUs needed to mount a square meter prototype are built and tested separately. The PCB production and the electronics cabling are done by industrial subcontractors. The MICROMEGAS meshes are installed by lamination at CERN MPGD workshop. Each ASU is then cooked in clean room and inserted in a dedicated test box. The test box allows to verify the good functioning of the ASUs by providing all electrical and gaseous services in a gas tight volume temporarily housing the ASU. The response of the ASU to cosmic rays and to ^{55}Fe can be checked and hence validate the ASU for definitive insertion in the square meter prototype. A photograph of an ASU lying in the opened test box in the clean room is shown in figure 6.4(a). An example of a test result is displayed in 6.4(b).

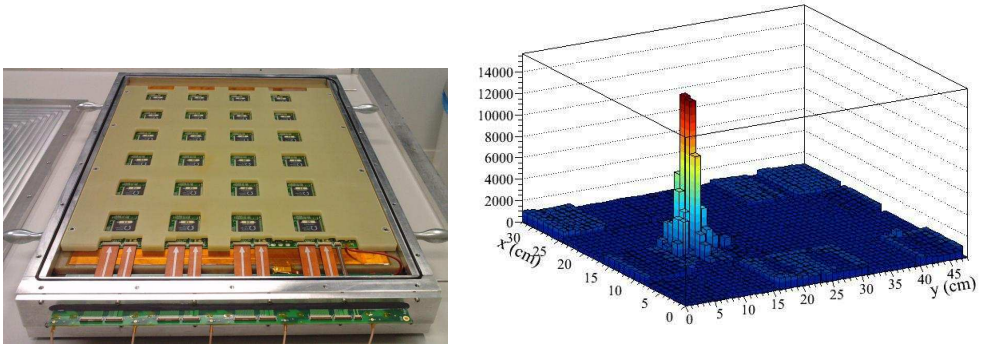

(a) (b)

Figure 6.4: Test box for single ASU validation. (a) one ASU inserted in the opened test box. (b) ^{55}Fe profile of an ASU in the test box.

6.2.2 Mechanical prototype

The mechanical square meter prototype did not house any real ASUs. In this version they were replaced by naked and very simple PCBs called *ghost* ASUs. It was intended to test the assembly process and the gas tightness of the final device. During the assembly, some minor possible improvement were found and therefore applied to the assembly of the physical prototype. A photograph of the mechanical prototype under construction is displayed in figure 6.5, the *ghost* ASUs at the foreground and the resin mask for the protection of the ASICs at the background are clearly seen. The spacer walls maintaining the drift volume are also seen at the border of each ASU. The mechanical prototype was gas tight and the assembly procedure was validated.

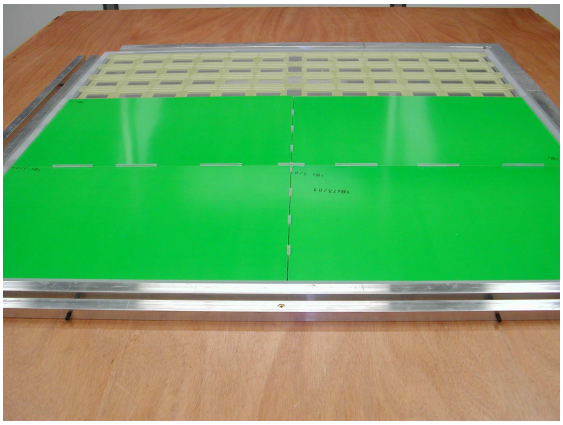

Figure 6.5: Photograph of the mechanical square meter prototype under assembly.

6.2.3 Physical prototype

Using the technical skill developed by our technicians on the mechanical prototype, the first physical square meter prototype was assembled. The first physical square meter prototype housed four HARDROC2 ASUs, one HARDROC2b ASU and one ghost ASU

due to the available chip collection at the time of building. The prototype layout is displayed in figure 6.6 and photographs of the prototype are shown in figure 6.7. The actual thickness the this prototype is 12 mm, including 4 mm of iron that are part of the absorber budget. The additional 0.5 mm are due to mechanical imperfections and glue. The square meter prototype was tested in a muon beam at CERN during summer 2010. The detector stack studied in chapter 5 was used as a beam telescope for event selection and reconstruction of the incoming particle tracks. The collected data is studied in detail in [79]. The main features are recapitulated as follows.

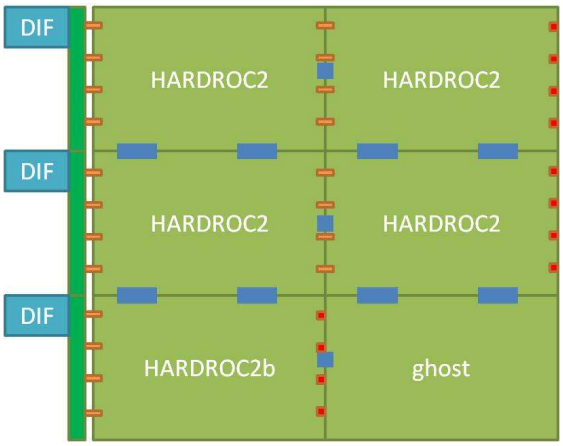

Figure 6.6: Layout of the first MICROMEGAS square meter physical prototype.

Figure 6.7: Square meter prototype assembled.

6.2.3.1 HARDROC calibration

Given the fact that the MICROMEGAS signal is rather feeble (MPV about 20 fC) and spread over time (150–200 ns, see section 3.2.2, p.44), the short shaping time of the HARDROC chip (≈10–20 ns) reveals it inappropriate to take proper advantage of MICROMEGAS technology. By keeping only about 10% of the signal, the HARDROC chip sees the MICROMEGAS signal MPV at only 2–3 fC. Therefore, to obtain valuable informations, a careful calibration is mandatory.

Calibration data A LabView program developed at LAPP allowed the control of the injection of calibrated pulses into the chip entry stage and to control the chip configuration. Calibration data was acquired while varying the chip threshold within its dynamic range (0–1023 DAC) and recording the chip response to the input charge. The process has been repeated for four values of the input charge: 0 (no charge, pedestal study), 10 fC, 50 fC and 100 fC.

S-curves The plot of the chip efficiency *versus* threshold is called an S-curve because of its specific shape showing a higher level plateau and a lower level one linked together by a continuous slope (recalling the shape of the letter 's'). The raw S-curves obtained for no charge injection for one single chip are displayed in figure 6.8(a). The pedestal of a channel is defined as the inflection point abscissa of its S-curves. The electronic noise of a channel is rendered by the width of its S-curve.

Calibration procedure Given that 1 DAC corresponds roughly to 1 fC, figure 6.8(a) shows that the pedestals are quite spread and present irregular widths. The calibration process is aimed at allowing the lowest possible threshold with the lowest possible electronic noise contamination in order to achieve the highest efficiency. The tunable parameters are the gain of each channel and the global chip threshold. It has been noticed in [79] that the pedestal value is linearly dependent on the channel gain and that the S-curve width on the contrary does not change much for different gains. Therefore it has been possible to align the S-curve lower levels so that they all start at the same Digital to Analog Count (DAC) value; the result is plotted in figure 6.8(b). This technique allows the threshold for each readout channel to be minimized but is disadvantaged by the spread of channel gains. However, it has been shown in chapter 5 that despite a certain disparity of the gain (gas gain in the former case, electronic gain in the present one) the efficiency disparity was strictly proportional to the value of the detection threshold. This assumption would not hold in the case of a multi-threshold readout.

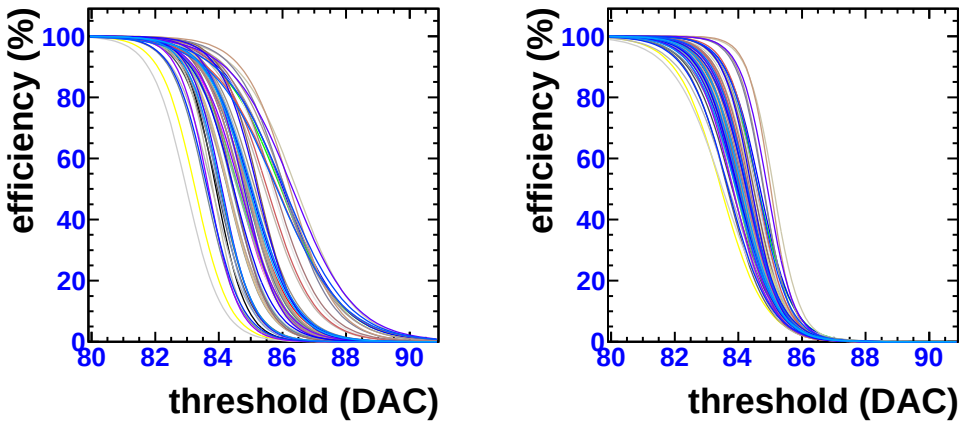

(a) (b)

Figure 6.8: Pedestal S-curves for chip #124 before (a) and after (b) calibration [79].

6.2.3.2 Square meter performance

It is worth recalling here that the results presented in this section do not reflect anywhere near the full potential of the bulk MICROMEGAS chambers. This first square meter prototype has played the role of a training tool allowing to develop all the skills needed for the next ones. The best performance was achieved with a 420 V amplification voltage, corresponding to a gas gain of $\approx 10^4$, at a channel threshold[1] of 1–2 DAC; see table 6.2. Performance with a more conservative amplification voltage of 410 V is displayed in table 6.3. Four positions in the prototype, denoted by the corresponding chip number, have been scanned.

Table 6.2: Best performance of the first square meter prototype

Mean efficiency	Efficiency disparity	Multiplicity	Multiplicity disparity
43.8%	5%	1.06	0.003

Table 6.3: Performance of the first square meter prototype at 410 V.

Chip	Mean channel threshold	Mean efficiency	Efficiency disparity	Multiplicity
114	4 DAC	11.2%	1.7%	1.07
112	5 DAC	11.9%	1.9%	1.06
134	12 DAC	4.5%	0.9%	1.09
138	12 DAC	3.8%	0.9%	1.08

6.2.4 Power pulsing

The power pulsing technique consists of powering off a device during a given idle time and switching it on when needed. If the idle time is sufficient, this technique allows a significant reduction of the average power consumption in comparison to having all the electronics working all the time. The target consumption for calorimeters at ILC is $\leq 25\,\mu$W/channel [52, 53]. The motivation for power pulsed electronics at future linear colliders is the need for calorimeter compactness. Cooling systems usually represent a large amount of cumbersome dead material in detectors. A lower power consumption results in a lower heat dissipation and hence a decreased need for cooling and, by consequence, smaller cooling systems.

The possibility to use the power pulsing technique comes from the beam clock cycle foreseen for the future linear colliders, as summarised in table 6.4. As shown in table 6.5 the electronics would be idling most of the time. The performance impact of the use of power pulsing technique i stherefore important to be investigated. A suitable readout chip should be able to be switched on and off sufficiently quickly to allow a significant off time and no impact on performance during on time. All the chips are designed for a power pulsed usage.

[1] A channel threshold is defined as the difference between the global chip threshold and the channel pedestal.

Table 6.4: Beam clock cycle at future linear colliders (500 GeV version) [80, 25]

Machine	bunches separation	train length	repetition period
CLIC	500 ps	177 ns	20 ms
ILC	369 ns	1 ms	200 ms

Table 6.5: Idle time at future linear colliders (500 GeV version)

Machine	Idle time between bunch trains	Duty time fraction
CLIC	19.998 ms	$1 \cdot 10^{-5}$
ILC	199.00 ms	$5 \cdot 10^{-3}$

A preliminary test of the effect of HARDROC2 power pulsing has been performed in a muon beam [79]. The square meter prototype was operated with a conservative amplification voltage of 410 V. During the test, the beam was kept on only one position in the square meter prototype corresponding to chip #124 with average channel threshold of 7 DAC, but all the chips were set to record data. The corresponding beam profiles are displayed in figure 6.9 and show no significant difference.

The detector efficiency has been measured with power pulsing activated and with power pulsing deactivated. In power pulsing mode, the chip was off during 10 ms and on during 2 ms, the external trigger was vetoed during the off periods of the chips. The corresponding pulsed current was about 7.5 A. The measured efficiencies are shown in table 6.6. The low efficiency is due to the short shaping time of the HARDROC chips allowing to see only about 10% of the MICROMEGAS signal. The ratio of the efficiency with over without power pulsing is compatible with 1.

Table 6.6: Effect of power pulsing on detection efficiency.

Power pulsing mode		Channel-to-channel
OFF	ON	ON/OFF ratio
$8.7 \pm 0.4\%$	$9.3 \pm 0.6\%$	1.06 ± 0.05

A crucial step in the development of the power pulsing technique will be the possibility to powering the apparatus with an averaged current rather than a peaked pulsed current. This may be done by powering with a low current an *ad hoc* capacitance close to the power pulsed electronics that will then deliver the power pulse in due time. The interest is then that the cabling between external power and the readout electronics would be reduced therefore some dead material would be saved.

6.2.5 Preliminary results on the second square meter prototype

The second square meter prototype has been built and is under beam tests at CERN/H4A beam line at the time of writing. It is composed of 6 ASUs bearing a total of 144 MICROROC chips and is designed 1 mm thinner than the previous prototype, 10.5 mm instead of 11.5 mm, thanks to a protective mask of 2 mm instead of 3 mm. The actual thickness of

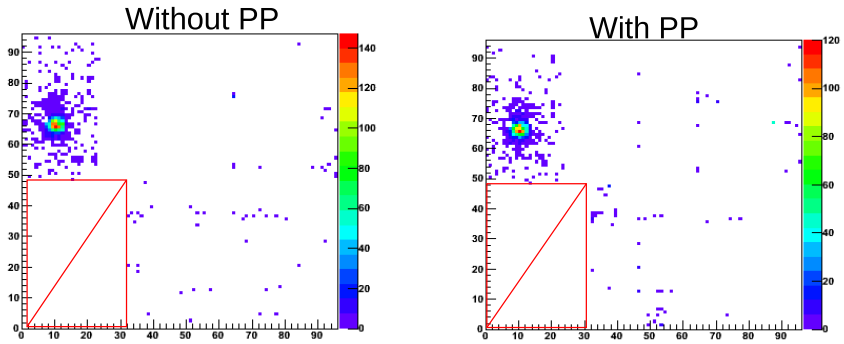

(a) (b)

Figure 6.9: Beam profiles without (a) and with (b) power pulsing activated. The red marks represent the ghost ASU.

this prototype is 11.5 mm. The thickness difference with the design is due to glue and to mechanical tolerances and also to aluminium adhesive ribbon used for Electromagnetic Compatibility (EMC). The electronic side steel lid is fixed with only screws and can be removed to access the embedded electronics for tests or maintenance or simply removed to give back the corresponding 2 mm of steel to the absorber structure of the calorimeter to increase its mechanical robustness. The gas tightness is insured by glue between the ASUs. The prototype's assembly took great advantage of the experience earned with the previous prototypes. It shows already preliminary performance beyond expectations: an efficiency up to 99% with a noise bias below 0.1% and a response multiplicity below 1.2.

6.3 Expected performance of a MICROMEGAS DHCAL prototype

6.3.1 Cubic meter project

In order to test the performance of International Linear Collider (ILC) or Compact Linear Collider (CLIC) calorimeters the natural idea is to build a small part of it as a prototype. The depth of the prototype should be the same as the baseline design of the final calorimeter in order have a realistic longitudinal containment of particle showers. The transverse dimensions should be sufficient to avoid lateral leakage. It has therefore been chosen to build a $4.5\,\lambda_I$ deep calorimeter with a $1 \times 1\,m^2$ transverse area. Such a prototype will consist of 40 instrumented layers (8 mm each) and 40 layers of steel (1.86 cm) giving a total thickness of 106.4 cm. This class of prototypes is therefore called a "cubic meter".

Several cubic meter prototypes involving different detection technologies are currently being built within the CALICE collaboration [54]. The main ones are the scintillator cubic meter from the Analog Hadronic Calorimeter (AHCAL) project held at *Deutsches Electronen Sychrotron, Hamburg* (DESY) and the RPC cubic meter from the DHCAL project at Argonne national laboratory, Illinois. Those two projects correspond to the baseline of the ILD and SiD detectors respectively.

Simulations have been performed to evaluate the performance of a MICROMEGAS based cubic meter. To do so, the geometry has been implemented in a GEANT4 application and the MICROMEGAS response was simulated separately.

MICROMEGAS response simulation The GEANT4 simulation only provides the amount of energy deposited in the 3 mm MICROMEGAS conversion gap. To achieve a more realistic simulation, the development of the MICROMEGAS signal was implemented step by step in a digitisation driver.

1. The raw deposited energy is divided by the effective ionisation potential of the gas $W_{\mathrm{I}} = 25.8\,\mathrm{eV}$ for $\mathrm{Ar}/i\mathrm{C_4H_{10}}$ (95/5) to obtain the number of primary electrons.
2. Each electron is tested to determine if it will reach the amplification gap or not. The size of the pillars give a probability of $\approx 4\%$ for an electron to crash on them. The mesh transparency was conservatively taken at 70%.
3. Each electron passing the previous tests is amplified following an exponential distribution (model described in [46] valid for field of a few tens of $\mathrm{kV}\cdot\mathrm{cm}^{-1}$). The gain is given as input parameter and the actual number of electrons in the avalanche is determined randomly in accordance with the fluctuation formula 3.1.
4. The induced charge on the anode pad corresponds to the sum of the charge of the avalanche of all the primary electrons (see appendix A for details)
5. A smearing factor is applied to the induced charge corresponding to the global detector energy resolution (7.5%) measured with 5.9 keV X-ray (see figure 4.1, p.54)
6. Electronics conversion factors are applied to the deposited charge to get an output in ADU (GASSIPLEX-like readout).

The following features will need to be be taken into account in a refined future version of this digitisation driver:

- Transverse diffusion of primary electrons (to induce the hit multiplicity, neglected so far)
- Time development of the signal (to allow modelisation of the electronics shaping of the signal and time stamping studies)
- Tunable probability of noise hit contamination

6.3.2 Mini-calorimeter alternative

Low energy showers can be studied with a calorimeter much smaller than $1\,\mathrm{m}^3$. For instance, in [81] and [58] studies of electromagnetic and hadronic showers respectively for energies below 16 GeV are presented. Those studies were done with RPC chambers mounted in a six layer stack interleaved with 2 cm thick steel plates. With only six ASUs such an experiment could be redone, offering cross checked measurements and a fair comparison between RPC and MICROMEGAS technologies.

(gather details from jan's simulation, when available... if ever available)

6.4 Layout studies towards the SiD DHCAL

6.4.1 Global geometry

LAPP has proposed the baseline design for SiD hadronic calorimeter geometry [82, 83, 52]. The principle was that projective cracks have a probability to hide information about tracks passing through them. The proposed geometry completely avoids projective cracks by being constituted of two types of module: rectangular and trapezoidal. See figure 6.10 for a comparative view of the classical projective geometry and the proposed non projective one. Simulation studies at LAPP[84] demonstrate that the non projective geometry in the vicinity of the cracks present better performance than the projective one. Such a conclusion was anticipated. Global improvement is evaluated by considering incoming particles not just in the immediate vicinity of the cracks. The same simulation model is used with a wider spacial dispersion of the incoming particles and conclude also in favour of the non-projective geometry.

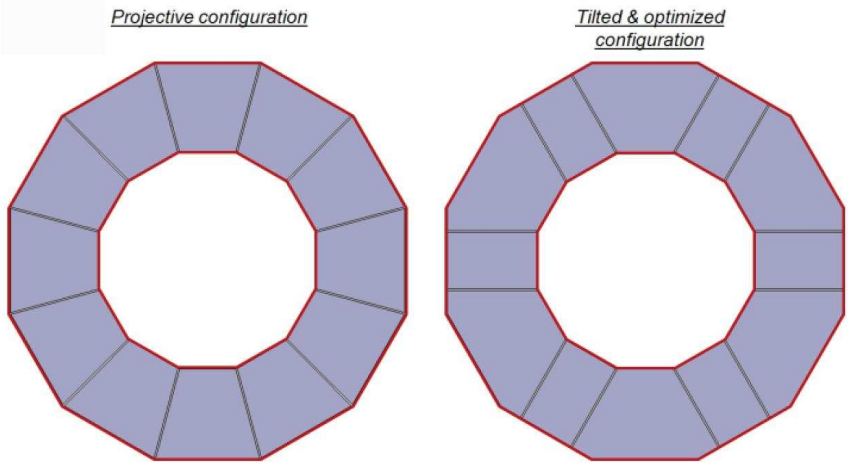

Figure 6.10: Comparative view of projective and non-projective HCAL barrel geometries.

6.4.2 Alternative DHCAL layout

Three alternative geometries have been considered beyond the baseline. The baseline design is a 40 layer calorimeter of 1.89 cm of stainless steel between MICROMEGAS planes as shown on figure 6.11(a). The question is if alternatives can be envisioned to increase mechanical robustness and to simplify integration with no degradations of the physics performances. Figure 6.11 sums up the different alternatives considered here. The overall dimension are conserved in each design: depth = 4.5 λ_I, 107.6 cm.

- Thick back plate geometry: the last active layer is removed and the two last absorber plates are merged to make a double thickness steel layer at the outside shell of the calorimeter to increase the detector robustness. The scheme is shown in figure 6.11(b).

- Progressive absorber thickness geometry: the 30 first layers are standard, then 5 layers are 2.09 cm thick and then 4 layers are 2.29 cm thick. See scheme in figure 6.11(c).

- Brass absorber geometry: As brass is way easier to machine than steel, only the first and last absorber layers are made of steel with standard thickness of 1.89 cm and the others are 1.85 cm thick brass layers. See scheme in figure 6.11(d).

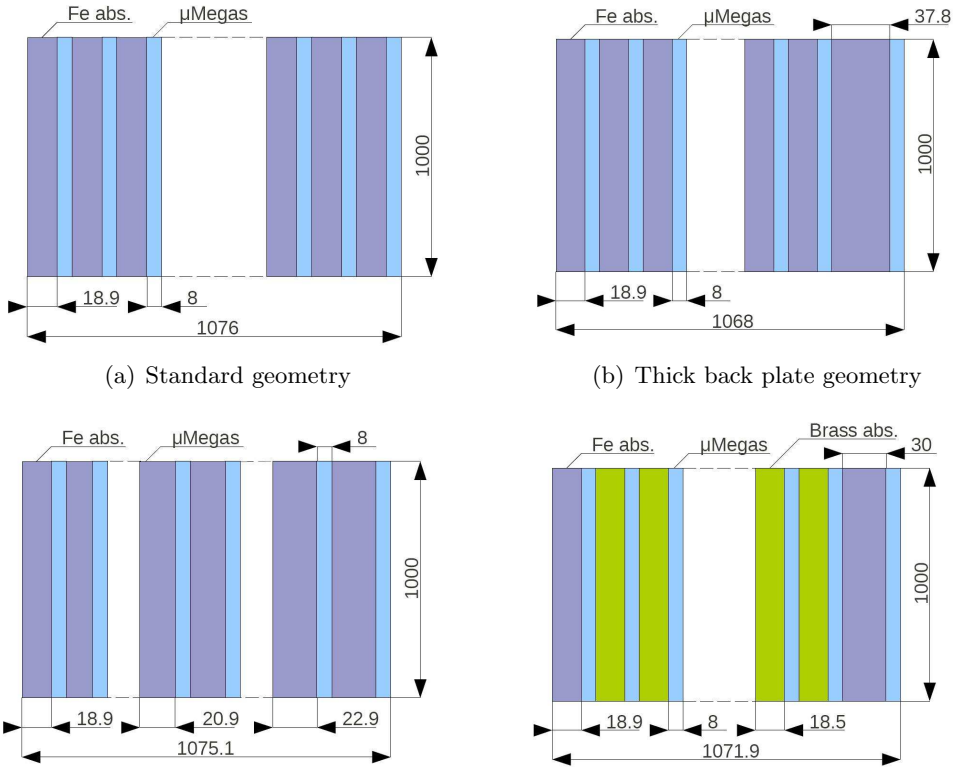

(a) Standard geometry

(b) Thick back plate geometry

(c) Progressive absorber thickness geometry

(d) Brass absorber geometry

Figure 6.11: Scheme and summary of the considered alternative geometries.

Résumé du chapitre

Les différentes étapes clés du projet de développement de chambres MICROMEGAS en tant qu'élément actif d'un calorimètre hadronique digital optimisé pour l'application d'un PFA auprès d'un futur collisionneur linéaire, après les mesures de caractérisations effectuées dans les deux chapitres précédents, sont résumées ici.

Électronique embarquée Les premiers prototypes de chambre MICROMEGAS avec *bulk* et électronique de lecture embarquée sur le PCB d'anode ont été assemblés et testés avec succès validant ainsi la technique d'assemblage. La puce de lecture, DIRAC1, et les autres composants sont soudés au four puis un masque de protection en résine est

installé sur l'électronique afin de lui permettre de résister à l'étape de lamination lors de la pose du *bulk*.

Après cette validation, une puce électronique optimisée pour la lecture des signaux de chambre MICROMEGAS a été développée en collaboration entre le LAPP et le LAL/Ω. Après plusieurs modèles testés, la puce MICROROC a été sélectionnée pour équiper les futurs prototypes de chambre MICROMEGAS de grande surface.

Chambre MICROMEGAS de grande surface pour la calorimétrie hadronique digitale Pour des raisons à la fois de limitation dans la taille des *bulks* et dans la taille des circuits imprimés de la complexité de ceux utilisés ici, un prototype d'un mètre carré consiste en six unités de détection indépendentes (*Active Sensor Unit* — ASU) partageant un unique volume de gaz. Les ASUs représentent des surfaces actives de $32 \times 48\,\mathrm{cm}^2$ chainés deux à deux dans la longueur et contrôlés par une carte d'interface (*Detector interface* — DIF). Trois de ces assemblages sont juxtaposés pour formé un plan de $96 \times 96\,\mathrm{cm}^2$ (soit 9 216 voies, voir schémas sur fig. 6.3 et photos sur fig. 6.7). Le premier prototype "Mètre Carré" équipé de l'électronique de lecture optimisé MICROROC montre des performances remarquables en accord avec les mesures de caractérisation.

Prototype "Mètre Cube" Des études de simulations d'un calorimètre d'un mètre cube (env. 40 plan de $1\,\mathrm{m}^2$), utilisant des chambres MICROMEGAS en tant que milieux actifs, sont menées afin de prédire les caractéristiques d'un tel calorimètre en terme de résolution en énergie, linéarité, ou encore contenance de l'énergie. Plusieurs prototypes "Mètre Cube" sont déjà construits avec d'autres technologies (Scintillateur, RPC). Les excellentes performances des chambres MICROMEGAS encouragent à la construction d'un Mètre Cube MICROMEGAS afin de comparer les différentes technologies envisagées de manière objective.

Design du calorimètre Hadronique de SiD Une étude mécanique menée au LAPP a conduit, lors de la rédaction de la lettre d'intention de SiD, au choix d'une géométrie non projective pour le calorimètre hadronique. Le schéma proposé est donné sur la figure 6.10. Des géométries alternatives de l'empilement absorbeur / couche active ont aussi été étudiées (voir fig. 6.11) et fournissent toutes différents avantages mécaniques sans détérioration de performance.

CHAPTER 7

Conclusion

MICROMEGAS chambers using bulk technology were built and tested with the object of evolving towards large area detectors for multiple applications, but most importantly as an active medium of a future linear collider (semi-)digital hadronic calorimeter. Small prototypes of $6\times16\,\mathrm{cm}^2$ (and one of $12\times32\,\mathrm{cm}^2$) with analog readout were first assembled for a detailed evaluation before evolving towards larger area with dedicated electronics.

The optimal working point was determined in X-ray laboratory tests. A mesh voltage of 420 V with a drift voltage of 470 V assure a high gas gain ($\approx 10^4$) and an optimal mesh transparency to electrons in $\mathrm{Ar}/i\mathrm{C_4H_{10}}$ (95/5). At the same time, a method of data correction for environmental gain fluctuations was proposed. This may be used for on-line gain control to ensure gain stability during long runs of data acquisition. This would be useful for operation at intermediate or high detection thresholds ($\geq$1 MIP MPV) where gain fluctuation has an impact on efficiency.

Beam tests at CERN at CERN allowed a series of detailed measurements. The gain non-uniformity, the MIP efficiency, its homogeneity and the hit multiplicity were measured. The MICROMEGAS prototypes were also exposed to high energy hadrons and showed very good behaviour even in very dense showers.

The key results are summed up below (for 1.5 fC detection threshold):

- MIP signal amplitude $\approx 20\,\mathrm{fC}$
- Efficiency $\geq 97\%$
- Efficiency disparity $\leq 1\%$
- Gain disparity $\sim$ 7–13%
- Multiplicity ≤ 1.1

Performance of the PFA in function of the active medium MIP efficiency was not available at the time of writing. However, PFA calls for calorimeters with tracking capabilities and therefore a very high efficiency is likely to be useful. A low multiplicity (close to 1)

should be very important for the PFA to clearly identify the hadronic shower starting positions and then match calorimeter hit clusters to charged tracks. Therefore, those results prove that the bulk MICROMEGAS is very suitable for application in PFA oriented digital calorimetry. The gain disparity is relatively high, but in the context of digital calorimetry, the efficiency disparity at the working threshold is the fundamental trait and is below 1%.

Collaborative results The first bulk MICROMEGAS chamber with embedded readout electronics has been successfully built and tested. This has validated the embedding process based on using a resin mask to protect the readout chips during the lamination of the bulk. ASUs with embedded readout electronics of size up to $32 \times 48\,\mathrm{cm}^2$ have been produced and then assembled into a square meter MICROMEGAS prototype tested in muon beam in 2009. The electronics used however was not optimal and the performance achieved were well below the full MICROMEGAS potential. However, precious technical experience has been earned and has already served for the second square meter prototype equipped with optimised readout electronics. This second square meter prototype is under beam tests at CERN at the time of writing and shows preliminary performance outperforming the expectations.

A proposal of non projective geometry, supported by simulation studies has been accepted as the SiD baseline for its hadronic calorimeter. Several alternative HCAL layouts have been also studied with MC simulations. The different layouts show various mechanical advantages compared to the baseline without any loss of performance.

Des chambres MICROMEGAS utilisant la technologie bulk *ont été construites et testées avec succès.Des mesures de caractérisation en rayons X ont permis d'établir le point de fonctionnement des détecteurs : tensions de grille applicables (autour de 400* V *en* Ar/iC_4H_{10} *(95/5), de 580 en* Ar/CO_2 *(80/20)), rapport des champs d'amplification et de dérive entre 150 et 200 (différence de potentiel de 50* V *en* Ar/iC_4H_{10} *(95/5)). Une méthode de correction des données pour les fluctuations de pression et température du gaz a été proposée. Cette méthode peut servir aussi à contrôler directement le gain lors de la prise de données afin de compenser les modifications des propriétés du gaz dans le cas de données digitales difficilement corrigeable. Des tests en faisceaux de muons ont fourni une série de mesures détaillées résumées ci-dessous pour un seuil de 1.5* fC*.*

- *Amplitude du signal des MIP* $\approx 20\,\mathrm{fC}$ *(pôle de la distribution)*
- *Efficacité* $\geq 97\%$
- *Non-uniformité de l'efficacité* $\leq 1\%$
- *Non-uniformité du gain* ~ 7–13%
- *Multiplicité* ≤ 1.1

Ces résultats démontrent que la technologie MICROMEGAS est appropriée pour une calorimétrie digitale optimisée pour l'application d'un PFA.

Les chambres ont aussi été exposées à des gerbes électromagnétiques et hadroniques de diverses énergies. Des profils de gerbes ont été mesurés illustrant la bonne tenue de ces chambres lors de l'exposition aux gerbes.

Résultats collaboratifs *les étapes suivantes du développement du projet ont été réalisées par le groupe au LAPP parallèlement et conjointement aux travaux principalement personnels décrit précédemment.*

- *Validation de la méthode d'assemblage des prototypes à électronique de lecture embarquée*
- *Développement d'une puce de lecture optimisée pour les signaux MICROMEGAS*
- *Assemblage d'un prototype "Mètre Carré" et conservation des performances (Mètre Carré MICROROC)*

Mais aussi, le design de base pour le calorimètre hadronique de SiD a été conçu au LAPP avec l'appui d'études de simulations. D'autres études de simulations ont investigué diverses géométries alternatives ouvrant de multiples fenêtres pour les choix mécaniques futurs pour la construction de SiD.

Ces réalisations, outre le dynamisme et la motivation de toute l'équipe, montrent la compétitivité de la technologie MICROMEGAS, très prometteuse pour de multiples applications dont la calorimétrie hadronique à imagerie pour les futures expériences de physique des particules.

Part III

Search for New Physics in the Field of the Top Quark at CLIC

CHAPTER 8

The top quark at CLIC

The condition of e^+e^- collisions at Compact Linear Collider (CLIC) are described before focusing on the case of the $t\bar{t}$ pair production in such collisions. Then, a method for $t\bar{t}$ event selection is proposed and evaluated.

8.1 e^+e^- collisions at 3 TeV

8.1.1 Initial State Radiation

Initial State Radiation (ISR) occurs in every process involving charged and/or coloured particles and can have a large influence on the outcome of the collision. It consist of the emission of a photon (in the case of electomagnetic particles) or a gluon (in the case of coloured particles) just before the collison. This tendency increases dramatically with higher energy and with smaller masses. Therefore, when an electron is to collide with a positron they both radiate a more or less energetic photon. This phenomena is called ISR. It induces a continuous smearing of the centre of mass energy of the actual collision, presenting a peak at the nominal centre of mass energy and a tail towards the lower values. Moreover, It introduces a random asymmetry in the collision, since the energy loss of the incoming particles is independent of each other, resulting in a boost of the centre of mass frame along the beam direction.

The calcHEP program [85] models this radiative energy loss of the collision initial state through the following formula giving the incoming particle energy spectrum, x, ranging from 0 to 1, being the fraction of the nominal beam energy carried by the incoming electron and F the corresponding probability density function:

$$\begin{aligned} F(x) &= exp\left(\kappa \cdot (3/4 - \gamma_{\text{Euler}})\right) \cdot \kappa \cdot (1-x)^{\kappa-1} \\ &\times \frac{(1+x^2) - \frac{1}{2} \cdot \kappa \cdot \left((1+3x^2)\,\frac{ln(x)}{2} + (1-x)^2\right)}{2\Gamma(1+\kappa)}, \end{aligned} \tag{8.1}$$

where $\gamma_{\text{Euler}} \approx 0.5772156649$ is the Euler-Mascheroni constant, Γ is the gamma function

and

$$\kappa = \frac{\alpha}{\pi}\left(2\,ln(E_{\text{scale}}/m_e) - 1\right)\,,$$

with α, the fine structure constant, m_e the electron mass and E_{scale}, the energy scale of the process, *i.e.* the nominal collision energy in case of e^+e^- collisions. The function 8.1 is represented for $E_{\text{scale}} = 3\,\text{TeV}$ in figure 8.1(a), the shape of the distribution is mainly defined by the contribution $\kappa \cdot (1-x)^{\kappa-1}$ which is plotted in figure 8.1(b) and which has the property that

$$\int_0^1 \kappa \cdot (1-x)^{\kappa-1}\,dx = 1\,.$$

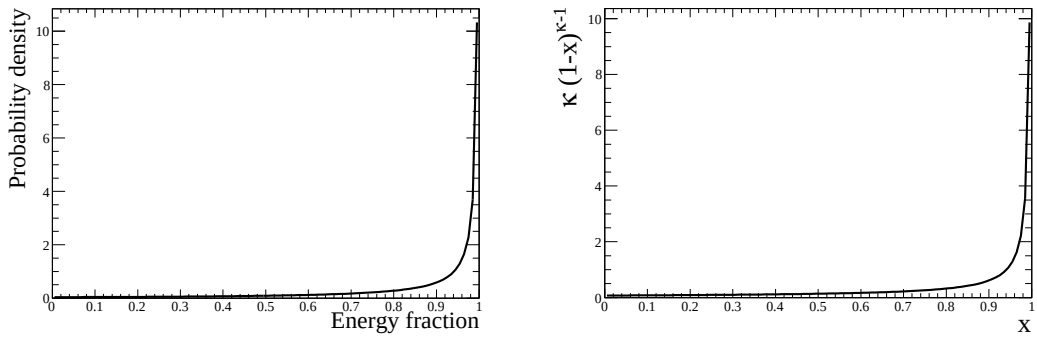

(a) (b)

Figure 8.1: Distribution of fraction of nominal energy available for the collisions

Luminosity spectrum The full luminosity takes all collisions into account, regardless of the amount of initial state energy that is lost. An interesting question arises: what would be the luminosity if we only consider the collision that occur at the nominal energy or very close (say 1%)? The values for CLIC are for instance :

- Full luminosity: $\mathcal{L} = 5.9 \cdot 10^{34}\,\text{cm}^{-2}\,\text{s}^{-1}$
- Luminosity in 1% of energy: $\mathcal{L}_{99\%} = 2.0 \cdot 10^{34}\,\text{cm}^{-2}\,\text{s}^{-1}$

The luminosity dependency on the considered energy is referred to as "Luminosity spectrum".

8.1.2 Beamstrahlung

The Beamstrahlung (BS) is an electromagnetic energy loss due to the interaction of an incoming particle with the electromagnetic field of the oncoming bunch. This phenomenon depends on the structure of the bunches. If a Gaussian shape is assumed, the resulting energy spectrum depends essentially on the two quantities N_{cl} and Υ, defined as follow:

$$N_{\text{cl}} = \frac{25\alpha^2 N}{12\,m_e(\sigma_x + \sigma_y)}\,, \tag{8.2}$$

$$\Upsilon = \frac{5\alpha\,N\,E_{\text{cm}}}{6m_e^3\sigma_z(\sigma_x + \sigma_y)}\,, \tag{8.3}$$

where α is the fine structure constant, m_e the electron mass, N the number of particles in the bunch, σ_i, $i \in \{x, y, z\}$ are the bunch dimension in term of Gaussian sigmas and E_{cm} is the nominal centre of mass energy.

The energy spectrum, in calcHEP, is given by:

$$F(x) = \frac{1}{N_{\text{cl}}}\left[(1 - E_{\text{cm}}^{-N_{\text{cl}}})\delta(1-x) + \frac{e^{-\eta(x)}}{1-x}h(\eta(x)^{1/3}, N_{\text{cl}})\right], \tag{8.4}$$

where δ is the Dirac function and $\eta(x)$ and $h(z, N_{\text{cl}})$ are functions of the quantities 8.2 and 8.3 defined as:

$$\eta(x) = \frac{2}{3\Upsilon}(1/x - 1), \tag{8.5}$$

$$h(z, N_{\text{cl}}) = \sum_{n\geq 1} \frac{z^n}{n!\Gamma(n/3)}\gamma(n+1, N_{\text{cl}}), \tag{8.6}$$

with Γ, the gamma function and γ the lower incomplete gamma function. A detailed and pedagogical approach to BS at future linear colliders is presented in [86]. The effect of BS on the initial energy spectrum is rather similar to that of ISR and its implementation in calcHEP is simply an increase of the ISR effect. The nominal parameters for BS at CLIC are presented in table 8.1 (taken from [28], N_{cl} and Υ computed with calcHEP). Note that the large values of Υ (≥ 1) indicate that the energy losses of the incoming particles can amount up to the particle total energy with significant probability.

Table 8.1: CLIC parameters used for BS calculation in calcHEP.

	σ_x	σ_y	σ_z	N	N_{cl}	Υ
Nominal	45 nm	1 nm	44 μm	$3.72{\cdot}10^9$	3.47	4.89
Conservative	83 nm	2 nm	44 μm	$3.72{\cdot}10^9$	1.88	2.65

8.1.3 Machine induced background

The very high luminosity foreseen at CLIC ($5.9{\cdot}10^{34}$ cm^{-2} s^{-1}) implies the use of dense and compact bunches of electrons and positrons. Beyond a significant BS effect, the high number of photons resulting from the beam-beam interaction will potentially produce a significant amount of e^+e^- and $q\bar{q}$ pairs. The diagram of the process of hadron production from $\gamma\gamma$ collisions is represented in figure 8.2(a), the same for coherent e^+e^- pair production in figure 8.2(b) and incoherent pair in figure 8.2(c). Table 8.2 shows the expected number of such interactions per bunch crossing (BX).

Table 8.2: Main machine background process contribution.

Process	Number of events/BX
$\gamma\gamma \to$ hadrons	2.7
$\gamma \to e^+e^-$	$3.8 \cdot 10^8$
$\gamma\gamma \to e^+e^-$	$\approx 10^5$

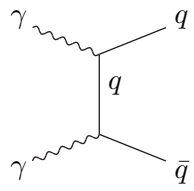

(a) $\gamma\gamma \rightarrow$ hadrons

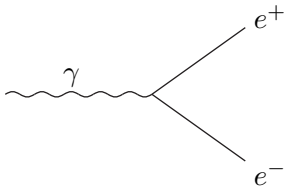

(b) Coherent pair production ($\gamma \rightarrow e^+e^-$)

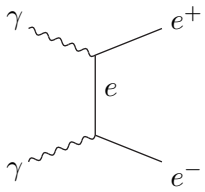

(c) Incoherent pair production $\gamma\gamma \rightarrow e^+e^-$

Figure 8.2: Main machine background process diagrams.

Those processes produce particles that tend to be very close to the beam axis, therefore a large part of them escape along the beam pipe and is invisible. The e^+e^- pair productions, given the small mass of the electron, are more boosted than the hadron produced in $\gamma\gamma$ collisions and in the end, they provide a signal only in detectors very close to beam axis (vertex and very forward detectors). On the other hand, the $\gamma\gamma \rightarrow$ hadrons process will pollute the full detector, mainly in the forward region but even the barrel detectors will be hit. However, if only one BX is considered, the contribution of the $\gamma\gamma \rightarrow$ hadrons background can be neglected. But in practice, since the bunch separation is only 0.5 ns, several bunches, or even a full train, depending on the considered sub-detector, will overlay physics events. The effect of $\gamma\gamma \rightarrow$ hadrons background is illustrated in figure 8.3. As can be seen in this figure, the jets with a high transverse momentum are not very affected, whereas the forward region is completely flooded with particles from the $\gamma\gamma$ interactions. In this example, the 60 BX overlaid event presents an excess of energy of 1.4 TeV due only to the $\gamma\gamma \rightarrow$ hadrons background. Therefore, in every analysis, the influence of this background must be considered.

8.2 $t\bar{t}$ events at CLIC

The production of $t\bar{t}$ pairs is essentially obtained through the s-channel process described by the Feynman diagram shown in figure 8.4. $t\bar{t}$ pairs can also be produced in the Standard Model (SM) together with neutrinos but the corresponding cross section is completely negligible for centre of mass energies below about 1 TeV[1]. The diagrams and

[1]Contrary to the s-channel cross section which is dramatically increased in presence of ISR and BS because of a lower centre of mass energy, the t-channel cross section does not benefit from a resonance

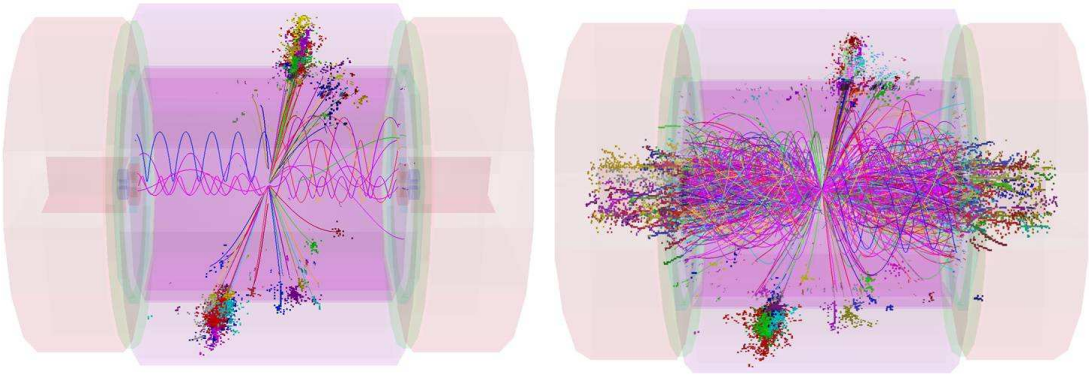

(a) No $\gamma\gamma \rightarrow$ hadrons (b) 60 BX overlaid

Figure 8.3: Illustration of the effect of $\gamma\gamma \rightarrow$ hadrons event overlay on a 1 TeV Z^0 event over 60 BX in the CLIC ILD detector (taken from [87])

cross sections for $t\bar{t}$ pair production together with SM neutrinos are given for reference in appendix B.

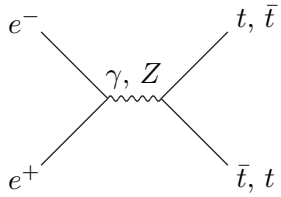

Figure 8.4: $t\bar{t}$ pair production diagram.

8.2.1 Total cross section as a function of the centre of mass energy

The total cross section of the channel $e^+e^- \rightarrow t\bar{t}$ is computed with calcHEP [85] in function of the centre of mass energy and displayed in figure 8.5. The dashed line in figure 8.5 is an interpolation of the points with a exponential added to a first order polynomial. This calculation shows that after the resonance (for $E_{\text{cm}} \approx 350$ – $400\,\text{GeV}$) the cross section drops very quickly. This feature makes the low energy region an interesting field for studies dedicated to top quarks near the production threshold. Whereas the high energy region, more sensitive to variations of $t\bar{t}$ event statistics, would be favourable to searches for new physics signatures, such as $t\bar{t}$ pair plus missing energy, where the SM $t\bar{t}$ pairs would be the major background.

The total cross section for $t\bar{t}$ pair production at a centre of mass of 3 TeV, computed by calcHEP, is $(19,87 \pm 8 \cdot 10^{-4})$ fb. But this number does not correspond to the cross section that would be observed at a 3 TeV CLIC. As shown in sections 8.1.1 and 8.1.2,

effect and stays very low.

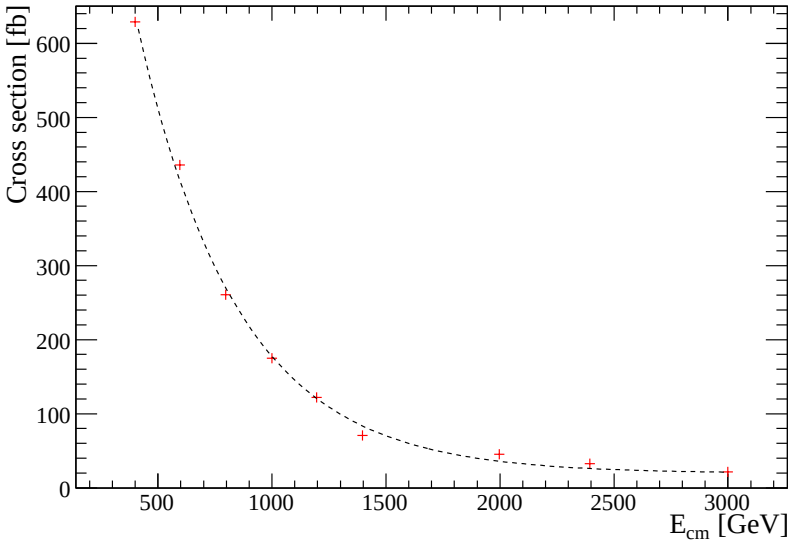

Figure 8.5: $e^+e^- \rightarrow t\bar{t}$ total cross section in function of centre of mass energy (interpolated with an exponential added to a first order polynomial).

the effective energy available in a 3 TeV e^+e^- collisions tends to be smaller than the nominal one because of electromagnetic energy losses of the incoming particles before the collision (ISR and BS). Therefore, according to the cross section dependency against centre of mass energy shown in figure 8.5, the average cross section of $t\bar{t}$ events in real 3 TeV e^+e^- collision will be higher than the raw prediction. The cross section predicted by calcHEP with ISR and BS are summed up in table 8.3. The nominal and conservative BS parameters are recalled in table 8.4. Table 8.3 illustrates well the impact of BS on the initial state: the dramatic increase of cross section is due to the large smearing of the initial collision energy, resulting from the beam-beam interaction at 2×1.5 TeV.

Table 8.3: Cross section of $t\bar{t}$ events for various level of electromagnetic initial state energy losses.

	σ [fb]
Raw	19.9
ISR included	26.2
ISR + Nominal BS	181.0
ISR + conservative BS	91.2

8.2.2 $t\bar{t}$ pair energy spectrum

The energy spectrum of the 3 TeV $t\bar{t}$ events produced at CLIC with nominal beam parameters, displayed in figure 8.6, presents a rather singular shape.The same shape is seen even more clearly when looking at the Monte Carlo (MC) centre of mass energy distribution of the $t\bar{t}$ events (figure 8.7).

Table 8.4: Beamstrahlung parameters for CLIC at 3 TeV

	Nominal	Conservative
$x + y$	46 nm	85 nm
z	44 μm	44 μm
Num. of part.	$3.72{\cdot}10^9$	$3.72{\cdot}10^9$
N_{cl}	3.47	1.88
Υ	4.89	2.65

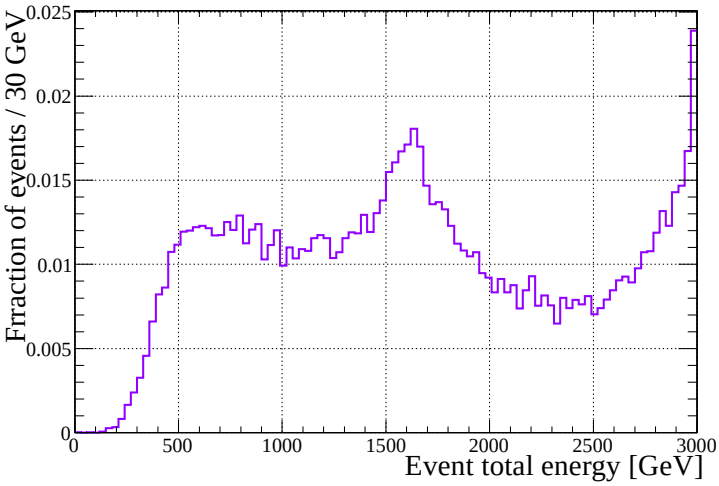

Figure 8.6: Total event energy spectrum of the $t\bar{t}$ events at CLIC (ISR and BS included).

The energy distribution of the colliding particles initial state has a shape close the one represented in figure 8.1 (p. 112) that might lead to expect a similar shape in the $t\bar{t}$ event energy spectrum. But such a shape corresponds to the energy spectrum of all the incoming $e^{\pm}$, regardless of the process or the final state of each event, whereas the spectrum of figure 8.7 corresponds to a selection of those collisions which have led to a $t\bar{t}$ event. Therefore, when the incoming particles collide at the nominal and most probable energy, the probability of obtaining a $t\bar{t}$ event is minimal (*cf.* figure 8.5). But when the centre of mass energy happens to be lower, the rate of $t\bar{t}$ events takes off. Thus, when considering a sample of $t\bar{t}$ events and checking at which centre of mass energy they have been produced, one will see that some of them have been produced at the nominal energy, whilst many of them at a much lower energy, due to a convolution between luminosity spectrum and cross section.

Now a second question arise: why is the secondary peak at about 1.5 TeV rather than around the $t\bar{t}$ resonance ($\approx$ 350 GeV). The explanation is due to the fact that the initial state energy losses (ISR and BS) occur independently for the two colliding particles. Therefore, since the most probable energy of the incoming particles is nearly the nominal one, significant reductions of the initial state energy are achieved, most of the time, when only one of the two incoming particles has lost a large amount of energy. This situation results in highly asymmetric collisions, where one initial particle is at

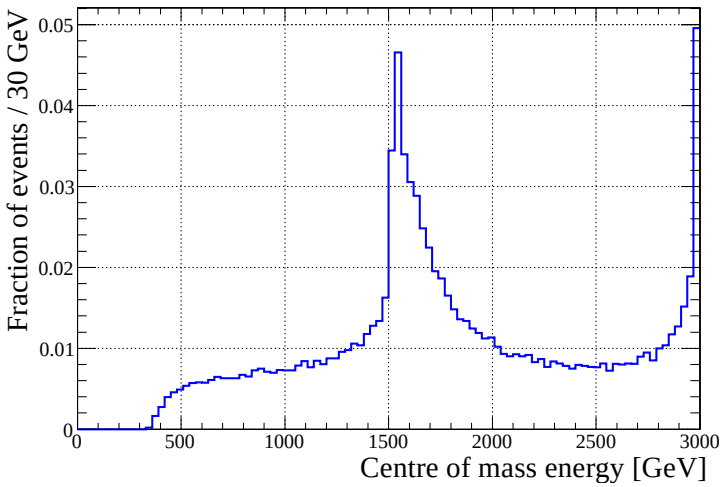

Figure 8.7: Initial energy spectrum of the $t\bar{t}$ events at CLIC (ISR and BS included).

nominal energy and the other one sometimes nearly at rest. Let $E_1 \approx 1500\,\text{GeV}$ be the energy of the first particle and $E_2 \ll E_1$ the energy of the second one. The resonance occurs when the effective centre of mass energy equals twice the top quark mass, *i.e.*:

$$4E_1E_2 = (2M_t)^2\,,$$

Which gives:

$$E_2 = \frac{M_t^2}{E_1} \approx 20\,\text{GeV}\,.$$

Therefore, in the laboratory reference frame the energy of such en event is $E_1 + E_2 = 1520\,\text{GeV}$ leading to the observed peak at 1.5 – 1.6 TeV of figure 8.7 and consequently the one observed in the event total energy spectrum of figure 8.6.

8.3 Top-tagging

In the framework of the CLIC Conceptual Design Report (CDR) preparation, $t\bar{t}$ events and other SM processes were simulated in detail. For the present study, the events were simulated at a nominal energy of 3 TeV and the simulation includes the ISR and the BS. Events were generated using WHIZARD [88] and a GEometry ANd Tracking, version 4 (GEANT4) [89] based program called MOKKA [90] was used to simulate the response of the CLIC_ILD detector[2]. Pythia 6 was used to simulate the propagation and the decay of the particles from the events generated by WHIZARD in the detector implemented in MOKKA. The data are then reconstructed using PandoraPFA [33] and Modular Analysis & Reconstruction for the LINear collider (MARLIN)[91]. All details about the simulation framework for the preparation of the CLIC CDR can be found in [92]

[2]CLIC version of the International Large Detector (ILD)

Using these data, a method to discriminate $t\bar{t}$ events from other SM processes is proposed. The method relies only on multi-variable analysis and no B-tagging[3] is used.

8.3.1 Background channels

In this section, the main background channels for a top quark study will be presented. To identify which physics channel would mimic the $t\bar{t}$ events, one identifies what characterises the final state of $t\bar{t}$ events, and then list all the physics processes with a significant cross section that would show similarities. The main characteristic of $t\bar{t}$ events relies on the top quark decay channel (only one observed so far):

$$t \to W^+ b\,, \tag{8.7}$$

which gives a six jet final state in case of hadronic decay of the W bosons, and a large number of particles. The $t\bar{t}$ events may also show some missing energy due to semi-leptonic decays of the B mesons coming from the hadronisation of the b quarks or in case of leptonic decay of the W bosons. The cross section of $t\bar{t}$ event in 3 TeV e^+e^- collision is ≈ 20 fb.

The background channels considered are the SM processes having a non negligible cross section together with some features comparable to $t\bar{t}$ events. They are listed as follow (cross sections are given for e^+e^- collision at 3 TeV computed with calcHEP [85]):

- $e^+e^- \to W^+W^-$ with $W^\pm \to hadr.$ is the largely dominant background channel because of its large cross section (212 fb in the hadronic decay modes) and a four jet structure with a high particle multiplicity and high hemisphere masses with tails ranging in the top quark mass vicinity.

- $e^+e^- \to W^+W^-Z^0$ with $W^\pm, Z^0 \to hadr.$ has the closest structure to $t\bar{t}$ events and a hadronic cross section of 10.3 fb.

- $e^+e^- \to Z^0Z^0$ with $Z^0 \to hadr.$ is very similar to the W^+ W^- events described in the first item, this process mainly just adds to the W^+ W^- background with a hadronic cross section of 12.4 fb.

- $e^+e^- \to b\bar{b}$ is a secondary background with a cross section of 10.2 fb.

8.3.2 Discriminative variables

The dominant background is the $e^+e^- \to W^+W^-$ process mainly in the case of hadronic decays of at least one of the $W^\pm$. Eighteen variables are used to discriminate the signal from the background, they are summarized in table 8.5. A few comments about them are given as follows.

[3] B-tagging consists of identifying the jets produced by B-mesons, their main characteristic is that they tend to emanate from a secondary vertex because of the "long" lifetime of B-mesons. The B-tagging can be useful to tag $t\bar{t}$ events since the top quark always decays into a b quark and a W. This method however becomes less powerful in the case of very boosted decaying top quarks since the b quark from the top decay tends to be very close to the W and not easily reconstructed.

- Number of particles: The number of reconstructed particles or Particle Flow Objects (PFOs). The reliability of Particle Flow Algorithm (PFA) is very important for this variable which happens to be the most discriminative one.

- Average cosine of polar angle: The average absolute value of the polar angle θ of all the reconstructed particles of the event. It also relies strongly on PFA reliability.

- Hemisphere related variables: All event particles are attributed to one or the other hemisphere. The hemispheres are separated by the plane orthogonal to the so-called event axis and containing the interaction point (IP). To each hemisphere corresponds then a four-vector from which the hemisphere related variables result. The two hemispheres are order in function of the energy they contain.

- Inclusive jets related variables: The event particles are clustered into jets using the k_t algorithm using a R parameter of 0.7[4]. See [93] for details about the k_t algorithm and other jet clustering algorithms. The resulting jets are sorted in decreasing order of energy. Inclusive jets (opposed to exclusive jets) result from the direct usage of the algorithm which gives a variable number of jets depending on the configuration of the event. Exclusive jets result from the attempt to constrain an event into a given number of jets, in this case the R parameter is recursively modified until the target number of jet is matched. The particle content of the exclusive jets depends on the type of k_t algorithm used. There are two of them, the "standard" k_t and the "*ee*" k_t which differ mainly in the definition of the exclusive jets. The *ee* algorithm clusters all the event particles into the requested number of jets, it is designed for application in the clean environment of e^+e^- collisions. Whereas the "standard" uses an additional so-called *beam jet* to which particles can be associated and discarded. The "standard" version is designed for hadronic collisions, where the beam jet is supposed to fetch all the beam remnants. The standard version happens to be very robust against CLIC $\gamma\gamma$ background (see section 8.1.3) and is therefore used instead of the *ee* algorithm.

- Event shape variables: They all relates to the generalised sphericity tensor eigenvalues λ_1, λ_2 and λ_3 with $\lambda_1 > \lambda_2 > \lambda_3$. The generalised sphericity tensor S^{ab} is defined as:

$$S^{ab} = \frac{\sum_i \left|\vec{p_i}^2\right|^{r-2} p_i^a \, p_i^b}{\sum_i \left|\vec{p_i}^2\right|}\,, \tag{8.8}$$

  with $a, b \in \{x, y, z\}$, $i \in \{event\ particles\}$ and p_i being the i^{th} particle momentum, r is a formal parameter used to tune the momentum power. The event shape variables used here are defined as follows:

  - Sphericity ($\mathcal{S}$): $r = 2$, $\mathcal{S} = 3/2(\lambda_2 + \lambda_3) \in [0, 1]$, $S = 0 \leftrightarrow$ pure di-jet event, $S = 1 \leftrightarrow$ isotropic event.

[4] Jet clustering associates together particles of the final state according to some distance definition and a distance threshold given here by the R parameter. Many algorithms exist and mainly differ by the definition of the distance.

Table 8.5: Summary of the discriminative variables used for $t\bar{t}$ event selection.

Variable	Description	Separation
`nPart`	Number of particles	6.773e-01
`cosTheta`	Average cosine of polar angle	2.640e-01
`jet1M`	Mass of hardest hemisphere	6.562e-01
`jet2M`	Mass of second hemisphere	3.271e-01
`jet1P`	Momentum of hardest hemisphere	3.712e-01
`jet2P`	Momentum of second hemisphere	1.473e-01
`jet1PT`	Trans. mom. of 1^{st} hemisphere	2.441e-01
`jet2PT`	Trans. mom. of 2^{nd} hemisphere	2.415e-01
`iJet1M`	Mass of hardest inclusive jet	4.350e-01
`iJet1P`	Mom. of hardest inclusive jet	2.996e-01
`iJet1PT`	Trans. mom. of 1^{st} inclusive jet	4.011e-01
`iJet2M`	Mass of second inclusive jet	4.253e-01
`iJet2P`	Mom. of second inclusive jet	3.402e-01
`iJet2PT`	Trans. mom. of 2^{nd} inclusive jet	3.865e-01
`coefC`	Event shape coefficient C	8.462e-02
`coefD`	Event shape coefficient D	3.062e-02
`sphericity`	Event sphericity	1.718e-01
`aplanarity`	Event aplanarity	1.196e-01

- Aplanarity ($\mathcal{A}$): $r = 2,\ \mathcal{A} = 3/2\lambda_3 \in [0, 0.5]$, $A = 0 \leftrightarrow$ plane event, $A = 0.5 \leftrightarrow$ isotropic event.
- C coefficient: $r = 1,\ C = 3(\lambda_1\lambda_2 + \lambda_1\lambda_3 + \lambda_2\lambda_3) \in [0, 1]$, C increases as the event tends to be closer to a perfect tri-jet
- D coefficient: $r = 1,\ D = 27\lambda_1\lambda_2\lambda_3 \in [0, 1]$, D increases as the event tends to be closer to a perfect quadri-jet.

Table 8.5 also shows the separation power of each variables, given for WW background separation. The C and D coefficient reveals themselves rather weakly discriminating, but as Boosted Decision Trees (BDTs) do not suffer from a high number of variables but rather benefit from every bit of information fed to them, those two variables have been kept in the analysis.

8.3.3 WW background rejection

The variables described above are fed to a BDT using the parameters given in table 8.6. The Toolkit for Multi-Variate Analysis (TMVA) [94] framework is used. See [95] for all tehnical details about BDTs and other multivariate algorithms. A total of 50 000 fully simulated $t\bar{t}$ events and as much of WW eventswere used for the training and testing of the BDT. The separation is illustrated by the BDT response distribution for signal and background displayed in figure 8.8 and the BDT performance is given in table 8.7.

Table 8.6: BDT parameters for $W^+ W^-$ events rejection.

Boost type	Adaptative
Number of trees	1000
Maximum depth	10
Minimum events per leaf	60
Prune method	Cost complexity
Prune strength	< 0 (auto)

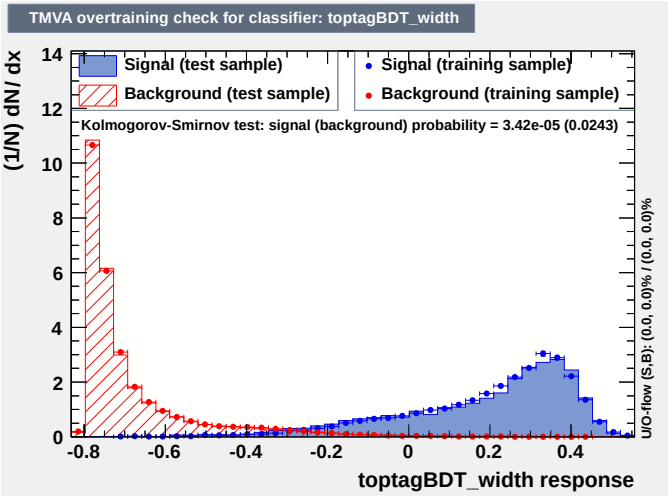

Figure 8.8: BDT response distribution for $t\bar{t}$ events and for WW events (all hadronic mode).

8.3.4 $t\bar{t}$ event selection performance

The selection cut should be able to reject much more than the WW background. Actually, the ZZ background should be rejected equivalently, the WWZ background should be significantly reduced and the $b\bar{b}$ background should be almost completely wiped out. This is illustrated in figure 8.9 where the BDT output spectra for $t\bar{t}$ signal and all the considered background are stacked. Each channel contribution is scaled to its cross section for an integrated luminosity of $275\,\mathrm{fb}^{-1}$. From the histograms of figure 8.9, the cut corresponding to the maximal significance (see definition in section 9.3) is found at 0.32. The statistics used, the cut efficiency and the event yield for each channel is given in table 8.8 together with the considered channel cross sections. The overall $t\bar{t}$ event selection efficiency of the method is 68.6% for a purity of 72.9%. For clarity, the top-tagging main performance is also given in lower part of table 8.7.

Résumé du chapitre

On décrira brièvement l'environnement des collisions e^+e^- à 3 TeV à CLIC, puis on résumera différents aspects des événements $t\bar{t}$ et enfin leur identification à CLIC.

Collision e^+e^- à 3 TeV et à CLIC La faible masse de l'électron le rend particulièrement sensible à divers phénomènes de perte d'énergie. D'une part, au moment de

Table 8.7: $t\bar{t}$ events selection performance. $\int$ ROC stands for the ROC curve integral, $S_{\max}$ denotes the maximal significance, cut $@S_{\max}$ denotes the BDT value leading to the cut with he highest significance. ϵ is the signal efficiency and B is the background efficiency, ϵ and B are evaluated for the specified cut.

Training/Testing performance	
$\int$ ROC	0.992
Application with all backgrounds	
$S_{\max}$	159
cut $@S_{\max}$	0.32
$\epsilon @ S_{\max}$	68.6%
purity	72.9%

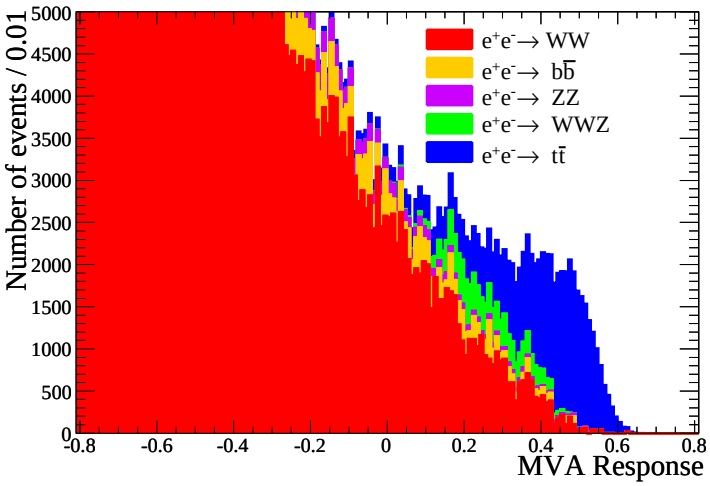

Figure 8.9: Stack of BDT response distributions for $t\bar{t}$ events and for all background channels (all decay channels included). Histograms are scaled to match their respective cross sections (computed by calcHEP) for an integrated luminosity of 275 fb^{-1}.

la collision les électrons peuvent émettre un photon et ainsi perdre une partie potentiellement importante de leur énergie. On parle de radiation de l'état initial (*Initial State Radiation* — ISR), le spectre de la fraction en énergie de l'électron après émission des ISR est représenté figure 8.1 (p. 112). D'autre part, en raison du grand nombre d'électrons par paquet lors des collisions, l'interaction d'une particule d'un paquet avec le champ électro-magnétique du paquet opposé occasionne une perte d'énergie supplémentaire. Le spectre en énergie dans le centre de masse des collisions reste piqué à la valeur nominale mais présente une large queue vers les basses valeurs où les collisions peuvent être hautement asymétriques. La grande quantité de photons émise lors de ces radiations provoque des réactions parasites (voir processus fig. 8.2 et table 8.2, p. 114 et 113 resp.). Le bruit de fond $\gamma\gamma \rightarrow$ hadrons peut s'avérer problématique en raison de l'impulsion transverse faible mais non négligeable (0.9 GeV/c en moyenne) des hadrons sortant d'une part, et d'autre part en raison de la cadence des collisions à CLIC (0.5 ns) superposant plusieurs

Table 8.8: Statistics for an integrated luminosity of 275 fb^{-1}, cut efficiency and event yield for each channel, cross sections for 3 TeV e^+e^- collision with ISR and CLIC BS as calculated by calcHEP are also given for each process.

Channel	cross section (fb)	Statistics	Efficiency (%)	Evt. yield
$e^+e^- \to t\bar{t}$	181	50000	68.6	34 300
$e^+e^- \to WW$	4145	1 139 875	0.64	7 295
$e^+e^- \to ZZ$	235	64 625	1.17	751
$e^+e^- \to b\bar{b}$	3370	926 750	0.14	1 297
$e^+e^- \to WWZ$	42	11 495	29.6	3 402

croisements de faisceau dans les données d'un seul événement et induisant ainsi une accumulation des hadrons parasites dans les calorimètres (voir illustration fig. 8.3, p. 115). Des coupures sur l'impulsion transverse ainsi que sur l'information temporelle sur les particules reconstruites permettent toutefois de grandement limiter l'impact de ce bruit de fond sur les analyses.

Le quark top à CLIC Le quark top se désintègre essentiellement en un boson W et un quark b. A son tour, le W se désintègre principalement soit en deux quarks légers soit en un lepton chargé et un neutrino. Les quarks finaux, s'hadronisant, conduisent chacun à un jet de particule dans l'état final. Les événement $t\bar{t}$ sont donc des événements présentant de 2 à 6 jets pouvant présenter de l'énergie manquante. Ils incluent typiquement un grand nombre de particules.

Le principal canal de production du quark top sous forme de paire $t\bar{t}$ est donné figure 8.4 (p. 115). Les principaux bruits de fond qui contaminent l'identification des événements $t\bar{t}$ sont les processus avec une section efficace de l'ordre de, ou supérieure à celle du signal, donnant un état final multi-jet, des jets lourds et un grand nombre de particules. La liste de ces canaux est donnée table 8.8 (p. 124) avec leur section efficace respective et celle du signal. On trouve dans cette même table les efficacités de sélection/réjection de chacun des canaux à l'issu de l'analyse.

L'analyse visant à identifier les événements $t\bar{t}$ parmi les différents bruits de fond est basée sur un algorithme multi-variable de type "arbre de décision" et un échantillon de données issus de simulations détaillées incluant les effets de machine et le détecteur, pour le signal et les bruits de fond. Ces données proviennent de la production officielle pour le CDR (*Conceptual Design Report*) de CLIC. Au total, 18 variables, résumée et décrites dans la table 8.5 (p. 121) sont utilisées pour parvenir à une efficacité de sélection de 68.6% pour une pureté de 72.9%.

À 3 TeV les produits de désintégration du top tendent à être très collimés et la reconstruction des jets tend à rassembler toutes les particules issus d'un quarks tops dans un même jet (*fat jet*). On notera aussi que le spectre en énergie totale des événements $t\bar{t}$ suit une distribution singulière (voir fig. 8.6, p. 117 et 8.7, p. 118) due à la convolution entre la distribution de l'énergie des électrons et positrons incidents et la section efficace de production des paires $t\bar{t}$ (fig. 8.5, p. 116).

Cette étude démontre l'observabilité du quark top à CLIC dans les collisions e^+e^- à 3 TeV et ouvre la porte à de nouvelles analyses telles que, par exemple, la recherche

d'un boson de jauge neutre additionnel léger décrite dans le chapitre suivant.

CHAPTER 9

Search for a light Z' in 3 TeV $t\bar{t}$ events

A specific new physics scenario is now considered. A brief outlook of the new physics landscape was sketched in section 1.3 and now, the studied model is introduced in section 9.1. A study of the cross section predictions of this model is detailed in section 9.2 with the aim to investigate the discovery potential of the particular Z' boson predicted by this model. Then, in section 9.4, follows a detailed generator level analysis where the sensitivity to this Z' is evaluated and a method for the measurement of its mass is established. In section 9.5, the informations from the detailed top tagging study performed in the previous chapter are used to correct the predictions from the generator level study of the Z'.

9.1 The Right Handed Neutrino Model

The reason why SM Dirac neutrinos[1] are not viable dark matter candidates is raised. A particular new interaction implying the existence of new heavy neutrinos, that would constitute good Dark Matter (DM) candidate, is then introduced.

The large coupling of SM Dirac neutrino to the Z^0 boson prevents them from providing the right DM relic density because of a much too high annihilation rate. If they however had the right relic density due to some non standard additional production process, the coupling to the Z^0 would as well have made them easily identified in direct detection experiments. In the model described in [97], another type of interaction for Dirac neutrinos is proposed involving a new neutral gauge boson coupling to the right handed states, a Z' boson that could come from an additional $U(1)'$ or $SU(2)_{\mathrm{R}}$. This Z' is suposed to have a small mixing with the SM Z^0 boson. In this model, called Right Handed Neutrino Model (RHNM), the right handed heavy Dirac neutrino, considered as

[1] Dirac neutrinos are opposed to Majorana neutrinos. Majorana particles are particle being their own anti-particle (like the photon). The exact nature of neutrinos is still unknown and depending on the model considered their are taken as Majorana or Dirac particles. Experiences like NEMO [96] are dedicated to the study of the nature of neutrinos.

a Weakly Interactive Massive Particle (WIMP) and denoted ν' in the following, becomes an interesting DM candidate because it has no coupling with the Z^0 (except through the small Z^0/Z' mixing). Therefore, with a suitable parametrisation, the model leads to the correct DM relic density and complies with the experimental direct detection constraints. The Z' may be observed at the Large Hadron Collider (LHC) [97] or at future linear colliders as studied hereafter. The Z' boson is supposed to couple mainly to the heaviest states of the SM, thus to the third SM fermion family. As top factories, the LHC and future linear colliders should be the best laboratories to discover and study those processes.

In the following, the work focuses on the Z' production in e^+e^- collisions. In the first section, a cross section study leads to the choice of the channel that will be studied at the generator level. The detailed analysis is done at a centre of mass energy of 3 TeV.

9.2 Cross section study

Three channels have been considered for the study of the Z' production. They are discussed below and their Feynman diagrams are displayed in figure 9.1. Cross sections have been computed using the software calcHEP (version 2.5.5) described in [85, 98] and references therein. The model is named: "RH_neutrino/RS-inspired". Centre of mass energy ranging from 0.5 – 3 TeV and Z' mass (MZ_P) from 200 GeV/c^2 to 3 TeV/c^2 have been considered. The out-going Z' boson decays in heavy leptons or in WIMPs. At this step, all model parameters have been taken to arbitrary default values (couplings at 1, Z'/Z^0 mixing at 1%).

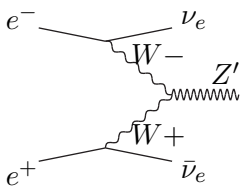

(a) $W^+\,W^-$ fusion: $e^+e^- \to \nu\bar{\nu}Z'$.

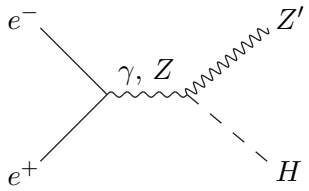

(b) "Pseudo-Higgsstrahlung": $e^+e^- \to HZ'$.

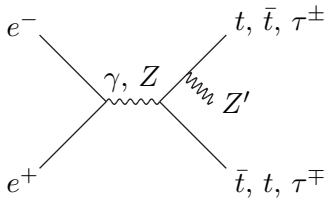

(c) Emission by an out-going fermion: $e^+e^- \to \tau^+\tau^-Z'$.

Figure 9.1: Z' production channels.

9.2.1 Channel $e^+e^- \to \nu\bar{\nu}Z'$

Figure 9.2 maps the Z' production cross section for the complete MZ_P and centre of mass energy ranges. Some values are tabulated in table 9.1. The values are computed with a 1% mixing. The dependency of the production cross section on the Z^0/Z' mixing is linear. The Z^0/Z' mixing and the Z' mass are the only non SM parameters involved in this process. The fact that the cross section keeps rising with the centre of mass energy tends to indicate a UV divergence. This hypothesis was verified by computing the cross section at energies up to 30 TeV. The result is plotted in figure 9.3 and clearly confirms the UV divergence. Therefore, this effective model is not appropriate to describe this process.

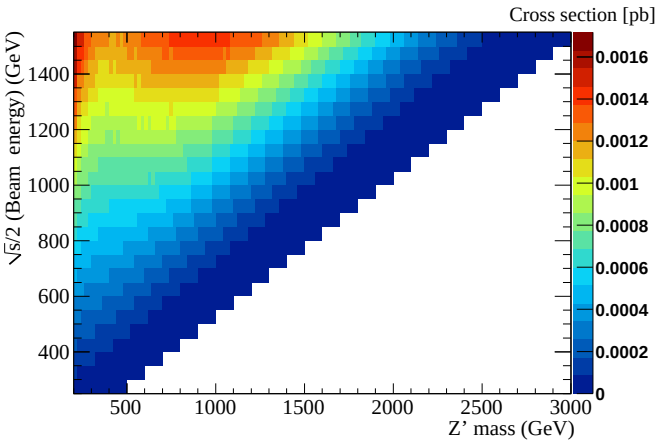

Figure 9.2: Map of the Z' cross section production in W^+ W^- fusion process.

Table 9.1: Cross section of the Z' production through W^+ W^- fusion.

MZ_P	200	500	1000
$\sqrt{s} = 3$ TeV	1.7 fb	1.2 fb	1.4 fb
$\sqrt{s} = 1$ TeV	0.27 fb	0.14 fb	—
$\sqrt{s} = 0.5$ TeV	0.05 fb	—	—

9.2.2 Channel $e^+e^- \to HZ'$

The Higgs boson mass has been set to 120 GeV/c^2. The cross section of the Z' production in this channels is mapped in figure 9.4 and tabulated in table 9.2. This process depends on the Higgs mass and Z' coupling to the Higgs boson as displayed in table 9.3. The dependency on the Higgs mass is mild but constitutes an extra parameter in the study. Provided the Higgs coupling to the Z' is not too low, this channel would have a large cross section and therefore this will be an interesting area of investigation when results about Higgs are made available by the LHC.

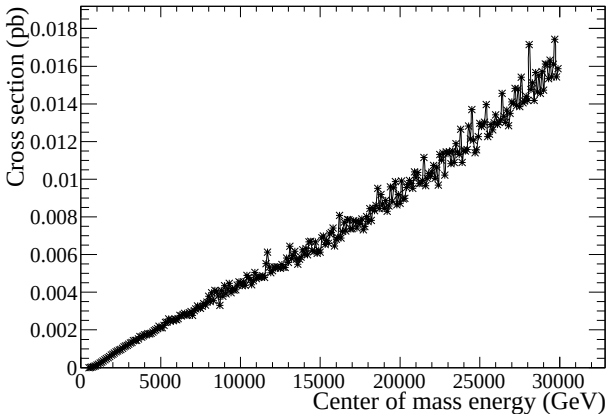

Figure 9.3: Divergence of the Z' cross section production in $W^+ W^-$ fusion process in the RHNM.

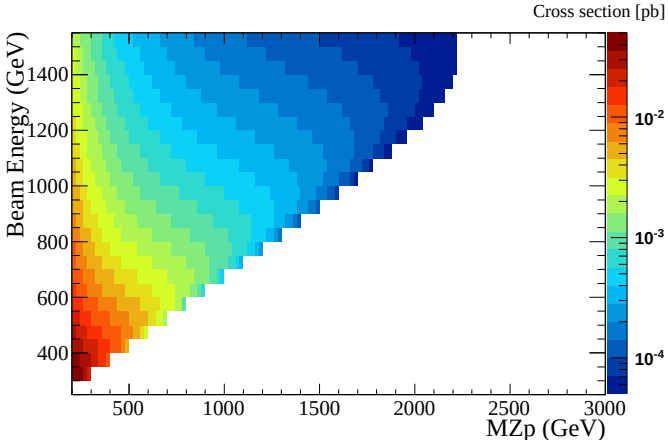

Figure 9.4: Map of the Z' production cross section *via* "pseudo-Higgstrahlung"

Table 9.2: Cross section of the Z' production through "pseudo-Higgstrahlung".

MZ_P	200	500	1000
$\sqrt{s} = 3$ TeV	2.2 fb	0.4 fb	0.2 fb
$\sqrt{s} = 1$ TeV	25.6 fb	8.1 fb	—
$\sqrt{s} = 0.5$ TeV	157.5 fb	—	—

9.2.3 Channel $e^+e^- \to \tau^+\tau^- Z'$

Figure 9.5 shows the maps of the Z' production *via* emission by an out-going top quark (figure 9.5(a)) or an out-going τ lepton (figure 9.5(b)). Cross section values are also tabulated in table 9.4. The behaviour of the Z' production cross section is very similar in both cases. The difference resides in the mass of the involved fermion. The cross section maps clearly indicate that the detection of a rather light Z' (below 1 TeV) is favoured.

Table 9.3: Cross section dependency on Higgs mass and Higgs coupling to the Z'.

H^0 mass	120	150	300
$gZH = 0.5$	6.4 fb	6.3 fb	5.2 fb
$gZH = 1$	25.6 fb	25.1 fb	20.8 fb
$gZH = 2$	102 fb	100 fb	83 fb

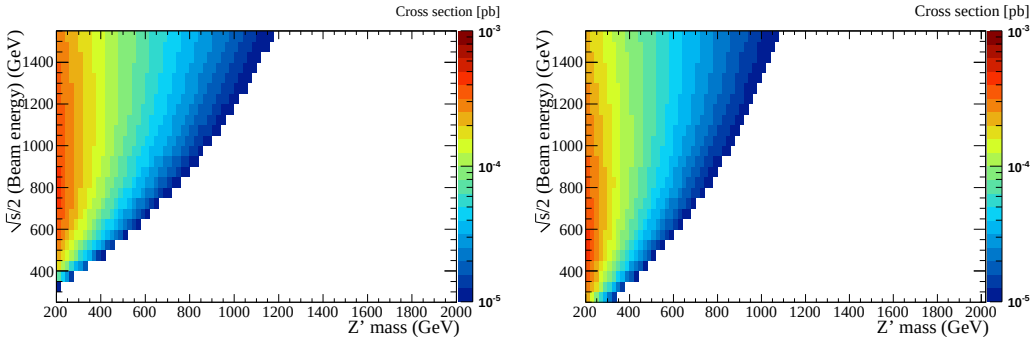

(a) case of an out-going top quark

(b) case of an out-going τ lepton

Figure 9.5: Map of the Z' production cross section *via* emission by an out-going fermion.

Table 9.4: Cross section of the Z' production *via* emission by an out-going fermion.

case of the top quark			
MZ_P	200	500	1000
$\sqrt{s} = 3$ TeV	3.4 fb	1.0 fb	0.2 fb
$\sqrt{s} = 1$ TeV	3.0 fb	0.04 fb	—
$\sqrt{s} = 0.5$ TeV	—	—	—
case of the τ lepton			
MZ_P	200	500	1000
$\sqrt{s} = 3$ TeV	2.5 fb	0.7 fb	0.1 fb
$\sqrt{s} = 1$ TeV	4.4 fb	0.2 fb	—
$\sqrt{s} = 0.5$ TeV	2.3 fb	—	—

9.2.4 Choice of the channel

The three channels considered to study the Z' production in high energy e^+e^- collisions have been discussed in the previous sections. Its production through W^+ W^- fusion has been discarded because of its UV divergence. The "pseudo-Higgsstrahlung" introduces extra parameters and its study should be resumed when the Higgs boson mass is measured (and if it actually exists). Moreover, the cross section is significantly larger at 500 GeV and therefore the study of this process would be a better case for International

Linear Collider (ILC). Remains the Z' production by emission from a fermion pair. The RHNM described in [97] is very general and a fixed set of parameter values based on physical arguments is needed. In [99] a parametrisation is proposed, where the Z' boson only couples to the SM only *via* the top quark. This argument has therefore driven the choice of the channel $e^+e^- \to t\bar{t}Z'$ for a detailed analysis. The modified parameters are summarized in table 9.5. The mass of the ν' does not influence the Z' cross section and therefore its precise value is not critical and must only be below $\mathrm{MZ_P}/2$. It appears, for $\mathrm{MZ_P} = 200\,\mathrm{GeV/c^2}$ and $m'_\nu = 85\,\mathrm{GeV/c^2}$, that this choice of parameter values gives the correct DM density and complies with the currrent experimental detection limits (see appendix D.1).

Table 9.5: Summary of the model parameters set to non default values.

parameter name	description	value
mixzzp	Z^0/Z' mixing	0.01
gZp	Z'- ν' coupling	3
gtr	Z'- t_R coupling	3
gUp	Z'- τ coupling	0
gtl	Z-$(t_\mathrm{L}, b_\mathrm{L})$ coupling	0
gll	Z'- τ coupling	0

9.2.5 Choice of the decay mode

The Z' boson has two decay modes:

1. $Z' \to$ invisible, where "invisible" stands for the DM candidate, since the model parameter settings have suppressed the other possibilities (if one neglects the effect of the small Z^0/Z' mixing).

2. $Z' \to t\bar{t}$, leading to four-top final states.

The corresponding total cross section and branching ratios times cross section are shown in table 9.6 for different mass of the Z'. The SM cross section for four-top events in e^+e^- collision at 3 TeV is about 20 ab. Thus, provided the four top events can be correctly tagged and reconstructed, this channel will have almost no background, but this scenario is very disfavoured by LHC data. For a DM candidate taken with a mass below $\mathrm{MZ_P}/2$, the decay of the Z' into $\nu'\bar{\nu}'$ will always be allowed. Therefore, for $\mathrm{MZ_P}$ below $2 \times m_\mathrm{top}$, the invisible decay channel will be the only available channel. In the following, the study focuses on the invisible decay of the Z'.

9.3 Event selection

The signal is the process $e^+e^- \to t\bar{t}Z'\,, Z' \to inv.$: after the e^+e^- interaction, one of the top is virtual and becomes on-shell by emitting a Z' more likely with a low energy, which in turn decays into WIMPs. Signal events therefore consist of multi-jet events

Table 9.6: Total process cross sections and Z' decay branching ratios times cross section.

MZ_P	Cross sect.	$\sigma_{Z'\to\text{inv.}}$	$\sigma_{Z'\to t\bar{t}}$
200 GeV/c^2	14.9 fb	14.9 fb	0
300 GeV/c^2	8.7 fb	8.7 fb	0
400 GeV/c^2	5.6 fb	2.4 fb	3.2 fb
500 GeV/c^2	3.7 fb	1.2 fb	2.5 fb
600 GeV/c^2	2.6 fb	0.8 fb	1.8 fb
700 GeV/c^2	1.8 fb	0.5 fb	1.3 fb

with a large number of particles and missing energy. It is expected to be very close to SM s-channel $t\bar{t}$ events which constitute the main background. The cross sections for different mass of the Z' are shown in table 9.6. The considered background processes are presented, then a method to discriminate the signal events is proposed.

9.3.1 Background

The signal is extracted from a sample of events tagged as $t\bar{t}$ events. In a first step, the tagging of the top events is assumed to have a full efficiency and purity. Therefore, the background considered for this study consists only of the SM inclusive $t\bar{t}$ events. The following background channels are leftover (total cross sections at 3 TeV):

- $e^+e^- \to W^+W^-$ (576 fb)
- $e^+e^- \to Z^0Z^0$ (32 fb)
- $e^+e^- \to W^+W^-Z^0$ (33 fb)
- $e^+e^- \to b\bar{b}$ (10 fb)

The present results shall then be scaled according to the realistic top tagging performance as studied in section 8.3.3 (p. 121).

Both s and t channels $t\bar{t}$ production are considered, their respective Feynman diagrams are displayed below.

1. background 1: $e^+e^- \to t\bar{t}$

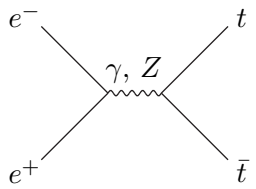

2. background 2: $e^+e^- \to t\bar{t} + \nu\bar{\nu}$

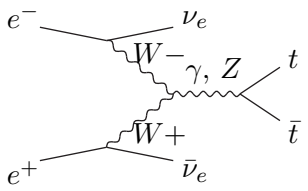

Their respective cross sections are summed up in table 9.7.

Table 9.7: background channel cross sections.

Channel	Cross sect.
$e^+e^- \to t\bar{t}$	19.87 fb
$e^+e^- \to t\bar{t} + \nu\bar{\nu}$	5 fb

9.3.2 Event generation

The program calcHEP was used to simulate the e^+e^- collisions and generate the resulting out-going particles. The information was stored in the "Les Houches Event" (LHE) format and fed to a Pythia8 instance [100, 101] which propagates and decays the particles.

The statistics generated correspond to the integrated luminosity of 1 ab^{-1}, *i.e.*: about three years of operation at a luminosity of about $10^{34}\,cm^{-2}\,s^{-1}$. In this study, the initial state energy spread takes into account the ISR only.

9.3.3 Discriminative variables

The final state variables listed in appendix D.5 were evaluated for each channel and their values were stored in a ROOT tree [102].

To give an intuitive idea of which variables are the most discriminating, the superimposition of the final state variables for the signal and the two backgrounds together with their correlations are displayed in appendix D.4 in the form of a correlation matrix with the variable spectra on the diagonal cells. Such a view leads to the conclusion that no direct cut on the variables would lead to a satisfactory separation between the signal and the two backgrounds. Some improvements are achieved by applying slanted cuts in the correlation planes of the variables, but no satisfactory discrimination is reached. The complexity of the problem together with the number of variables involved called for the use of Multi-Variate Analysis (MVA) tools. The TMVA framework [95, 103] offers many functionalities which are used in this study.

Background, as well as signal, events involve a $t\bar{t}$ pair. It is rather obvious that variables like jet masses, or the number of visible particles (or any particle counter from appendix D.3) will not discriminate between signal and background. The difference lies

rather in the event dynamics, shape and variables related to missing energy. The final variable set retained for performing the event selection is shown in the table of appendix D.5 and superimpositions of their spectrum for the signal and the two background channels, are displayed in appendix D.8.

9.3.4 Classifier training and testing

A BDT was trained separately on the two backgrounds. The training and testing have been done on 2×4500 events of each type. The input variables spectra are displayed in appendix D.8.1 for background 1, and in D.8.2 for background 2. The BDT settings are shown in table 9.8 and the performance of the training are given in table 9.9. The ROC integral is a good indicator of the classifier's performance but, in the present case, the most important aspect is the discriminating power of the classifier when cutting at the maximum significance. The significance is given by:

$$S = \frac{\epsilon\, N_{\text{signal}}}{\sqrt{\epsilon\, N_{\text{signal}} + B\, N_{\text{bg.}}}},$$

where ϵ is the signal efficiency at the given cut, N_{signal} is the total number of signal events, B is the background efficiency and $N_{\text{bg.}}$ the total number of background events. Table 9.9 shows that in our case the classifier gives good performance.

Table 9.8: BDT parameters

Boost type	Adaptative
Number of trees	1000
Maximum depth	20
Prune method	Cost complexity
Prune strength	90

Table 9.9: BDT performance. $\int$ ROC stands for the ROC curve integral, $S_{\max}$ denotes the maximal significance, cut $@S_{\max}$ denotes the BDT value leading to the cut with he highest significance. ϵ is the signal efficiency and B is the background efficiency, ϵ and B are evaluated for the specified cut.

	BDT-BG1 cut Sig. *vs* Bg1	BDT-BG2 cut Sig. *vs* Bg2
$\int$ ROC	0.955	0.971
$S_{\max}$	99.6	113.8
cut $@S_{\max}$	-0.0378	-0.3391
$\epsilon @ S_{\max}$	90.8%	97.4%
$B @ S_{\max}$	18.0%	14.6%

The BDT output for both discrimination steps are shown in figures 9.6(a) and 9.6(b) for signal *vs.* background 1 and signal *vs.* background 2 respectively. The outputs

computed with the training event sample are superimposed to those computed with the testing one. A small difference between the two spectra is noticeable and is reflected by the low Kolmogorov-Smirnov probability. This indicates a slight over-training of the algorithm. A higher prune strength can avoid this (a value of 95 instead of 90 is sufficient here) but at the price of lower separation even on the test sample. Therefore, it has been considered reasonable to tolerate this slight over-training. The global efficiency of the event selection is 0.884 ± 0.004.

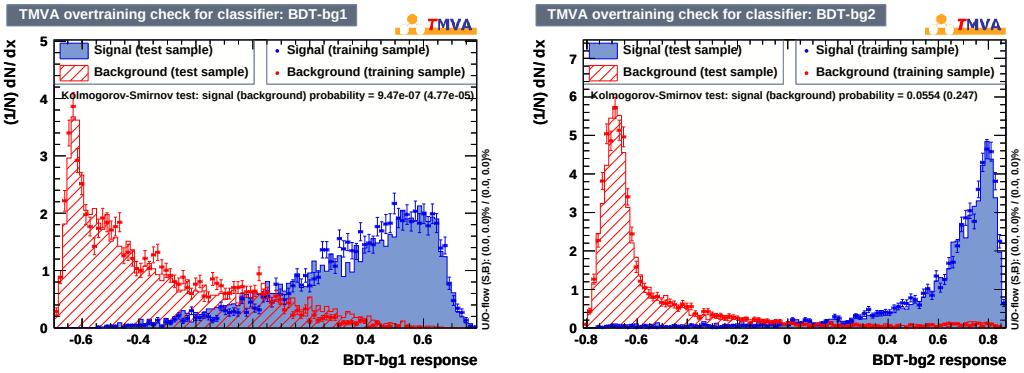

(a) (b)

Figure 9.6: Response of BDT trained for bg1 rejection (9.6(a)) and for bg2 rejection (9.6(b)) .

In the next section, the trained MVA methods are used to apply the two successive cuts given in table 9.9 on the different event samples to select the event sample from which the Z' production cross section and mass is to be measured.

9.4 Measurements

The Z' boson mass and the $e^+e^- \to t\bar{t}Z'$, $Z' \to inv.$ process cross section were measured subsequently to the event selection just described. A background subtraction is described below and applied before performing the mass and the cross section measurement as follows.

9.4.1 Z' mass measurement method

The mass of the Z' is measured using the event invariant mass spectrum obtained after the event selection described above. Given that the Z' decays to invisible and tend to be emitted at rest or very low energy, the event total invariant mass spectrum should show a sharp upper edge corresponding to the value of the nominal centre of mass energy of 3 TeV/c^2 minus the mass of the Z'. Nevertheless, the ISR induces a smearing of the event total invariant mass spectrum and then a smoothing of the spectrum upper edge. A function, called "smooth gate" in the following, defined in eq. 9.1, is fitted to the event total invariant mass spectrum without presence of the signal. This way the background contribution is modelled and is subtracted from the total spectrum. The area of the remaining spectrum is then proportional to the cross section of the $e^+e^- \to t\bar{t}Z'$ process

(see section 9.4.3). To measure the Z' mass, the "smooth gate" is fitted to this spectrum and the s_2 parameter, corresponding to the upper slope inflexion point, is related to $\mathrm{MZ_P}$ through the relation 9.4 established in section 9.4.2.2.

The "smooth gate" is defined as:

$$f(x) = \frac{A}{(e^{\frac{s_1-x}{p_1}}+1)(e^{\frac{x-s_2}{p_2}}+1)}, \tag{9.1}$$

where s_i, $i \in \{1,2\}$ are the inflection point abscissae and p_i, $i \in \{1,2\}$ are the slope steepnesses, see graphical representation with arbitrary values of the parameters in figure 9.7.

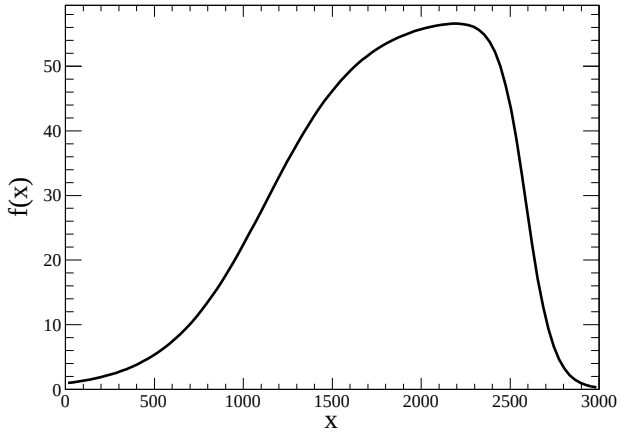

Figure 9.7: Smooth gate function with arbitrary parameter values.

After event selection, the cross section is calculated subtracting the background and correcting for event selection efficiency and then dividing by the $1\,\mathrm{ab}^{-1}$ luminosity.

9.4.2 Z' mass measurement results

The analysis procedure is detailed in the next seection for $\mathrm{MZ_P} = 200\,\mathrm{GeV}/c^2$. Then, in section 9.4.2.2, this analysis is repeated for several values of $\mathrm{MZ_P}$ and its measurement is described. Finally, in section 9.4.2.3, the resolution on the Z' mass is estimated.

9.4.2.1 Details for $\mathrm{MZ_P} = 200\,\mathrm{GeV}/c^2$

All events from the two backgrounds (20000 and 5000 for background 1 and 2 respectively) and the signal (15000) are tested with the two BDT cuts. The cut for background 2 rejection is applied first. The event invariant mass spectrum is plotted with the remaining events and displayed in figure 9.8. The contributions from the different sources are represented with different colours. The second background has almost vanished and the signal represents a clear excess with respect to the SM background.

The number of background events remaining after the Z' selection cut is 4714 ± 69. The background contribution alone is plotted in figure 9.9 and the "smooth gate"

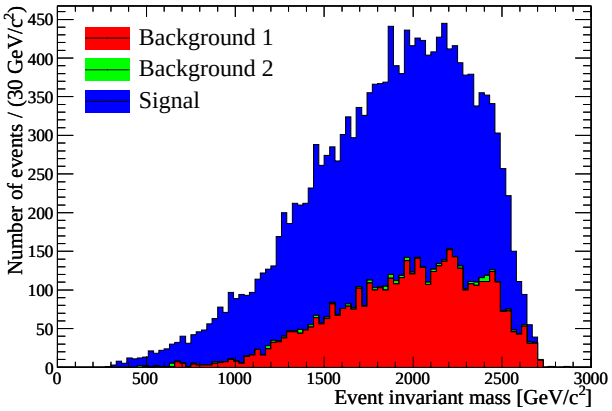

Figure 9.8: Event total invariant mass spectrum for signal and both backgrounds (MZ_P =200 GeV/c^2).

function is fitted to it. The fit results are displayed in figure 9.9 and summarized in table 9.10. The total histogram (corresponding to the addition of the three contributions of the stack histogram from figure 9.8) is corrected by removing from each bin the value returned by the fitted "smooth gate" function evaluated at the bin centre abscissa. The corrected histogram is displayed in figure 9.10 and the "smooth gate" is fitted to it. The corresponding fit results are displayed on the picture and summarized in table 9.11.

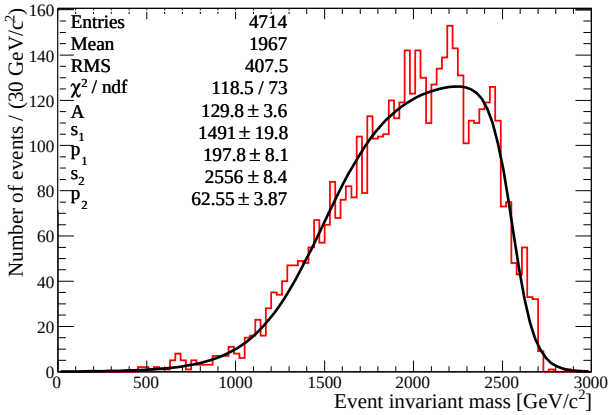

Figure 9.9: Event total invariant mass spectrum after event selection, for background only, fitted with the "smooth gate" function.

It may not be obvious at first glance how the Z' mass can be read from those fit parameters, but remember that $s_i\,, i \in \{1, 2\}$ are the inflexion point abscissae. With no smearing at all the upper limit of the spectrum would show a steep end-point at 3 TeV-MZ_P. This corresponds to the limit when p_2 goes to 0. Then p_2 can be considered as an indicator of the smearing strength. In the same view, s_2 would match $E_{CM} - MZ_P$ in the low smearing limit. Therefore, there should be a set of parameters relating s_2 to MZ_P as:

$$s_2 \quad = \quad k - \alpha MZ_P\,, \tag{9.2}$$

where k and α are parameters to determine.

Table 9.10: Fit results for background contribution.

χ^2/ndf	118.5/73
A	129.8 ± 3.6
s_1	1491 ± 19.8
p_1	197.8 ± 8.1
s_2	2556 ± 8.4
p_2	62.6 ± 3.9

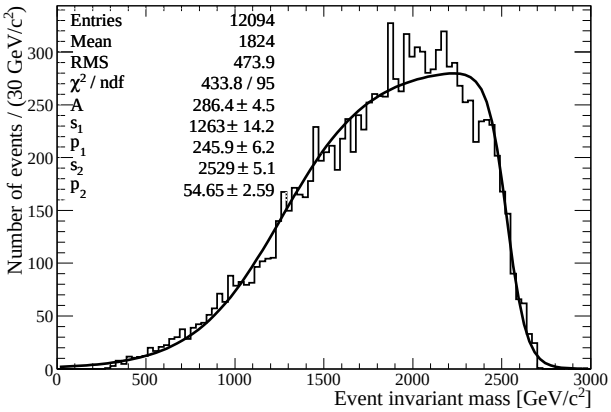

Figure 9.10: Event total invariant mass spectrum after event selection and background subtraction fitted with the "smooth gate" function for $\mathrm{MZ_P} = 200\,\mathrm{GeV/c^2}$.

Table 9.11: Fit results for the corrected event invariant mass spectrum.

χ^2/ndf	118.5/73
A	286.4 ± 4.5
s_1	1263 ± 15
p_1	245.9 ± 6.2
s_2	2529 ± 5.1
p_2	54.7 ± 2.6

In the next section, the same procedure was repeated for various values of $\mathrm{MZ_P}$ to determine the values of the parameters of eq. 9.2.

9.4.2.2 Sensitivity to $\mathrm{MZ_P}$

The procedure described in the previous section is applied for $\mathrm{MZ_P}$ from 200 to 700 GeV/c^2 with a constant statistics before Z' selection cut. The use of a constant statistics is meant to probe the s_2 dependence to $\mathrm{MZ_P}$ only. The resulting event invariant mass spectra are displayed in figure 9.11. Their fitted "smooth gate" upper inflexion point abscissa are summed up in table 9.12 and plotted in figure 9.12. This figure also shows how a straight line is fitted to the data point and the residuals are shown in the figure corner

histogram. The fit information allows to set values to the parameters in eq. 9.2 which now reads:

$$s_2 \quad = \quad (2757 \pm 8) - (1.05 \pm 0.02) \times \mathrm{MZ_P}\,, \tag{9.3}$$

which gives a direct formula for $\mathrm{MZ_P}$:

$$\mathrm{MZ_P} \quad = \quad \frac{(2757 \pm 8) - s_2}{1.05 \pm 0.02}\,. \tag{9.4}$$

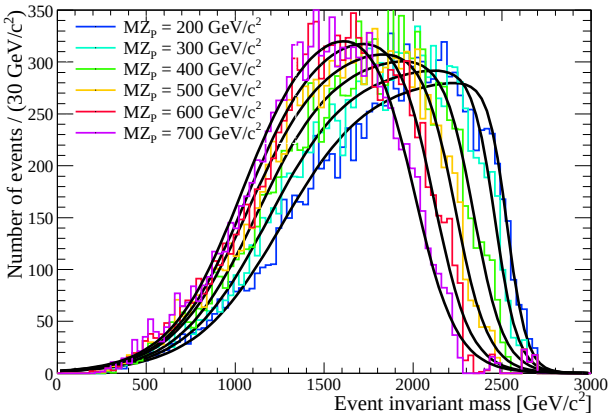

Figure 9.11: Event invariant mass spectra for various Z' masses.

Table 9.12: Summary of the "smooth gate" upper inflexion point abscissae (s_2).

$\mathrm{MZ_P}$	s_2
200	2530 ± 5.4
300	2458 ± 5.6
400	2340 ± 6.6
500	2235 ± 6.7
600	2119 ± 7.5
700	2005 ± 9.4

9.4.2.3 Resolution on $\mathrm{MZ_P}$

Using eq. 9.4, it is now possible to predict the Z' mass from a $t\bar{t}$ event invariant mass spectrum to which a "smooth gate" function is fitted (see definition in eq. 9.1). As $\mathrm{MZ_P} = (\mathrm{k} - \mathrm{s_2})/\alpha$, the error on $\mathrm{MZ_P}$ is given by:

$$\begin{aligned} \Delta\mathrm{MZ_P} \quad &= \quad \underbrace{\frac{\Delta k}{\alpha}}_{\substack{\text{constant}\\ \text{term}}} \oplus \underbrace{\frac{\mathrm{MZ_P}\Delta\alpha}{\alpha}}_{\substack{\text{linear}\\ \text{term}}} \oplus \underbrace{\frac{\Delta s_2}{\alpha}}_{\substack{\text{fit}\\ \text{term}}}\,. \\ &= \quad 7.8\,\mathrm{GeV}/c^2 \oplus 0.95\Delta s_2 \oplus 1.9\%\mathrm{MZ_P} \end{aligned} \tag{9.5}$$

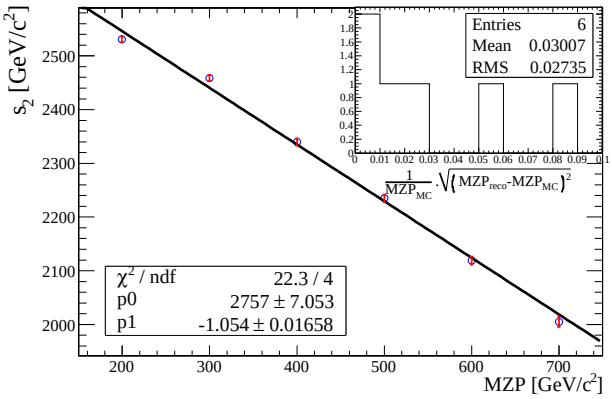

Figure 9.12: s_2 parameter *versus* MZ_P.

See appendix D.7 for the detailed calculation of this error.

The errors Δk and $\Delta\alpha$ are inherent to the measurement method itself. Hence, the constant and the linear term of eq. 9.5 describe systematic uncertainties. They may be reduced by refining the analysis on the s_2 dependency on MZ_P described in the previous section (9.4.2.2). For instance, using more statistics for each value of MZ_P and/or using more values of MZ_P constitute possible refinements. Whereas the error Δs_2 comes from the event invariant mass spectra fitted with the "smooth gate" function. Therefore, Δs_2 can only be improved by the accumulation of more statistics. Thus, the so-called "fit term" reflects the statistical uncertainty on MZ_P.

To evaluate the expected resolution on MZ_P, the statistics predicted by the model must be used. Table 9.13, for each mass of the Z' boson, shows the value of the s_2 parameter with its error and the resulting measured MZ_P. It appears here that above MZ_P =500 GeV/c^2 the event yield is not sufficient to perform a reliable fit and the s_2 returned values do not make sense any more, thus the Z' mass could not be measurable. Nevertheless, given that the considered SM background channels give about 4700 events after the Z' selection cuts, the Z' discovery may still be allowed up to about 700 GeV/c^2 in virtue of the obtained significance. The cross section measurement is presented in the next section.

Table 9.13: Z' mass measurement results

MZ_P (GeV/c^2)	s_2 (GeV/c^2)	Measured MZ_P (GeV/c^2)
200	2529 ± 6	217 ± 11
300	2448 ± 8	294 ± 13
400	2342 ± 20	395 ± 22
500	2282 ± 40	454 ± 40
600	2374 ± 69	365 ± 67
700	2527 ± 77	219 ± 74

Table 9.13 summarizes the value of the s_2 parameter with its error for each Z' mass and the corresponding measured mass deduced from relation 9.4. It appears that above about 500 GeV, the mass measurement is less precise and underestimates the true value. This effect even increases with MZ_P. The origin of this effect is that the

lower signal statistics at higher MZ_P makes the fit of the "smooth gate" more sensitive to background fluctuations and introduces a bias not taken into account by the MZ_P uncertainty formula (eq. 9.5). A bin to bin background subtraction may reduce this effect but the accumulation of more data would be the best solution to reduce it. However, the conclusion is that additionnal care must be taken for background subtraction to make this method reliable in the case of fewer than about 1000 events passing the selection cuts.

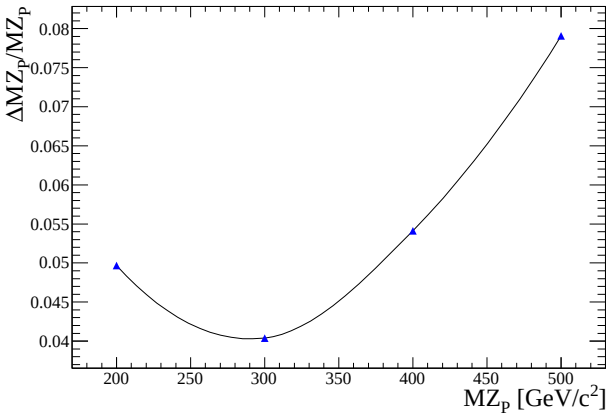

Figure 9.13: MZ_P error *vs.* MZ_P.

9.4.3 Cross section measurement

The cross section of the $e^+e^- \to t\bar{t}Z'$, $Z' \to inv.$ process is calculated as the number of events passing the Z' selection cut and surviving the background subtraction used for the mass measurement divided by the integrated luminosity of $1\,ab^{-1}$. The measured cross sections are shown in table 9.14. The present method tends to underestimate the process cross section for low MZ_P and slightly over-estimate it at higher values.

Table 9.14: Z' cross section measurement results.

MZ_P	True cross sect.	events yield	significance	Measured cross sect.
200	14.9 fb	12094 ± 110	92.7	13.7 ± 0.2 fb
300	8.7 fb	7411 ± 87	66.6	8.4 ± 0.1 fb
400	2.4 fb	2150 ± 47	24.6	2.4 ± 0.1 fb
500	1.2 fb	1192 ± 35	13.5	1.3 ± 0.1 fb
600	0.8 fb	815 ± 29	8.4	0.9 ± 0.1 fb
700	0.5 fb	642 ± 26	5.6	0.7 ± 0.1 fb

9.5 Performance estimation with full detector simulation

One of the reason why the study presented above was first done at the generator level was because the RHNM was not implemented in the CLIC CDR simulation framework. Originally, the plan was to smear the generator level data to get realistic results. The problem is that the large number of variables used and their correlations makes a realistic smearing very difficult. The various methods that have been tested are summarised in appendix E with their respective advantages and drawbacks. None of them gave really satisfactory results. Moreover, if an appropriate smearing was found using the fully simulated background data, it can not be easily applied to calcHEP data because of some approximations that are made in calcHEP concerning the BS that may not be valid at energies as high as 3 TeV [104]. In calcHEP, the BS seems underestimated which leads to a strong bias in the total event energy spectrum, as shown on figure 9.14. This bias would largely overestimate the missing energy related variables and prevent the Z' event selection to work.

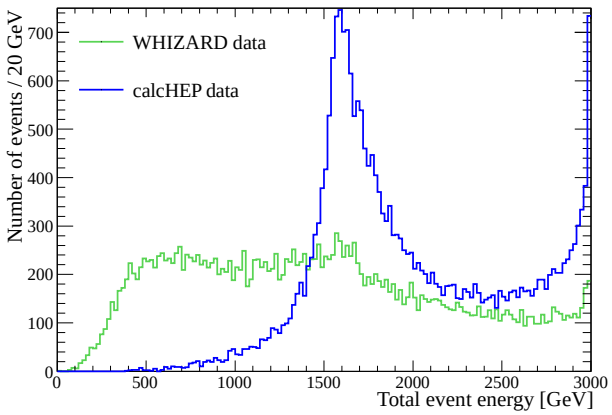

Figure 9.14: Total event energy spectra for data from both generators.

Finally, the $t\bar{t}$ event selection described in section 8.3, based on full detector simulation were used to apply corrections leading to corrected significance values. The following procedure is applied:

- The Z' event selection is performed at generator level, assuming full top-tagging efficiency and purity.

- The Z' event yield is reduced according to the $t\bar{t}$ event selection efficiency of 68.6%.(see section 8.3.4, p. 122).

- The total background for the Z' study corresponds to all the channels involved in the top-tagging study (signal and background). The number of background events after $t\bar{t}$ event selection is estimated from the top-tagging study for a 1 ab^{-1} integrated luminosity using table 8.8 (p. 124).

- This number is then scaled down according to the Z' event selection background

rejection of 82% (see table 9.9, p. 135, displaying the s-channel background contamination of 18%) resulting in a value of $13\,339 \pm 115$.

The corrected significances for various Z' masses are displayed in table 9.15.

In view of the corrected significances, a discovery of the studied Z' is possible for a $1\,\text{ab}^{-1}$ integrated luminosity if its mass is below about $600\,\text{GeV}/c^2$. The Z' mass measurement window is likely to be reduced from $[200, 500]\,\text{GeV}/c^2$ to $[200, 400]\,\text{GeV}/c^2$, corresponding to the mass window where the significance is above 10. A complete simulation of the Z' events and a refined Z' event selection procedure including all the SM background channels listed in section 8.3, may lead to more precise results and better performance. Such a refined analysis would be mandatory if the LHC happen to discover hints of new physics in the search for massive invisible particles (like graviton search [105] in which a massive invisible particle is actively searched).

Table 9.15: Z' signal significance correction using the $t\bar{t}$ event selection performance. Statistics are based on a $1\,\text{ab}^{-1}$ integrated luminosity. Z' cross sections are calculated using calcHEP with ISR and CLIC nominal BS.

MZ_P	σ (fb)	Event yield	Corrected significance (uncorreceted)
200	13.07	7 929	54.4 (92.7)
300	5.35	3 246	25.2 (66.6)
400	2.65	1 608	13.2 (24.6)
500	1.45	880	7.4 (13.7)
600	0.86	522	4.4 (8.5)
700	0.53	321	2.7 (5.6)

Résumé du chapitre

Dans ce chapitre, un modèle particulier de physique au delà du Modèle Standard est envisagé. Il s'agit d'un modèle effectif non-supersymétrique, proposant une solution alternative au problème de la matière noire dans les théories de Randall et Sundrum. La phénoménologie qui en découle ne se limite cependant pas à ces modèles et implique notamment un boson de jauge neutre additionnel Z' couplant aux particules d'hélicité droite ainsi qu'une particule ayant les propriétés d'un neutrino d'hélicité droite ν' qui devient dans ce contexte un bon candidat pour la matière noire. On se propose d'étudier ce Z' à travers des simulations de physique au niveau générateur.

Le choix de paramètres considéré implique que la seule particule du Modèle Standard couplant directement au Z' soit le quark top d'hélicité droite, un faible couplage avec le reste des particules du Modèle Standard est possible à travers un faible mélange entre le boson faible Z^0 et le Z'. Le canal privilégié pour cette étude est donc la production de paires $t\bar{t}$ où l'un des tops, d'abord virtuel, émet un Z' afin de retourner sur sa couche de masse (voir diagramme fig. 9.1(c) p. 128). Le Z' ainsi émis peut se désintégrer soit en paire $\nu'\ \bar{\nu}'$ soit en paire $t\bar{t}$ si sa masse est suffisante. On se focalisera sur l'étude du cas $Z' \to \nu'\bar{\nu}'$ où l'état final consiste en événements $t\bar{t}$ présentant de l'énergie manquante.

On cherchera tout d'abord à séparer le signal Z' d'événements $t\bar{t}$ purement standards avec et sans énergie manquante (*cf* diagrammes p. 133). Cette sélection se fait à l'aide

d'un algorithme multi-variable de type "arbre de décision". Au total, 13 variables sont utilisées, basées sur l'énergie manquante ou la géométrie de l'événement, énumérées et décrites dans la table en appendice D.5. Une coupure est réalisée sur chaque bruit de fond pour une efficacité totale de 88.4%. Le bruit de fond rémanant pourra être modélisé et soustrait.

Le spectre de la masse totale du système $t\bar{t}$ est utilisé pour pratiquer une série de mesures. Après les coupures de sélection, la contribution du bruit de fond peut être évaluée, modélisée et enfin soustraite afin de mesurer la section efficace du processus étudié. La mesure comparée au calcul direct est donnée dans la table 9.14 p. 142, une découverte du boson Z' est envisageable jusqu'à une masse d'environ 700 GeV/c^2 dans le cadre du modèle étudié. Ce spectre permet aussi de mesurer la masse du Z' si la statistique disponible est suffisante (baisse de fiabilité pour moins d'environ 1000 événements $t\bar{t}$ Z'). Pour ce faire, la fonction (eq. 9.1, représentation graphique fig. 9.7, p. 137) utilisée pour la modélisation de la contribution au bruit de fond est à nouveau utilisée et ajustée sur le spectre où la contribution du fond a été soustraite. Le point d'inflexion supérieur de la courbe ainsi obtenue est directement lié à la masse du Z' (voir fig. 9.11 et 9.12, p. 140 et 141) par la formule 9.4 avec une résolution estimée par propagation des erreurs sur les différents paramètres donnée par la formule 9.5. La résolution attendue est meilleure que 8% sur toute la gamme de masse du Z' étudiée avec un optimum d'environ 4% autour de 300 GeV/c^2 et un biais tendant à une sous-estimation de la masse si celle-ci est élevée. Ce biais, du aux fluctuations statistiques du bruit de fond, n'est pas pris en compte dans l'estimation de la résolution.

Cependant ces résultats sont un peu idéalisés. En effet, étudier la séparation des événements Z' des événements $t\bar{t}$ standards revient à supposer une parfaite sélection des événements $t\bar{t}$. Or nous avons vu au chapitre précédent qu'une efficacité de 69% et une pureté de 73% étaient envisageables. L'étude du Z' au niveau générateur s'est faite sans simulation du beamstrahlung, celle-ci n'étant pas optimisée dans calcHEP pour les conditions de CLIC, Pour cette raison, les données complètement simulées et les données au niveau générateur sont très difficilement mélangeables. De ce fait, les performances de sélection des événements $t\bar{t}$ peuvent seulement être utilisées pour corriger les significances obtenues en fonction de la masse du Z'. Cette correction se fait en réduisant le nombre d'événements $t\bar{t}$ et $t\bar{t}$ Z' de l'efficacité de sélection des événements $t\bar{t}$ et ensuite en augmentant le nombre d'événements de bruit de fond utilisé dans le calcul de la significance en fonction de la pureté de la sélection $t\bar{t}$ (voir résultats table 9.15, p. 144). On observe une diminution de la significance d'un facteur proche de 2 diminuant le potentiel de découverte du Z' étudié à la gamme de masse 200 – 500 GeV/c^2 (significance supérieure à 7).

CHAPTER 10

Conclusion

The collision environment at CLIC has been described. The smearing of the initial state due to electromagnetic interaction between incoming particles (ISR) and between incoming bunches (BS) has been presented. The machine induced backgrounds have also been described, the most problematic one beeing the $\gamma\gamma \rightarrow hadrons$ process.

The main top physics issues have been sketched and the production condition of $t\bar{t}$ events at CLIC have been depicted. The work has been done on fully simulated events of 3 TeV e^+e^- collisions at CLIC with CLIC ILD detector. A method for $t\bar{t}$ event selection at the detector level, based on multivariate analysis, has been proposed and showed a signal efficiency of 68.6% for 99.2% of WW background rejection regardless of the $t\bar{t}$ pair decay mode. This performance indicates that $t\bar{t}$ events can be selected with a good purity without major loss of signal. The WW rejection allows as well to cut the ZZ and $b\bar{b}$ backgrounds and also reduce the WWZ background to finally achieve a purity of the $t\bar{t}$ event sample of 72.9%.

A glimpse of the new physics landscape have been given to introduce a specific Randall-Sundrum-inspired New Physics scenario predicting a new vector boson denoted Z' and a dark matter candidate in the form of a heavy right handed neutrino. The new physics signal was extracted from samples of SM $t\bar{t}$ events. The study focused on the $e^+e^- \rightarrow t\bar{t}Z'$ channel at a centre of mass energy of 3 TeV, with the Z' decaying into WIMPs. The study was done at generator level. The proposed event selection method shows an efficiency of 88.4% and a background rejection above 80% for the two background channels considered, namely the s and t channel SM $t\bar{t}$ events. An excess over the background is measurable for Z' masses ranging from 200 to 800 GeV. For Z' masses below 500 GeV, the mass can be measured with an uncertainty better than 8% and with an optimum around 300 GeV of 4%. The full detector simulation of the SM background channels has allowed to correct the results obtained with generator level simulation. The maximum measurable Z' mass is decrease to about 400 GeV/c^2 instead of 500 GeV/c^2 and the discovery potential becomes very low above 600 GeV/c^2 (significance below 5). However, the detector level study of the background give rather conservative resultsand real performance should then lie between the raw and the corrected performance.

Many refinements of the presented analysis are possible. Concerning the tagging of $t\bar{t}$ events: a B-tagging information may improve the tagging of the less boosted top quarks and a jet sub-structure analysis can improve the tagging of highly boosted top quark jets (for hadronic decay modes). In a near future, the CLIC simulation framework will provide the possibility to fully simulate and reconstruct Z' events. A new study for signal and background, including the improvements listed above, could lead to better performance of the Z' cross section and mass measurement.

Différents aspects des collisions e^+e^- à haute énergie ont été abordés dans le contexte de l'expérience CLIC. Des pertes significatives d'énergie des particules incidentes conduisent à de grandes fluctuations de l'énergie initiale. Les interactions entre les photons ainsi générés produisent de grandes quantités de particules parasites dont des hadrons pouvant polluer significativement le signal relevé dans les détecteurs.

*Dans cet environnement, par des simulations détaillées, la production de paires quark/anti-quark top a été étudiée et la sélection des événements $t\bar{t}$, parmi une série de canaux de bruits de fond (WW, ZZ, $b\bar{b}$, WWZ), par une approche multi-variable, a été évaluée. Une efficacité de 68.6% ainsi qu'une pureté de l'échantillon final de 72.9% ont été déterminées démontrant aisni l'observabilité du quark top auprès de CLIC, à 3*TeV*.*

*Un modèle de physique au delà du modèle standard, prédisant notamment un boson Z' ainsi qu'un candidat de matière noire couplé à celui-ci, a été considéré. La détection de ce Z' décroissant en particules de matière noire a été étudiée au niveau générateur. Le canal étudié ($e^+e^- \rightarrow t\bar{t}Z'$, $Z' \rightarrow \nu'\bar{\nu}'$) consiste en une production de paires $t\bar{t}$ présentant de l'énergie manquante. Une méthode de sélection de ces événements parmi des événements $t\bar{t}$ purement standards, basée sur des algorithmes multi-variables, a été établie. Une efficacité de 88.4% sur le signal a été atteinte. Le bruit de fond irréductible est ensuite modélisé et retranché du spectre de la masse invariante du système $t\bar{t}$ permettant à la fois de mesurer la section efficace du processus observé et la masse de la particule invisible émise. On observe toutefois quelques biais dus aux fluctuations du bruit de fond. La section efficace tend à être légèrement sous-estimée pour une faible masse du Z' et légèrement surestimée pour les plus hautes masses. De même, la masse du Z' tend à être sous-estimée au delà d'environ 500*GeV/c^2*. En dessous de cette valeur, la résolution sur la masse du Z' est meilleure que 8% avec un optimum de 4% autour de 300*GeV/c^2*.*

*Dans l'incapacité d'utiliser des données Z' complètement simulées, à l'instar des données de l'étude du quark top, une situation idéale aurait été d'utiliser ces dernières pour le bruit de fond de l'étude du Z' et d'appliquer un ajustement des données Z' pour mimer les effets de bruit de fond machine et de résolution des détecteurs. Mais une différence dans la simulation du beamstrahlung, et par conséquent dans le spectre de l'énergie de centre de masse des événements, rendait une telle combinaison des données impossible. Ainsi, seule une simple correction des significances du signal Z', basée sur les performances de sélection des événements $t\bar{t}$ peut être appliquée à une étude du Z' au niveau générateur avec les canaux de production de paire $t\bar{t}$ comme bruit de fond de référence. Cette correction conduit à une diminution de moitié environ des significances attendues réduisant l'observabilité du Z' à la fenêtre 200 – 500*GeV/c^2*. D'autres dégradations du même ordre sont à prévoir, mais ne peuvent être évaluées avec les moyens disponibles lors de ces travaux.*

Appendices and back matter

APPENDIX A

MICROMEGAS signal computation

The following sketch represents the MICRO MEsh GAseous Structure (MICROMEGAS) amplification gap, of thickness g, with a mesh voltage V_0:

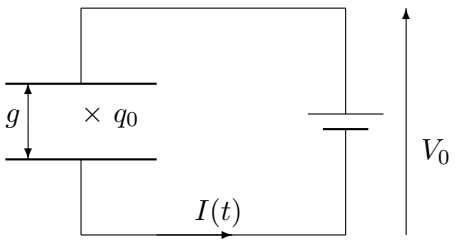

Charge induced on the anode by a moving charge. This computation is usually done by applying the method of Shockley and Ramo [106, 107] based on the Green's reciprocity theorem. This method is relevant if the moving charges are brought to induce current on various electrodes like thin strips or wires. In the present case, as electrons are moving in front of large pads of $\approx 1\,\mathrm{cm}^2$, it is reasonable to approximate that all the signal from one incoming electron is induced on only one pad. Therefore another, but equivalent, way to perform this calculation is used here. Inspired from [108], it is based on a simple energy conservation principle and is thought to be more intuitive. Even though the final results are compatible to others in the literature (see [42, 109, 110] for instance).

The energy required to move a charge q_0 from x to $x + dx$ in an electric field E is given by:

$$\begin{aligned} dW &= q_0 \, \vec{E} \cdot \vec{dx} \\ dW &= q_0 \, \frac{V_0}{g} \, dx \, . \end{aligned} \tag{A.1}$$

The movement of q_0 initiates a current $I(t)$ that must be conserved throughout the circuit. It relates directly to the movement of q_0 by the expression of its energy:

$$\begin{aligned} dW &= P\,dt \\ dW &= V_0\,I(t)\,dt \\ dW &= V_0\,dQ_{\text{in}}\,, \end{aligned} \tag{A.2}$$

where P is the power and dQ_{in} is the charge put in movement along the circuit. Thus one get, by identifying A.1 and A.2:

$$q_0\,\frac{V_0}{g}dx = V_0\,dQ_{\text{in}} \tag{A.3}$$

$$ie:\ dQ_{\text{in}} = \frac{1}{g}\,q_0(x)\,dx\,. \tag{A.4}$$

The total charge induced on the anode plane by a MICROMEGAS cascade is then given by:

$$\begin{aligned} Q_{\text{in}} &= \frac{1}{g}\int_0^g q_0(x)\,dx \\ Q_{\text{in}} &= \frac{1}{g}\int_0^g q_-(x) + q_+(x)\,dx\,, \end{aligned} \tag{A.5}$$

where $q_-(x)$ stands for the electron contribution and $q_+(x)$ for the ion one.

Number of moving charge in the amplification gap. The charge $q_\pm(x)$ relates to the number of moving charge $n_\pm(t)$ *via*:

$$q_\pm(x)\,dx = -e\,n_\pm(t)\,v_\pm\,dt\,, \tag{A.6}$$

where e is the elementary electric charge and $v_\pm$ the average speed of the electrons/ions. Note that the minus sign holds for both electron and ion contributions, it comes from electron charge on the one hand, and from the ion speed on the other hand. The speed of ions is at least two order of magnitude below the electron one.

Let T_- be the time for the electrons to cross the amplification gap and get collected on the anode and T_+ be the time for the ions to drift towards the mesh and get collected. T_+ will coincide with the total duration of the MICROMEGAS signal.

Following the gas amplification model described in section 3.2.2 (page 44), the number of electron $n_-(t)$, for $t < T_-$, is given by:

$$n_-(t) = n_0\,e^{\alpha v_-\,t}\,, \tag{A.7}$$

where it is assumed that all electrons are collected at the same time T_-. The number of ions results from two contributions:

- creation along the path of the electrons,
- collection as they progressively reach the mesh.

thus, for $t < T_-$:

$$n_+(t) \;=\; \underbrace{n_0\, e^{\alpha v_-\, t}}_{\text{creation}} - \underbrace{n_0\, e^{\alpha v_+ t}}_{\text{collection}} \tag{A.8}$$

and for $t > T_-$:

$$n_+(t) \;=\; \underbrace{n_0\, e^{\alpha g}}_{\text{creation over}} - \underbrace{n_0\, e^{\alpha v_+ t}}_{\text{collection}} . \tag{A.9}$$

Total induced charge. From the relations A.5 and A.7 to A.9 one can compute the induced charge as function of time (note that $v_\pm/g = T_\pm$):

$$Q_{\text{in}}(t) \;=\; \frac{-e\, n_0}{g} \int_0^t \left[v_-\, n_-(t) + v_+\, n_+(t)\right] dt \tag{A.10}$$

The cases $t < T_-$ and $t > T_-$ must be treated separately:

- $t < T_-$:

$$Q_{\text{in}}(t) \;=\; \frac{-e\, n_0}{g} \int_0^t (v_- + v_+)\, e^{\alpha\, v_-\, t} + v_+ e^{\alpha\, v_+\, t}\, dt\,,$$

by integrating and applying the approximation $v_- \gg v_+$ or equivalently $T_+ \gg T_-$:

$$Q_{\text{in}}(t) \;\overset{v_- \gg v_+}{\approx}\; -\frac{e\, n_0}{\alpha\, g} \left(e^{\alpha\, v_-\, t} - e^{\alpha\, v_+\, t}\right) \tag{A.11}$$

- $t > T_-$:

$$Q_{\text{in}}(t) \;=\; Q_{\text{in}}(T_-) + \underbrace{\frac{e\, n_0\, v_+}{g} \int_{T_-}^{T_+} \left[e^{\alpha\, g} - e^{\alpha\, v_+\, t}\right] dt}_{\mathcal{A}}\,,$$

after integration one have to cancel a term $\frac{-e\, n_0}{\alpha\, g} e^{v_+\, T_-}$ then:

$$\mathcal{A} \;\overset{T_+ \gg T_-}{\approx}\; -e\, n_0 \left(e^{\alpha\, g} \frac{t}{T_+} - \frac{1}{\alpha\, g} e^{\alpha\, v_+\, t}\right)$$

which gives:

$$Q_{\text{in}}(t) \;=\; -e\, n_0 \left(e^{\alpha\, g} \frac{t}{T_+} + \frac{1}{\alpha\, g} \left(e^{\alpha\, g} - e^{\alpha\, v_-\, t}\right)\right) \tag{A.12}$$

Evaluating equation A.12 at $t = T_+$, one get the total charge induced on MICROMEGAS anode plane.

$$Q_{\text{TOT}} = Q_{\text{in}}(T_+) = -e\, n_0 e^{\alpha\, g}\,. \tag{A.13}$$

One can also consider the amount of signal due to the electrons by evaluating equation A.11 at $t = T_-$ and get:

$$Q_{\text{e}} = Q_{\text{in}}(T_-) = \frac{-e\, n_0}{\alpha\, g} e^{\alpha\, g}\,. \tag{A.14}$$

Note that the relative contribution of the electron is given by:

$$\eta_{\text{e}} = \frac{Q_{\text{e}}}{Q_{\text{TOT}}} = \frac{1}{\alpha\, g} = \frac{1}{ln(G)}\,. \tag{A.15}$$

APPENDIX B

$t\bar{t}$ production in the SM together with neutrinos

All diagrams and cross sections are computed with calcHEP [85]. The Higgs boson mass, when implied, is taken at 120 GeV.

B.1 Production diagrams

The leading channel is $e^+e^- \to t\bar{t}\nu_e\bar{\nu}_e$, giving higher cross sections as well as more diagrams. the channels with τ and μ neutrinos are completely symmetric.

B.1.1 $e^+e^- \to t\bar{t}\nu_e\bar{\nu}_e$

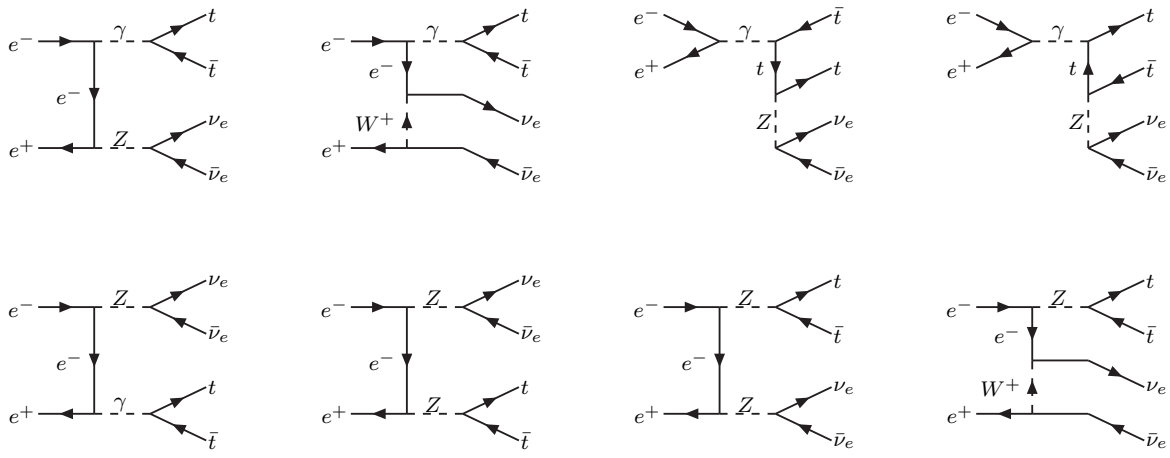

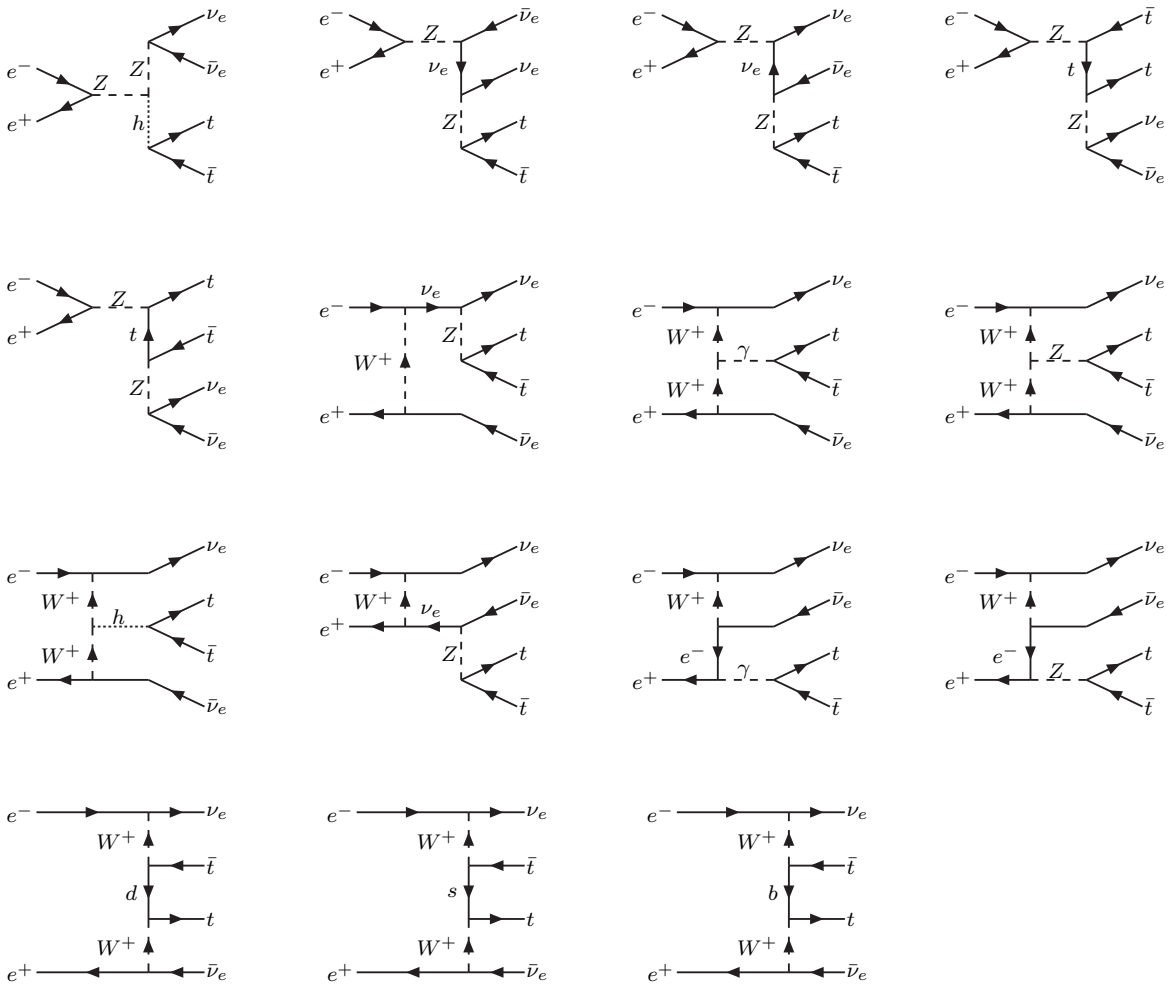

B.1.2 $e^+e^- \to t\bar{t}\nu_\mu\bar{\nu}_\mu$

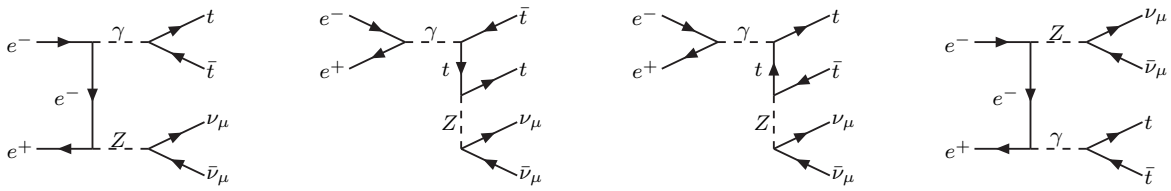

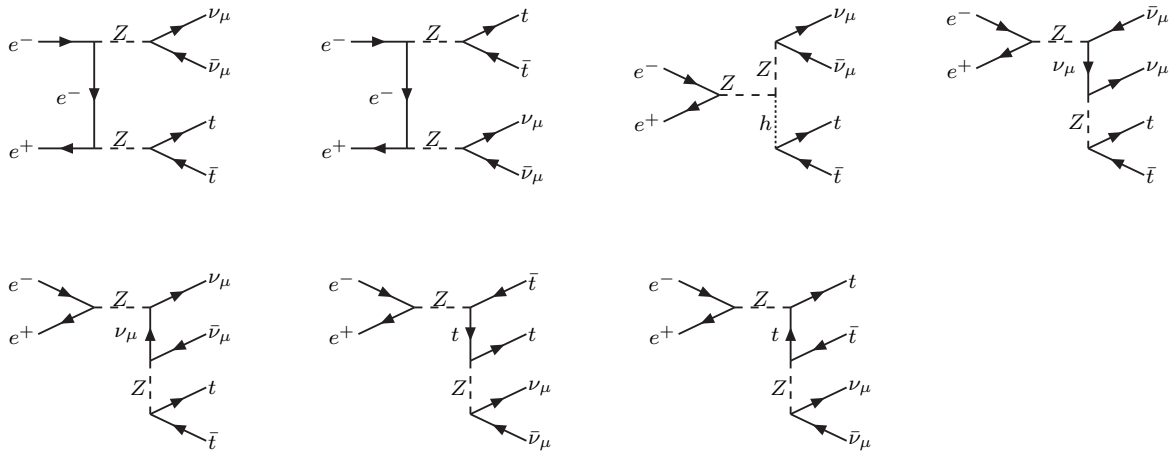

B.1.3 $e^+e^- \to t\bar{t}\nu_\tau\bar{\nu}_\tau$

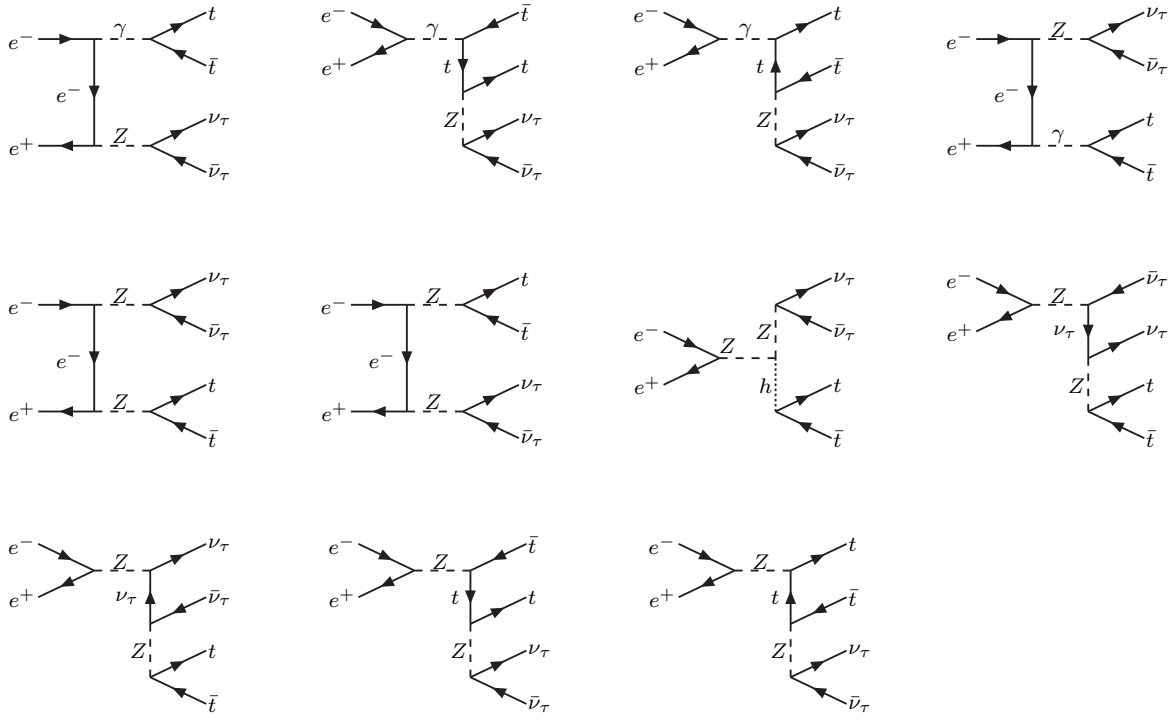

B.2 Cross section

The cross sections of the three SM channels of $t\bar{t}$ production with neutrinos are summed up in the following table. All numbers are given in unit of femto-barn.

Table B.1: Cross section of $t\bar{t}$ plus neutrinos in the SM. Numbers are given in femto-barn.

E_{cm}	$e^+e^- \to t\bar{t}\nu_e\bar{\nu}_e$	$e^+e^- \to t\bar{t}\nu_\mu\bar{\nu}_\mu$	$e^+e^- \to t\bar{t}\nu_\tau\bar{\nu}_\tau$
400	$5{\cdot}10^{-5}$	$2{\cdot}10^{-8}$	$2{\cdot}10^{-8}$
800	0.2	0.2	0.2
1200	1.0	0.3	0.3
2000	2.7	0.1	0.1
3000	5.1	$5{\cdot}10^{-2}$	$5{\cdot}10^{-2}$

APPENDIX C

Toy Model of $t\bar{t}$ event energy spectrum

The following piece of code is to be run, as is, as a ROOT macro. It illustrates the explanations of the $t\bar{t}$ event energy spectrum given in section 8.2.2 (p.116). The first tunable is the beam energy `Ebeam` in order to test various energies. The second and most important parameter is `strength`, which values would reasonably range between 0 and $\approx 1-2$, allows to tune the intensity of the initial state energy losses (ISR andBS). The default values proposed hereafter reproduce roughly the observed spectrum. The $t\bar{t}$ cross section used here are the one already presented in section 8.2.1 (p.115). The distribution is extended thanks to a sigmoid to simulate the threshold as shown in figure C.1. The initial state energy losses are modelised by a simple analytical function $\frac{1}{100}\,tan\,(x\,\frac{\pi}{2})^{1/\texttt{strength}}$ displayed for `strength` $= 1$ in figure C.2 together with its reciprocal $\frac{2}{\pi}\,atan(100\,x^{\texttt{strength}})$. Results for different values of the `strength` parameter are displayed in figure C.3.

```
{
  /*
    Toy model to understand
    the spectrum of the total energy of the ttbar events
    a peak appear at Ecm/2:
    it is due to the competition between
    the decreasing probability to have a collision at lower energy
    and the increasing probability that this collision give a ttbar event
  */
  //Parameter giving the nominal beam energy:
  const int Ebeam=1500;

  //Parameter allowing to tune the ‘‘strength’’ of the initial state energy losses:
  const float strength=1.9;

  //Raw ttbar cross section vs Ecm (no ISR no BS)  from calcHEP:
```

```
  TGraph * ttxs = new TGraph(9);
  ttxs->SetPoint(0,400,628);
  ttxs->SetPoint(1,600,435);
  ttxs->SetPoint(2,800,260);
  ttxs->SetPoint(3,1000,173);
  ttxs->SetPoint(4,1200,121);
  ttxs->SetPoint(5,1400,69);
  ttxs->SetPoint(6,2000,44);
  ttxs->SetPoint(7,2400,31);
  ttxs->SetPoint(8,3000,20);

  //Modelisation of ttbar production cross section versus Ecm:
  TF1 * fitxs = new TF1("fitxs","expo(0)+pol1(2)");fitxs->SetParLimits(3,-1,0);
  ttxs->Fit("fitxs","","",400,3000);
  double p0 = fitxs->GetParameter(0);
  double p1 = fitxs->GetParameter(1);
  double p2 = fitxs->GetParameter(2);
  double p3 = fitxs->GetParameter(3);
  TF1 * fxs = new TF1("fxs","(expo(0)+pol1(2))/(exp(([4]-x)/[5]) + 1)",0,3000);
  fxs->SetParameters(p0,p1,p2,p3,350,10);
  fxs->SetTitle(";E_{cm} [GeV];#sigma [fb]");

  //Toy approximation of QED initial state energy losses (ISR + BS):
  TF1 * ISRBS = new TF1("ISRBS","(0.01*tan(TMath::PiOver2()*x))**[0]",0,0.999);
  TF1 * ISRBSp = new TF1("ISRBS","2/TMath::Pi()*atan(100*x**[0])",0,0.999);
  ISRBS->SetParameter(0,1/strength);
  ISRBSp->SetParameter(0,strength);

  //Histogram to hold the simulated energy spectrum:
  TH1F * ttbarE = new TH1F("ttbarE",";t#bar{t} energy [GeV];a. u.",100,0,2*Ebeam);

  //Get the random energy of each beam
  //and fill histogram with weight = ‘‘ttbar xsect. at the corresponding Ecm’’.
  for(int i=0;i<100000;i++){
      float E1 = Ebeam*ISRBSp->Eval(gRandom->Uniform(0,0.999));
      float E2 = Ebeam*ISRBSp->Eval(gRandom->Uniform(0,0.999));
      float Ecm = sqrt(4*E1*E2);
      float Etot = E1+E2;
      ttbarE->Fill(Etot,fxs->Eval(Ecm));
  }
  ttbarE->DrawNormalized();
}
```

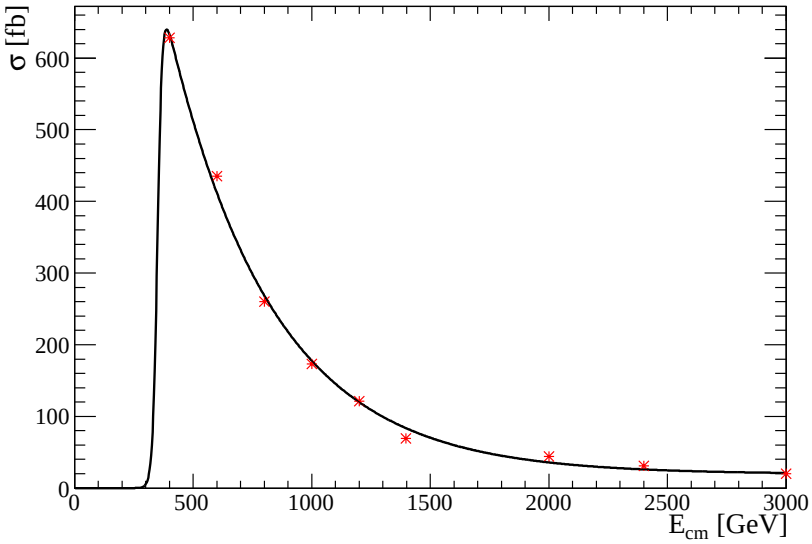

Figure C.1: $t\bar{t}$ event cross section for the toy model.

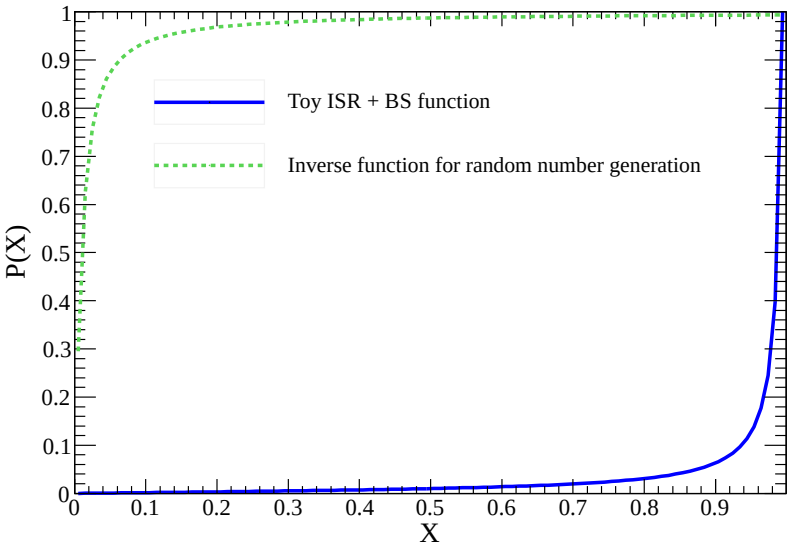

Figure C.2: Distribution of initial state energy losses (strength = 1) and its reciprocal for random number generation for the toy model.

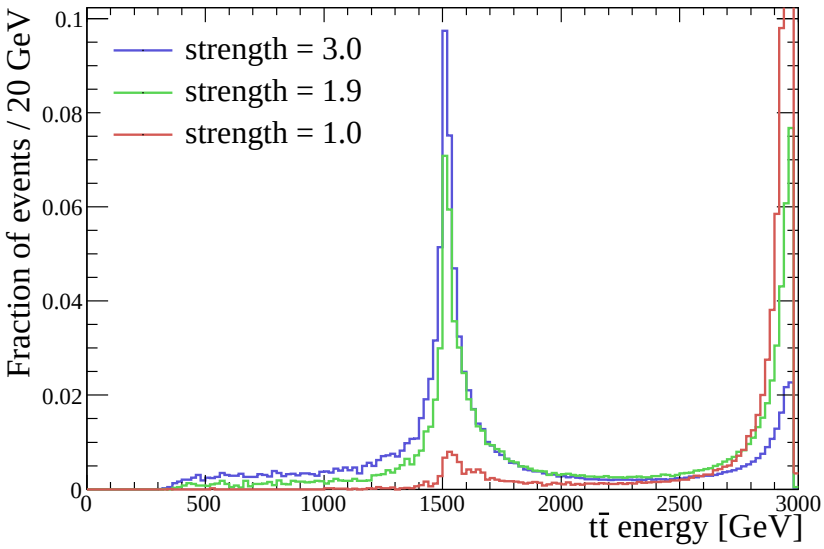

Figure C.3: Output of the toy model for different values of the strength parameter.

APPENDIX D

Appendix to the RHNM generator level study

D.1 Dark matter relic density and detection rate

The DM relic density and the direct detection event rate are calculated using micrOMEGAS2.2, with $\mathrm{MZ_P} = 200\,\mathrm{GeV}/c^2$ and $m_{\nu'} = 85\,\mathrm{GeV}/c^2$.

$$\Omega_{\nu'} = 0.11$$

WIMP-nucleon spin independent scattering cross section:

$$\sigma_{\nu'-\mathrm{p}} = 5.8 \cdot 10^{-9}$$
$$\sigma_{\nu'-\mathrm{n}} = 5.3 \cdot 10^{-7}$$

Direct detection event rate for ^{73}Ge and ^{131}Xe targets:

^{73}Ge: 0.058 /day/kg
^{131}Xe: 0.12 /day/kg

D.2 Summary of the cross sections and statistics for the signal.

$\mathrm{MZ_P}$ (GeV/c^2)	Cross sect.	Width($Z' \to$ inv.)	Width($Z' \to t\bar{t}$)	Br($Z' \to$ inv.)	$Z' \to$ inv.
200	15.0 fb	19.4 GeV	0 GeV	100%	15000
300	8.7 fb	32.8 GeV	0 GeV	100%	8700
400	5.6 fb	45.5 GeV	60.3 GeV	43.0%	2408
500	3.7 fb	57.9 GeV	115.0 GeV	33.0%	1240
600	2.6 fb	70.1 GeV	162.0 GeV	30.2%	785
700	1.8 fb	82.3 GeV	205.5 GeV	28.6%	515

D.3 Index of the final state variables

Variable name	Description	Range
ttM	$t\bar{t}$ system invariant mass	0–3000 GeV/c^2
evtM	Event invariant mass	0–3000 GeV/c^2
missE	Missing energy	0–3000 GeV
missP	Missing momentum	0–3000 GeV/c
missA	Cosine of polar angle of missing momentum	-1–1
missPT	Missing transverse momentum	0–3000 GeV/c
missM	Missing mass	0–3000 GeV/c^2
sphericity	Event sphericity	0–1
aplanarity	Event aplanarity	0–0.5
jet1P	First jet momentum	0–3000 GeV/c
jet1PT	First jet transverse momentum	0–3000 GeV/c
jet1E	First jet energy	0–3000 GeV
jet1M	First jet mass	0–3000 GeV/c^2
jet2P	Second jet momentum	0–3000 GeV/c
jet2PT	Second jet transverse momentum	0–3000 GeV/c
jet2E	Second jet energy	0–3000 GeV
jet2M	Second jet mass	0–3000 GeV/c^2
nPart	Number of particles	$\in \mathcal{N}$
nTrack	Number of charged particles	$\in \mathcal{N}$
nHadr	Number of hadrons	$\in \mathcal{N}$
nHadrC	Number of charged hadrons	$\in \mathcal{N}$
nGamma	Number of photons	$\in \mathcal{N}$
nElect	Number of electrons	$\in \mathcal{N}$
nMu	Number of muons	$\in \mathcal{N}$

D.4 Final state correlation matrix

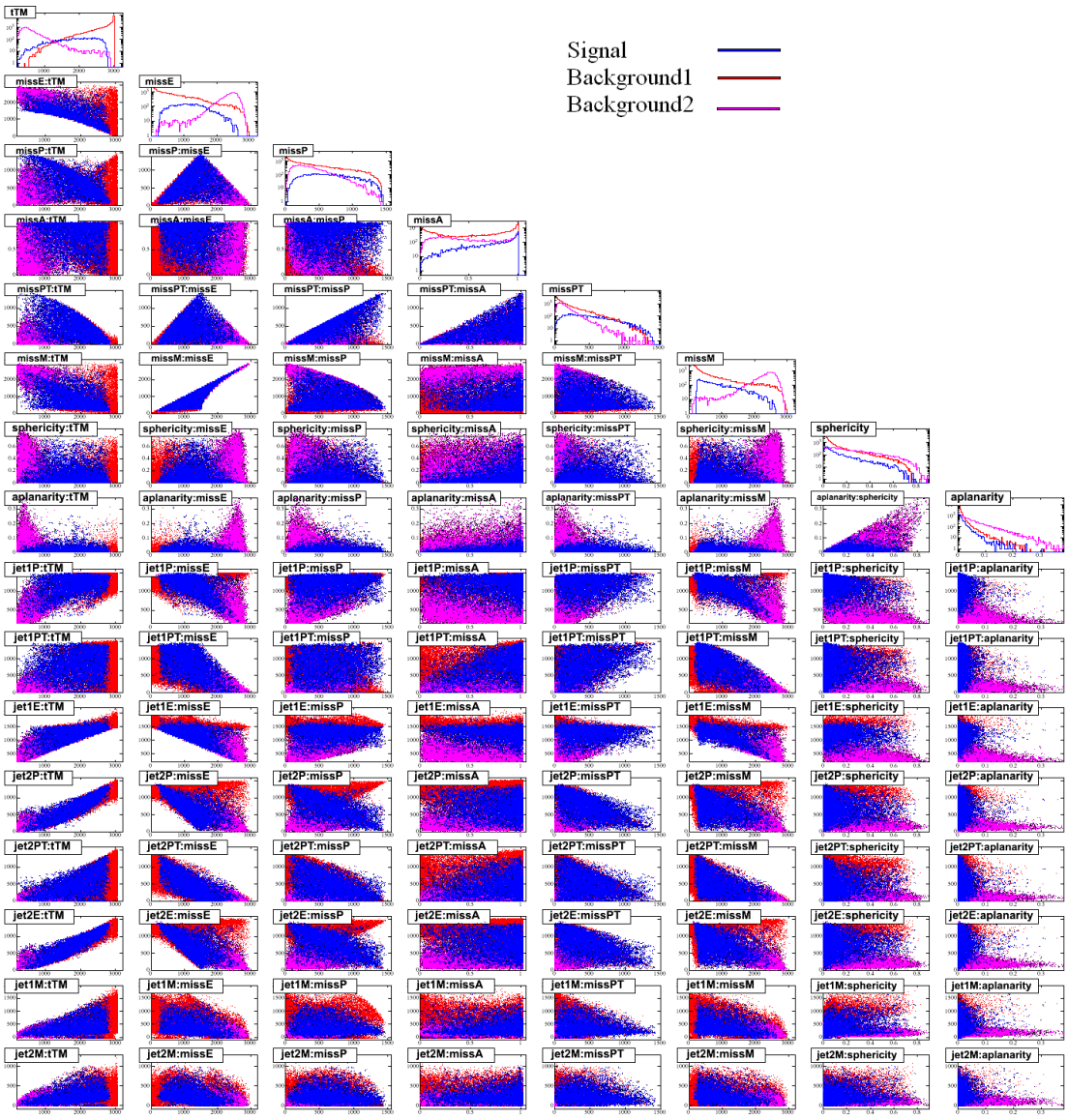

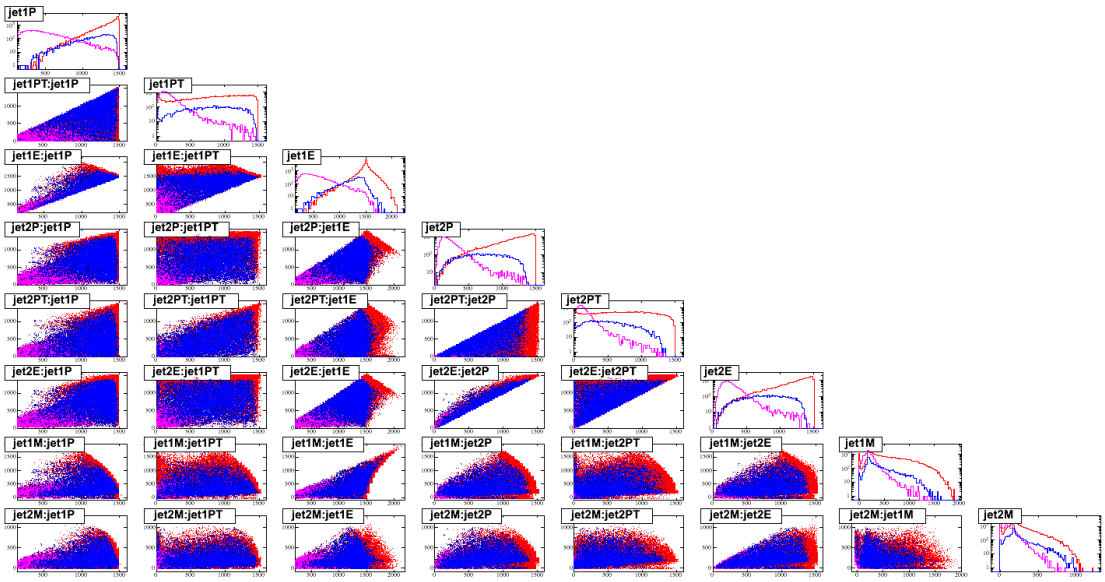

D.5 Summary of the analysis variables

Variable name	Description	Discriminating power
missPT	Missing transverse momentum	3.462e-01
missE	Missing energy	3.114e-01
jet1E	First jet energy	3.012e-01
jet2E	Second jet energy	2.496e-01
jet2P	Second jet momentum	2.365e-01
missP	Missing momentum	2.250e-01
jet1P	First jet momentum	2.138e-01
jetPTdiff:=jet1P-jet2P	jet PT diffrence	2.122e-01
missA	Angle of missing momentum	1.134e-01
jet2PT	Second jet transverse momentum	1.078e-01
sphericity	Sphericity	1.024e-01
aplanarity	Aplanarity	9.443e-02
jetEratio:=jet2E/jet1E	Jets energy ratio	9.302e-02
Jet1PT	First jet transverse momentum	7.763e-02
jetEdiff:=jet1E-jet2E	Jets energy difference	6.089e-02

D.6 BDT variable importance ranking

Rank	Variable	Importance
1	missPT	1.929e-01
2	missE	1.366e-01
3	jet1P	1.069e-01
4	jet1E	8.365e-02
5	jet1PT	6.978e-02
6	missA	5.944e-02
7	missP	5.346e-02
8	jet2E	4.576e-02
9	jetEratio	4.288e-02
10	jetPTdiff	4.001e-02
11	jet2PT	3.919e-02
12	jet2P	3.636e-02
13	sphericity	3.534e-02
14	jetEdiff	2.973e-02
15	aplanarity	2.799e-02

D.7 MZ_P measurement error calculation.

As described in section 9.4.2.2, the Z' mass relates to the upper inflection point abscissa of the "smooth gate" fitted on the event invariant mass spectrum, denoted s_2. The error is derived from this relation:

$$
\begin{aligned}
m_{Z'}(s_2) &= \frac{k - s_2}{\alpha} \\
\Rightarrow \frac{\Delta^2 m_{Z'}}{(m_{Z'})^2} &= \frac{\Delta^2(k - s_2)}{(k - s_2)^2} + \frac{\Delta^2 \alpha}{\alpha^2} \qquad \text{with } \Delta^2(k - s_2) = \Delta^2 k + \Delta^2 s_2 \\
\Rightarrow \frac{\Delta^2 m_{Z'}}{(m_{Z'})^2} &= \frac{\Delta^2 k}{(k - s_2)^2} + \frac{\Delta^2 s_2}{(k - s_2)^2} + \frac{\Delta^2 \alpha}{\alpha^2} \qquad \text{but } (k - s_2)^2 = \alpha^2 (m_{Z'})^2 \\
\Rightarrow \Delta^2 m_{Z'} &= \frac{\Delta^2 k}{\alpha^2} + \frac{\Delta^2 s_2}{\alpha^2} + \frac{m_{Z'} \Delta^2 \alpha}{\alpha^2} \\
\Rightarrow \Delta m_{Z'} &= \sqrt{\frac{\Delta^2 k}{\alpha^2} + \frac{\Delta^2 s_2}{\alpha^2} + \frac{m_{Z'} \Delta^2 \alpha}{\alpha^2}} \qquad \text{which also reads :} \\
\Delta m_{Z'} &= \frac{\Delta k}{\alpha} \oplus \frac{\Delta s_2}{\alpha} \oplus \frac{m_{Z'} \Delta \alpha}{\alpha}
\end{aligned}
$$

D.8 MVA input variable spectrum

D.8.1 Signal versus background 1

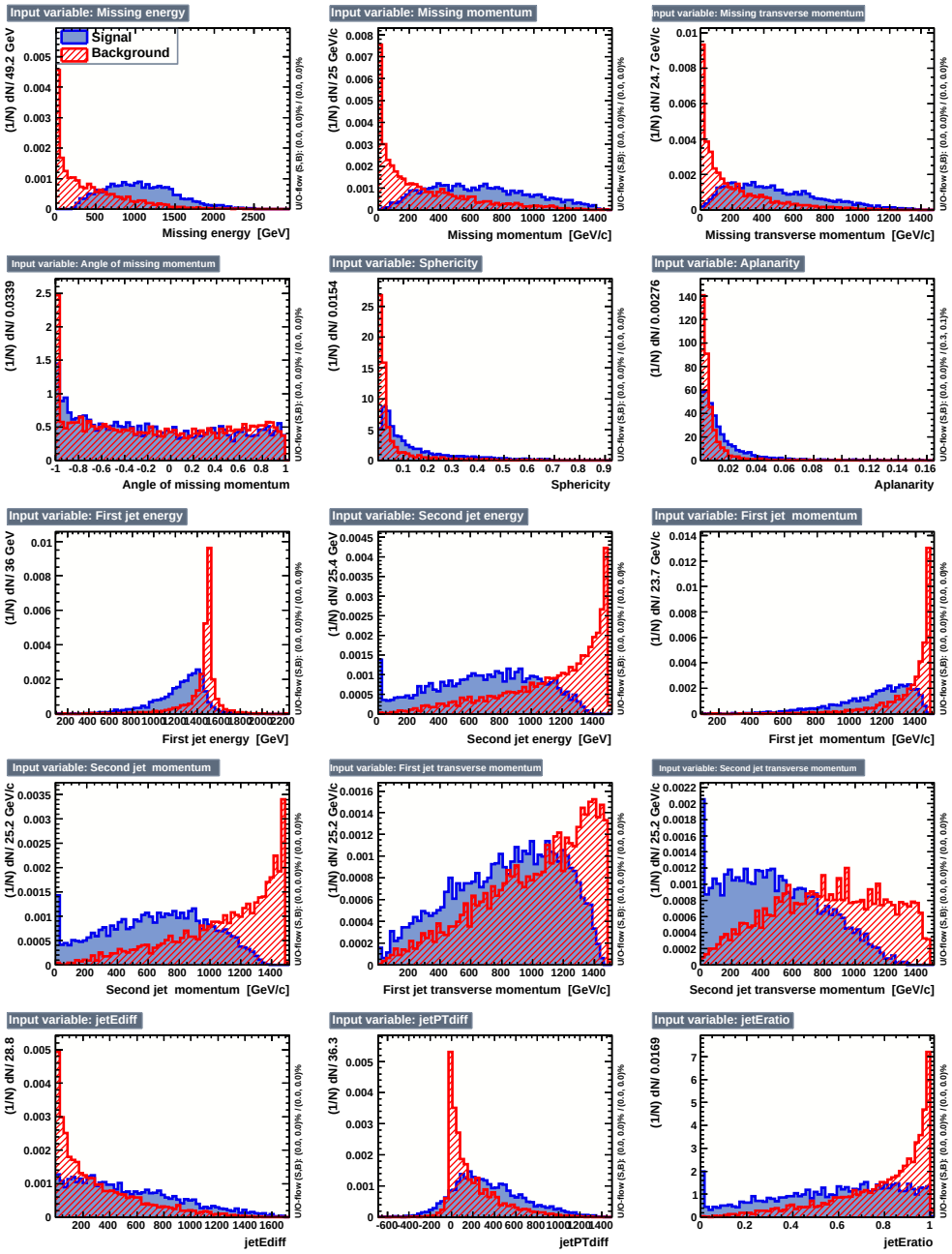

D.8.2 Signal versus background 2

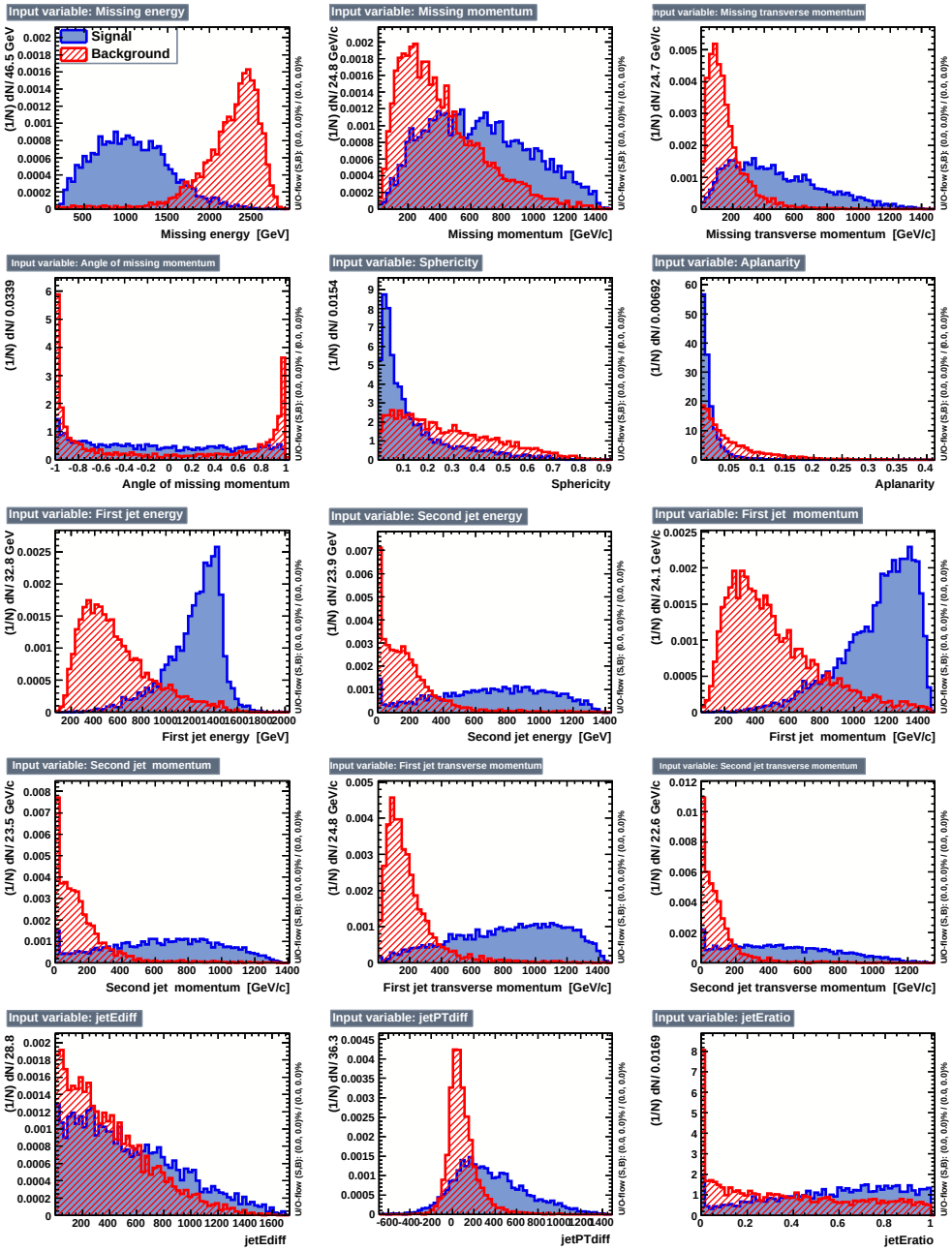

APPENDIX E

Smearing techniques

E.1 Basic single particle smearing

The first attempt to apply a smearing to generator level data in order to simulate the effect of PFA reconstruction and detector resolution is to apply the suitable sub-detector resolution on the four-vector $(\vec{p}, E)^T$ of each final state particle.

- Charged particles are smeared according to a tracker resolution of the the order of $\Delta p/p^2 = 2 \cdot 10^{-5}$.
- Photons four-vector are smeared according to a Electromagnetic Calorimeter (ECAL) resolution which is about $\sigma_E/E = 10\%/\sqrt{E}$.
- Neutral hadrons are smeared according to a Hadronic Calorimeter (HCAL) resolution of about $\sigma_E/E = 40\%/\sqrt{E}$.

This very straightforward technique is roughly valid if the energy scale is of the order of a few hundred GeV (100–300 GeV) allowing the PFA confusion to be neglected. This technique is therefore not applicable at CLIC energies (O(1–3 TeV)).

E.2 Jet smearing

At CLIC energies the confusion term is a foreground issue. Therefore, the simple technique described above is not realistic but the jet energy resolution semi-empirical formula (eq. 2.7, p. 33) proposed in [33] can be applied to smear reconstructed jet four-vectors. This formula is recalled as follows:

$$\frac{\mathrm{rms}_{90}}{E} = \underbrace{\frac{21\%}{\sqrt{E}} \oplus 0.7\%}_{\substack{\text{classical stochastic} \\ \text{and constant terms}}} \oplus \underbrace{0.004\,E}_{\substack{\text{leakage and} \\ \text{threshold effect}}} \oplus \underbrace{2.1\% \left(\frac{E}{100\,\mathrm{GeV}}\right)^{0.3}}_{\text{confusion term}}.$$

This formula has been derived from prefect di-jet events, namely $e^+e^- \to Z^0 \to u\,(d,s)\bar{u}\,(\bar{d},\bar{s})$. Therefore, its application to multi-jet final state processes is not straightforward. The question weather to apply the smearing to the hemisphere-jets or to the k_t inclusive jets (see section 8.3.2, p. 119) is hard to answer and once a choice is made, the question remains how to smear the jets of the other definition. The reasonable choice is to apply the formula to the lightest jets, namely the k_t inclusive jets, and then rebuild the hemispheres from the smeared light jets. This technique does not allow any smearing of non-jet-related variables (see table 8.5, p. 121 and D.5, p. 166 for lists of the involved variables). And finally, even if the smearing of the non-jet-related variables is neglected, the formula only gives an energy smearing whereas a jet mass and/or momentum resolution are compulsory complementary information. Therefore, as this technique leads to a large number of approximations, it has been considered unreliable and discarded.

E.3 Single particle smearing

The information available in [33] allows to envision including confusion effects in the single particle smearing already sketched in section E.1. The confusion mainly comes from three distinct sources:

- photon hits lost from association to charged hadron clusters,
- hits from neutral hadrons lost from association to charged hadron clusters,
- hits from charged hadrons lost from association to neutral clusters.

These effects, as well as leakage effect, contribute to the jet energy resolution as shown in figure E.1, where the point are taken from [33] and where the interpolation is done with the following functions:

- photon to charged hadron:

$$f_{\gamma\to C} = 0.99 \pm 0.03 \left(\frac{E}{100}\right)^{0.27\pm0.04}$$

- neutral to charged hadron:

$$f_{N\to C} = 0.54 \pm 0.04 \log E - 1.18 \pm 0.18$$

- charged neutral hadron:

$$f_{C\to N} = 1.67 \pm 0.18\, e^{-E/128.8\pm19.6}$$

- leakage:

$$f_{\text{leak}} = 0.520 \pm 0.013 \log E - 1.887 \pm 0.062$$

These functions can therefore be used to extrapolate the various contributions to arbitrary energy and therefore provide a more realistic smearing than in section E.1. Such an extrapolation is obviously subject to large uncertainties that can not be easily estimated at this step.

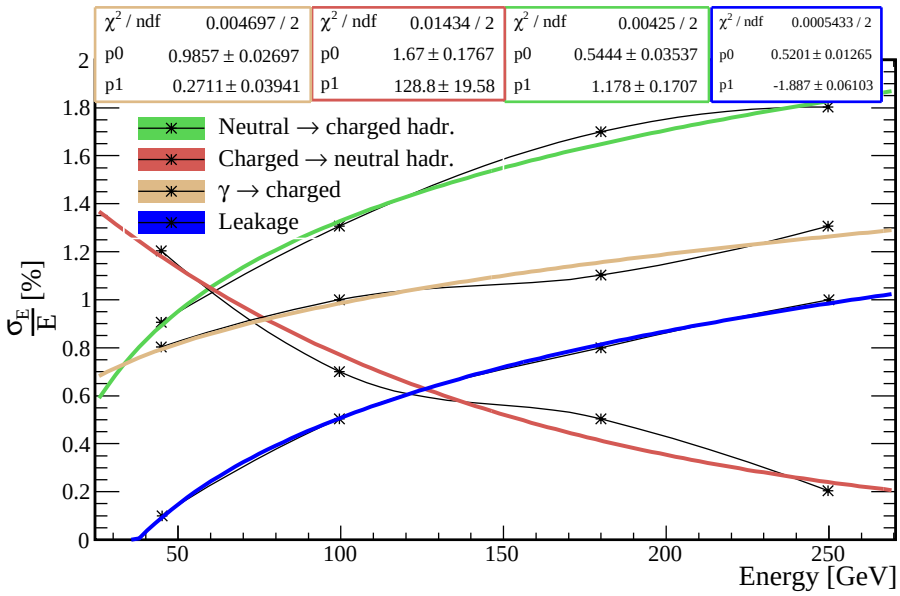

Figure E.1: Individual contribution to jet energy resolution for each confusion effects and for leakage.

This method, as a refinement of the basic single particle smearing of section E.1, is more realistic for CLIC energies in principle. However, the extrapolation at CLIC energies of the confusion term contributions is very uncertain. In [111], a CLIC optimised PFA has been announced. It provides a jet energy resolution below 3.6% for the whole ILC and CLIC energy range by relying on a trade-off between particle and energy flows. Therefore, the previous conclusions became obsolete and an equivalent study should be done on this CLIC optimised PFA. Moreover, this technique has two additional drawbacks:

- As in the method described in section E.2, the performance is evaluated on very clean di-jet events, from the process $e^+e^- \rightarrow Z^0 \rightarrow u\,(d,s)\bar{u}\,(\bar{d},\bar{s})$, and may be not completely exact for more complex final states with different jet clustering strategies.

- This method only affects the resolution on the final state particle four-vectors, but in the PFA it is possible that particles are completely missed as well as completely invented. This uncertainty, that actually induces a smearing in the number of particles in the event, can not be rendered by this method. Moreover, in realistic conditions, the number of particles in the event should be affected as well by the machine induced $\gamma\gamma \rightarrow hadrons$ background.

Those drawbacks led this method to be discarded to explore another possibility, described in the next section.

E.4 Final state variables smearing

A last smearing method was envisioned in the aim to get the most realistic possible results. The method is based on the eventwise comparison, for each variable of the analysis, of its value at the generator level and its value at the detector level using a sample of fully simulated data. This could be done with $t\bar{t}$ events from CLIC CDR production. This method is meant to include every possible effects since it somehow simply transforms the generator level information into the detector level information using random coefficients.

E.4.1 Description of the method

For each event, the ratio between generator and detector level values is plotted *versus* the generator level value, giving a 2D histogram called *smearing map*. The example of the total event invariant mass of $t\bar{t}$ events is displayed in figure E.2(a). Once this map is obtained, it is cut into vertical slices to give distributions of the ratio between generator and detector level values of the variables, for a given generator level value. The smearing is then done by considering the generator level value to smear and selecting the corresponding slice of the smearing map to generate a random coefficient to be multiplied with the generator level value.

Building a slice A slice is simply an 1D histogram of the map entries corresponding to a given horizontal range projected on the vertical axis. It is built as follows. It consists at first of the content of all the y-axis bins corresponding to only one x-axis bin. If the number of entries is too low, the next x-axis bin is considered and all its entries are added to the slice histogram and so forth until the minimum statistics is matched. If the last slice can't reach the minimum statistics, it is merged with the previous one. Examples of such slices from the map of figure E.2(a) are shown in figure E.2(b). The slice histograms are slightly smoothed before generating a random smearing coefficient.

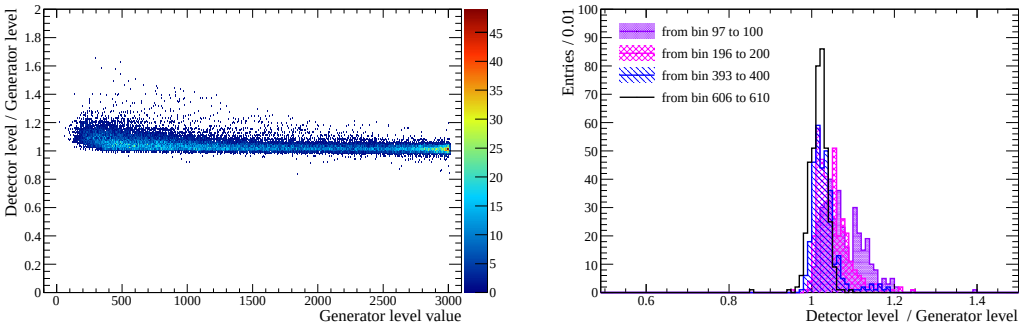

(a) Smearing map for the total event invariant mass.

(b) Example of slice histograms from the total event invariant mass smearing map.

Figure E.2: Illustration of the working principle of the smearing map method.

Low value divergence and smeared value calculation For values of the variable spectrum which are close to 0, the ratio between generator and detector level values tend to diverge. This is avoided by shifting the distribution away from 0. So the ratio r is actually calculated as

$$r = \frac{x_{\text{det}} + k}{x_{\text{gen}} + k}\,,$$

where x_{det} is the detector level value of the variable x and x_{gen}, the generator level one, k is the arbitrary offset taken here as the difference between maximum $x_{\max}$ and minimum value $x_{\min}$ of the variable x:

$$k = x_{\max} - x_{\min}\,.$$

A too large offset induces a compression of the distributions and would cause the smearing coefficients to be undervalued. More refined definitions of k can allow to insure a good distance to 0 without going to too high values either. The smeared value x_{smeared} is therefore calculated as

$$x_{\text{smeared}} = ((x_{\text{gen}} + k) \times r_{\text{rand}}) - k\,,$$

where r_{rand} is the random smearing coefficient generated from the smearing map slice corresponding to x_{gen}.

E.4.2 Performance of the method

Figures E.3 and E.4 illustrate respectively the achievable quality of the smearing thanks to this method and the possible problems that may be encountered. This method can be very effective to smear generator level data for which a fully simulated sample exists in order to increase the statistics. However, it appears that when using a large number of variables, the distribution of some of them are not well rendered. Moreover, the correlation between variables is lost when using this method directly. The correlations can be approximatively restored if the smearing coefficients of correlated variables are deduced from each others or, in the case of simple relation between variables, if the smeared value of a correlated variable is directly computed from the smeared value of another correlated variable obtained through the smearing map method.

This method should therefore be more reliable when using few uncorrelated variables or with simple correlations. In the case of the studies described in chapters 8 and 9, given the number of involved variables and their sometimes complex correlations, a good strategy could be to apply the smearing only on the output of the BDTs. The example of the top-tagging BDT output is displayed in figure E.5.

Evaluating the generator level Z' event selection BDT on $t\bar{t}$ events from CLIC CDR simulated data do not give a reliable smearing map because the distribution are too different due to the large difference of the centre of mass energy spectra explain in section 9.5. The latter argument prevented from using this method for the smearing of the Z' study results.

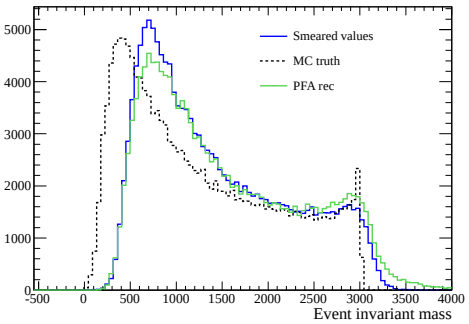

(a)

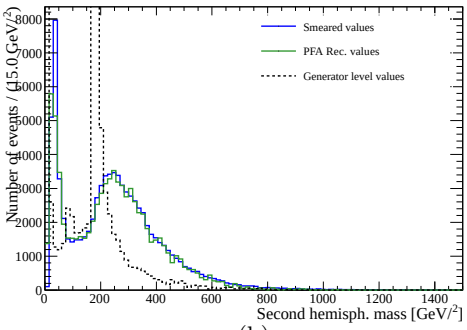

(b)

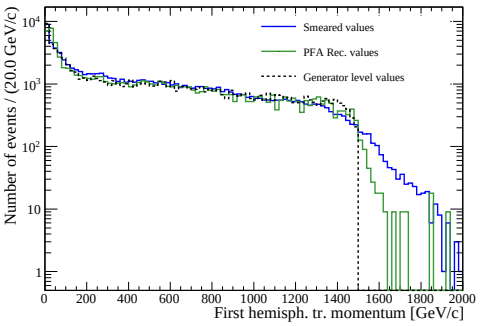

(c)

Figure E.3: Illustration of the achievable quality of the smearing on single variables. (a) illustrates the performance of the technique on the total event invariant mass which has been taken as example above. (b) illustrates the ability of the method to deal with a complicated spectrum. (c) illustrates how the method allow to populate distribution tails even with limited initial statistics.

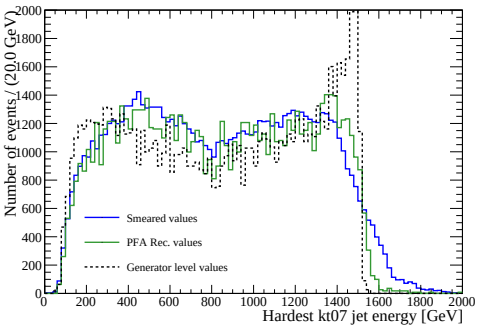

(a)

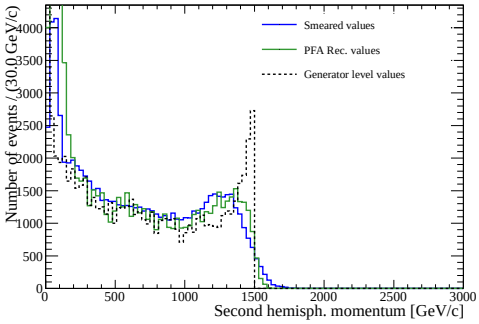

(b)

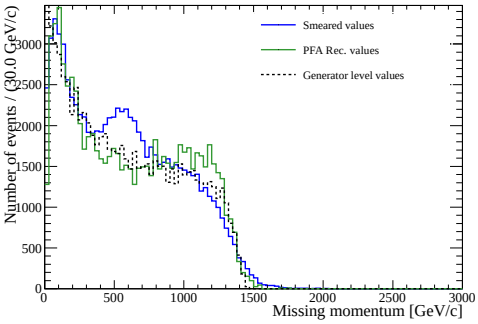

(c)

Figure E.4: Illustration of some problems that may occur when smearing single variables. (a) illustrates how the method can overvalue the smearing around a steep end point. (b) shows as well the end point problem and also a low value discrepancy due to the low value divergence of the smearing coefficient. (c) displays an artefact of this technique where a bump appear with no obvious reason, attempts to tune the method parameters have failed to suppress this effect.

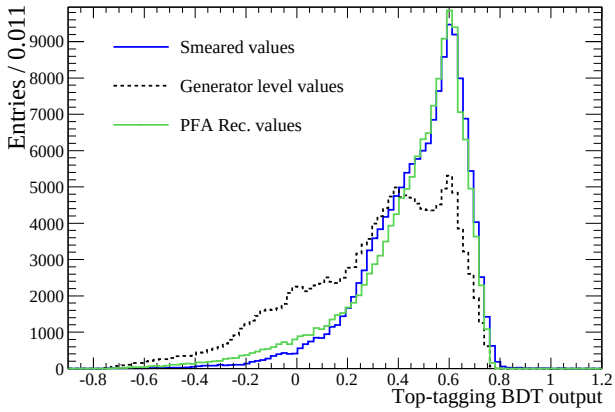

Figure E.5: Smearing of the BDT output

Acknowledgement — Remerciements

Dans ces quelques lignes je vais essayer de mentionner tous ceux qui, dans mon entourage, ont joué un rôle positif autour de cette thèse et avant tout je voudrais remercier tous ceux qui, peut être à mon insu et/ou au leur, ont contribué à l'aboutissement de ce projet et serait peut être alors absents de ces lignes.

Je commencerai par la fin et par conséquent les premiers remerciements vont aux membres de mon jury, qui ont bien voulu se réunir à Annecy et m'octroyer le titre de "Docteur de l'Université de Grenoble" suite à la soutenance. Des remerciements plus particuliers vont à mes rapporteurs, Felix Sefkov et Paul Colas, qui sont parvenus à lire et analyser mon manuscrit en un temps record et ainsi permettre l'accomplissement du travail dans les délais impartis. Je voudrais aussi remercier tout particulièrement Jean-Jacques Blaising, qui a pris très au sérieux son rôle de président de jury et qui a veillé, avec bienveillance et rigueur, à me pousser pour améliorer la qualité du manuscrit et de la présentation pour la soutenance. Jean-Jacques fut aussi d'une aide précieuse et d'un conseil avisé durant tout mon travail d'étude de simulation sur quark top et le Z'.

Un des remerciements les plus importants est pour Catherine Adloff qui m'a donné ma chance et m'a soutenu déjà lors de mon stage de Master en 2007 puis pour l'obtention de ce poste de doctorant au LAPP. Catherine a su m'accompagner dans les premiers temps et me laisser prendre mon autonomie au fur et à mesure, elle fut à la fois une directrice de thèse impliquée et une voisine de bureau amicale. Des remerciements vont aussi bien sur à Yannis Karyotakis, qui malgré sa charge de directeur du laboratoire, a beaucoup contribué à l'équilibre du travail.

Je voudrais aussi mentionner toute l'équipe DHCAL MICROMEGAS du LAPP en incluant aussi bien les acteurs passés que j'ai connus. Merci donc à Denis Fougerons pour les PCB des chambres à lecture analogique et pour les discussions instructives et sympathiques. Merci à Jean-Marc Dubois pour ce système de gaz qui alimente toujours et encore nos détecteurs, merci aussi pour ta sympathie, ta bonne humeur et ta disponibilité en cas de besoin. Merci à Ino Monteiro pour la structure porteuse des détecteurs sans laquelle fort peu aurait pu être accompli. En ce qui concerne l'équipe actuelle, la liste des hauts faits de chacun serait immense ... Il y a Jean Jacquemier,

héros de l'informatique, disponible et pédagogue. Nicolas Geffroy et Fabrice Peltier qui ont conçu et réalisé tant de pièces mécaniques et ainsi matérialisé ce projet, le tout dans la bonne humeur et la convivialité, Fabrice qui a aussi assemblé tous les prototypes MICROMEGAS et même les scintillateurs décrits dans ce manuscrit. Du côté électronique, Julie Prast, Cyril Drancourt, Sébastien Cap, Guillaume Vouters et Renaud Gaglione, dont le savoir faire et l'implication ont permis la bonne évolution du projet (design des circuits imprimés des détecteurs, des cartes intermédiaires et d'interface, des puces, tests électroniques, calibrations, etc ...).

Du côté administratif, je souhaite remercier en particulier Brigitte Putanier et Marie-Claude Lacombe à la fois pour leur efficacité, leur disponibilité et leur sympathie, faisant de la préparation des missions une formalité finalement plaisante. Je voudrais aussi remercier ce cher support-info qui m'a dépanné à tant de reprises avec efficacité et sympathie. De manière plus général je tiens à saluer la cordialité et l'efficacité de tous les personnels du laboratoire, qui contribuent à faire du LAPP un endroit où il fait bon travailler.

Je voudrais encore remercier au passage certains collègues extérieurs au groupe du LAPP: Stephane Poss (CERN), disponible, efficace, merci pour les données CLIC_ILD ; Frank Simon (MPI), *thank you for the tips about top physics* ; Louis Helari (LAPP), merci pour tous les tuyaux administratifs sans lesquels j'aurais sûrement été bien plus en retard pour mes inscriptions à l'université ; David Attié (CEA), merci pour ton aide précieuse dans la quête pour joindre Paul lors de ses déplacements ;). *Thanks as well to Torbjörn Sjöstrand and Peter Skands for their help with Pythia 8. The little collaboration with Peter Skands was a great pleasure and helped me well even if we didn't have the time to make it lead to a real contribution to Pythia 8 code.*

Certains collègues en particulier ont joué un rôle fondamental au quotidien, humainement autant que scientifiquement, au cours de ses années au LAPP. Nous formions une véritable équipe, soudée et dynamique tant dans le travail qu'à la fête ! Le noyau dur : Jan Blaha , Max Chefdeville et Guillaume Vouters survit encore après que Jan et moi ayons quitté le LAPP. Merci les gars pour tous ces bon moments !

Du côté de la famille, il est juste que je commence par remercier profondément mes grand-parents, Claude et Bernard, qui m'ont hébergés lors des mois de mon stage de Master 2, puis qui ont su rester présents mais discrets, toujours disponibles et d'un grand soutien au cours de ses années de thèse. Dans les derniers mois, Belle maman Solange m'a donné un précieux coup de pouce, merci pour les fleurs de Bach ! Dans la fin de la rédaction du manuscrit, merci à Miko pour la relecture de l'anglais !! Et enfin merci à mes parents et beau parents pour l'organisation du pot de soutenance. Je souhaite aussi finalement remercier tout particulièrement Dorothée, qui m'a épaulé, accompagné, encouragé, supporté et bien plus encore ! Elle a autant que moi enduré ces années de labeurs de stress et de doutes et a pourtant apporté un soleil indescriptible sur toute cette période ... Et merci à Célestin d'avoir été le plus adorable des bébés !!

Bibliography

[1] Sven Heinemeyer, Sabine Kraml, Werner Porod, and Georg Weiglein. Physics impact of a precise determination of the top quark mass at an e^+e^- linear collider. *JHEP*, September 2003. 7, 14

[2] Murray Gell-Mann. A schematic model of baryons and mesons. *Phys. Lett.*, 8, 1964. 8

[3] Georges Zweig. An su(3) model for interaction symmetry and its breaking. *CERN Libraries*, 1964. 8

[4] Sheldon Glashow, Jean Iliopoulos, and Luciano Maiani. Weak interactions with lepton-hadron symmetry. *Phys. Rev. D*, 11, 1970. 8

[5] LEP Collaborations. Updated parameters of the Z^0 resonance from combined preliminary data of the LEP experiments. *CERN preprint:* CERN/PPE/93-157 *http://aseps.in2p3.fr/cgi-bin/twiki.source/pub/FAPPS/StudentPresentations/LEP_comb.pdf*, 1993. 9

[6] Carlo Rovelli. Notes for a brief history of quantum gravity. In World Scientific, editor, *Proceedings of the ninth Marcel Grossmann Meeting on General Relativity R.T. Jantzen, R. Ruffini, V. G. Gurzadyan editors*, pages 742–768, Singapore, 2002. 10, 11

[7] F. Zwicky. On the Masses of Nebulae and of Clusters of Nebulae. *Astrophysics Journal*, 86:217–+, October 1937. Provided by the SAO/NASA Astrophysics Data System. 10

[8] Bill Carithers and Paul Grannis. *Discovery of the Top Quark*, 1995. http://www.slac.stanford.edu/pubs/beamline/25/3/25-3-carithers.pdf. 11

[9] E. Kh. Akhmedov. Neutrino physics. *arXiv:hep-ph/0001264v2*, 2000. 11

[10] Sidney coleman and Jeffrey Mandula. All possible symmetries of the s matrix. *Physical Review*, 159(5), july 1967. 12

[11] Adel Bilal. Introduction to supersymmetry. *arXiv:hep-th/0101055v1*, 2001. 13

[12] Manuel Drees. An introduction to supersymmetry. *arXiv:hep-ph/9611409v1*, 1996. 13

[13] JOSEPH D. LYKKEN. Introduction to supersymmetry. *arXiv:hep-th/9612114v1*, 1996. 13

[14] Gunnar Nordström. Über die möglichkeit, das elektromagnetische feld und das gravitationsfeld zu vereinigen. *Physikalische Zeitschrift*, 1914. 13

[15] Theodor Kaluza. On the problem of unity in physics. *Sitzungsber. Preuss. Akad. Wiss. Berlin. (Math. Phys.)*, 1921. 13

[16] Oskar Klein. Quantum theory and five dimensional theory of relativity. *Z. Phys.*, 37, 1926. doi:10.1007/BF01397481. 13

[17] Lisa Randall and Raman Sundrum. *A Large Mass Hierarchy from a Small Extra Dimension. Phys. Rev. Lett.*, 83, 1999. [arXiv:hep-ph/9905221]. 13

[18] Kaustubh Agashe and Géraldine Servant. Warped unification, proton stability, and dark matter. *Phys. Rev. Lett.*, 93(23):231805, Dec 2004. 14

[19] Kaustubh Agashe and Géraldine Servant. Baryon number in warped grand unified theories: model building and (dark matter related) phenomenology. *Journal of Cosmology and Astroparticle Physics*, 2005(02):002, 2005. 14

[20] The DØ Collaboration. Determination of the width of the top quark. DØ Note 6034-CONF, 2010.
http://www-d0.fnal.gov/Run2Physics/WWW/results/prelim/TOP/T87/T87.pdf. 14

[21] ILC collaboration. Reference design report, volume 2: Physics at the ilc. Technical report, ILC Global Design Effort and Worldwide Study, 2007.
url:http://arxiv.org/PS_cache/arxiv/pdf/0709/0709.1893v1.pdf. 14, 19

[22] Lisa Randall and Raman Sundrum. Large mass hierarchy from a small extra dimension. *Phys. Rev. Lett.*, 83(17):3370–3373, Oct 1999. 14

[23] ILC home page.
http://www.linearcollider.org/. 19, 21

[24] CLIC home page.
http://clic-study.org/. 19, 21

[25] ILC collaboration. Reference design report, volume 3: Accelerator. Technical report, ILC Global Design Effort and Worldwide Study, 2007.
http://ilcdoc.linearcollider.org/record/6321/files/ILC_RDR_Volume_3-Accelerator.pdf?version=4.
21, 98, 195

[26] CTF3 Collaboration. Ctf3 home page.
http://ctf3.home.cern.ch/ctf3/CTFindex.htm. 20

[27] CTF3 Collaboration. Ctf3 parameter list.
http://ctf3.home.cern.ch/ctf3/New_parameters.htm. 20

[28] CLIC Study Team. CLIC CDR baseline parameter list, 2010.
http://clic-meeting.web.cern.ch/clic-meeting/clictable2010.html. 21, 113, 195

[29] CLIC Study Team. A 3 tev e^+e^- linear collider based on clic technology. *CERN document server*, 2000.
http://cdsweb.cern.ch/record/461450?ln=fr. 21

[30] Particle Data Group. *Particle Physics Booklet*. Extracted from Physics Letters B 667, 1, 2008. 23, 24, 85, 86

[31] Claude Leroy and Pier-Giorgio Rancoita. Principles of Radiation Interaction In Matter And Detection. World Scientific, 2004. 24, 26, 82, 85, 86

[32] Jean-Claude Brient. *Improving the jet reconstruction with the particle flow method: An introduction*. In *Proceedings of 11th International Conference on Calorimetry in High-Energy Physics (Calor 2004),Perugia, Italy*, March 2004.
http://hal.archives-ouvertes.fr/docs/00/02/82/00/PDF/ParticleFlow-Brient-V2.pdf. 31, 32, 46

[33] M. A. Thomson. *Particle Flow Calorimetry and the PandoraPFA Algorithm. Nuclear Instruments and Methods in Physics Research A*, 611, july 2009. [arXiv:0907.3577v1]. 31, 33, 34, 46, 118, 171, 172

[34] ATLAS/Tile Calorimeter Collaboration. Atlas tile calorimeter technical design report, 1996.
http://atlas.web.cern.ch/Atlas/SUB_DETECTORS/TILE/TDR/TDR.html. 32

[35] E. Rutherford and H. Geiger. An electrical method of counting the number of a particles from radioactive substances. *Proceedings of the Royal Society (London) Series A*, 81(546), 1908. 39

[36] H. Geiger and W. Müller. Elektronenzählrohr zur messung schwächster aktivitäten. *Naturwissenschaften*, 16:617–618, 1928. 10.1007/BF01494093. 39

[37] N. N. Das Gupta and S. K. Ghosh. A report on the wilson cloud chamber and its applications in physics. *Rev. Mod. Phys.*, 18(2):225–290, Apr 1946. 39

[38] Carl D. Anderson. *Physical Review*, 43, 1933. 39

[39] Seth H. Neddermeyer and Carl D. Anderson. Note on the nature of cosmic-ray particles. *Phys. Rev.*, 51(10):884–886, May 1937. 39

[40] G. Charpak, R. Bouclier, T. Bressani, J. Favier, and C. Zupancic. The use of multiwire proportional counters to select and localize charged particles. *Nuclear Instruments and Methods*, 62(3):262 – 268, 1968. 40

[41] G. Charpak, D. Rahm, and H. Steiner. Some developments in the operation of multiwire proportional chambers. *Nuclear Instruments and Methods*, 80(1):13 – 34, 1970. 40, 41

[42] Gilles Barouch. *Analyse des Phénomènes Physiques Liés au Fonctionnement du Détecteur Gazeux à Micropistes MICROMEGAS*. PhD thesis, Université de Paris-Sud, UFR scientifique d'Orsay, 2001. 41, 151

[43] A. Oed. position-sensitive detector with microstrip anode for electron multiplication with gases. *Nucl. Instr. Meth. A*, 263, 1987. 41, 42

[44] F. Angelini, R. Bellazzini, A. Brez, M.M. Massai, R. Raffo, G. Spandre, and M.A. Spezziga. The micro-gap chamber. *Nucl. Instr. Meth. A*, 335, 1993. 42, 43

[45] Ioannis Giomataris, Ph. Rebourgeard, J. P. Robert, and Georges Charpak. *MICROMEGAS: a high-granularity position-sensitive gaseous detector for high particle-flux environments. NIM A*, 376:29–35, 1996. 43, 45

[46] Robert A. Wijsman. *Breakdown Probability of a Low Pressure Gas Discharge. Phys. Rev.*, 75(5):833–838, Mar 1949. 44, 100

[47] P. Abbon at al. The compass experiment at cern. *Nuclear Instruments and Methods in Physics Research Section A: Accelerators, Spectrometers, Detectors and Associated Equipment*, 577(3):455 – 518, 2007. 45

[48] F. Kunn, P. Abbon, J. Ball, Y. Bedfer, C. Bernet, E. Delagnes, A. Giganon, J. M. Le Goff, A. Magnon, D. Neyret, H. Pereira, S. Platchkov, P. Rebourgeard, G. Tarte, and D. Thers. The gaseous microstrip detector micromegas for the compass experiment at cern. *Nuclear Physics A*, 721:C1087 – C1090, 2003. 45

[49] J. Deré, Georges Charpak, A. Gigagnon, Ioannis Giomataris, D. Jourde, C. Koshowski, S. Loucatos, G. Puill, Ph. Rebourgeard, and J. P. Robert. *First beam test with Micromegas, a high rate, high resolution detector. NIM A*, 412:47–60, 1998. 45

[50] J. Deré, Gilles Barouch, A. Bay, S. Bouchigny, Georges Charpak, F. Didierjean, J. C. Faivre, Ioannis Giomataris, C. Koshowski, F. Kunne, J.-M. Le Goff, F. Lehar, Y. Lemoigne, S. Loucatos, J.-C. Lugol, A. Magnon, B. Mayer, J.-P Perroud, S. Platchkov, G. Puill, Ph. Rebourgeard, Y. Terrien, D. Thers, and H. Zaccone. *Development of a fast gaseous detector: 'MICROMEGAS'. NIM A*, 423:32–48, 1999. 45

[51] I. Giomataris, R. De Oliveira, S. Andriamonje, S. Aune, G. Charpak, P. Colas, G. Fanourakis, E. Ferrer, A. Giganon, Ph. Rebourgeard, and P. Salin. *Micromegas in a bulk. NIM A*, 560:405–408, 2006. 45, 46

[52] SiD. Letter of Intent, March 2009. http://silicondetector.org/download/attachments/46170132/SiliconDetectorLetterOfIntent.pdf. 46, 91, 97, 101

[53] ILD Concept Group. The International Large Detector Letter of Intent, March 2009. http://www.ilcild.org/documents/ild-letter-of-intent. 46, 97

[54] Calice official web page.
https://twiki.cern.ch/twiki/bin/view/CALICE/WebHome. 47, 99

[55] Rd51 home page.
http://rd51-public.web.cern.ch/rd51-public/Welcome.html. 47

[56] A. Espargilière. Micromegas, caractérisation d'un détecteur pour le futur ILC. LAPP internship report, 2007. 47

[57] Yuri Kudenko. *The near neutrino detector for the T2K experiment. Nuclear Instruments and Methods in Physics Research A*, 598, 2009. 47, 91

[58] José Repond et al. Hadron showers in a digital hadron calorimeter. *JINST 4 P10008*, 2009. 47, 100

[59] J. C. Santiard and K. Marent. *The Gassiplex0.7-2 Integrated Front-End Analog Processor for the HMPID and the Dimuon Spectrometer of ALICE.* In 5^{th} *Conference on Electronics for LHC Experiments, Snowmass, CO, USA*, pages 431 – 435, 20 – 24 Sep. 1999.
http://cdsweb.cern.ch/record/523473/files/p431.pdf. 48, 63, 78

[60] Hervé Mathez Renaud Gaglione. *DIRAC: A DIgital Readout Asic for hAdronic Calorimeter.* In *Nuclear Science Symposium Conference Record*, pages 1815 – 1819, 19 – 25 Oct. 2008. doi:10.1109/NSSMIC.2008.4774745. 49, 89, 90

[61] R. Gaglione et al. Dirac v2 : a digital readout asic for hadronic calorimeter. In *TWEPP*, pages 117–121, Nov. 2009. 49, 89

[62] S. Callier et al. Hardroc1, readout chip of the digital hadronic calorimeter of ilc. In *IEEE Nuclear Science Symposium Conference Record*, volume 3, pages 1851–1856, 2007. 49, 89

[63] R. Gaglione. Microroc and DAQ status. Presentation at CALICE collaboration meeting, 19-21 May 2011 CERN
http://indico.cern.ch/getFile.py/access?contribId=21&sessionId=7&resId=0&materialId=slides&confId=136864, 2011. 49, 90

[64] C. Adloff, D. Attie, J. Blaha, S. Cap, M. Chefdeville, P. Colas, A. Dalmaz, C. Drancourt, A. Espargiliere, R. Gaglione, R. Gallet, N. Geffroy, I. Giomataris, J. Jacquemier, Y. Karyotakis, F. Peltier, J. Prast, and G. Vouters. *MICROMEGAS chambers for hadronic calorimetry at a future linear collider. JINST*, Nov. 2009. 49

[65] Didier Roy. Manuel utilisateur, CENTAURE version 21lv 8.5, 2009.
http://www-subatech.in2p3.fr/~electro/infoaq/CENTAURE21lv85/pdfdoctxt/centaure21lv85.pdf. 53, 64, 78

[66] Magboltz cross sections web page.
http://rjd.web.cern.ch/rjd/cgi-bin/cross. 54

[67] Fabio Sauli. Principle of operation of multiwire proportionnal and drift chambers,"yellow report". CERN, 1977. 56

[68] T. Geralis, G. Fanourakis, Y. Giomataris, and K. Zachariadou. *The data acquisition of the MICROMEGAS detector for the CAST experiment*. 19 – 25 Oct. 2003. 64

[69] C. Adloff, M. Chefdeville, A. Espargilière, and R. Gaglione. *Calibration of electronic readout chains for MICROMEGAS chambers*. Technical report, LAPP Technical note, 2009. LAPP-TECH-2009-02, HAL: in2p3-00400295. 65

[70] C. Adloff, J. Blaha, J.-J. Blaising, M. Chefdeville, A. Espargiliere, and Y. Karyotakis. *Monte Carlo study of the physics performance of a digital hadronic calorimeter. Submitted to JINST (JINST_002P_0809)*, 2009. arXiv:0910.2636v1. 74

[71] Jan Blaha. Study of shower profile for a test beam. LAPP internal meeting, 2009. http://lappweb.in2p3.fr/~blaha/talks/lapp240509.pdf. 78

[72] R. Gaglione, C. Adloff, M. Chefdeville, A. Espargilière, N. Geffroy, Y. Karyotakis, and R. De Oliveira. A micromegas chamber with embedded dirac asic for hadronic calorimeter. In *1st International Conference On Micro Pattern Gaseous Detectors*, page JINST 4 P11011, 2009. 90

[73] ILD Joint steering board. Definition of the ild reference detector. http://ilcild.org/documents/misc-doc/ILDreferencedetector-20081113.pdf/view, 2008. 91

[74] T. Alexopoulos, A.A. Altintas, M. Alviggi, M. Arik, S.A. Cetin, V. Chernyatine, E. Cheu, D. Della Volpe, M. Dris, D. Fassouliotis, E.N. Gazis, R. Giordano, V. Gratchev, L. Guan, P. Iengo, P. Ioannou, C. Li, K. Johns, V. Kaushik, A. Khodinov, C. Kourkoumelis, S. Maltezos, K. Mermigka, H. Muller, K. Nikolopoulos, W. Park, S. Persembe, C. Petridou, R. Petti, V. Polychronakos, M.V. Purohit, D. Sampsonidis, G. Sekhniaidze, M. Shao, Y.J. Sun, G. Tsipolitis, R. Veenhof, X.L. Wang, J. Wotschack, S.X. Wu, T. Zhao, and Z.G. Zhao. Development of large size micromegas detector for the upgrade of the atlas muon system. *Nuclear Instruments and Methods in Physics Research Section A: Accelerators, Spectrometers, Detectors and Associated Equipment*, 617(1-3):161 – 165, 2010. 11th Pisa Meeting on Advanced Detectors - Proceedings of the 11th Pisa Meeting on Advanced Detectors. 91

[75] N. Lesparre et al. Geophysical muon imaging: feasibility and limits. *Geophysical Journal International*, 2010. doi: 10.1111/j.1365-246X.2010.04790.x. 92

[76] S. Andriamonje et al. Experimental studies of a micromegas neutron detector. *Nuclear Instruments and Methods in Physics Research A*, 481, 2002. 92

[77] G. K. Fanourakis, T. Geralis, K. Kousouris, K. Zachariadou, I. Giomataris, N. Giokaris, G. Loudos, M. Lebessi, and E. Stiliaris. The use of the micromegas

technology for a new imaging system. *Nuclear Instruments and Methods in Physics Research Section A: Accelerators, Spectrometers, Detectors and Associated Equipment*, 527(1-2):62 – 67, 2004. Proceedings of the 2nd International Conference on Imaging Technologies in Biomedical Sciences. 92

[78] Leszek Ropelewski and Maxim Titov. Leszek ropelewski, November 6, 2009. http://rd51-public.web.cern.ch/RD51-Public/Activities/Documents/CERN_ENICE_06112009.pdf. 92

[79] Maximilien Chefdeville et al. Test of a 1 m^2 micromegas prototype in a muon beam. *To be released*, 2011.
related slides:
http://indico.in2p3.fr/getFile.py/access?contribId=4&resId=0&materialId=slides&confId=5087. 95, 96, 98

[80] CLIC study group. 500 GeV to 3 tev evolution, 2010. http://clic-meeting.web.cern.ch/clic-meeting/clic500-3000.html. 98, 195

[81] José Repond et al. Measurement of positron showers with a digital hadron calorimeter. *JINST 4 P04006*, 2009. 100

[82] N. Geffroy, C. Girard, Y. Karyotakis, M. Oriunno, M. Breidenbach, and K. Krempetz. Proposal of a new hcal geometry avoiding cracks in the calorimeter. Technical report, LAPP, 2008. LAPP-TECH-2008-02
http://hal.in2p3.fr/docs/00/32/48/23/PDF/LAPP-TECH-2008-02.pdf. 101

[83] N. Geffroy, C. Girard, Y. Karyotakis, M. Oriunno, M. Breidenbach, and K. Krempetz. Proposal of a new hcal forward geometry without crack. Technical report, LAPP, 2008. LAPP-TECH-2008-07
http://hal.in2p3.fr/docs/00/33/93/57/PDF/LAPP-TECH-2008-07.pdf. 101

[84] J. Blaha, N. Geffroy, and Y. Karyotakis. Impact of dead zones on the response of a hadron calorimeter with projective and non-projective geometry. Technical report, LAPP, 2011. LAPP-TECH-2011-01 and CALICE Note CIN-018, arXiv:1102.1363. 101

[85] Alexander Pukhov. CalcHEP 2.3: MSSM, structure functions, event generation, batchs, and generation of matrix elements for other packages. *arXiv:hep-ph/0412191*, 2004. 111, 115, 119, 128, 155

[86] Daniel V. Schroeder. Beamstrahlung and QED backgrounds at future linear colliders. *SLAC-0371*.
available at http://www.slac.stanford.edu/pubs/slacreports/slac-r-371.html. 113

[87] Mark Thomson. CLIC ILD reconstruction status.
http://indico.cern.ch/getFile.py/access?contribId=10&resId=1&materialId=slides&confId=125936,
CLIC meeting, 16 Feb. 2011. 115, 192

[88] Wolfgang Kilian, Jürgen Reuter, Thorsten Ohl, and Christian Speckner. WHIZARD web page.
http://projects.hepforge.org/whizard/. 118

[89] S. Agostinelli *et al.* Geant4 - a simulation toolkit. *Nuclear Instruments and Methods A*, 506, 2003. 118

[90] Mokka home page.
http://polzope.in2p3.fr:8081/MOKKA/. 118

[91] ILC soft team. MARLIN web page.
http://ilcsoft.desy.de/portal/software_packages/marlin/index_eng.html. 118

[92] CLIC collaboration. CLIC conceptual design report vol. 2: Physics and detectors at CLIC.
https://edms.cern.ch/file/1160419/1/CLIC_CDR_Review_080911.pdf, 2011. 118

[93] Stephen D. Ellis and Davison E. Soper. Successive combination jet algorithm for hadron collisions. *Phys. Rev. D*, 48(7):3160–3166, Oct 1993. 120

[94] Andreas Hoecker, Peter Speckmayer, Joerg Stelzer, Jan Therhaag, Eckhard von Toerne, and Helge Voss. TMVA: Toolkit for Multivariate Data Analysis. *PoS*, ACAT:040, 2007. 121

[95] A. Hoecker, P. Speckmayer, J. Stelzer, J. Therhaag, E. von Toerne, and H. Voss. *TMVA 4 User Guide*, arxiv:physics/0703039 edition, November 2007.
http://tmva.sourceforge.net/docu/TMVAUsersGuide.pdf. 121, 134

[96] NEMO Collaboration. Home page.
http://www.hep.ucl.ac.uk/nemo/index.html. 127

[97] Geneviève Bélanger, Alexander Pukhov, and Géraldine Servant. Dirac neutrino dark matter. *Journal of Cosmology and Astroparticle Physics*, january 2008. doi: 10.1088/1475-7516/2008/01/009. 127, 128, 132

[98] A. Pukhov. Calchep - calculator for high energy physics - a package for evaluation of feynman diagrams, integration over multi-particle phase space, and event generation, 2005. User's manual for version 2.3.5 downloadable at:
http://theory.sinp.msu.ru/~puckov/calchep.html. 128

[99] C.B. Jackson, Géraldine Servant, Gabe Shaughnessy, Tim M.P. Tait, and Marco Taoso. Higgs in space! *Journal of Cosmology and Astroparticle Physics*, 2010(04):004, 2010. 132

[100] Pythia 8 home page.
http://home.thep.lu.se/~torbjorn/Pythia.html. 134

[101] Torbjörn Sjöstrand. Introduction to pythia8. Talk at Nordic Workshop on LHC and Beyond, June 2008.
http://home.thep.lu.se/~torbjorn/talks/nordita08.pdf. 134

[102] ROOT home page.
http://root.cern.ch. 134

[103] TMVA home page.
https://twiki.cern.ch/twiki/bin/view/TMVA/WebHome. 134

[104] Alexander Puckov. Private communications. 143

[105] Kaoru Hagiwara, Partha Konar, Qiang Li, Kentarou Mawatari, and Dieter Zeppenfeld. Graviton production with 2 jets at the lhc in large extra dimensions. *Journal of High Energy Physics*, 2008(04):019, 2008. 144

[106] W. Shockley. Currents to conductors induced by a moving point charge. *Journal of Applied Physics*, 9, October 1938. 151

[107] Simon Ramo. Currents induced by electron motion. *Proceedings of the I.R.E.*, September 1939. 151

[108] Marc Labalme. *Etude d'un système de trajectographie Micromegas pour le spectromètre dimuon d'ALICE*. PhD thesis, Université de Nantes, 2001. 151

[109] Gael Puill. *Le Développement de MICROMEGAS, Un Nouveau Détecteur Gazeux de Position à Microgrille*. PhD thesis, Université de Caen/Basse Normandie, 2000. 151

[110] Maximilien Chefdeville. *Development of a Micromegas-like gaseous detector using a pixel readout chip as collecting anode*. PhD thesis, University of Amsterdam/Université Paris Sud XI, 2009. 151

[111] Mark Thomson. Pandora PFA at high energies. Talk at IWLC 2010
http://ilcagenda.linearcollider.org/getFile.py/access?contribId=93&sessionId=56&resId=1&materialId=slides
2010. 173

List of Figures

List of Tables

Acronyms glossary

ADU Analog to Digital Unit 64

AHCAL Analog Hadronic Calorimeter 99

ALICE "A Large Ion Collider Experiment" 10

AMS Alpha Magnetic Spectrometer

ASIC Application Specific Integrated Circuit 47

ASU Active Sensor Unit 89

ATLAS "A Toroidal Large System" 91

BDT Boosted Decision Tree 121

BS Beamstrahlung 112

BX bunch crossing 113

CALICE Calorimetry for Linear Colliders Experiments 46

CDR Conceptual Design Report 118

CERN *Organisation Européenne pour la Recherche Nucléaire* 63

CLIC Compact Linear Collider 111

CMS "Compact Muon Solenoid" 10

CTF3 CLIC Test Facility 3 20

DAC Digital to Analog Count 96

DAQ Data Acquisition System 47

DESY *Deutsches Electronen Sychrotron, Hamburg* 99

DHCAL Digital Hadronic Calorimeter 47

DIF Detector Interface 47

DM Dark Matter 127

ECAL Electromagnetic Calorimeter 171

EMC Electromagnetic Compatibility 99

FNAL Fermi National Accelerator Laboratory, Illinois 9

GEANT4 GEometry ANd Tracking, version 4 118

GEM Gas Electron Multiplier 46

GUT Grand Unified Theory 9

HCAL Hadronic Calorimeter 171

ILC International Linear Collider . . . 131

ILD International Large Detector . . . 118

IPNL *Institut de Physique Nucléaire de Lyon* . . . 89

IP interaction point . . . 120

ISR Initial State Radiation . . . 111

KK Kaluza-Klein . . . 12

LAL *Laboratoire de l'Accélérateur Linéaire, Paris* . . . 47

LAPP *Laboratoire d'Annecy-le-vieux de Physique des Particules* . . . 47

LEP Large Electron Positron collider . . . 9

LHCb "LHC experiment for B physics" . . . 10

LHC Large Hadron Collider . . . 128

LHE "Les Houches Event" . . . 134

LSP Lightest Super Symmetric (SUSY) Particle . . . 13

MAMMA Muon ATLAS MICROMEGAS Activity . . . 91

MARLIN Modular Analysis & Reconstruction for the LINear collider . . . 118

MC Monte Carlo . . . 116

MGC Micro-Gap Chambers . . . 40

MIP Minimum Ionizing Particle 77

MICROMEGAS MICRO MEsh GAseous Structure 151

MPGD Micro-Pattern Gaseous Detector 92

MPV Most Probable Value 70

MSGC Micro-Strip Gas Chamber 40

MSSM Minimal Super-symmetric Standard Model 12

MVA Multi-Variate Analysis 134

MWPC Multi-Wire Proportional Counter 191

MZ_P Z' mass 128

PCB Printed Circuit Board 41

PETS Power Extraction and Transfer Structure 20

PFA Particle Flow Algorithm 120

PFO Particle Flow Object 120

PS Proton Synchrotron 66

QCD Quantum Chromo-Dynamics 14

QED Quantum Electrodynamics 25

R&D Research and Development 39

RF Radio Frequency . . . 17

RHNM Right Handed Neutrino Model . . . 127

ROC Receiver Operating Characteristic

RPC Resistive Plate Chamber . . . 46

RS Randall-Sundrum . . . 12

SLAC Stanford Linear Accelerator Center, California . . . 9

SM Standard Model . . . 114

SPS Super Proton Synchrotron . . . 65

SUSY Super Symmetric . . . 199

SUSY Super Symmetry . . . 10

SiD Silicon Detector . . . 91

TMVA Toolkit for Multi-Variate Analysis . . . 121

TOE Theory Of Everything . . . 9

TPC Time Projection Chamber . . . 91

UED Universal Extra Dimension . . . 12

WIMP Weakly Interactive Massive Particle . . . 128